As on Earth, So on Mars: Magmatic Records of Planetary Evolution

Thesis by
Juan David Hernández Montenegro

In Partial Fulfillment of the Requirements for the
Degree of
Doctor of Philosophy



CALIFORNIA INSTITUTE OF TECHNOLOGY
Pasadena, California

2026
Defended January 29, 2026

© 2026

Juan David Hernández Montenegro
ORCID: 0000-0001-7505-4650

All rights reserved

DEDICATORIA

En estos tiempos extraños, quiero dedicar esta tesis a esas personas que se ven como yo, que hablan como yo, que caminan como yo.

A quienes se acusa de criminales por tener un acento, por no parecer de aquí y por haber llegado sin permiso, aunque hayan estado aquí primero.

A las madres que han sido separadas de sus hijos, y a los niños y niñas que permanecen lejos de sus familias y de sus amigos de la escuela.

A las voces discretas que calman el llanto de hijos ajenos y los cuidan con un amor que se expresa en otra lengua.

A los brazos fuertes que, ladrillo a ladrillo, levantan ciudades enteras y que, bajo el sol y con sombreros anchos, cuidan los jardines de barrios prósperos.

A las pieles curtidas que resisten el sol de la siembra y de la cosecha para poner comida en los platos de todo un país.

A quienes luchan guerras que no son suyas, arriesgando la vida por la promesa de un papel que proteja a los suyos.

A quienes trabajan en horas que pocos ven, para que todo esté en orden cuando comienza el día.

A esa gente que también es mi gente: esta tesis es para ustedes.

DEDICATION

In these strange times, I want to dedicate this thesis to those who look like me, who speak like me, who walk like me.

To those whom some accuse of being criminals for having an accent, for not seeming to belong here, and for having arrived without permission, even though they may have been here first.

To the mothers who have been separated from their children, and to the boys and girls who remain far from their families and their friends at school.

To the quiet voices that soothe the cries of children who are not their own and care for them with a love that speaks in another language.

To the strong arms that, brick by brick, build entire cities and that, under the sun and with wide hats, tend the gardens of prosperous neighborhoods.

To the weathered skin that endures the sun of planting and harvest so that food may reach the tables of a whole country.

To those who fight wars that are not theirs, risking their lives for the promise of a document that may protect the ones they love.

To those who work at hours few people see, so that everything is in order when the day begins.

To those people who are also my people: this thesis is for you.

In memory of George Rossman...

ACKNOWLEDGEMENTS

This thesis is the result of the support, guidance, and companionship of many people who have been part of my life in very different ways. I am deeply grateful to all of them.

First and foremost, I would like to thank my two advisors, Claire Bucholz and Paul Asimow, for their invaluable mentorship and support throughout my time at Caltech. Thank you for believing in me, for encouraging me to pursue my own ideas, and for helping me turn those ideas into stronger and more meaningful scientific questions. I am undoubtedly a better scientist thanks to your brilliance and the remarkable breadth of knowledge you shared with me across the many fields I explored during my PhD. I am also deeply grateful for the trust you placed in me by allowing me to approach my research with a significant degree of independence.

I would also like to thank both my advisors and the GPS Division for the many opportunities they opened for me during my time at Caltech. Through these opportunities, I was able to experience aspects of science that I could hardly have imagined before starting my PhD. In particular, I am incredibly grateful for the opportunity to participate in NASA's Mars 2020 mission through my projects with Paul, as well as for the chance to join field trips and travel to places I could only have dreamed of visiting if it were not for Caltech and the support of my advisors. Many of these research and fieldwork opportunities were also made possible through collaborations with colleagues who became both mentors and friends. I am especially grateful to David Hernández-Uribe, Emma Sosa, Óscar Castellanos, Richard Palin, Paul Tackley, Claude Herzberg, Daniel Ibarra, Kar Wai Cheng, François Tissot, Michael Kipp, Andres Rodríguez, Dayana Schonwalder, Mariek Schmidt, Tanya Kisovski, and the PIXL team.

The administrative staff of the GPS Division also played an essential role during my PhD. I want to thank all the people who made it possible for me to conduct my research and who supported our community in countless ways. Beyond their hard work in the administrative office, they created a welcoming environment that made the department feel like a home. Whether it was taking the time to check in and ask how we were doing, keeping their doors open to hear our concerns and requests, setting up the coffee that fueled both our caffeine needs and many research conversations, providing candy, donuts, and cookies to accompany that

coffee, organizing meals and events, or sometimes simply sharing leftovers from meetings, these gestures meant a great deal. I would especially like to thank Julie Lee, Emy D'Sa, Jen Shechet, Mark Garcia, Gabriela Nuño Navarro, Claire Fredrickson, Margaret Carlos, Julia Zuckerman, and Mary Scott. I owe you all so much, and it was always a pleasure to say hello and interact with you.

I also want to thank the amazing friends I made during my time at Caltech. You made my life brighter and helped me feel welcomed and supported, even when my somewhat introverted personality got in the way. I carry you all with me, and I hope we can continue building our friendships for many years to come. To my friends Shane, Justin, Josh, Eran, Noam, Ren, David Hernández-Uribe, David Larios, Maria, Alexis, Yutian, Elvira, Daniela, Ben, Adriana, and many others: I will miss you all.

To my friends in Colombia, especially Yerson and Daniel: thank you for being there when I needed you the most. I also want to thank Juan Camilo, Estefania, Alejandra, Marianna, Andrea, Ricardo, Jorge, Javi, Yesid, and Óscar. I am sure I am forgetting many other important friends in my life, but it would not be me if I were not forgetting someone.

Finally, I want to thank my family. To my mom, my dad, and my sister: you are my greatest source of inspiration and my main motivation. Thank you for always supporting me and loving me more than I deserve. I also want to thank the rest of my family, including my aunts and cousins, and the Sosa family, who have always made me feel like part of their own.

And of course, to Emma Sosa: thank you for your generous and unconditional love. It has been wonderful to (literally) walk with you to all the places we have gone. I ask for nothing more than to keep walking through life with you and to continue having unexpected adventures together wherever this path takes us.

ABSTRACT

Magmatic processes play a central role in the thermal, chemical, and hydrologic evolution of rocky planets by linking deep planetary interiors to their crusts and surface environments. This thesis integrates igneous and metamorphic petrology, stable isotope geochemistry, and thermodynamic modeling to investigate how magmatic rocks record the coupled evolution of planetary interiors and surface environments on both Earth and Mars. On Earth, I focus on sediment-derived magmas—strongly peraluminous granites (SPGs) and associated pelitic migmatites—which form by partial melting of metasedimentary crust and preserve geochemical signatures inherited from surface-processed materials. On Mars, I focus on primary and weakly evolved mafic magmas, which provide direct constraints on mantle temperatures, crustal differentiation, and the role of magmatism in sustaining subsurface water. The first part of the thesis examines how sedimentary signatures are transferred into granitic magmas during crustal anatexis and what these signatures reveal about Earth's long-term surface evolution. Iron isotope measurements and petrological modeling of the Neoarchean Ghost Lake Batholith show that partial melting largely homogenizes extreme sedimentary isotopic heterogeneity while preserving a resolvable record of bulk source composition, establishing SPGs as robust archives of secular iron isotope evolution in siliciclastic sediments. Building on this framework, triple-oxygen-isotope analyses of garnet in sediment-derived granites and migmatites are used to reconstruct weathering temperatures and meteoric water compositions from the Neoarchean to the Mesozoic, revealing discrete climate regimes linked to atmospheric oxidation, glaciation, and supercontinent cycles and demonstrating that sediment-derived magmas provide a lithology-integrated archive of Earth's surface environments. The second part of the thesis addresses how Martian magmatism records the thermal evolution of a stagnant-lid planet and its interaction with the hydrosphere. I introduce PRIMARSMELT, a new petrological modeling tool for reconstructing primary magma compositions and mantle potential temperatures from Martian meteorite and rover data. Application of this approach indicates that Martian mantle temperatures have remained nearly constant—or may have increased—through time, consistent with inefficient heat loss in the absence of plate tectonics. I further show that, although Martian magmas inevitably generate water-rich fluids during differentiation, fluid–rock reactions rapidly seal permeability, implying that any present-day liquid water in the Martian crust must be

continuously supplied by active magmatic degassing. Finally, mineral-scale observations from the Perseverance rover in Jezero crater demonstrate that ultramafic cumulates of the Séítah formation and basaltic lavas of the Máaz formation formed within the same magmatic system, linking intrusive and extrusive processes and illustrating how crystal accumulation and differentiation generate lithologic diversity in the Martian crust. Together, these studies show how magmatic processes record the thermal evolution of planetary interiors and mediate their interactions with crustal and hydrologic systems, providing a comparative framework for understanding how rocky planets build crusts, cycle volatiles, and evolve toward—or away from—habitability.

PUBLISHED CONTENT AND CONTRIBUTIONS

Hernández-Montenegro, J. D., P. D. Asimow, and C. T. Herzberg, Estimating Primary Magmas From Mars With PRIMARSMELT: Implications for the Petrogenesis of Some Martian Rocks and the Thermal Evolution of Mars, *Journal of Geophysical Research: Planets*, *129*(11), e2024JE008,508, doi: 10.1029/2024JE008508,

Author contributions: J.D. Hernández-Montenegro developed the PRIMARSMELT modeling framework under the supervision of P.D. Asimow. J.D. Hernández-Montenegro performed the petrological modeling and thermal evolution analysis, and wrote the manuscript. P.D. Asimow and C.T. Herzberg contributed to conceptual development, interpretation of results, and manuscript revisions., 2024a.

Hernández-Montenegro, J. D., C. E. Bucholz, E. S. Sosa, M. A. Kipp, and F. L. H. Tissot, Iron isotope fractionation during partial melting of metapelites and the generation of strongly peraluminous granites, *Geochimica et Cosmochimica Acta*, *380*, 112–130, doi:10.1016/j.gca.2024.07.016,

Author contributions: J.D. Hernández-Montenegro and Claire E. Bucholz conceived the study. J.D. Hernández-Montenegro conducted iron isotope measurements, performed petrological and isotope-fractionation modeling, interpreted the results, and wrote the manuscript. Coauthors contributed to discussions, analytical support, and manuscript revisions., 2024b.

Hernández-Montenegro, J. D., et al., Petrogenesis of the olivine cumulate outcrop *Issole* – The missing link between the Séítah and Máaz formations in Jezero crater, Mars, *Icarus*, *437*, 116,620, doi:10.1016/j.icarus.2025.116620,

Author contributions: J.D. Hernández-Montenegro performed petrological modeling and geochemical interpretation of PIXL compositional data, contributed to data analysis and interpretation, and wrote the manuscript. Coauthors contributed rover data acquisition, mineralogical interpretation, extensive discussions, and manuscript revisions., 2025.

TABLE OF CONTENTS

Acknowledgements vi
Abstract viii
Published Content and Contributions x
Table of Contents x
List of Illustrations xii
List of Tables xvi
Chapter I: Introduction 1
Chapter II: Iron isotope fractionation during partial melting of metapelites and the generation of strongly peraluminous granites 9
Chapter III: Triple-oxygen isotopes in granitic magmas reveal major shifts in Earth's weathering conditions through time 80
Chapter IV: Estimating primary magmas from Mars with PRIMARSMELT: Implications for the petrogenesis of some Martian rocks and the thermal evolution of Mars 134
Chapter V: Active magmatic degassing is required to sustain liquid water in the Martian crust 201
Chapter VI: Petrogenesis of the olivine cumulate outcrop *Issole* – the missing link between the Séítah and Máaz formations in Jezero crater, Mars 225

LIST OF ILLUSTRATIONS

Number *Page*

2.1 Temporal variation of iron isotope compositions in sedimentary and igneous rocks 11
2.2 Geological Map of the Sioux Lookout Terrane, Ontario, Canada . . . 17
2.3 Major and trace element ratios for samples from the GLB. 24
2.4 Major element compositions of metasedimentary rocks 25
2.5 δ^{56}Fe of rocks from the GLB and the Zealand unit 26
2.6 Phase equilibrium modeling results metapelite SP-16-16 28
2.7 Predicted iron isotope fractionation between granitic melts and residues for partial melting of metapelite SP-16-16 at 0.4 GPa 31
2.8 Iron isotope fractionation model sensitivity test for metapelite SP-16-16 at 0.4 GPa 39
2.9 Predicted iron isotope compositions for granitic SPG melts and residues for metapelite SP-16-16 at 0.4 GPa varying oxygen fugacity . 41
2.10 Rayleigh fractionation example of melt and corresponding cumulate . 45
2.11 Literature comparison of δ^{56}Fe in Archean-Proterozoic sedimentary rocks and minerals 49
S2.1 Fe isotope compositions of all measured samples 66
S2.2 Phase equilibrium modeling results for metapelite SP-16-16 from FMQ-2 to FMQ+2 67
S2.3 Phase equilibrium modeling results for metapelite SP-16-16 from 600°C to 1000°C, water undersaturated 69
S2.4 Phase equilibrium modeling results for metapelite SP-16-16 from 600°C to 1000°C, minimally water-saturated 70
S2.5 Predicted equilibrium iron isotope fractionation between granitic melts and residues for metapelite SP-16-16 71
S2.6 Equilibrium isotopic fractionation considering batch melting and melt loss events 74
S2.7 Estimated $\Delta^{56}Fe_{fluid-melt}$ values between 669 °C (solidus) and 1000 °C for melt compositions with $Fe^{3+}/\Sigma Fe = 0$ and $Fe^{3+}/\Sigma Fe = 0.5$ 76
S2.8 Iron isotope composition vs. geochemistry of metasedimentary samples 76
S2.9 Iron isotope composition vs. whole-rock chemistry. 77

3.1 Isotopic compositions of granitic garnets and calculated bulk siliciclastic sediments through time. 84
3.2 Isotopic compositions of granitic garnets and calculated bulk siliciclastic sediments in triple oxygen isotope space. 86
3.3 Calculated weathering temperatures through time. 87
S3.1 Bellows pressure versus sample weight. 108
S3.2 Modeled $\Delta^{18}O$ fractionation between phases produced during anatexis and the sedimentary protolith. 111
4.1 Schematic flow chart of PRIMARSMELT algorithm 138
4.2 Melt fraction vs. anorthite component 143
4.3 Literature solidus expressions for Martian mantle compared to PRIMARSMELT solidus and liquidus 147
4.4 Measured vs. predicted temperatures for experimental data 148
4.5 $K_D^{Ol/Liq}$ vs. liquid composition 150
4.6 F_{AFM} primary magma solutions for all basaltic and olivine-phyric shergottites 157
4.7 F_{AFM} primary magma solutions for NWA 7034/7533 igneous clasts . 157
4.8 F_{AFM} primary magma solutions for chassignite meteorites 158
4.9 F_{AFM} primary magma solutions Gusev crater and Jezero crater basalts 159
4.10 F_{AFM} primary magma solutions for Gale crater basalts 160
4.11 Estimated mantle potential temperatures for Martian basalts vs. inferred age 169
4.12 Estimated initial melting pressure and melting depth for Martian basalts vs. inferred age 172
S4A.1 Mg# vs. Mg/Ca diagram 190
S4.1 F_{AFM} primary magma solutions for all basaltic and olivine-phyric shergottites assuming a mantle source Mg# 79 192
S4.2 F_{AFM} primary magma solutions for NWA 7034/7533 igneous clasts assuming mantle source Mg# = 79 193
S4.3 F_{AFM} primary magma solutions chassignite meteorites assuming mantle source Mg# = 79 193
S4.4 F_{AFM} primary magma solutions Gusev crater and Jezero crater basalts assuming mantle source Mg# = 79 194
S4.5 F_{AFM} primary magma solutions for Gale crater basalts assuming mantle source Mg# = 79 194
5.1 Seismic data and cartoon interpretation from InSight data 202

5.2 Volatile exsolution and TAS diagrams for Martian magams 204
5.3 Evolution of permeability and fluid flux during conductive cooling . . 206
5.4 Estimated sealing time of the permeable column as a function of model parameters 208
S5.1 TAS diagram grid of liquid lines of descent for Martian magmas assuming DW mantle composition 216
S5.2 TAS diagram grid of liquid lines of descent for Martian magmas assuming YM mantle composition 217
S5.3 Schematic representation of reactive flow in a crustal column. 218
6.1 Overview of Jezero crater and study area 227
6.2 Ternary diagrams showing compositional and mixing trends for Quartier basalts 236
6.3 Compositional maps from PIXL data in Quartier 1 and Quartier 2 scan areas 237
6.4 Overview images of the Quartier abrasion patch in Issole 262
6.5 Compositional diagrams of primary minerals in Quartier and other Martian cumulates 263
6.6 Petrographic textures within the Quartier abrasion patch and comparable textures from Martian meteorites and magma cooling experiments 264
6.7 'Pseudoliquidus' diagram for intercumulus melts produced by partial Quartier melting and TAS diagram 265
6.8 Modal boxes of phases produced by equilibrium crystallization of calculated intercumulus melts for different melt proportions 266
6.9 Modal boxes of phases produced by fractional crystallization of calculated intercumulus melts for different melt proportions 267
6.10 Bivariate diagrams of compositional changes during fractional and equilibrium crystallization of preferred Quartier parental melt 268
6.11 Schematic illustration of the emplacement model for Séítah olivine cumulates as an igneous intrusion 269
S6.1 Diffraction map of the two PIXL scan regions 278
S6.2 Reclassified image from MCC and XRF data 279
S6.3 'Pseudoliquidus' diagram of intercumulus melts produced by Quartier partial melting and TAS diagram with $Fe^{3+}/\Sigma Fe$ of 0.10 280
S6.4 'Pseudoliquidus' diagram of intercumulus melts produced by Quartier partial melting and TAS diagram with $Fe^{3+}/\Sigma Fe$ of 0.15 281

S6.5 Modal boxes of phases produced by equilibrium crystallization of intercumulus melts for different melt proportions with $Fe^{3+}/\Sigma Fe = 0.10$ 282
S6.6 Modal boxes of phases produced by fractional crystallization of intercumulus melts. $Fe^{3+}/\Sigma Fe = 0.05$ 283
S6.7 Modal boxes of phases produced by fractional crystallization of intercumulus melts. $Fe^{3+}/\Sigma Fe = 0.10$ 284
S6.8 Modal boxes of phases produced by fractional crystallization of intercumulus melts. $Fe^{3+}/\Sigma Fe = 0.15$ 285
S6.9 Bivariate diagrams for fractional equilibrium crystallization of the preferred Quartier parental melt. $Fe^{3+}/\Sigma Fe = 0.05$ 286
S6.10 Bivariate diagrams for fractional equilibrium crystallization of the preferred Quartier parental melt. $Fe^{3+}/\Sigma Fe = 0.10$ 287
S6.11 Bivariate diagrams for fractional equilibrium crystallization of the preferred Quartier parental melt. $Fe^{3+}/\Sigma Fe = 0.15$ 288

LIST OF TABLES

Number *Page*

2.1 Force constants for Fe-carrying phases. 62
2.2 Iron isotope compositions of granites, metapelites, sulfides, and geostandards. 63
S3 Triple oxygen isotope compositions of S-type granites, leucosomes, and diatexites analyzed in this study. 123
S5.1 Parameter space explored in model runs. 213
6.1 Quartier major element compositions. 261
6.2 Average olivine and augite compositions. 262
6.3 Average feldspar and spinel compositions. 270
6.4 Intercumulus melt compositions obtained from partial melting of the Quartier bulk composition. Oxides are expressed in weight percent. . 271
6.5 Predicted compositions of primary phases during equilibrium crystallization of intercumulus melts ($Fe^{3+}/\Sigma Fe = 0.05$). 272
6.6 Predicted compositions of primary phases during fractional crystallization of intercumulus melts ($Fe^{3+}/\Sigma Fe = 0.05$). 274

Chapter 1

INTRODUCTION

Magmatic processes play a central role in shaping the physical and chemical evolution of rocky planets. By transferring material and energy between the deep interior and the surface, magmatism links mantle dynamics, crust formation, and volatile cycling, defining the long-term differentiation and thermal evolution of a planet (*Schubert et al.*, 2001). This transfer of energy from the deep interior to the surface constitutes the fundamental engine that drives tectonic processes and elemental cycling on terrestrial planets, exerting a first-order control on their climate evolution and habitability. Crucially, the diverse magmatic processes generated by this engine leave geochemical and isotopic signatures in rocks that record the physicochemical conditions prevailing at the time of their formation. Igneous rocks are therefore not merely records of melting and crystallization, but archives of how planets differentiate, cool, and interact with their surface environments through time.

Among terrestrial planets, Earth and Mars provide our most accessible and best-studied examples of worlds in which crust–mantle differentiation and magmatic activity have powered long-lived geological systems and left enduring imprints on their surfaces and rock records. Both are rocky bodies with silicate mantles and metallic cores; both preserve evidence for prolonged volcanism; and both record extensive interactions between fluids and crustal rocks. They also share several first-order physical similarities: the length of a Martian sol is nearly identical to that of an Earth day, and the surfaces of both planets are characterized by volcanoes, canyons, impact basins, and sedimentary deposits shaped by water. Yet despite these similarities, Earth and Mars have followed strikingly different evolutionary paths. Earth developed plate tectonics, a compositionally diverse continental crust (*Hawkesworth and Kemp*, 2006), and a climate system that has sustained surface liquid water—and life—for billions of years (*Nisbet and Sleep*, 2001). Mars, in contrast, appears to have lost most of its early atmosphere and hydrosphere, ceased global tectonic activity early in its history, and today preserves a predominantly basaltic crust and a cold, dry surface (*Nimmo and Stevenson*, 2000; *Breuer and Spohn*, 2003; *Sleep*, 1994). Whether Mars ever hosted life remains an open question, but recent observations by the Perseverance rover suggest that some Martian rocks may preserve potentially biogenic signatures (*Hurowitz et al.*, 2025).

Many of the differences between the two planets ultimately reflect first-order contrasts in planetary size, heat budget, and accretion history. Earth is roughly twice the diameter of Mars and an order of magnitude more massive, resulting in higher internal pressures and long-lived mantle convection. Mars, with its lower gravity and smaller size, is thought to have cooled more rapidly and entered a stagnant-lid tectonic regime early in its history (*Nimmo and Stevenson*, 2000; *Taylor et al.*, 2006). However, differences in bulk composition also play a critical role. Earth accreted primarily from relatively reduced and volatile-depleted materials, sequestering most of its iron into a large metallic core. Mars, in contrast, likely formed from more oxidized building blocks, resulting in a smaller core and a mantle substantially richer in iron oxide (*Dreibus and Wänke*, 1984). This compositional distinction implies that partial melting of the Martian mantle naturally produces more iron-rich magmas and, by extension, a more iron-rich crust.

These planetary-scale differences between Earth and Mars are expressed most clearly in crustal composition and mineralogy. On Earth, repeated cycles of melting, differentiation, and crustal reworking have produced a chemically stratified crust, including the uniquely silica-rich continental crust (*Rudnick and Gao*, 2003; *Hawkesworth and Kemp*, 2006; *Hacker et al.*, 2015). On Mars, magmatism appears to have been dominated by basaltic and ultramafic compositions (*Taylor*, 2013), with only limited evidence for large-scale production of evolved, continental-like lithologies (*Wray et al.*, 2013; *Sautter et al.*, 2015). Understanding why these two planets diverged so profoundly requires understanding not only how magmas form, but also how they interact with crustal materials, volatiles, and surface reservoirs, and how these interactions have changed through time.

In this thesis, I integrate igneous and metamorphic petrology with geochemical and thermodynamic modeling to investigate complementary aspects of the evolution of Earth and Mars using key rock types from their magmatic records. On Earth, I focus on a distinctive class of granitic magmas generated by partial melting of siliciclastic sedimentary rocks: strongly peraluminous granites (SPGs) and associated pelitic migmatites. On Mars, I focus on reconstructing the compositions and formation conditions of primary magmas using data from Martian meteorites and *in situ* compositional analyses. These primary magmas provide quantitative constraints on mantle temperatures through time, crustal differentiation pathways, and the role of magmatism in sustaining—or failing to sustain—liquid water in the subsurface.

In the first part of this thesis, I explore how sedimentary signatures are transferred

into granitic magmas during partial melting and what these signatures reveal about Earth's long-term surface evolution. This work focuses on SPGs, characterized by an excess of aluminum relative to alkalis and calcium and by the presence of aluminous phases such as garnet, muscovite, cordierite, or sillimanite (*Bucholz and Spencer*, 2019). Unlike metaluminous or weakly peraluminous granites, which commonly form through differentiation of mantle-derived or lower-crustal igneous magmas, SPGs are produced predominantly by anatexis of metasedimentary crust (*Chappell and White*, 1992; *Sylvester*, 1998). Their generation is intimately linked to pelitic migmatites, which are hybrid rocks containing both an igneous domain (the strongly peraluminous melt) and a metamorphic domain (the residual, partially melted sediment) (*Brown*, 2013).

Because SPGs and the magmas hosted in migmatites are derived from materials that have interacted with fluids at Earth's surface, they are not simply products of igneous differentiation. Instead, they inherit chemical and isotopic signatures from sedimentary processes and thus occupy a unique position at the interface between surface environments and the deep crust. As a result, SPGs and migmatites encode information about past climates, surface conditions, and long-term interactions among the crust, hydrosphere, and atmosphere (e.g., *Mikhail et al.*, 2023; *Bucholz*, 2022; *Bucholz and Hernández-Montenegro*, 2025), which is not preserved in mantle-derived igneous rocks.

In Chapter 2, I investigate iron isotope fractionation during partial melting of metapelites and the generation of SPGs. Although sedimentary rocks exhibit large iron isotope variability—especially in the Archean and Proterozoic—it remains unclear how much of this variability survives metamorphism and anatexis. By combining high-precision iron isotope measurements with phase-equilibrium and isotope-fractionation modeling, this chapter shows that partial melting largely homogenizes extreme sedimentary heterogeneity while preserving a resolvable record of bulk source composition. Although iron isotopes in SPGs are largely influenced by melting conditions and by secondary processes during magma segregation and granite emplacement, their variability is significantly smaller than that of the sedimentary record, making SPGs a promising proxy for tracking secular changes in the iron isotope composition of siliciclastic sediments.

Chapter 3 extends this logic to the oxygen isotope system and its application to paleoclimate reconstruction. By analyzing triple-oxygen-isotope compositions of garnet in sediment-derived granites and migmatites and inverting these data through

thermodynamic modeling, this chapter reconstructs weathering temperatures and meteoric water compositions from the Neoarchean to the Mesozoic. The results reveal discrete climate regimes at various points in Earth's history and demonstrate that granitic magmas can serve as a previously under-exploited, lithology-integrated archive of Earth's surface conditions. Together, these two chapters establish sediment-derived magmatism as a fundamental bridge between surface processes and the deep crust.

The second part of this thesis turns to Mars and examines how magmatism both records and regulates the thermal and hydrologic evolution of a stagnant-lid planet. This work focuses on primary and weakly evolved mafic magmas, which provide the most direct constraints on the thermal state of the Martian mantle. Primary magmas are melts that segregate directly from the mantle and have not yet been substantially modified by crustal differentiation (*O'Hara*, 1965); their major-element compositions therefore retain quantitative information about the pressure, temperature, and extent of partial melting (e.g., *Lee et al.*, 2009; *Herzberg and Gazel*, 2009; *Herzberg and Asimow*, 2015). Reconstructing primary magma compositions from Martian meteorites and rover-based analyses thus allows mantle potential temperatures to be estimated and the thermal evolution of Mars to be tracked through time.

Martian magmatism is also intimately linked to the planet's hydrologic history. Orbital and geomorphological observations indicate that liquid water was once abundant at the surface (*Scheller et al.*, 2022), while recent seismic data suggest that fluids may still persist in the crust today (*Wright et al.*, 2024; *Katayama and Akamatsu*, 2024; *Knapmeyer-Endrun et al.*, 2025). In parallel, observations by the Perseverance rover in Jezero crater have revealed ultramafic cumulate rocks closely associated with basaltic lava flows, demonstrating that Martian magmatic systems undergo crystal accumulation and differentiation in the crust in ways analogous to terrestrial layered intrusions (*Liu et al.*, 2022; *Schmidt et al.*, 2025). Together, these observations motivate an integrated petrological framework for understanding how Martian magmas are generated in the mantle, evolve in the crust, and interact with—and potentially sustain—water in the subsurface.

Chapter 4 introduces PRIMARSMELT, a new petrological modeling tool designed to reconstruct primary magma compositions and mantle potential temperatures from Martian meteorite and rover data. Applying this tool reveals that Martian mantle temperatures have remained nearly constant—or may even have increased—over time, consistent with inefficient heat loss in the absence of plate tectonics. These

results contrast with plume-dominated interpretations of Martian volcanism and instead point to a long-lived, sluggishly cooling mantle, challenging current views of how Mars has thermally evolved.

In Chapter 5, I address one of the most consequential implications of Martian magmatism: its relationship to subsurface water. Motivated by seismic evidence from the InSight mission suggesting the possible presence of mid-crustal fluids, this chapter combines thermodynamic models of magma degassing with physical models of fluid–rock reaction and permeability evolution. The results show that, although Martian magmas inevitably produce water-rich fluids during crystallization, these fluids are rapidly consumed by hydration reactions that seal permeability on geologically short timescales. Sustained liquid water in the Martian crust therefore requires continuous resupply by active magmatism, directly linking the present-day hydrologic state of Mars to its ongoing thermal and magmatic evolution.

Finally, Chapter 6 uses mineral-scale observations from the Perseverance rover to examine how Martian magmatic systems differentiate in the crust. By combining compositional and textural data from the PIXL instrument with thermodynamic modeling, this chapter shows that ultramafic cumulates of the Séítah formation and basaltic lavas of the Máaz formation in Jezero crater likely formed from the same magmatic system, linking intrusive and extrusive processes in the Martian crust and illustrating how crystal accumulation and melt evolution generate lithologic diversity even on a dominantly basaltic planet.

Taken together, these studies investigate how magmatic processes record the thermal evolution of planetary interiors and their interactions with crustal and hydrologic systems. On Earth, sediment-derived granites preserve evidence for how surface environments, climate, and crustal composition coevolved over billions of years. On Mars, mafic magmas record the thermal history of the mantle and constrain the planet's capacity to sustain water in its crust. Although these two planets share common physical principles, their contrasting sizes, compositions, and tectonic regimes have driven them toward profoundly different outcomes. By integrating petrology, geochemistry, and planetary science, this thesis aims to illuminate how those differences arose—and, more broadly, how rocky planets build crusts, cycle volatiles, and evolve toward or away from habitability.

References

Breuer, D., and T. Spohn, Early plate tectonics versus single-plate tectonics on Mars: Evidence from magnetic field history and crust evolution, *Journal of Geophysical Research: Planets*, *108*(E7), doi:10.1029/2002JE001999, 2003.

Brown, M., Granite: From genesis to emplacement, *GSA Bulletin*, *125*(7-8), 1079–1113, doi:10.1130/B30877.1, 2013.

Bucholz, C. E., Coevolution of sedimentary and strongly peraluminous granite phosphorus records, *Earth and Planetary Science Letters*, *596*, 117,795, 2022.

Bucholz, C. E., and J. D. Hernández-Montenegro, Temporal variation in oxygen isotopes of peraluminous granites derived from sedimentary sources, *Lithos*, *492–493*, 107,864, doi:10.1016/j.lithos.2024.107864, 2025.

Bucholz, C. E., and C. J. Spencer, Strongly Peraluminous Granites across the Archean–Proterozoic Transition, *Journal of Petrology*, *60*(7), 1299–1348, doi:10.1093/petrology/egz033, 2019.

Chappell, B. W., and A. J. R. White, I- and S-type granites in the Lachlan Fold Belt, *Earth and Environmental Science Transactions of The Royal Society of Edinburgh*, *83*(1-2), 1–26, doi:10.1017/S0263593300007720, 1992.

Dreibus, G., and H. Wänke, Accretion of the Earth and the inner planets, in *Proceedings of the 27th International Geological Congress*, vol. 11, pp. 1–20, 1984.

Hacker, B. R., P. B. Kelemen, and M. D. Behn, Continental Lower Crust, *Annual Review of Earth and Planetary Sciences*, *43*(Volume 43, 2015), 167–205, doi:10.1146/annurev-earth-050212-124117, 2015.

Hawkesworth, C. J., and A. I. S. Kemp, Evolution of the continental crust, *Nature*, *443*(7113), 811, 2006.

Herzberg, C., and P. D. Asimow, PRIMELT3 MEGA.XLSM software for primary magma calculation: Peridotite primary magma MgO contents from the liquidus to the solidus, *Geochemistry, Geophysics, Geosystems*, *16*(2), 563–578, doi:10.1002/2014GC005631, 2015.

Herzberg, C., and E. Gazel, Petrological evidence for secular cooling in mantle plumes, *Nature*, *458*(7238), 619–622, doi:10.1038/nature07857, 2009.

Hurowitz, J. A., et al., Redox-driven mineral and organic associations in Jezero Crater, Mars, *Nature*, *645*(8080), 332–340, doi:10.1038/s41586-025-09413-0, 2025.

Katayama, I., and Y. Akamatsu, Seismic discontinuity in the Martian crust possibly caused by water-filled cracks, *Geology*, *52*(12), 939–942, doi:10.1130/G52369.1, 2024.

Knapmeyer-Endrun, B., et al., Porosity and hydrous alteration of the Martian crust from InSight seismic data, *Physics of the Earth and Planetary Interiors*, *366*, 107,383, doi:10.1016/j.pepi.2025.107383, 2025.

Lee, C.-T. A., P. Luffi, T. Plank, H. Dalton, and W. P. Leeman, Constraints on the depths and temperatures of basaltic magma generation on Earth and other terrestrial planets using new thermobarometers for mafic magmas, *Earth and Planetary Science Letters*, *279*(1-2), 20–33, doi:10.1016/j.epsl.2008.12.020, 2009.

Liu, Y., et al., An olivine cumulate outcrop on the floor of Jezero crater, Mars, *Science*, doi:10.1126/science.abo2756, 2022.

Mikhail, S., E. E. Stüeken, T. J. Boocock, M. Athey, N. Mappin, A. J. Boyce, J. Liebmann, C. J. Spencer, and C. E. Bucholz, Strongly peraluminous granites provide independent evidence for an increase in biomass burial across the Precambrian–Phanerozoic boundary, *Geology*, *52*(1), 87–91, doi:10.1130/G51800.1, 2023.

Nimmo, F., and D. J. Stevenson, Influence of early plate tectonics on the thermal evolution and magnetic field of Mars, *Journal of Geophysical Research: Planets*, *105*(E5), 11,969–11,979, doi:10.1029/1999JE001216, 2000.

Nisbet, E. G., and N. H. Sleep, The habitat and nature of early life, *Nature*, *409*(6823), 1083–1091, 2001.

O'Hara, M. J., Primary magmas and the origin of basalts, *Scottish Journal of Geology*, *1*(1), 19–40, doi:10.1144/sjg01010019, 1965.

Rudnick, R. L., and S. Gao, Composition of the continental crust, *Treatise on geochemistry*, *3*, 659, 2003.

Sautter, V., et al., In situ evidence for continental crust on early Mars, *Nature Geoscience*, *8*(8), 605–609, doi:10.1038/ngeo2474, 2015.

Scheller, E. L., et al., Aqueous alteration processes in Jezero crater, Mars—implications for organic geochemistry, *Science*, *378*(6624), 1105–1110, doi:10.1126/science.abo5204, 2022.

Schmidt, M. E., et al., Diverse and highly differentiated lava suite in Jezero crater, Mars: Constraints on intracrustal magmatism revealed by Mars 2020 PIXL, *Science Advances*, *11*(4), eadr2613, doi:10.1126/sciadv.adr2613, 2025.

Schubert, G., D. L. Turcotte, and P. Olson, *Mantle Convection in the Earth and Planets*, Cambridge University Press, 2001.

Sleep, N. H., Martian plate tectonics, *Journal of Geophysical Research: Planets*, *99*(E3), 5639–5655, doi:10.1029/94JE00216, 1994.

Sylvester, P. J., Post-collisional strongly peraluminous granites, *Lithos*, *45*(1), 29–44, doi:10.1016/S0024-4937(98)00024-3, 1998.

Taylor, G. J., The bulk composition of Mars, *Geochemistry*, *73*(4), 401–420, doi: 10.1016/j.chemer.2013.09.006, 2013.

Taylor, G. J., et al., Bulk composition and early differentiation of Mars, *Journal of Geophysical Research: Planets*, *111*(E3), doi:10.1029/2005JE002645, 2006.

Wray, J. J., S. T. Hansen, J. Dufek, G. A. Swayze, S. L. Murchie, F. P. Seelos, J. R. Skok, R. P. Irwin III, and M. S. Ghiorso, Prolonged magmatic activity on Mars inferred from the detection of felsic rocks, *Nature Geoscience*, *6*(12), 1013–1017, 2013.

Wright, V., M. Morzfeld, and M. Manga, Liquid water in the Martian mid-crust, *Proceedings of the National Academy of Sciences*, *121*(35), e2409983,121, doi: 10.1073/pnas.2409983121, 2024.

Chapter 2

IRON ISOTOPE FRACTIONATION DURING PARTIAL MELTING OF METAPELITES AND THE GENERATION OF STRONGLY PERALUMINOUS GRANITES

Hernández-Montenegro, J. D., C. E. Bucholz, E. S. Sosa, M. A. Kipp, and F. L. H. Tissot, Iron isotope fractionation during partial melting of metapelites and the generation of strongly peraluminous granites, *Geochimica et Cosmochimica Acta*, *380*, 112–130, doi:10.1016/j.gca.2024.07.016,

Author contributions: J.D. Hernández-Montenegro and Claire E. Bucholz conceived the study. J.D. Hernández-Montenegro conducted iron isotope measurements, performed petrological and isotope-fractionation modeling, interpreted the results, and wrote the manuscript. Coauthors contributed to discussions, analytical support, and manuscript revisions., 2024.

Abstract

The large variability in Fe isotope ratios of sedimentary rocks (particularly those from the Archean and Proterozoic) contrasts with that of igneous rocks, which display a much more limited range in values. Notably, among igneous rocks, those inferred to form via partial melting of siliciclastic sediments – strongly peraluminous granites (SPGs) – exhibit greater variability in their Fe isotope compositions, suggesting SPGs may capture isotopic variations in the sedimentary record. However, the extent and mechanisms of iron isotope fractionation between SPGs and their source remain poorly understood. Our study integrates iron isotope analyses with petrological modeling to investigate equilibrium isotopic fractionation during generation of SPG magmas. As a case study, we focus on the Neoarchean Ghost Lake Batholith and the adjacent metasedimentary rocks in Ontario, Canada. These units represent an internally differentiated SPG batholith and metamorphosed sedimentary rocks interpreted as the source of the batholith. We measured δ^{56}Fe compositions of SPG samples, metasedimentary rocks, and a restitic rock. Sulfide grains were also measured in four metapelite samples and a granite sample. We find no correlation between the δ^{56}Fe composition of metasedimentary rocks and their metamorphic grade, indicating iron isotopes behave as a closed sys-

tem during metamorphism. Modeling results show that iron isotopes in SPGs from the Ghost Lake batholith are consistent with equilibrium fractionation during biotite dehydration melting, with predicted δ^{56}Fe values for melts and restitic assemblages mainly controlled by the source composition. Our results predict negligible isotopic fractionation between the residue and the source, whereas~0.177-0.277 ‰ is expected between SPG melts and the residue, accounting for high δ^{56}Fe values in granite samples. Lower δ^{56}Fe values may indicate that some granites represent mixtures of melt and cumulus material or result from assimilation of restite or source/host rock. However, despite deviations from pure equilibrium fractionation, the variability in δ^{56}Fe values for SPGs is about one order of magnitude smaller than that seen in the sedimentary record for the Archean and Proterozoic (~0.2 ‰ vs. > 2 ‰). We posit that this narrower range of isotopic variation in SPGs results from metamorphism and partial melting, which can homogenize large isotopic variations in sedimentary protoliths. Thus, SPGs represent reliable archives for the bulk iron isotope evolution of siliciclastic sedimentary rocks through time.

1. Introduction

Numerous studies have examined iron isotopes in sedimentary rocks to probe variations in the marine Fe cycle due to the sensitivity of this system to variations in dissolved O_2 and S concentrations (e.g., *Johnson et al.*, 2003, 2008; *Matthews et al.*, 2004; *Rouxel et al.*, 2005; *Yamaguchi et al.*, 2005; *Hofmann et al.*, 2009; *Bekker et al.*, 2010; *Planavsky et al.*, 2012; *Busigny et al.*, 2014; *Marin-Carbonne et al.*, 2014, 2020; *Yoshiya et al.*, 2015b; *Heard et al.*, 2020; *Ostrander et al.*, 2022; *Dupeyron et al.*, 2023). Variability of several permil in δ^{56}Fe (where $\delta^{i}Fe_{unknown}$ = $[(^{i}Fe/^{54}Fe)_{unknown}/(^{i}Fe/^{54}Fe)_{standard}$ - 1] $\times 10^3$) has been documented in bulk-rock analyses and mineral separates (e.g., *Rouxel et al.*, 2005; *Dauphas et al.*, 2017; *Heard and Dauphas*, 2020; *Ostrander et al.*, 2022; *Dupeyron et al.*, 2023; Figure 1a). In particular, temporal trends in iron isotope ratios of sedimentary rocks and pyrites have been widely interpreted to reflect the evolution of the global oceanic Fe cycle and its relationship to changes in atmospheric oxygenation through time (*Beard and Johnson*, 2004; *Dauphas et al.*, 2004, 2017; *Johnson et al.*, 2004; *Rouxel et al.*, 2005; *Anbar and Rouxel*, 2007; *Planavsky et al.*, 2012; *Busigny et al.*, 2014; *Ostrander et al.*, 2022; *Dupeyron et al.*, 2023).

One complexity that arises in interpreting Fe isotope compositions from sedimentary rocks is comparing data from different scales of analysis (i.e., bulk-rock, bulk-

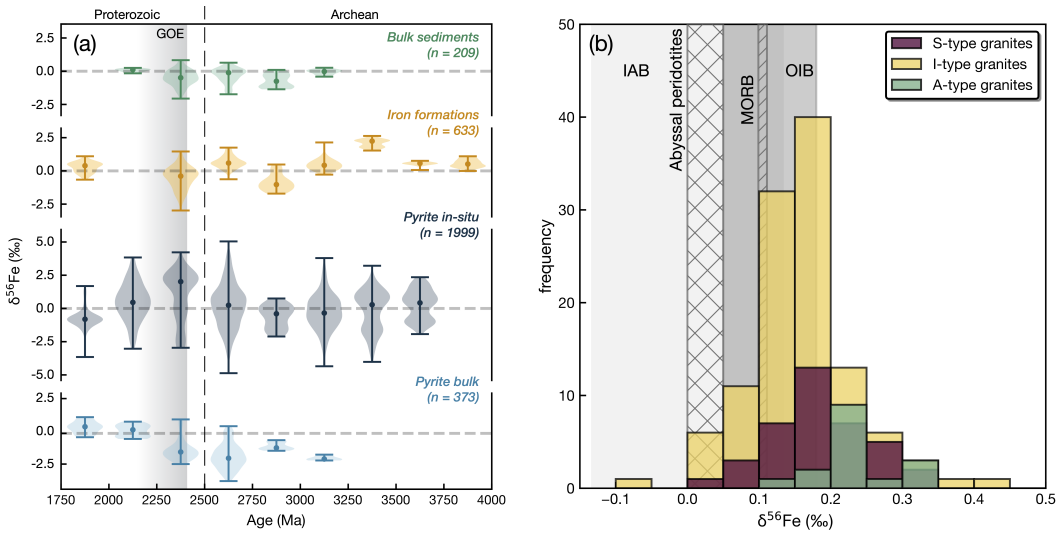


Figure 2.1: Iron isotope compositions of the main sedimentary reservoirs (a) and different types of igneous rocks (b). (a) Violin plots show compiled data of iron isotope compositions for bulk sediments (green), iron formations (yellow), and pyrite grains (in-situ: dark blue; bulk: light blue) in time-bins of 250 Ma. Most data for iron formations and pyrite come from previous compilations by *Heard and Dauphas* (2019) and *Dupeyron et al.* (2023), updated with additional measurements from *Fabre et al.* (2011), *Heard et al.* (2020), and *Ostrander et al.* (2022). Bulk sediments include measurements of shales and greywackes from *Yamaguchi et al.* (2005), *Heard et al.* (2020), and *Ostrander et al.* (2022). (b) Proterozoic to Phanerozoic granites (sensu lato: SiO_2 > 66%; S-type (red), I-type (yellow), and A-type (green)) reach higher δ^{56}Fe values than more mafic rocks (*Poitrasson and Freydier*, 2005; *Heimann et al.* 2008; *Telus et al.* 2012; *Sossi et al.* 2012; *Foden et al.* 2015, 2018; *He et al.* 2017; *Liang et al.* 2022; *Liou et al.* 2022; *Ma et al.* 2022; *Zhang et al.* 2023). Abyssal peridotites, representative of the mantle source of mid-ocean ridge basalts (MORB), have δ^{56}Fe of 0.025 ‰ ± 0.025 ‰ (*Craddock et al.* 2013), whereas MORBs display a more homogeneous composition of 0.105 ‰ ± 0.006 ‰ (*Teng et al.* 2013). Ocean island basalts (OIB) have δ^{56}Fe values ranging from 0.05 to 0.18 ‰ (*Teng et al.* 2013), and island arc basalts (IAB) vary between −0.133 and 0.133 ‰ (*Sossi et al.* 2016).

mineral, or in-situ mineral). For example, most studies have focused on bulk-rock δ^{56}Fe compositions (e.g., *Matthews et al*., 2004; *Yamaguchi et al*., 2005; *Johnson et al*., 2008; *Fabre et al., 2011*; *Busigny et al*., 2014; *Heard et al*., 2020; *Ostrander et al*., 2022) or bulk mm-scale pyrite grains extracted from their matrix in sedimentary rocks (e.g., *Rouxel et al*., 2005; *Archer and Vance*, 2006; *Hofmann et al*., 2009). Recognizing that this latter approach can introduce sampling bias towards visible pyrite grains, other studies have conducted in-situ analyses of pyrites at the micron scale (e.g., *Yoshiya et al*., 2012, 2015a, b; *Marin-Carbonne et al*., 2014, 2020; *Agangi et al*., 2015; *Dupeyron et al*., 2023). These latter studies have demonstrated large and constant ranges of δ^{56}Fe values in pyrite, ranging from around -4 to +4 ‰ through geologic time (*Dupeyron et al*., 2023; Figure 1a). Thus, the scale of isotopic variability in sedimentary rocks may be on the inter- or even intra-mineral scale and analyses of mineral separates or in-situ analyses will not necessarily be representative of bulk-rock compositions.

Furthermore, bulk-rock samples from individual Precambrian sedimentary formations can have δ^{56}Fe values that vary by > 1‰ (e.g., *Yamaguchi et al*., 2005; *Johnson et al*., 2008; *Bekker et al*., 2010; *Fabre et al*., 2011; *Busigny et al*., 2014; *Heard et al*., 2020; *Ostrander et al*., 2022), reflecting the relative proportions of isotopically distinct mineral components. Detrital and authigenic silicates, which typically dominate siliciclastic rocks, are expected to have δ^{56}Fe values averaging zero, similar to that of near-modern loess, river loads, and marine sediments, as well as the average of igneous rocks (*Beard and Johnson*, 2004; *Yamaguchi et al*., 2005; *Dauphas et al*., 2017; *Slotznick et al*., 2018; Figure 1b). In contrast, sulfide-rich rocks can have highly variable iron isotope compositions. For example, Archean bulk sediments, largely influenced by pyrite-rich black shales, display prominent excursions toward negative δ^{56}Fe values (*Rouxel et al*., 2005; *Yamaguchi et al*., 2005; *Ostrander et al*., 2022; *Dupeyron et al*., 2023; Figure 1a).

Given the inherent variability and complexities of the sedimentary iron isotope record, this work focuses on strongly peraluminous granites (SPGs), derived from partial melting of siliciclastic sediments. SPGs are defined by their bulk-rock chemistry, with aluminum saturation values (ASI = molar Al_2O_3/[CaO + Na_2O + K_2O]) greater than 1.1, and are often informally referred to as "S-types" (*Chappell and White*, 1992; *Clarke*, 2019; *Nabelek*, 2020; *Bucholz*, 2024). Because SPGs homogenize their sedimentary source material, they may represent a complementary archive to siliciclastic rocks, potentially recording significant changes in global cycles and

geological processes throughout Earth's history (e.g., *Bucholz and Spencer*, 2019; *Bucholz et al.*, 2020; *Liebmann et al.*, 2021; *Bucholz*, 2022). It is important to note, however, that unlike chemical sediments, which may reflect changes in ocean chemistry over time, the iron isotope composition of SPGs will also be influenced by the composition of detrital sediments sourced from proximal continental settings.

Before being able to potentially use SPGs to track changes in the bulk Fe isotopic composition of sedimentary rocks, it is critical to understand whether metamorphism and partial melting of metasedimentary rocks fractionate iron isotopes and, if so, to what extent? Here, we investigate the fractionation of iron isotopes during partial melting of metasedimentary rocks and how this process is imprinted in the isotopic signature of SPGs through analysis of natural samples capturing this process and associated modeling. First, we measured the iron isotope composition of the SPGs from the Neoarchean Ghost Lake batholith (GLB) in Ontario, Canada, and associated metasedimentary rocks from the Zealand unit, thought to be representative of its source. We then used thermodynamic phase equilibrium modeling to assess the extent of equilibrium isotopic fractionation during partial melting of the metasedimentary source and production of SPGs and compare this to our data. We discuss the influence of various factors, such as the source rock, fO_2, *P–T* conditions, mineral composition changes, and the melt fraction, on the isotopic composition of the melts from which the GLB crystallized and assess whether SPGs faithfully record the iron isotope composition of their metasedimentary source rocks.

2. Fe isotopes during metamorphism and generation of SPG magmas

Currently, there are only limited SPG Fe isotope data, comprising a broad survey of Paleozoic SPGs mainly from Australia and Tasmania (n = 15; *Foden et al.*, 2015), as well as a more focused study on migmatites (n = 11; six leucosomes and five melanosomes) and granites (n = 11) from the Paleoproterozoic Harney Peak granite in South Dakota (*Telus et al.*, 2012). SPGs (and granites in general) have heavy and variable iron isotope compositions compared to more mafic igneous rocks, with δ^{56}Fe in SPGs up to +0.32 ‰ (*Telus et al.*, 2012; *Foden et al.*, 2015; *Dauphas et al.*, 2017; *Bucholz*, 2024; Figure 1b). Several mechanisms have been proposed to explain the heavy isotopic composition of granites; however, most studies point to equilibrium fractionation during fractional crystallization or partial melting, producing isotopically light cumulates or restites and heavy granitic melts (e.g., *Schuessler et al.*, 2009; *Telus et al.*, 2012; *Sossi et al.*, 2012; *Foden et al.*, 2015, 2018). *Dauphas et al.* (2014) found that the mean force constants for iron in silicate

glasses increased with higher SiO_2 contents and $Fe^{3+}/\Sigma Fe$ ratios (i.e., $Fe^{3+}/(Fe^{3+} + Fe^{2+})$). These relationships imply that the magnitude of isotopic fractionation in silicate melts also increases as melts become more SiO_2-rich, reflecting changes in the average coordination of iron with higher degrees of polymerization. Thus, highly differentiated melts, such as those from fractional crystallization or low degrees of partial melting, should be isotopically heavier than less polymerized melts at a given oxidation state.

When considering SPGs specifically, however, if and how metamorphism and anatexis of metasedimentary rocks fractionate iron isotopes have yet to be thoroughly explored. The effects of metamorphism prior to anatexis have received more attention since most Precambrian sedimentary rocks have experienced some metamorphism (*Marin-Carbonne et al*., 2020; *Dupeyron et al*., 2023), which may affect the associated iron isotope record. In general, it is expected that, as temperature increases, variability in δ^{56}Fe between minerals will diminish (*Dauphas et al*., 2007a, b). *Frost et al*. (2007) and *Hyslop et al*. (2008), for example, showed that at low metamorphic grades, banded iron formations preserve large inter-mineral isotopic variations, but at higher grades, isotopic ratios are homogenized. However, complete isotopic re-equilibration may not occur for all minerals during metamorphism. Studies focusing on pyrite across various metamorphic grades, for example, reveal persistent intra-sample variability in δ^{56}Fe values from prehnite-pumpellyite to amphibolite facies (*Whitehouse and Fedo*, 2007; *Galić et al*., 2017; *Marin-Carbonne et al*., 2020; *Dupeyron et al*., 2023). Regardless of whether inter-mineral homogenization occurs or not, metamorphism of sedimentary rocks can generally be considered a near-closed system process, at least in terms of Fe isotopes, where the isotopic composition of the protolith is preserved by bulk rocks (e.g., *Frost et al*., 2007; *Dauphas et al*., 2007a, b; *Hyslop et al*., 2008; *Marin-Carbonne et al*., 2020; *Dupeyron et al*., 2023). This means that prograde metamorphism should preserve the bulk isotopic composition of the protolith, even if original isotopic variations are erased due to isotopic homogenization or mineral transformations occurring during metamorphism.

Significant isotopic fractionation may, however, occur between the melt and the residual sedimentary source upon crossing the solidus. Production of SPG magmas dominantly occurs via dehydration reactions that produce melt and residual minerals with varying compositions as melting progresses (*Thompson*, 1982; *Le Breton and Thompson*, 1988; *Patiño Douce and Beard*, 1995; *Patiño Douce and Harris*,

1998; *Sylvester*, 1998; *Spear et al*., 1999). *Telus et al*. (2012) used the Harney Peak granite migmatites as a natural experiment to investigate this process. They measured five leucosome-melanosome pairs and two samples each of the Harney Peak granite and host-rock schists. They found that the δ^{56}Fe of the leucosomes, representative of migmatite partial melts, were elevated by 0.05-0.20 ‰ compared to their melanosome pairs, suggesting an equivalent magnitude of fractionation between partial melt and residue during anatexis. The δ^{56}Fe values of the leucosomes (+0.246 to +0.480 ‰) were higher by 0-0.2 ‰ than that of the two analyzed Harney Peak granite samples (+0.161±0.052 ‰ and +0.240±0.041 ‰). No other study of natural samples representing the partial melting process of metasedimentary rocks has been undertaken. However, *Xu et al*. (2017) measured the iron isotope composition of migmatitic rocks from the Dabie orogen, China, likely derived from a dioritic to granodioritic protolith (*Wang et al*., 2013). The observed iron isotope fractionation between leucosomes and melanosomes from these rocks ranges between ~0 and 0.36 ‰, with leucosomes displaying higher δ^{56}Fe values than melanosomes. These results suggest significant equilibrium isotopic fractionation produced during partial melting, controlled mainly by differences in the iron bonding environment in granitic anatectic melts and complementary restites.

The extent of equilibrium isotopic fractionation during partial melting of metasedimentary rocks and generation of SPGs can be calculated using melting reactions and iron force constants for iron-bearing phases relevant to the generation of magmas via high-grade metamorphism and partial melting (e.g., *Dauphas et al*., 2014; *Nie et al*., 2021; *Polyakov et al*., 2007; *Roskosz et al*., 2022, 2015). Such phases include silicate melts, biotite (annite), garnet (almandine), spinel (aluminum-bearing and magnetite), ilmenite, and orthopyroxene. *Nie et al*. (2021) produced a simplified model of biotite dehydration melting where 75 % of the iron produced via biotite breakdown entered garnet and the remaining 25 % entered the melt. They estimated the δ^{56}Fe of the produced melt to be 0.2-0.3 ‰ higher than the residue, in agreement with the empirical study of *Telus et al*. (2012). Anatexis is, however, a complex process where mass transfer is controlled by metamorphic reactions driven by changes in the equilibrium state of the system. Thus, more complex models incorporating changes in phase stability and composition along metamorphic paths are needed to capture iron isotope fractionation during partial melting more accurately. For example, the modal abundance of a phase, the amount of iron hosted in it, and the iron oxidation state are functions of the pressure (P), temperature (T), water content, and oxygen fugacity (fO_2) of the system, and all these variables influence the magnitude

of iron isotope fractionation between minerals and melt.

To address the complexities of metamorphism and partial melting, we use a modeling approach that couples iron force constants with predicted stable phase assemblages under specific *P-T-*fO_2 conditions. This method effectively accounts for isotopic fractionation along a given metamorphic path, where continuous changes in phase compositions and proportions influence the iron bonding environment. In this study, we specifically apply this model to Fe isotopic fractionation between SPG magmas from the Ghost Lake batholith and its adjacent metasedimentary rocks, interpreted as the source of the batholith. We use this site as an ideal natural example where both SPGs and their protolith are preserved, allowing us to validate the model against actual Fe isotope measurements. However, while the results presented herein are particular to the Ghost Lake batholith, the findings have broader implications for other SPGs across the geological record.

3. Regional Geology

The Ghost Lake batholith and Zealand unit are part of the Sioux Lookout terrane in the Superior Province, Canada (Figure 2), which lies at the boundary between granitic rocks of the Winnipeg River subprovince to the north and metavolcanic rocks from the Wabigoon subprovince to the south (*Blackburn et al*., 1991; *Breaks and Moore*, 1992). The sedimentary protoliths of the Zealand unit were turbiditic greywackes and mudstones and minor banded iron formations deposited at ~ 2730-2700 Ma in an arc-proximal basin (*Davis et al*., 1988; *Breaks and Moore*, 1992). These sediments were later metamorphosed during the collision of the Wabigoon and Winnipeg River subprovinces, resulting in extensive melt production that produced the GLB (*Breaks and Moore*, 1992), which has a crystallization age obtained via U-Pb zircon geochronology of 2654 ± 24 Ma (*Liebmann et al*., 2021). Peak metamorphic conditions have been estimated to reach ~0.3-0.4 GPa and ~550-750 °C (*Breaks and Moore*, 1992; *Bucholz et al*., 2020); however, rocks in the Zealand unit include a range of metamorphic facies, ranging from greenschist to upper-amphibolite facies with zones of incipient migmatization. Specifically, at the contact between the Zealand unit and the Wabigoon subprovince, the metamorphic grade is defined by the biotite-chlorite isograd, and it progressively increases to the north through the isograds of andalusite, garnet, sillimanite, and sillimanite–K-feldspar proximal to the GLB (*Breaks and Moore*, 1992). Migmatization and incipient partial melting of the Zealand unit are common at the west and northwest contacts with the GLB but absent at the east and south of the batholith (*Bucholz et al*., 2020).

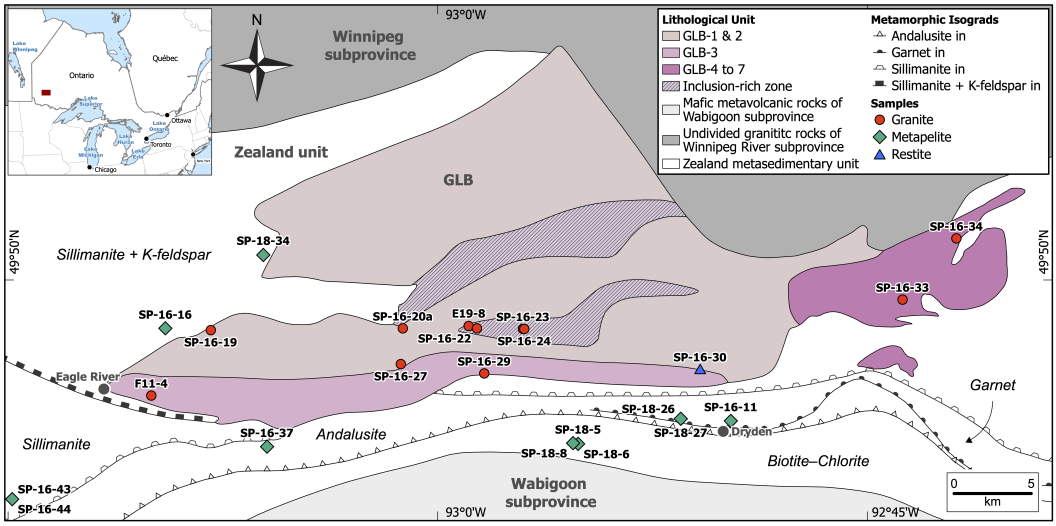


Figure 2.2: Geological map of the Sioux Lookout terrane (Ontario, Canada, see inset **a**) in the region of the Ghost Lake batholith (GLB) and associated metasedimentary rocks corresponding to the Zealand unit (b). The map is modified from *Breaks and Moore* (1992) and *Bucholz et al.* (2020).

Variability in mineral abundance and igneous textures defines eight subunits within the GLB (*Breaks and Moore*, 1992; *Bucholz et al.*, 2020). The largest subunit, GLB-1, is a biotite and biotite-cordierite granite containing two elongated zones with abundant enclaves, identical to high-grade metamorphic rocks of the Zealand unit. GLB-2 is located at the western part of GLB-1, close to the contact with partially melted metasedimentary rocks from the Zealand unit. It consists of distinctive fine-grained, weakly deformed biotite granite dikes. GLB-3 is a ~25x2 km strip along the southern contact of the GLB with the Zealand unit. This subunit consists of fine-grained biotite and muscovite granite with occasional accessory garnet and sillimanite. Segregations of leucogranite and K-feldspar-bearing pegmatites are ubiquitous within GLB-3. Finally, GLB-4 to -8 are restricted to the eastern portion of the GLB. These subunits form a complex of pegmatitic tourmaline+muscovite granites that lack metasedimentary enclaves. Overall, the western and central parts of the GLB are weakly deformed, with foliation decreasing toward the east, where the batholith appears more massive and commonly preserves magmatic foliation. A detailed study of the geology and geochemistry of the units that compose the GLB is provided in *Breaks and Moore* (1992).

4. Methods

4.1 Sample preparation

Granites (n = 11), metasedimentary rocks from all metamorphic grades (n = 11), and one restite from the GLB and Zealand unit were selected for whole-rock major and trace element chemistry and Fe isotope measurements. The initial sampled material consisted of several rock fragments (3-10 per sample), each weighing ~1-5 kg, collected in-situ. Notably, for coarse-grained granite and pegmatite samples, either a greater number or larger volume of fragments were collected to account for their larger grain sizes. Rock powders for some of the samples studied here (n = 9) were prepared for X-ray fluorescence (XRF) analysis and reported in previous studies (i.e., *Bucholz and Spencer*, 2019; *Bucholz et al.*, 2020). These powders were reused for Fe isotope measurements, and the whole-rock compositional data was taken from the original study (given in Supplementary Table S1). We prepared the remaining samples for which powders and XRF analyses were unavailable, following the procedure described below.

Only homogeneous rocks free of significant alteration or contamination were selected for Fe isotope analysis. Using a rock saw with a diamond blade, the samples were trimmed into cm-scale pieces to remove any altered surfaces. The cut rock pieces were then sanded to remove saw marks and sonicated in deionized water. After drying, samples were broken into 1-2 cm pieces with a rock hammer and further reduced to a grain size of 2-3 mm using a jaw crusher. Aliquots of ~ 50-100 g were typically taken from each sample. However, for coarse-grained granite and pegmatite samples, larger aliquots of ~ 200 g were collected to ensure representative sampling. Finally, after thorough homogenization, smaller aliquots of ~ 40 g were powdered in an agate grinding vessel with a ball mill.

Pyrrhotite grains were also separated from some samples to assess the effect of sulfides on the Fe isotopic composition of bulk-rock metapelites and granite samples. About 100–200 g sample powder was obtained by crushing cm-scale chips in an agate mortar. A pool of weakly magnetic grains was separated from the powder, and sulfide grains were manually picked under the microscope. 3–8 grains per sample with sizes <500 μm were then sonicated in DI water for five minutes to remove minute particles attached to them.

4.2 Whole-rock and trace-element analysis

The major element composition of granites and metasedimentary rocks was determined by XRF analysis at Caltech. Powdered samples were dried at 110°C overnight, and loss on ignition (LOI) was determined by sintering the dried powders for one hour at 1050°C. The sintered powders were then homogenized with an agate mortar and pestle and fused into glass discs using platinum crucibles and molds. The glass discs were analyzed for major elements using a Panalytical Zetium 4 kW XRF spectrometer using the same analytical conditions described in *Bucholz and Spencer* (2019). After XRF analyses, chips of the glass discs were digested in acid and analyzed for trace element concentrations via inductively coupled mass spectrometry (ICPMS), also at Caltech (*Lewis et al*., 2021).

4.3 Fe isotope measurements

Whole-rock Fe isotope measurements were performed at the Isotoparium (Caltech) following the methods of *Dauphas et al*. (2004, 2009b). Between 5 and 20 mg of sample powder was transferred to acid cleaned Teflon (PFA) vials. To monitor accuracy, USGS reference rock powders (geostandards) AGV-2 and BHVO-1 with known Fe isotope compositions (*Craddock and Dauphas*, 2011) were processed and analyzed alongside the samples. Samples were digested in the Teflon vials using concentrated mixtures of acid on hot plates: (i) 1.5 mL of 2:1 HF-HNO_3 for 5 hours at 100°C; (ii) 1.25 mL of 3:1 HCl-HNO_3 (aqua regia) overnight at 140°C; (iii) 1.5 mL of 2:1 HCl-HNO_3 overnight at 140°C; (iv) 1 mL HCl at 180°C for 48 hours. Each digestion step was followed by thorough drying with open vials at 120-130 °C. The final dried samples were then dissolved in 0.5 mL of 6 M HCl for Fe separation via column anion-exchange chromatography.

Bio-Rad Poly-prep columns were filled with ~1 mL of BioRad AG1-X8 200-400 resin conditioned by following the procedure outlined by *Dauphas et al*., (2004). The samples were then loaded into the columns where the matrix and interfering elements were eluted by passing 9 mL of 6 M HCl. The concentrated Fe in the columns was recovered in Teflon beakers with 8 mL of 0.4 M HCl. This process was repeated after sample evaporation and dissolution in 0.5 mL of 6 M HCl. The eluted solutions were then evaporated and refluxed overnight in concentrated HNO_3 at 140 °C. Samples were evaporated again to a small drop (< 25 μL) and finally dissolved at 130 °C in 5 mL of 0.3 M HNO_3 for isotopic analyses.

Samples and standard solutions were introduced into the mass spectrometer as an

aerosol at a nominal flow rate of 50 μL/min using a PFA nebulizer coupled with a glass spray chamber. The solutions were diluted to 5 μg/g in 0.3 M HNO_3, which resulted in beam intensities of 20-25 V on ^{56}Fe: a sensitivity of 4-5 V/ppm of Fe. To monitor system memory effects of the sample introduction system and establish baselines, on-peak-zeros (OPZ) were acquired before all unknown and standard solution measurements. These measurements involved a 90 s sample uptake and 40 s on-peak acquisition, using a clean acid solution from the same batch used to dilute the samples. The typical background intensity recorded was $\sim 10^{-5}$ V on ^{56}Fe.

Isotopic fractionation due to instrumental shift was corrected by standard bracketing, using the IRMM-524a metallic iron standard as reference material. The standard solution was diluted in the same batch of acid as the unknown samples and geostandards at a concentration of 5 μg/g (±5 %). Sample measurement procedure consisted of a 90 s sample uptake, followed by 50 cycles of data acquisition, each with an integration time of 4.192 s, which yields 210 s of continuous on-peak measurement. After each measurement, the inlet system was rinsed for 120 seconds using 3 vol.% HNO_3. Along with the unknown samples, one of the two geostandards was measured within each analysis session.

Each reported sample composition is the arithmetic mean of n replicates measured during the same analysis session (typically between 5 and 9). The analytical uncertainties reported here are 95% confidence intervals calculated as $(2 \times \sigma_{\text{std}})/\sqrt{n}$, where σ_{std} is the standard deviation of repeat measurements of the IRMM-524a standard bracketed by itself during the session (*Dauphas et al.*, 2009). This approach provides an accurate estimate of variability across the entire analysis session. For reference, we also calculated uncertainties as two times the standard error (SE), where SE is calculated as $\sigma_{\text{samples}}/\sqrt{n}$. These estimates were lower than or similar to those derived from the bracketing standard, indicating consistent measurements during individual sample analyses.

All the collected iron isotope data were expressed relative to IRMM-524a in delta notation in terms of δ^{56}Fe and δ^{57}Fe. We measured the iron isotope composition of IRMM-524a using the well-characterized IRMM-014 reference material as the bracketing standard (*Taylor et al.*, 1992). The average δ^{56}Fe and δ^{57}Fe obtained were +0.005 ± 0.018 ‰ and -0.003 ± 0.026 ‰, respectively (n = 59), confirming that IRMM-524a is isotopically identical to IRMM-014 within analytical uncertainty (*Craddock and Dauphas*, 2011). We subsequently discuss our results using only δ^{56}Fe, since all data are mass-dependent (i.e., δ^{57}Fe = 1.5 x δ^{56}Fe; Supplementary

Figure S1).

4.4 Phase equilibrium modeling

Phase equilibrium modeling was used to estimate mineral and melt proportions and compositions during partial melting. The calculations were performed using the software Theriak-Domino at fixed pressures of 0.3 and 0.4 GPa and a temperature range of 600–1000 °C. We used the compositional system MnO–Na_2O–K_2O–CaO–FeO–MgO–Al_2O_3–SiO_2–H_2O–TiO_2–O_2 (MnNKCFMASHTO), which is appropriate for partial melting of metasedimentary rocks (*White et al.*, 2014b). The thermodynamic dataset we selected includes the internally consistent database of *Holland and Powell* (2011) and activity–composition ($a\check{}x$) relations appropriate for typical stable phases during anatexis of metapelites: biotite (Bt), garnet (Grt), cordierite (Crd), orthopyroxene (Opx), chlorite (Chl), and staurolite (St) (*White et al.*, 2014b); silicate melt (Melt) and white mica (Ms) (*White et al.*, 2014a); ilmenite–hematite (Ilm–Hem) (*White et al.*, 2000); spinel–magnetite (Spl–Mag) (*White et al.*, 2002); plagioclase (Pl) and K-feldspar (Kfs) (*Holland and Powell*, 2003); and epidote (Ep) (*Holland and Powell*, 2011). Pure phases include quartz (Qtz), rutile (Rt), titanite (Ttn), sillimanite (Sil), andalusite (And), kyanite (Ky), and hydrous fluid (H_2O). Mineral abbreviations herein follow *Warr* (2021).

We focused on partial melting occurring at minimally saturated water conditions (~0.5 mol% H2O at the solidus), which avoids unconstrained overestimation of the melt fraction with fluid-present melting. However, phase equilibrium calculations were also conducted under water-undersaturated and water-excess conditions for reference. We performed calculations with oxygen fugacity buffered at FMQ+2, FMQ, and FMQ-2, where FMQ corresponds to the fayalite-magnetite-quartz buffer. Because the $a - x$ model for silicate melt has no ferric iron component, we independently estimated the $Fe^{3+}/\Sigma Fe$ proportion of the calculated melt phase using the algorithm from *Kress and Carmichael* (1991). We note that different models have been proposed for the estimation of $Fe^{3+}/\Sigma Fe$ ratios in silicate melts based on their composition (e.g., *Kress and Carmichael*, 1991; *Borisov et al*., 2015; *O'Neill et al*., 2018), but none of these have been calibrated for felsic systems. We preferred the *Kress and Carmichael* (1991) parametrization as, unlike the other models, all the required chemical components are included in the melt *a-x* relationships from *White et al*. (2014a).

4.5 Isotopic fractionation during partial melting

Quantitative estimates of isotopic fractionation due to partial melting were calculated using phase equilibrium modeling. For each Fe-bearing phase predicted to be in equilibrium at a given temperature, a force constant $[F]$ was assigned a constant value or calculated using a composition-dependent expression compiled from the literature (see Table 1). Since no force constants have been measured for cordierite, we assumed the same value as that of biotite without ferric iron since both are aluminosilicates with mostly Fe^{2+} ($Fe^{3+}/\Sigma Fe < 0.1$) accommodated in octahedral sites in reduced granites and (meta-)sedimentary rocks (*Guidotti and Dyar*, 1991; *Khomenko et al*., 2001; *Bucholz et al*., 2018).

A bulk value of $[F]$ for the residue was calculated as the weighted average of all solid phases, using the formula $\sum_n^i F_i p_i$ where F_i and p_i are the force constant and molar proportion of phase i, respectively, and n is the number of iron-bearing phases in the system at a given temperature. For solid-solution phases whose force constant is defined for one of the endmembers, their molar proportion was adjusted to the content of that endmember in the phase. For instance, if biotite and garnet are present at 70 mol% and 30 mol%, respectively, with 60% annite in biotite and 80% almandine in garnet, the recalculated p_{biotite} and p_{garnet} would be 64% and 36%, respectively. From $[F]_{\text{melt}}$ and $[F]_{\text{residue}}$, the fractionation factor between coexisting melt and solid residue ($\Delta^{56}\text{Fe}_{(melt-residue)}$) was then obtained over the temperature interval of interest in terms of delta notation using the expression from *Dauphas et al*. (2014):

$$\Delta^{56}Fe_{melt-residue} = \delta^{56}Fe_{melt} - \delta^{56}Fe_{residue} = 2853 \times \frac{[F]_{\text{melt}} - [F]_{\text{residue}}}{T^2} \quad (2.1)$$

The values for δ^{56}_{melt} and $\delta^{56}_{residue}$ were then calculated assuming mass balance in a closed system.

5. Results

5.1 Petrography and geochemistry

5.1.1 Granites

Bulk-rock major and trace elements and petrographic descriptions for granitic samples are given in Tables S1 and S2, respectively. The location from which these samples were collected is shown in Figure 2b. The granite samples vary between

medium- to coarse-grained granites (sensu stricto) and pegmatitic granites with variable proportions of K-feldspar, quartz, plagioclase, and other Al-bearing phases such as garnet, tourmaline, sillimanite, cordierite, biotite, or muscovite. The granite samples from the GLB are strongly peraluminous, with all samples displaying ASI values higher than ~1.1. On an anhydrous basis, the silica contents and total alkalis (Na_2O + K_2O) range from ~72–76 wt.% and ~6–10 wt.%, respectively. Samples are also alkali calcic to alkalic, with the modified alkali–lime index (MALI; Na_2O + K_2O – CaO; *Frost et al.*, 2001) varying between ~4–9 wt.% and K_2O/Na_2O ratios of ~0.5–2.5. FeO_T + MgO + TiO_2 values for most granite samples vary between 0.7–1.8 wt.% (FeO_T = FeO + 0.9·Fe_2O_3); however, the cordierite-bearing sample SP-16-19 has 4.2 wt.% of these oxides. This sample also has higher ASI and lower MALI values than other samples (1.47 and 3.80, respectively) and higher Na_2O/K_2O (2.4 compared to <1.5 in other samples). In general, the granite samples from the GLB show medium to low CaO/Na_2O and intermediate to high Al_2O_3/TiO_2 compared to other peraluminous granites (Figure 3a). The Al_2O_3/TiO_2 and CaO/Na_2O ratios are inversely correlated, and the selected samples from the GLB follow a trend similar to that of other Archean and Proterozoic strongly peraluminous granites (Figure 3a).

5.1.2 Metasedimentary rocks

Bulk-rock major and trace elements and petrographic descriptions for metasedimentary samples from the Zealand unit are also summarized in Tables S1 and S2. These rocks include micaceous phyllites from the biotite-chlorite zone, quartzo-feldspathic schists with biotite ± garnet from the andalusite and garnet zones, and quartzo-feldspathic gneisses with biotite, muscovite, sillimanite ± andalusite from the sillimanite and sillimanite–K-feldspar zones, the latter of which show evidence of incipient partial melting. The SiO_2 and Al_2O_3 of the analyzed metasedimentary rocks range ~54–64 wt.% and ~16–22 wt.%, respectively, with more pelitic samples having lower SiO_2 and higher Al_2O_3 (Figure 4). However, the metasedimentary rocks broadly contain intermediate molar Al_2O_3 compared to a global compilation of pelitic rocks (Forshaw and Pattison, 2022; Figure 4a-b). For most samples, FeO_T and MgO contents are positively correlated and vary between ~5–9 wt.% and ~2.5–4 wt.%, respectively, following the trend defined by the global compilation of metapelites. The two exceptions are samples SP-16-11 and SP-18-27, with high FeO contents (10.9-12.3 wt.%), reflecting the presence of abundant sulfide grains in the former and ilmenite in the latter.

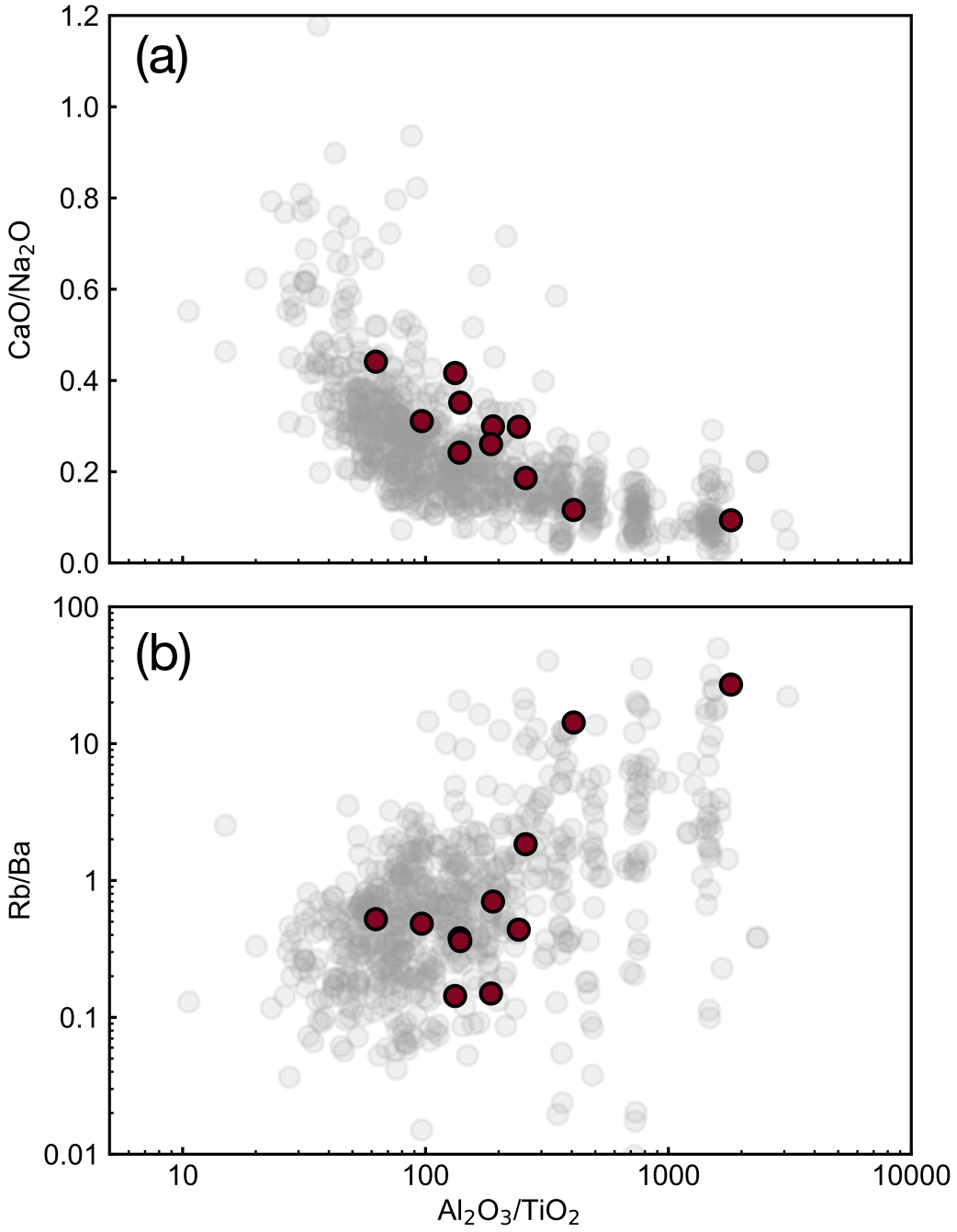


Figure 2.3: Major and trace element ratios for samples from the GLB. Filled red circles are individual granite samples. The light gray circles correspond to compositions from a global compilation of Archean and Proterozoic SPGs by *Bucholz and Spencer* (2019). a) CaO/Na_2O versus Al_2O_3/TiO_2 and b) Rb/Ba versus Al_2O_3/TiO_2.

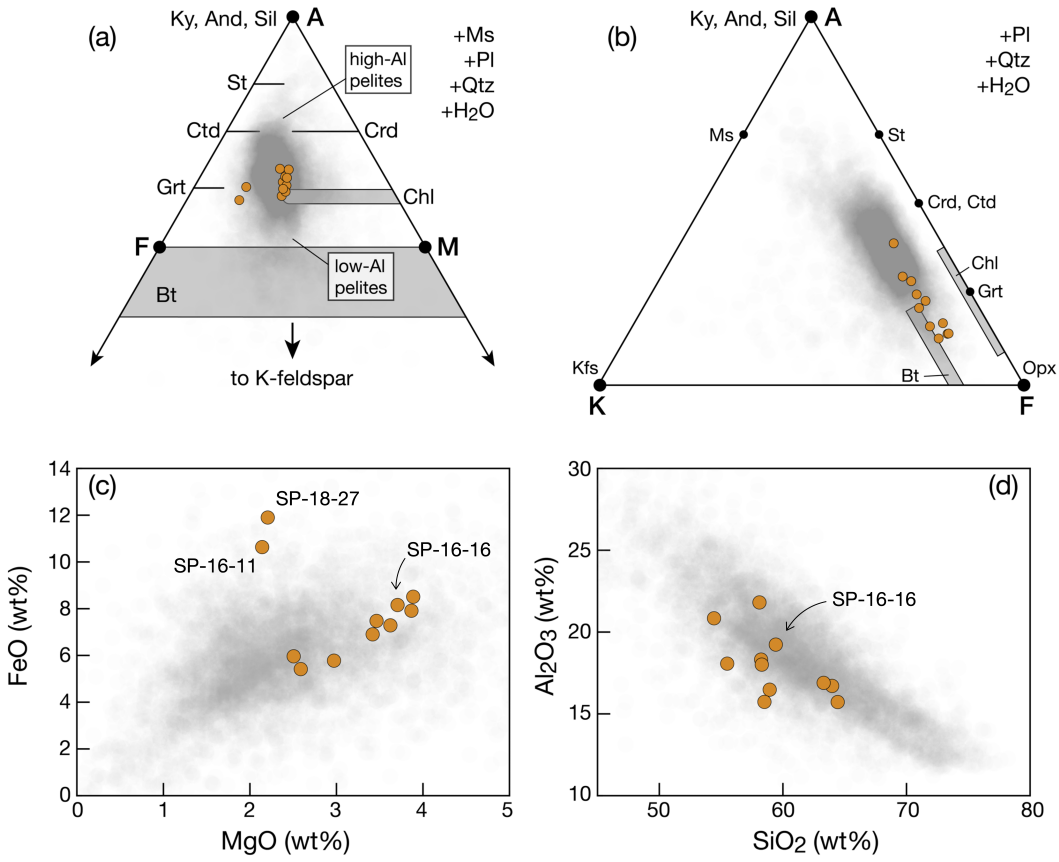


Figure 2.4: Compositional features of metasedimentary rocks from the Zealand unit. Filled orange circles are individual samples. The shaded regions are data points from a global compilation of metapelites from *Forshaw and Pattison* (2022). (a) AFM ternary diagram — A = molar Al_2O_3 – 3*K_2O; F = molar FeO_T; M = molar MgO. (b) AKF ternary diagram — A = molar Al_2O_3 – (Na_2O + K_2O + CaO); K = molar K_2O; F = molar FeO_T + MgO + MnO. (c) FeO_T versus MgO. (d) Al_2O_3 versus SiO_2.

5.2 Iron isotopes

Figure 5 and Table 2 summarize the iron isotope measurements for the granite, metapelite, restite, sulfide, and geostandard samples. The measured δ^{56}Fe values for geostandard samples are identical, within uncertainty, to the reference values recommended by *Craddock and Dauphas* (2011). Granite samples have δ^{56}Fe values spanning +0.111 ± 0.018 ‰ to +0.315 ± 0.038 ‰, averaging +0.192 ‰. Overall, granites are isotopically heavier than the average of the metapelites, although there is some overlap at the lower end of the granite δ^{56}Fe values (Figure 5). Notably, the granite samples from the inclusion-rich zone in GLB-1 tend to be isotopically heavier with δ^{56}Fe ranging from +0.194 to +0.315 ‰. No apparent correlation exists between granite units and measured δ^{56}Fe values (Figure 5).

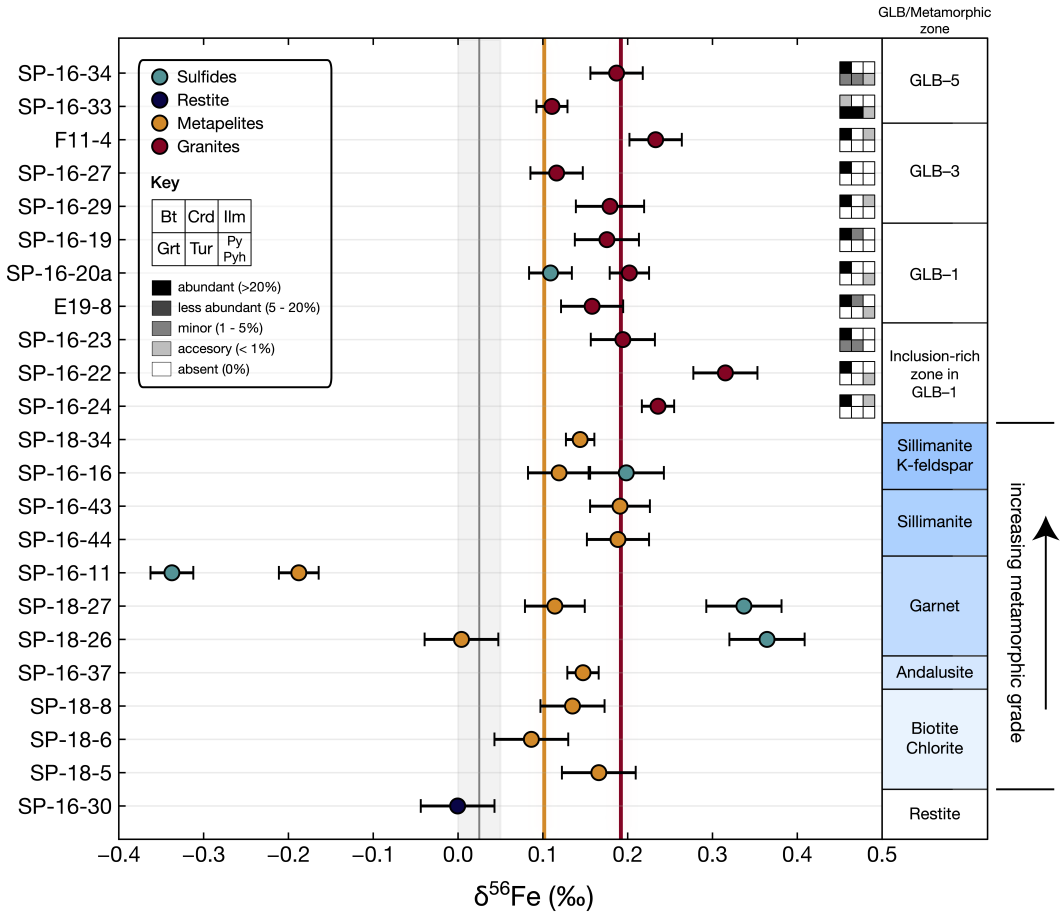


Figure 2.5: δ^{56}Fe of rocks from the GLB and the Zealand unit. Bulk-rock analyses of granite samples are shown in red, metapelites in orange, and the restite in dark blue; sulfides from four metapelites and a granite sample are shown in green. Colored vertical lines are averages for granites (red) and metapelites (orange). The grey vertical region is the average mantle composition (+0.025 ± 0.025 ‰; *Craddock et al.*, 2013). The presence and abundance of iron-bearing minerals for granite samples are shown qualitatively in the square grid diagrams. Mineral abundance was visually estimated from thin sections using a reference chart for modal proportions (*Terry and Chilingar*, 1955). The GLB zones for granite samples and metamorphic zones for metapelites are shown in the columns to the right.

The δ^{56}Fe of the metasedimentary samples ranges from –0.188 ± 0.023 ‰ to +0.191 ± 0.035 ‰, averaging +0.101 ‰ (or +0.130 ‰ when excluding SP-16-11). Although there is no correlation between measured δ^{56}Fe compositions and increasing metamorphic grade (Figure 5), it is noteworthy that the two samples from the sillimanite zone have the heaviest isotopic composition. In contrast, samples from the garnet zone display the lowest δ^{56}Fe values. SP-16-43 and SP-16-44 represent an andalusite-bearing interbedded metapelite and metawacke, respectively, with incipient replacement of andalusite by sillimanite. The two samples were sampled within a meter of each other and have, within error, the same isotopic composition: δ^{56}Fe +0.191 ± 0.035 ‰ and +0.189 ± 0.037 ‰, respectively. The samples from the garnet zone were interbedded with banded iron formations in the Zealand unit. These samples show δ^{56}Fe ranging from –0.188 to +0.114 ‰, where sample SP-16-11 has the lightest isotopic composition, δ^{56}Fe = –0.188 ± 0.023 ‰, consistent with the presence of abundant isotopically light sulfides (see sulfide results below), while the other two samples, SP-18-26 and SP-18-27, have δ^{56}Fe of +0.004 ± 0.043 ‰ and +0.114 ± 0.035 ‰, respectively. Samples SP-18-5, SP-18-6, and SP-18-8, from the biotite–chlorite zone, show a 0.08 ‰ range in δ^{56}Fe with values of +0.166 ± 0.044 ‰, +0.086 ± 0.044 ‰, and +0.134 ± 0.038 ‰, respectively. By contrast, SP-16-16 and SP-18-34, from the sillimanite–K-feldspar zone, and SP-16-37, from the andalusite zone, display isotopic compositions intermediate to the range observed in the biotite-chlorite zone with δ^{56}Fe +0.119 ± 0.037 ‰, +0.144 ± 0.017 ‰, and +0.147 ± 0.018 ‰, respectively. Finally, the restitic sample SP-16-30 has δ^{56}Fe = 0.000 ± 0.043 ‰.

Sulfide grains display significant isotopic variability among samples. The lightest composition corresponds to pyrrhotite in sample SP-16-11 with δ^{56}Fe of –0.337 ± 0.025 ‰. By contrast, pyrrhotite in metapelite samples SP-16-16, SP-18-26, and SP-18-27 have δ^{56}Fe of +0.198 ± 0.044 ‰, +0.364 ± 0.044 ‰, and +0.337 ± 0.044 ‰, respectively. Finally, granite sample SP-16-20a has pyrrhotite with a δ^{56}Fe of +0.109 ± 0.025 ‰.

5.3 Phase equilibrium modeling

Figure 6 shows the results of phase equilibrium calculations for sample SP-16-16 within a temperature range of 600–1000 °C and constant pressure of 0.4 GPa, interpreted to be the approximate peak pressure of metamorphism for the metasedimentary rocks that comprise the Zealand unit. Sample SP-16-16 was selected for modeling as it is a representative composition of the metasedimentary rocks of the

Zealand Unit (Figure 4). The modeling results described here are relevant for closed system conditions (batch melting), where all the stable phases are in equilibrium with each other at any given temperature. Modeling results at different conditions of the system are presented and discussed in the Supplementary Material. This includes results at 0.3 GPa (Figure S2) and initial H_2O contents corresponding to water-undersaturated and water-excess conditions at the solidus (Figure S3). We also include results for partial melting considering melt extraction each time the system reached a critical melt fraction of 7 vol.% (Figure S4).

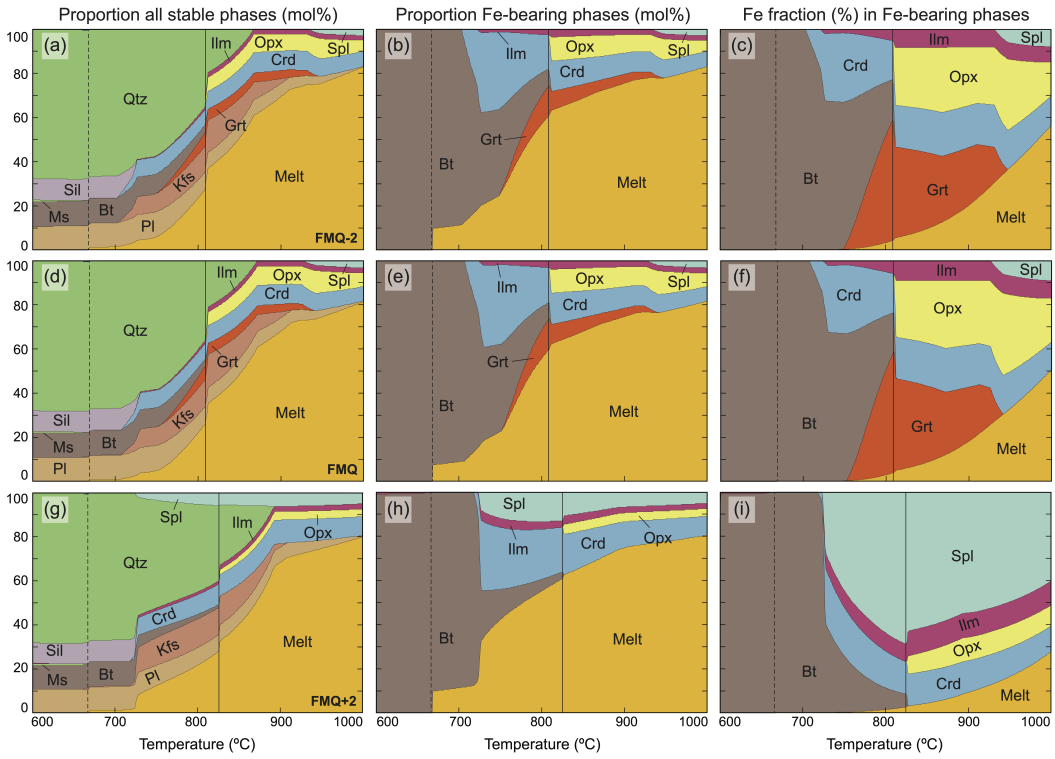


Figure 2.6: Phase equilibrium modeling results for a metapelite with the composition of sample SP-16-16. The calculations were done at a constant pressure of 0.4 GPa, ranging from 600 °C to 1000 °C under three different oxygen fugacity conditions: FMQ-2 (a-c), FMQ (d-f), and FMQ+2 (g-i). Panels in the column to the left display the modal proportions in mol% for all the equilibrium phases in the system, the middle column shows the modal proportion in mol% for Fe-bearing phases only, and the column to the right displays the fraction of the total amount of iron in the system that each Fe-bearing phase contains. The vertical dashed line marks the position of the solidus, and the solid line indicates the appearance of orthopyroxene in the mineral assemblage near the end of biotite dehydration melting.

Phase stability is similar between the FMQ-2 and FMQ model runs, with only minor variations in stability fields and higher $Fe^{3+}/\Sigma Fe$ for phases incorporating ferric iron in the FMQ model (Figure 6a-f). For simplicity in the discussion, we consider the

model results run at FMQ-2 and FMQ first and discuss the results of the model run at FMQ+2 later. Under these lower oxygen fugacity conditions, partial melting starts with H_2O release from biotite dehydration at ~670 °C, which reacts with quartz and plagioclase to produce melt (*Spear*, 1993). Production of melt via this reaction is minimal, and iron concentrations in the produced granitic melt are low (< ~0.25 wt.% on an anhydrous basis). At ~700 °C, melting continues via the reaction:

$$Bt + Sil + Qtz = Melt + Crd + Kfs \pm Ilm \tag{2.2}$$

which takes place until sillimanite is exhausted at ~725°C. During this melting interval, most of the iron is accommodated in cordierite, ilmenite, and biotite, and only a negligible amount is transferred to the melt. From ~725–750 °C, a small quantity of melt is produced due to plagioclase reaction with quartz. Then, at ~750 °C, garnet is introduced to the mineral assemblage via the reaction:

$$Bt + Qtz + Pl = Melt + Grt + Crd + Ilm \tag{2.3}$$

Reaction 2 proceeds until ~810 °C, increasing the amount of melt to ~30 mol% and transferring ~5% of the bulk Fe in the system to the melt. Finally, orthopyroxene becomes stable in the residual assemblage at 815 °C, and the melt fraction increases to ~36 mol% when biotite is quickly consumed through reaction 3:

$$Bt + Qtz + Grt = Melt + Opx + Crd + Ilm \tag{2.4}$$

For temperatures above 815 °C, melt and orthopyroxene are steadily produced by feldspar reaction with quartz and garnet. Then, at ~930 °C, spinel becomes stable, and the melt-producing reaction rapidly consumes quartz and garnet until garnet runs out at ~950 °C. Melt and spinel then continue to be produced through the reaction of orthopyroxene with plagioclase, reaching a total melt fraction of ~80 mol% with ~55% of Fe in the bulk system residing in the melt at 1000 °C (Figure 6a-f).

The subsolidus mineral assemblage and initial melting reaction for the most oxidized model (i.e., FMQ+2) are the same as for lower oxygen fugacity calculations. At ~720 °C, melt is produced through reaction (1) until sillimanite is entirely consumed at ~730 °C. The formation of spinel (magnetite) and ilmenite at ~725 °C quickly

consumes biotite and increases the rate of melt production. Biotite readily disappears at ~825 °C when orthopyroxene joins the mineral assemblage via reaction 3, with the proportion of melt increasing to ~30 mol%. Orthopyroxene and melt are then produced by the reaction of feldspar with quartz, magnetite, and cordierite, which eventually consumes all the available quartz and K-feldspar. Melt generation continues at the expense of plagioclase and orthopyroxene, reaching ~80 mol% melt at 1000 °C (Figure 6g-i).

The subsolidus equilibria and partial melting products at a constant pressure of 0.3 GPa closely resemble those predicted at 0.4 GPa, with the most notable differences related to cordierite and garnet stability. At 0.3 GPa, the stability field of cordierite extends to temperatures below the solidus, replacing sillimanite and increasing its modal proportion relative to other iron-bearing phases. The main partial melting reaction can be written as follows:

$$Bt + Crd + Qtz \pm Pl = Melt + Kfs \pm Grt \pm Ilm \tag{2.5}$$

which proceeds until biotite is exhausted at ~790 °C. Notably, reaction 2.5 produces only a small amount of garnet, which is quickly consumed by reaction 2.4 before biotite depletion. While reactions 2.4 and 2.5 increase the melt fraction from ~10 mol% to ~30 mol% between ~780-790 °C, less than ~5% of the bulk Fe in the system is in the melt. Melt production then continues via the reaction of feldspar with quartz, where orthopyroxene and cordierite are the peritectic phases. When quartz is used up at ~835 °C, melt is produced by reaction between feldspar and orthopyroxene, with cordierite remaining relatively stable.

5.4 Equilibrium fractionation of iron isotopes

Since the phase relationships for a system with oxygen fugacity conditions varying from FMQ-2 to FMQ are nearly identical, the lines defined by the resulting fractionation factors between the melt phase and complementary residual solid vs. temperature trajectories are almost parallel across the whole temperature range considered (Figure 7). The model run at FMQ is offset ~0.04‰ towards higher $\Delta^{56}Fe_{melt-residue}$ relative to FMQ-2 due to the greater proportion of Fe^3+ in the melt. By contrast, the fractionation factors vs temperature trajectories for melts produced at the FMQ+2 buffer only parallels the more reduced models at the onset of partial melting (Figure 7). At the solidus, the estimated $\Delta^{56}Fe_{melt-residue}$ values are ~+0.225, ~+0.290, and ~+0.450 ‰ for the FMQ-2, FMQ, and FMQ+2 models,

respectively. These values then decrease nearly monotonically until garnet enters the mineral assemblage at ~750 °C (Figure 7). From this temperature, the increase in $\Delta^{56}Fe_{melt-residue}$ reflects the continued loss of biotite from the solid assemblage and the increasing modal proportion of garnet ($[F]$ = 110 N/m) relative to biotite ($[F]$ > 188 N/m). With biotite exhausted, the modeled $\Delta^{56}Fe_{melt-residue}$ drops by ~0.03‰ and then decreases at a constant rate from ~815 °C to ~930 °C. Garnet is consumed when spinel joins the mineral assemblage, and cordierite and orthopyroxene decrease their proportions, further decreasing melt-residue fractionation (Figure 7).

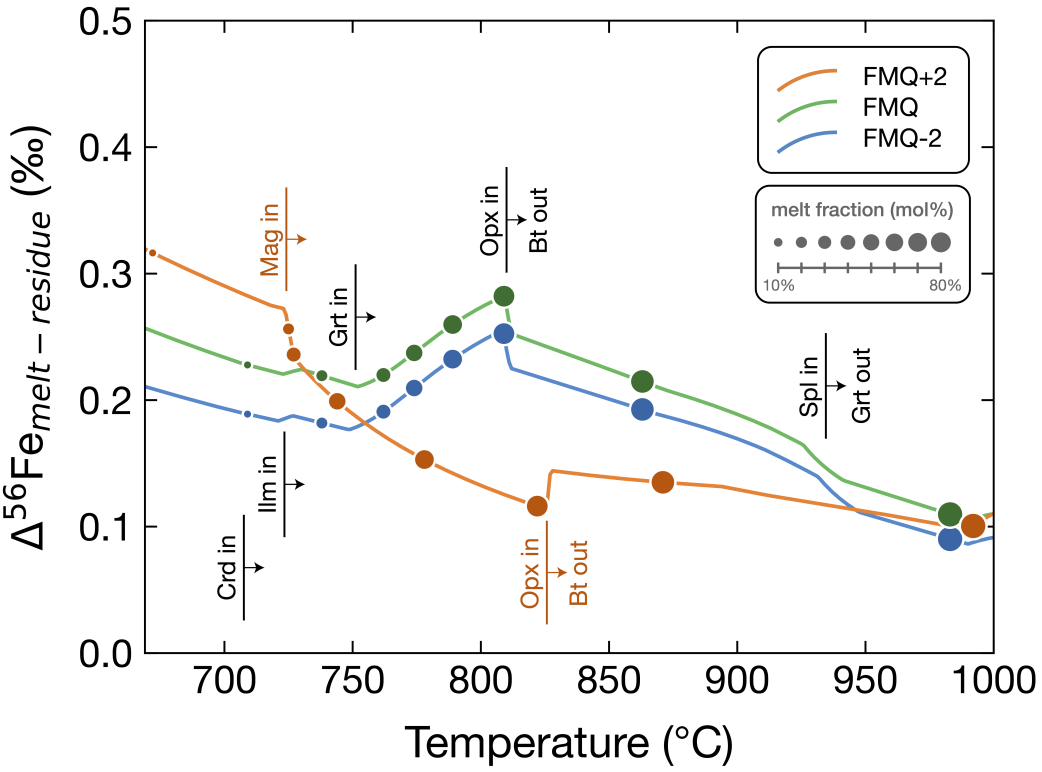


Figure 2.7: Predicted iron isotope fractionation between granitic melts and complementary residues produced by partial melting of metapelite SP-16-16 at 0.4 GPa. Oxygen fugacity conditions are FMQ-2 (blue), FMQ (green), and FMQ-2 (orange). Circles with variable sizes represent melt fractions varying from 10% to 80%. Vertical lines mark the approximate temperature of orthopyroxene stability and biotite exhaustion.

In contrast, for the model run at FMQ+2, sillimanite replacement by cordierite coincides with ilmenite and spinel joining the mineral assemblage, while biotite is rapidly consumed (Figure 7). This results in an abrupt transition to lower $\Delta^{56}Fe_{melt-residue}$ values, which decrease at a relatively constant rate due to the replacement of biotite by orthopyroxene at ~825 °C and a decrease in the modal

abundance of magnetite (modeled as an endmember of the spinel solid-solution). Finally, the $\Delta^{56}Fe_{melt-residue}$ gradually decreases for temperatures above ~825 °C since the distribution of solid Fe-bearing phases remains relatively constant at these temperatures.

6. Discussion

6.1 Iron isotopes in the metasedimentary source rock

Mineral heterogeneity in the sedimentary protolith (e.g., relative abundance of clay versus feldspars) of the Zealand unit metasedimentary rocks can be translated into variable isotopic compositions upon metamorphism, which in turn can be transferred to the melt during anatexis. Indeed, the Zealand unit metasedimentary rocks display a range of isotopic compositions consistent with the variability in the GLB samples. However, the relationship between the mineralogy and isotopic composition of the Zealand unit samples is complex and particular to each sample. For instance, sample SP-16-11 has the lowest δ^{56}Fe, resulting from its high modal proportion (~10-15 %) of pyrrhotite with $\delta^{56}Fe_{po}$ = –0.337 ± 0.025 ‰, which is also reflected in a high FeO/MgO compared to other metapelites (Figure 4c). Sample SP-18-27 also has elevated FeO/MgO, consistent with abundant ilmenite observed in that sample; however, ilmenite drives this sample towards a positive bulk δ^{56}Fe value (+0.114 ± 0.035 ‰). Sample SP-18-26, collected from the same location as SP-18-27, in contrast, contains garnet and biotite as main iron carriers, and its isotopic composition is thus lighter (δ^{56}Fe = +0.004 ± 0.043 ‰). Both SP-18-27 and SP-18-26 contain similar proportions of biotite and garnet and only minor pyrrhotite, which, while having elevated δ^{56}Fe (+0.364 ± 0.044 ‰ and +0.337 ± 0.044 ‰; Figure 5; Table 2), exerts little control on the bulk-rock δ^{56}Fe. Therefore, the large isotopic difference between these two samples is attributed to the significant presence of ilmenite in SP-18-27. It is also worth noting that garnet plays an essential role in the isotopic composition of samples from the Zealand unit. Since most iron in garnet is located in a cubic site, with high coordination number, garnet preferentially partitions light iron isotope species. Thus, samples in which garnet is lacking (or occurs in relatively low amounts) tend to show heavier isotopic compositions (> +0.119 ‰).

Isotopic heterogeneities in the metasedimentary source of the GLB can result from metamorphism starting at low grade and culminating in partial melting. During prograde metamorphism, iron is generally mobilized between different phases through metamorphic reactions from lower-greenschist to granulite facies (*Slotznick et al.*,

2018). Fractionation of iron isotopes is, therefore, a natural outcome of the metamorphic process. However, the magnitude and direction of the isotopic fractionation will depend on the $P^{\smile}T$ conditions, the stable mineral assemblages, and the extent of fluid exchange within and out of the system (*Valley*, 1986). For rocks from the Zealand unit, there is no apparent correlation between metamorphic grade and δ^{56}Fe values (Figure 5), suggesting that increasing $P^{\smile}T$ conditions during prograde metamorphism have a negligible or non-systematic effect on the iron isotope composition of the metasediments.

The role of fluid transfer on iron isotope fractionation during metamorphism may be relatively minimal, although it has yet to be studied in detail. In an open system, prograde metamorphism is dominated by mineral dehydration and fluid loss from the system (*Guiraud et al*., 2001). An overall decrease of light isotopic species is thus expected as ferrous iron tends to be more soluble in aqueous fluids at metamorphic conditions than ferric iron (*Azimov and Bushmin*, 2007). If external fluids are introduced, by contrast, retrograde metamorphism will produce hydrated phases, and the isotopic composition of the system will move towards the composition of the fluids. However, large fluid-to-rock ratios would be required to significantly modify the isotopic composition of the host rock, as most metamorphic fluids typically have low iron contents (i.e., «1 wt.%; *Yardley*, 2005, 2013; *Hermann et al*., 2013; *Yardley and Bodnar*, 2014). For example, as much fluid as rock mass must be expelled from (or introduced to) the system to change the δ^{56}Fe by ±0.1‰ (i.e., a fluid-to-rock ratio of ~2:1–3:1 in volume). This estimate assumes 1% and 5% iron contents and initial δ^{56}Fe values of -0.5‰ and 0.1‰ for the fluid and the rock, respectively (*Yardley*, 2005; *Dauphas et al*., 2017).

Progressive metamorphism is generally expected to homogenize isotopic variability given sufficient time at elevated temperatures (*Frost et al*., 2007; *Dauphas et al*., 2007a, b; *Hyslop et al*., 2008). However, the development of metamorphic foliation and the growth of porphyroblasts can result in domains (i.e., bands) with contrasting isotopic compositions and large inter-mineral isotopic heterogeneities, as these processes are accompanied by significant mass transfer (*Ague*, 1991, 2014). Mineral recrystallization is thus expected to result in the redistribution of isotopic species. Heavier iron isotopes will be preferentially incorporated in phases with low coordination, whereas lighter isotopes will follow phases with iron in high coordination (*Bigeleisen and Mayer*, 1947; *Urey*, 1947; *Schauble*, 2004). For example, the growth of garnet and biotite at the expense of chlorite, muscovite, and quartz (*Spear*, 1993)

should result in significant isotopic fractionation, producing isotopically light garnet and heavier biotite, while the system composition remains approximately constant. This process is important because the garnet contribution to biotite dehydration melting at the solidus is minimal, which means that the effective source isotopic composition of some SPGs may be heavier than the bulk metasedimentary rock. It is worth noting, however, that inter-mineral equilibrium isotopic fractionation does not always seem to be achieved during burial and metamorphism, or at least not for all phases. For example, some pyrite grains in metasedimentary samples, from prehnite-pumpellyite to amphibolite facies, show non-equilibrated δ^{56}Fe compositions, consistent with previous studies showing that pre-metamorphic isotopic signatures can survive high grades of metamorphism (*Whitehouse and Fedo*, 2007; *Galić et al*., 2017; *Marin-Carbonne et al*., 2020; *Dupeyron et al*., 2023).

Besides iron-bearing aluminosilicates, sulfides are a significant iron pool for metasedimentary rocks. Even small abundances of sulfides can significantly influence the bulk-rock isotopic composition as these phases contain a large amount of iron, and their iron isotope composition can be as variable as several per mil in δ^{56}Fe (*Rouxel et al*., 2005; *Dauphas et al*., 2017). Sulfides in metasedimentary rocks from the Zealand unit are dominated by pyrrhotite, likely formed from desulfidation of sedimentary pyrite during metamorphism (*Ferry*, 1981; *Craig and Vokes*, 1993). The transformation of pyrite to pyrrhotite requires an overall decrease in the Fe/S ratio, which can be accomplished by introducing dissolved iron in free fluids, reaction with iron-bearing silicates or oxides, or loss of sulfur to a fluid phase (*Ferry*, 1981; *Craig and Vokes*, 1993; *Bucholz et al*., 2020). The latter is likely the dominant mechanism of pyrrhotite formation in pyrite-poor, mica-rich sediments because dehydration reactions during prograde metamorphism can drive pyrite breakdown, which requires sulfur loss to maintain equilibrium conditions (*Tomkins*, 2010; *Bucholz et al*., 2020). If this is the case, the iron isotope composition of pyrrhotite should be similar to that of its pyrite precursor.

In summary, the relative abundance of iron-bearing phases controls the isotopic composition of metapelites from the Zealand unit. Iron transfer during metamorphic reactions can drive isotopic fractionation between phases and distinct chemical domains formed during metamorphism. However, the bulk sediment will likely preserve a composition similar to that of the protolith (*Frost et al*., 2007; *Dauphas et al*., 2007a, b; *Hyslop et al*., 2008; *Marin-Carbonne et al*., 2020; *Dupeyron et al*., 2023). Iron mobility during metamorphism can be regarded as a process

occurring under near-closed system conditions, where fluid exchange may contribute minimally to the composition of the metasedimentary rocks. Hence, the range of isotopic compositions of the metasedimentary rocks from the Zealand unit likely represents the compositions of the source sediment and its isotopic variability. Specifically, samples dominated by biotite as the primary iron host, including the restitic sample SP-16-30, are likely close to the effective isotopic composition of the source with δ^{56}Fe values between 0‰ and 0.191‰.

6.2 Controls on equilibrium isotope fractionation during anatexis

Before discussing the isotopic composition of granitic rocks from the GLB, it is important to consider the variables that control isotopic fractionation once the system has crossed the solidus. Equilibrium isotopic fractionation during partial melting can be assessed in terms of variations in force constants, $[F]$, for the melt and its complementary residue. These variations in $[F]$ values reflect changes in the composition of coexisting phases, the mineral assemblage, and the oxygen fugacity of the system (Figure 8a). $[F]_{\text{melt}}$ decreases with decreasing melt SiO_2 content and $Fe^{3+}/\Sigma Fe$, which occurs as temperature and melt fraction increase. Changes in temperature and melt fraction strongly influence $\delta^{56}Fe_{\text{melt}}$, with maximum fractionation between the melt and the source ranging from ~+0.1 to +0.3 ‰ (Figure 8b). Likewise, $\delta^{56}Fe_{\text{residue}}$ only deviates significantly from the source isotopic composition at large melt fractions (Figure 8b). Mineral $Fe^{3+}/\Sigma Fe$ ratios and the relative proportions of iron-bearing minerals in equilibrium with the melt control the magnitude of $[F]_{\text{residue}}$, as this quantity represents a weighted average of the force constants for all solid phases in the system (Figure 8c). Thus, isotopic fractionation between the melt and the residue is expected to decrease in a non-monotonic fashion as partial melting progresses (Figure 8a–b).

6.2.1 Availability of water during melting

The initial water content of the system strongly controls the solidus temperature and the amount and composition of melt produced during partial melting. However, the difference in predicted $\delta^{56}Fe_{\text{melt}}$ values between water-undersaturated and water-saturated models at equivalent temperatures is relatively small (Supplementary Figure S5). Additionally, calculated melt compositions under minimally water-saturated conditions at the solidus are consistent with major element and isotopic compositions observed in natural SPGs (see Supplementary Material for discussion). This, along with the observation that fluid-absent reactions dominate the formation

of granitic rocks produced by partial melting (*Stevens and Clemens*, 1993; *Clemens et al*., 2020), suggests that minimal water-saturation at the solidus is a reasonable assumption for SPG generation. In contrast, while fluid-excess melting may be important for generating leucosomes in some anatectic migmatites, the low pore space in metamorphic rocks restricts the availability of free fluid, thereby limiting the potential for substantial production of granitic rocks through fluid-excess reactions (*Stevens and Clemens*, 1993).

6.2.2 Effects of melt loss

Melt loss events (MLE) in open systems drive changes in the bulk composition of the system during anatexis. Such changes result in different phase compositions and mineral assemblages as compared to batch melting, which translates into distinct isotopic fractionation between the melt and the residue. However, melt extraction during biotite dehydration melting leads to only small differences in $\Delta^{56}Fe_{(melt-residue)}$ values relative to fractionation values predicted for batch melting at equivalent temperatures. Overall, the δ^{56}Fe of partial melts produced in a system that undergoes melt extraction would only deviate from values for batch melting when biotite is completely exhausted, with estimated differences of less than 0.05 ‰ (Figure S6). Conversely, continuous aggregation of melt batches from successive MLEs forms hybrid melts that are more strongly influenced by isotopic composition of the earliest batches. As a result, aggregated melts generated at temperatures above biotite-out boundary tend to resemble the isotopically heavier melts produced during biotite dehydration melting (Figure S6).

6.2.3 Oxygen fugacity

Oxygen fugacity is also expected to influence the extent of isotopic fractionation, having a strong control on the stability of iron-bearing phases and $Fe^{3+}/\Sigma Fe$ ratios (Figure 8c). For example, up to ~15 mol% garnet is produced during partial melting of SP-16-16 at 0.4 GPa at reducing conditions (i.e., FMQ-2 or FMQ oxygen fugacity), but under more oxidizing conditions (e.g., FMQ+2), approximately the same amount of magnetite would be produced instead of garnet (Figures 6 and 7). Although such oxidizing conditions are unlikely to have existed during partial melting of the Zealand metasedimentary rocks, replacing garnet with magnetite would result in lower isotopic fractionation between the melt and the residue. Thus, granitic melts derived during partial melting of pelitic metasedimentary rocks under

higher oxygen fugacity conditions are expected to be isotopically heavier than those formed at lower oxygen fugacity at low temperatures (<775 °C) and isotopically lighter at higher temperatures.

Differences in the iron isotope compositions of melts produced under different fO_2 conditions can be resolvable with current analytical precision, particularly for granitic samples representing low melt fractions. However, retrieving redox conditions from Fe isotopes in natural granite samples would necessitate complementary information about the major-element and isotopic composition of the protolith, as well as estimates of the melt fraction and metamorphic conditions at which the melt formed. It is also worth noting that overlapping regions in the iron isotope composition of melts produced at different oxygen fugacity may exist. For example, at ~750 °C or ~40 mol.% melt, the model for partial melting of the Zealand unit predicts nearly the same Fe isotope composition for all considered fO_2 conditions (Figures 8b and 8d), rendering Fe isotopes ineffective as a redox indicator in such cases. Nevertheless, even under variable fO_2 conditions, the predicted iron isotope compositions of SPGs and their complementary residual lithologies display smaller fractionation relative to their source than the large variability observed in the sedimentary record.

6.2.4 Pressure

Finally, the pressure conditions during metamorphism and anatexis can affect isotopic fractionation between the melt and the complementary residue (Figure 8d). During the modeled melting behavior of SP-16-16, the stability field of biotite extends to higher temperatures at 0.4 GPa compared to 0.3 GPa as additional H_2O is necessary to minimally saturate the system at the solidus (see Supplementary Figure S2). As a result, biotite dehydration melting occurs over a wider temperature range and produces more extensive melting at 0.4 GPa (~60 mol%) than at 0.3 GPa (~40 mol%). The difference in $\Delta^{56}Fe_{(melt-residue)}$ between the two pressures from the solidus to the temperature of biotite exhaustion at 0.3 GPa is minimal since partial melting in both cases is caused by H_2O released from biotite reacting with feldspar and quartz to produce melt + garnet (*Spear*, 1993). However, the amount of garnet produced during biotite dehydration controls the magnitude of $\Delta^{56}Fe_{(melt-residue)}$. For example, in the FMQ-2 and FMQ models, isotopic fractionation at 0.4 GPa increases by ~0.18‰ from ~750 °C to ~810 °C before biotite is completely consumed, as the melting reaction also produces a significant amount of garnet (Figure

8d). At 0.3 GPa, only a small amount of garnet is produced, and $\Delta^{56}Fe_{(melt-residue)}$ decreases nearly monotonically until biotite is exhausted (Figure 8d). In general, garnet stability increases with pressure, but it also depends on the major element composition of the system. With SP-16-16, a small proportion of garnet is stable at 0.3 GPa over a reduced temperature range; other more Al- or Mn-rich metapelite compositions, however, may stabilize more garnet at these pressure conditions, resulting in significant isotopic fractionation between the melt and the stable mineral assemblage.

In summary, the iron isotopic composition of SPGs is controlled by several factors during partial melting. Variations in mineral chemistry and metamorphic conditions lead to changes in the iron bonding environment, which translate into variable iron force constant values for the melt and residue phases. The initial H_2O content controls the position of the solidus, as well as the melt fraction and composition. For all H_2O contents, isotopic fractionation between the melt and the complementary solid is greatest near the solidus and decreases as the proportion of iron in the melt increases. However, regardless of the initial hydration state of the system, melts generated at the same temperature conditions are predicted to have similar $\delta^{56}Fe_{melt}$. Furthermore, the stability of iron-bearing phases is strongly dependent on fO_2 conditions, thus influencing the extent of isotopic fractionation. Partial melts produced under different fO_2 conditions may be distinguished with current analytical precision if the protolith composition and metamorphic conditions are known. It is also possible for melts produced under different fO_2 conditions to have identical $\delta^{56}Fe_{melt}$ compositions, in which case Fe isotopes cannot be used as redox proxies. Pressure conditions also play a role, affecting the stability and proportion of minerals like garnet and biotite, which in turn influence isotopic fractionation between the melt and the solid residue. The interplay of these variables results in granitic melts and restitic rocks that generally reflect the isotopic composition of their metasedimentary sources, with only minor fractionation relative to the source.

6.3 Equilibrium Fe isotope fractionation in the GLB

There is general agreement between the iron isotope composition of the granite samples and their mineralogy. Relatively high $\delta^{56}Fe$ values (~+0.2-0.3 ‰) correspond to samples in which biotite and accessory ilmenite are the main iron-bearing phases (Figure 5). In contrast, the isotopic composition of SP-16-33, with the lowest $\delta^{56}Fe$ among the granite samples (+0.111 ± 0.018 ‰), is strongly influenced by abundant garnet and tourmaline in similar modal proportions. Although we did not measure

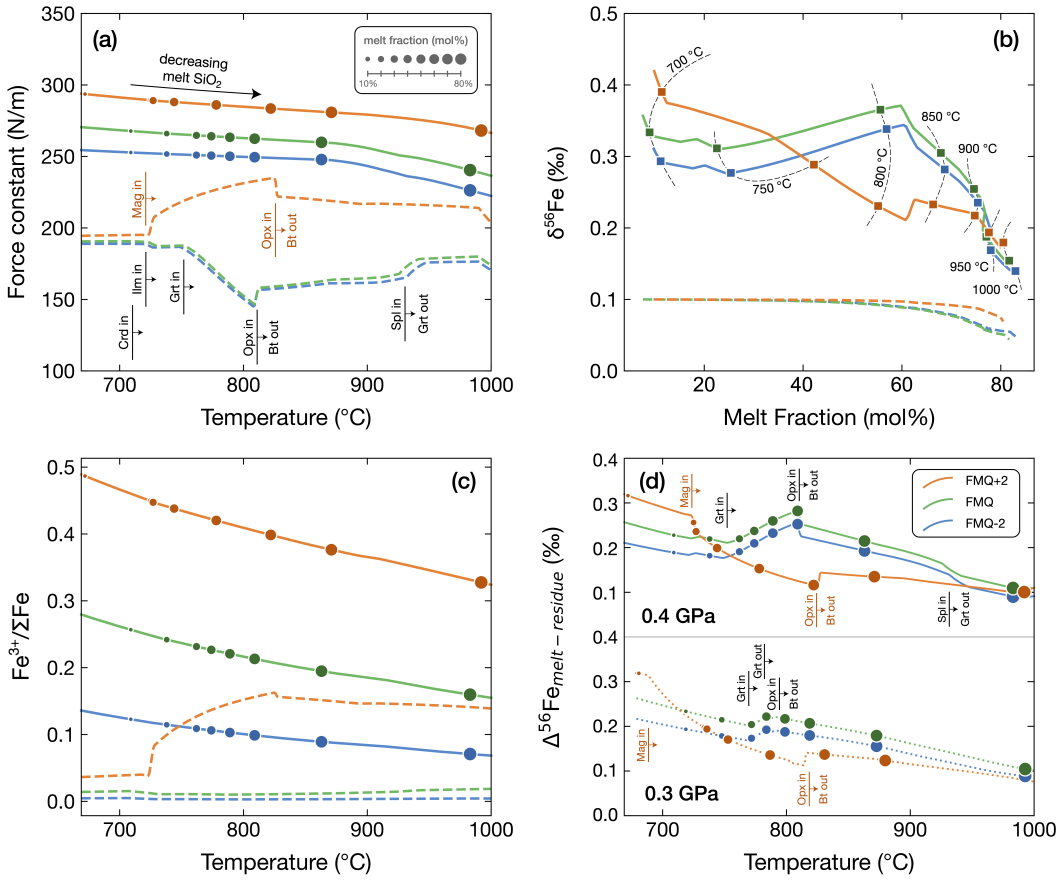


Figure 2.8: Variation of parameters relevant to iron isotope fractionation during partial melting of metapelite SP-16-16 at 0.4 GPa. In all panels, continuous lines represent the melt, and dashed lines are the solid residue. The different line colors represent different redox conditions of the system: FMQ-2 (blue), FMQ (green), and FMQ+2 (orange). Circles with variable sizes represent melt fractions varying from 10% to 80% in increments of 10%. (a) Changes in the force constant of the melt phase and the residue as the temperature increases. (b) Relationship between δ^{56}Fe, melt fraction, and system temperature. The squares mark the temperature of the system at the corresponding melt fraction. (c) $Fe^{3+}/\Sigma Fe$ for the melt and the solid residue as temperature increases. For the melt, the ferric iron content is estimated using the formulation from Kress and Carmichael (1991), as the thermodynamic model for the melt from White et al., 2014a do not include Fe^{3+}. (d) Difference in $\Delta^{56}Fe_{(melt-residue)}$ for partial melting at 0.4 GPa (continuous lines) and 0.3 GPa (dotted lines).

individual garnet grains, garnet is expected to be isotopically light and can significantly lower the whole-rock isotopic composition when present in a large proportion (Figure 5). Tourmaline in equilibrium with garnet is expected to have a higher δ^{56}Fe (*Nie et al*., 2021), but its contribution to the whole-rock isotopic composition is less than that of garnet because it contains less iron (~13 wt. % FeO in tourmaline versus ~36 wt.% FeO in garnet for sample SP-16-33; Supplementary Table S3). The higher δ^{56}Fe of sample SP-16-34, also containing garnet + tourmaline, can be explained by a larger proportion of biotite.

Equilibrium isotopic fractionation due to biotite dehydration melting can explain the, on average, higher δ^{56}Fe of the GLB compared to the Zealand unit metasedimentary rocks (+0.192 ‰ versus +0.101 ‰, respectively). The predicted $\Delta^{56}Fe_{(melt\text{-}residue)}$ is at a maximum during the later stage of biotite dehydration melting for the FMQ and FMQ–2 oxygen buffers (~800–810 °C), reaching values of ~+0.300 ‰ and ~+0.250 ‰, respectively (Figure 7). The shape of the $\Delta^{56}Fe_{(melt\text{-}residue)}$ model is almost identical to $\delta^{56}Fe_{melt}$, as the transfer of iron to the melt is minor and the iron fraction in the residue is considerably higher than in the melt (Figures 7, 8d, and 9). Thus, biotite dehydration melting causes significant isotopic fractionation between the melt and the source (up to ~0.250–0.300 ‰), but negligible fractionation between the source and the residue (<0.012 ‰ at ~800–810 °C). Therefore, the restitic sample SP-16-30, with δ^{56}Fe of 0 ‰, represents a reasonable estimate of the isotopic composition of the source for the GLB magmas, in addition to the metapelites from the Zealand unit.

Figure 9 shows the predicted $\delta^{56}Fe_{melt}$ assuming the source to have the range of isotopic compositions observed in Zealand unit metasedimentary rocks (i.e., δ^{56}Fe from –0.188 to +0.191 ‰, averaging +0.1 ‰). The range of isotopic compositions measured in the granite samples varies between +0.111 ± 0.018 ‰ and +0.315 ± 0.038 ‰ (grey band in Figure 9), which is a narrower range (0.204 ‰) than that defined by the metasedimentary samples (0.379 ‰), partly explained by isotopic homogenization during anatexis (see Section 6.4). Calculated $\delta^{56}Fe_{melt}$ values at the onset of melting (~680 °C) increase with increasing oxygen fugacity, reaching a peak at the onset of partial melting in all modeled redox conditions and also at the latter stages of biotite dehydration melting in the case of the FMQ-2 and FMQ oxygen buffers. Progressive lowering of $\delta^{56}Fe_{melt}$ values is expected for the FMQ+2 buffer during biotite dehydration melting as magnetite stabilizes instead of garnet. However, the absence of equilibrium assemblages containing magnetite or

other highly oxidized species suggests that magma generation for the GLB occurred under more reduced conditions, as determined by previous work (maximum inferred oxygen fugacity of ~FMQ-1; *Bucholz et al.*, 2018).

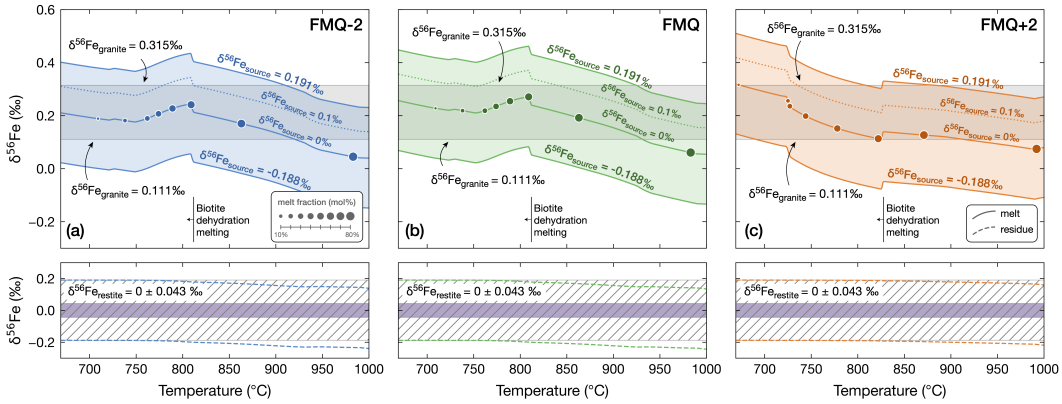


Figure 2.9: Predicted iron isotope compositions for granitic SPG melts (top panels) and complementary residues (bottom panels) produced by partial melting of metapelite SP-16-16 at 0.4 GPa at variable oxygen fugacity conditions: (a) FMQ-2 (blue), (b) FMQ (green), and (c) FMQ+2 (orange). In the top panels, continuous lines are the predicted isotopic compositions with variable source compositions, whereas dotted lines are predicted melt iron isotope compositions with the mean δ^{56}Fe of the Zealand unit metasedimentary rocks (0.1‰). The gray region is the range of measured isotopic compositions for the GLB. Circles with variable sizes represent melt fractions varying from 10% to 80% in increments of 10%. In the bottom panels, the purple region is the isotopic composition of the restitic sample SP-16-30. Colored dashed lines mark the range of predicted isotopic compositions for the residual assemblages produced during partial melting with source δ^{56}Fe compositions varying from -0.188‰ to 0.191‰ (the range measured in Zealand unit rocks). The hatched area is the range of isotopic compositions measured in the metapelite samples from the Zealand unit.

The range of δ^{56}Fe measured in the granites is contained within the calculated $\delta^{56}Fe_{melt}$ values for the FMQ-2 and FMQ models during biotite dehydration melting, using the range of observed compositions from the Zealand unit (-0.188 ± 0.023 to +0.191 ± 0.035 ‰) (Figure 9). However, when considering the mean δ^{56}Fe of the Zealand unit metasedimentary rocks as the source composition (+0.101 ‰), only the heaviest granite compositions (> +0.277 ‰) are predicted by the FMQ-2 model at temperatures <850ºC, whereas the FMQ model predicts higher $\delta^{56}Fe_{melt}$ than the values measured in most the granite samples (> +0.310 ‰). Excluding the sulfide-rich metapelite SP-16-11 from the metasedimentary average and assuming the source composition is 0 ‰, the FMQ-2 model predicts most of the measured granite iron isotope compositions except for values < +0.177 ‰, whereas the FMQ

model predicts the heaviest granite (> +0.210 ‰) compositions.

In summary, the iron isotope compositions of granite samples from the GLB reflect their mineral content. High δ^{56}Fe values are associated with biotite and ilmenite, and the lowest to garnet and tourmaline-rich samples. Equilibrium iron isotope fractionation due to biotite dehydration melting at low oxygen fugacity (FMQ-2 and FMQ buffers) accounts for measured isotopic differences between the GLB and the Zealand unit metapelites (~0.12-0.30 ‰). This process also results in negligible fractionation between the source and the solid residue, consistent with previous studies on iron isotope fractionation between strongly peraluminous granites and their source (*Telus et al*., 2012; *Xu et al*., 2017; *Nie et al*., 2021). Thus, restitic lithologies, like sample SP-16-30, may closely approach the bulk composition for the source of SPG magmas.

Furthermore, most measured δ^{56}Fe values in granite samples from the GLB can be explained by equilibrium isotope fractionation during biotite dehydration melting under reducing conditions, if the source has δ^{56}Fe of 0 ‰. In contrast, the average δ^{56}Fe measured in metapelite samples (+0.101 ‰) can only account for isotopically heavy granite samples. In general, the source composition dictates the equilibrium δ^{56}Fe composition of granite samples. Thus, if equilibrium fractionation is the process that contributes the most to the iron isotope composition of SPGs, these rocks can be used to trace the composition of their sedimentary source.

6.4 Isotopic variability within the GLB

While the range of Fe isotope compositions in granite samples from the GLB is relatively narrow (~0.2 ‰), equilibrium fractionation between SPG magmas and the average composition of their source can only account for δ^{56}Fe values greater than +0.177 ‰. In this section, we explore the roles of assimilation, magmatic differentiation, and fluid exsolution, processes that are likely to occur during anatexis and batholith emplacement. Specifically, we discuss whether these processes could impart the magmas from which the GLB crystallized with an isotopic composition that is lighter than what equilibrium fractionation models predict.

The amount of restitic or source/host rocks required to be mixed in the melt to explain the lowest δ^{56}Fe values measured in the granite depends on the composition of the source. For example, using the FMQ-2 model at ~770 °C with a source δ^{56}Fe = +0.1 ‰ and FeO = 5 wt.%, the calculated $\delta^{56}Fe_{melt}$ is ~+0.3 ‰ with a FeO content of ~1 wt.%. Assimilation of ~20–80% by mass of source or restitic

rocks is needed to produce melt compositions with δ^{56}Fe between +0.1 and +0.2 ‰. By contrast, assuming a source δ^{56}Fe = 0‰, the δ^{56}Fe of the melt is ~+0.2 ‰ at ~770 °C, which would require less than 15% of source rock or restite to produce the lowest granite compositions measured. It is also possible for the melt to assimilate peritectic phases such as garnet. For instance, if a melt containing 1 wt. % FeO and δ^{56}Fe = +0.3 ‰ absorbs ~5 % by mass of an almandine-rich garnet composition with 30 wt. % FeO and δ^{56}Fe = 0 ‰, the δ^{56}Fe of the melt would decrease to +0.12 ‰. No correlation between δ^{56}Fe and FeO is observed, however, so peritectic garnet entrainment is likely not the dominant control on the δ^{56}Fe in the granites.

During partial melting, assimilation of source rock material can also result in dissolution of sulfides in the melt as FeS species (*Clémente et al.*, 2004; *Klimm et al.*, 2012; *Bucholz et al.*, 2020). Less than 1% of isotopically light pyrrhotite like that in SP-16-11 would need to be dissolved in the melt to produce the lowest δ^{56}Fe measured in granite samples. However, pyrrhotite in the Zealand unit metasedimentary rocks has variable isotopic composition, with δ^{56}Fe ranging from -0.337 to +0.364 ‰ (Figure 5), and assimilation of isotopically heavy sulfides could also increase the melt δ^{56}Fe. An example of this process could be the sample SP-16-22, which has the highest δ^{56}Fe composition among the measured granite samples. Evidence of sulfide dissolution in this sample comes from sulfur isotopes showing incomplete re-equilibration between the melt phase and fluid H_2S from pyrite breakdown during assimilation of the metasedimentary host rock (*Bucholz et al.*, 2020).

An alternative model for the isotopic variability observed in the GLB is related to the internal differentiation of the magmatic pluton. Granitic plutons can be understood as variable mixtures of magmatic liquids and cumulus material produced by magmatic crystallization (*Bea et al.*, 1994; *Chappell and Wyborn*, 2004; *Chappell and Hine*, 2006). During differentiation, the melt component is expected to have a heavier iron isotope composition than the cumulate counterpart due to its higher $Fe^{3+}/\Sigma Fe$ and SiO_2 content. If a granite sample represents a large melt-to-cumulate ratio, its iron isotope composition would be heavier than a sample with a lower melt component. A simple Rayleigh fractionation model illustrates this scenario (Figure 10). Let us consider a crystallizing liquid produced at ~800 °C during partial melting of SP-16-16 at FMQ–2. The liquid composition is multiply saturated with the phases in the residual assemblage and will thus start to crystallize the same assemblage with $\Delta^{56}Fe_{(melt\text{-}cumulate)}$ of ~0.2 ‰ (same as $\Delta^{56}Fe_{(melt\text{-}residue)}$). The melt and crystallizing assemblage become isotopically heavier as fractional crystallization progresses, but

the melt is always heavier. If the cumulate produced after crystallization of the initial 20% iron fraction (δ^{56}Fe = +0.04 ‰) is arbitrarily mixed with the liquid containing 40% of the original iron fraction (δ^{56}Fe = +0.38 ‰) in a melt-to-cumulate ratio of 1:4, the resulting granite δ^{56}Fe will be +0.112 ‰. Local variability in melt segregation may allow mixing of variable melt-to-cumulate proportions in addition to mixing of melts and cumulates produced at different iron fractions. Therefore, the range of iron isotope compositions measured in the granite samples from the GLB can be attributed to variable melt–cumulus proportions. In this model, the average of the metapelites can produce melts with heavier iron isotope compositions due to equilibrium fractionation. Subsequent partial crystallization and incomplete magma segregation would produce variable proportions of the cumulate versus melt in the solidified granite.

Hydrothermal fluids exsolved during magma crystallization can transport significant amounts of metals, forming economic ore deposits (*Richards, 2011; Audétat*, 2019). This process can cause iron isotopic fractionation as the exsolving fluids can remove sufficient iron with a particular isotopic composition to alter that of the original magma (e.g., *Wawryk and Foden*, 2015; *Wang et al.*, 2021). The extent of isotopic fractionation depends on the fraction of fluid exsolved from the melt during crystallization and the iron content of that fluid. The amount of fluid released is determined by fluid solubility in the magma at specific $P - T$ conditions, and whether the fluid is released as a free phase or incorporated into crystallizing hydrous phases. Our phase equilibrium calculations yield melt compositions with ~6-8 wt.% dissolved H_2O, consistent with common estimates for silicic magmas (*Clemens*, 1984). On the other hand, the proportion of iron in the fluid is controlled by the partitioning of iron between the fluid and the magma, which may depend on factors such as the salinity of the fluid, the magma composition, and the depth of exsolution (*Simon et al.*, 2004; *Zajacz et al.*, 2008). The partition coefficients between magmatic-hydrothermal fluids and melt ($D_{\text{fluid/melt}}$) can vary by one to two orders of magnitude, with a strong dependence on the chlorine content of the fluid (*Zajacz et al.*, 2008; *Audétat*, 2019). Accordingly, Fe contents in magmatic fluids can range from less than 1 wt.% up to ~5 wt.% (e.g., *Audétat and Pettke*, 2003; *Zajacz et al.*, 2008; *Bartoli et al.*, 2013; *Audétat*, 2019). To decrease $\delta^{56}\text{Fe}_{\text{melt}}$, however, the fluid must be isotopically heavier than the crystallizing magma, which contradicts $\Delta^{56}\text{Fe}_{(\text{melt}-\text{residue})}$ estimations for chlorine-bearing fluids in equilibrium with magmas produced by partial melting of the GLB protolith (see Supplementary Material). Thus, fluid exsolution may not have significantly impacted the isotopic

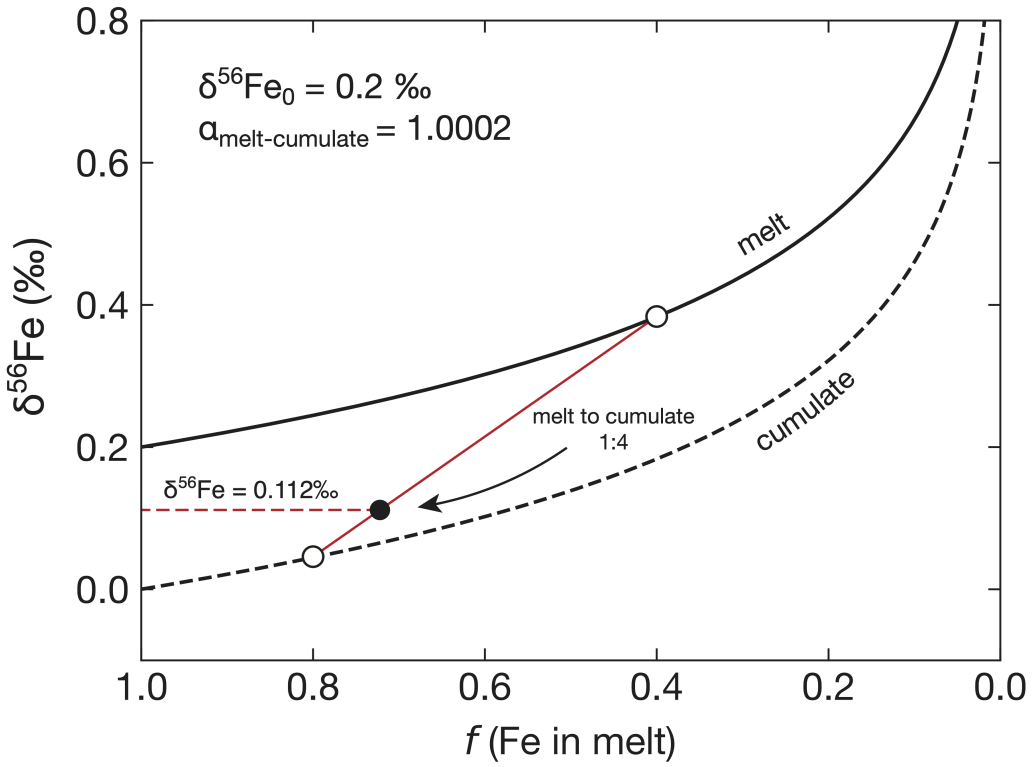


Figure 2.10: Rayleigh fractionation model illustrating fractional crystallization of a melt (continuous line) and the corresponding cumulus assemblage (dashed line) as the fraction of iron decreases with decreasing temperature. The initial melt has $\delta^{56}\text{Fe} = 0.2$, similar to that produced at 800 °C with the FMQ–2 model. The fractionation factor between the melt and the crystallizing assemblage ($\Delta^{56}\text{Fe}_{\text{melt–cumulate}}$) is assumed to be 0.2 ‰ ($\alpha_{\text{melt–cumulate}} = 1.0002$). The white dots represent an arbitrary melt when the remaining iron fraction is 0.4 and a cumulus assemblage produced when the iron fraction in the melt was 0.8. Mixing 20% melt with 80% cumulate results in a granite isotopic composition of $\delta^{56}\text{Fe} = 0.112$.

composition of granite samples from the GLB. However, this process may still be important for the iron isotope composition of other granites (*Poitrasson and Freydie*, 2005; *Heimann et al.*, 2008), including SPGs where large amounts of iron-rich fluids have been exsolved (e.g., *Wawryk and Foden*, 2015).

In summary, assimilation of source/host rock or sulfides with lighter iron isotope composition could drive the composition of isotopically heavy partial melts to lower δ^{56}Fe values. However, no correlation exists between δ^{56}Fe values and FeO_T in the GLB samples (see Supplementary Figure S4), indicating that entrainment and assimilation of restites, host lithologies, peritectic phases, or sulfides probably did not significantly contribute to most granite iron isotope compositions. Alternatively, the iron isotope variability in granite samples could be attributed to variable proportions

of granitic melt and cumulate minerals (such as biotite, garnet, and Fe-Ti oxides). In this case, granite samples with low δ^{56}Fe values would be indicative of lower melt-to-cumulus ratios, whereas isotopically heavier granites may be closer to crystallized liquids, with iron isotope compositions mainly controlled by equilibrium fractionation.

6.5 Implications for iron isotopes in SPGs and their relationship with the sedimentary record

Although the results we present here are specific to the GLB, the implications extend to most SPGs. Metamorphism and partial melting can both cause iron isotope fractionation between SPGs and their sedimentary sources. The influence of metamorphism, however, is expected to be minimal, as progressive fluid loss from the protolith during metamorphism may not significantly modify its composition. Moreover, prograde metamorphism is expected to partially redistribute iron isotopes among stable phases, minimizing inter-mineral heterogeneities without significantly affecting the bulk isotopic composition of the protolith. Consequently, the iron isotope composition of SPG protoliths should closely resemble the average composition of the original sedimentary rock before metamorphism.

Most isotopic fractionation occurs during partial melting, resulting in relatively small isotopic differences between SPGs and their sources. The magnitude of this equilibrium fractionation depends on several interdependent factors, including the composition of the phases involved in partial melting reactions, *P-T* conditions, and the oxidation state of the system. For reduced sedimentary sources typical of most SPGs, maximum isotopic fractionation may occur at two distinct points: the earliest stages of partial melting, close to the wet granite solidus, or at temperatures close to near-complete biotite dehydration melting. The former could be related to some anatectic migmatites, while the latter could be more likely recorded in larger granitic bodies like SPG batholiths, most often formed through fluid-absent melting reactions (*Stevens and Clemens*, 1993; *Clemens and Watkins*, 2001; *Clemens*, 2003; *Clemens et al.*, 2020). It is noteworthy that the magnitude and direction of isotopic fractionation between SPGs and their source is controlled by the conditions at which partial melting occurs, which are likely specific to each locality. However, the extent of equilibrium fractionation is expected to remain within a few tenths of a permil for most SPGs, as the major element compositions of sedimentary protoliths and derived partial melt compositions are relatively uniform over time and space (*Sylvester*, 1998; *Clemens*, 2003; *Nabelek*, 2019; *Bucholz and Spencer*, 2019).

Additional processes during batholith emplacement and magma crystallization can also influence the isotopic composition of partial melts. These include assimilation of isotopically lighter lithologies and minerals from the source or host rock, entrainment of iron-bearing peritectic phases like garnet, and exsolution of chlorine-rich fluids enriched in Fe. Moreover, granite rocks can consist of mixtures of crystallized liquid and cumulus minerals, each with distinct isotopic compositions. Variable proportions of these components in granite samples will lead to variations in their iron isotope composition. Notably, while these processes can modify the iron isotope composition of SPGs, the deviations from equilibrium fractionation are expected to be minor.

Importantly, SPGs not only inherit isotopic compositions close to that of their source but also display a significantly smaller range of variation in iron isotope compositions compared to sedimentary rocks. For example, while the Archean and Proterozoic bulk-rock sedimentary record exhibits a dispersion exceeding 2 ‰, variability in SPGs is only ~0.2 ‰ (Figure 11). Even within individual sedimentary formations, bulk-rock samples can exhibit δ^{56}Fe variability >1 ‰ (e.g., *Yamaguchi et al.*, 2005; *Johnson et al.*, 2008; *Bekker et al.*, 2010; *Fabre et al.*, 2011; *Busigny et al.*, 2014; *Heard et al.*, 2020; *Ostrander et al.*, 2022). The smaller range of variability in SPGs likely results from isotopic homogenization of the partially melted protolith during anatexis and the dominant source of Fe being derived from detrital minerals in the protolith (rather than chemical). Therefore, SPGs can serve as a reliable archive of the iron isotope evolution in the bulk siliciclastic sedimentary record.

7. Conclusions

Fe isotope fractionation between SPGs and their metasedimentary source results from a complex interplay between metamorphic and magmatic processes during anatexis. Equilibrium isotopic fractionation during partial melting is primarily controlled by the iron isotope composition of the protolith, which can be diverse even within the same unit. Metamorphism may cause only minimal isotopic fractionation so that the protolith likely reflects the isotopic signature of the sedimentary source. However, inter-mineral fractionation can persist or develop at high metamorphic grades.

As partial melting progresses, the equilibrium mineral assemblage controls the Fe isotope composition of the melt. Both mineral stability and phase compositions change in response to variations in the *P–T* conditions of the system and are

strongly dependent on fO_2. It is commonly assumed that higher temperatures lead to lower isotopic fractionation between phases at equilibrium, such as melt and restitic phases. However, temperature changes can stabilize phases with a different iron bonding environment and alter the average force constant, $[F]$, of the solid phases, thereby varying the extent of isotopic fractionation between the melt and the residual assemblage. Similarly, variations in pressure can affect the stability field of phases like garnet at a given temperature, which can impact the extent of isotopic fractionation between the melt and the residue. Significant differences in iron isotope fractionation are also expected between melts produced under contrasting fO_2 conditions. For reduced metasedimentary sources, typical of those inferred for the generation of SPG magmas, the maximum isotopic fractionation between the melt and the residue is predicted at low melt fractions and at temperatures approaching near-complete biotite dehydration melting.

Since anatexis can homogenize the isotopic composition of the sedimentary protolith, the average source composition determines the iron isotope composition of partial melting products. Isotopic differences between SPGs and their source can be attributed to equilibrium fractionation during biotite dehydration melting, while restitic lithologies exhibit almost no fractionation from the source. Other processes occurring during anatexis and magma emplacement may cause isotopic variability in SPG magmas. These processes, however, have only a minor contribution to the iron isotope composition of SPGs relative to equilibrium fractionation. Therefore, SPGs and associated restitic rocks can provide a reliable record of the iron isotope evolution in sedimentary rocks. This is further evidenced by the small range of variability in SPGs compared to the broader sedimentary record.

In sum, the Fe isotope composition of SPGs is controlled by the isotopic composition of their sedimentary protolith. While it is essential to consider other factors, such as *P*–*T* and fO_2 conditions during melt generation, as well as processes during magma segregation and granite emplacement, the extent of iron isotope fractionation they introduced is minimal when compared to broader isotopic variations in the sedimentary record. The Fe isotope variability in SPGs is ~0.2 ‰, significantly smaller than variations exceeding 2‰ found in the sedimentary record (Figure 11). Hence, SPGs can represent a reliable proxy to track changes in the iron isotope composition of siliciclastic sedimentary rocks over time (Figure 1a).

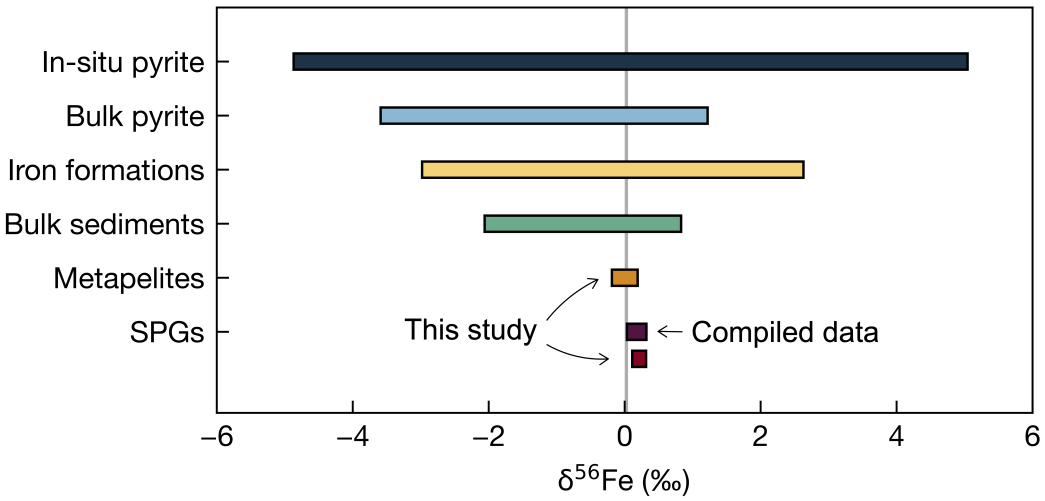


Figure 2.11: Variations in δ^{56}Fe for lithologies representative of the Archean-Proterozoic sedimentary record from the same dataset as in Figure 1a. Significantly less isotopic variability exists in metapelites and SPGs. Compiled data for SPGs includes our results and compositions from *Telus et al.* (2012) and *Foden et al.* (2015). The gray vertical line is the mantle composition (*Craddock et al.*, 2013).

References

Agangi, A., Hofmann, A., Rollion-Bard, C., Marin-Carbonne, J., Cavalazzi, B., Large, R. and Meffre, S. (2015) Gold accumulation in the Archaean Witwatersrand Basin, South Africa—Evidence from concentrically laminated pyrite. *Earth-Science Reviews* 140, 27–53.

Ague, J. J. (2014) Fluid flow in the deep crust. In *Treatise on Geochemistry*, Second Edition (eds. H. D. Holland and K. K. Turekian). Elsevier, Oxford, pp. 203–247.

Ague, J. J. (1991) Evidence for major mass transfer and volume strain during regional metamorphism of pelites. *Geology* 19, 855.

Anbar, A. D. and Rouxel, O. (2007) Metal stable isotopes in paleoceanography. *Annual Review of Earth and Planetary Sciences* 35, 717–746.

Archer, C. and Vance, D. (2006) Coupled Fe and S isotope evidence for Archean microbial Fe(III) and sulfate reduction. *Geology* 34, 153–156.

Audétat, A. (2019) The metal content of magmatic–hydrothermal fluids and its relationship to mineralization potential. *Economic Geology* 114, 1033–1056.

Audétat, A. and Pettke, T. (2003) The magmatic–hydrothermal evolution of two barren granites: A melt and fluid inclusion study of the Rito del Medio and Canada

Pinabete plutons in northern New Mexico (USA). *Geochimica et Cosmochimica Acta* 67, 97–121.

Azimov, P. Ya. and Bushmin, S. A. (2007) Solubility of minerals of metamorphic and metasomatic rocks in hydrothermal solutions of varying acidity: Thermodynamic modeling at 400–800 °C and 1–5 kbar. *Geochemistry International* 45, 1210–1234.

Bartoli, O., Cesare, B., Poli, S., Bodnar, R. J., Acosta-Vigil, A., Frezzotti, M. L. and Meli, S. (2013) Recovering the composition of melt and the fluid regime at the onset of crustal anatexis and S-type granite formation. *Geology* 41, 115–118.

Bea, F., Pereira, M. D., Corretgé, L. G. and Fershtater, G. B. (1994) Differentiation of strongly peraluminous, perphosphorus granites: The Pedrobernardo pluton, central Spain. *Geochimica et Cosmochimica Acta* 58, 2609–2627.

Beard, B. L. and Johnson, C. M. (2004) Fe isotope variations in the modern and ancient Earth and other planetary bodies. *Reviews in Mineralogy and Geochemistry* 55, 319–357.

Bekker, A., Slack, J. F., Planavsky, N., Krapež, B., Hofmann, A., Konhauser, K. O. and Rouxel, O. J. (2010) Iron formation: The sedimentary product of a complex interplay among mantle, tectonic, oceanic, and biospheric processes. *Economic Geology* 105, 467–508.

Bigeleisen, J. and Mayer, M. G. (1947) Calculation of equilibrium constants for isotopic exchange reactions. *Journal of Chemical Physics* 15, 261–267.

Blackburn, C., Johns, G., Ayer, J. and Davis, D. (1991) Wabigoon Subprovince. *Geology of Ontario* 4, 303–381.

Borisov, A., Behrens, H. and Holtz, F. (2015) Effects of melt composition on Fe^{3+}/Fe^{2+} in silicate melts: A step toward modeling ferric/ferrous ratio in multicomponent systems. *Contributions to Mineralogy and Petrology* 169, 24.

Breaks, F. W. and Moore, J. M. (1992) The Ghost Lake Batholith, Superior Province of northwestern Ontario; a fertile, S-type, peraluminous granite–rare-element pegmatite system. *Canadian Mineralogist* 30, 835–875.

Bucholz, C. E. (2022) Coevolution of sedimentary and strongly peraluminous granite phosphorus records. *Earth and Planetary Science Letters* 596, 117795.

Bucholz, C. E. (2024) The diversity and origin of granites. In *Treatise on Geochemistry* (eds. A. Anbar and D. Weis). Elsevier.

Bucholz, C. E., Biasi, J. A., Beaudry, P. and Ono, S. (2020) Sulfur isotope behavior during metamorphism and anatexis of Archean sedimentary rocks: A case study from the Ghost Lake Batholith, Ontario, Canada. *Earth and Planetary Science Letters* 549, 116494.

Bucholz, C. E. and Spencer, C. J. (2019) Strongly peraluminous granites across the Archean–Proterozoic transition. *Journal of Petrology* 60, 1299–1348.

Bucholz, C. E., Stolper, E. M., Eiler, J. M. and Breaks, F. W. (2018) A comparison of oxygen fugacities of strongly peraluminous granites across the Archean–Proterozoic boundary. *Journal of Petrology* 59, 2123–2156.

Busigny, V., Planavsky, N. J., Jézéquel, D., Crowe, S., Louvat, P., Moureau, J., Viollier, E. and Lyons, T. W. (2014) Iron isotopes in an Archean ocean analogue. *Geochimica et Cosmochimica Acta* 133, 443–462.

Chappell, B. W. and Hine, R. (2006) The Cornubian Batholith: An example of magmatic fractionation on a crustal scale. *Resource Geology* 56, 203–244.

Chappell, B. W. and White, A. J. R. (1992) I- and S-type granites in the Lachlan Fold Belt. *Earth and Environmental Science Transactions of the Royal Society of Edinburgh* 83, 1–26.

Chappell, B. W. and Wyborn, D. (2004) Cumulate and cumulative granites and associated rocks. *Resource Geology* 54, 227–240.

Clarke, D. B. (2019) The origins of strongly peraluminous granitoid rocks. *Canadian Mineralogist* 57, 529–550.

Clemens, J. D. (1984) Water contents of silicic to intermediate magmas. *Lithos* 17, 273–287.

Clémente, B., Scaillet, B. and Pichavant, M. (2004) The solubility of sulphur in hydrous rhyolitic melts. *Journal of Petrology* 45, 2171–2196.

Craddock, P. R. and Dauphas, N. (2011) Iron isotopic compositions of geological reference materials and chondrites. *Geostandards and Geoanalytical Research* 35, 101–123.

Craddock, P. R., Warren, J. M. and Dauphas, N. (2013) Abyssal peridotites reveal the near-chondritic Fe isotopic composition of the Earth. *Earth and Planetary Science Letters* 63–76.

Craig, J. R. and Vokes, F. M. (1993) The metamorphism of pyrite and pyritic ores: An overview. *Mineralogical Magazine* 57, 3–18.

Dauphas, N., Cates, N. L., Mojzsis, S. J. and Busigny, V. (2007a) Identification of chemical sedimentary protoliths using iron isotopes in the >3750 Ma Nuvvuagittuq supracrustal belt, Canada. *Earth and Planetary Science Letters* 254, 358–376.

Dauphas, N., Janney, P. E., Mendybaev, R. A., Wadhwa, M., Richter, F. M., Davis, A. M., Van Zuilen, M., Hines, R. and Foley, C. N. (2004) Chromatographic separation and multicollection-ICPMS analysis of iron. *Analytical Chemistry* 76, 5855–5863.

Dauphas, N., John, S. G. and Rouxel, O. (2017) Iron isotope systematics. *Reviews in Mineralogy and Geochemistry* 82, 415–510.

Dauphas, N., Pourmand, A. and Teng, F.-Z. (2009) Routine isotopic analysis of iron by HR-MC-ICPMS: How precise and how accurate? *Chemical Geology* 267, 175–184.

Dauphas, N. et al. (2014) Magma redox and structural controls on iron isotope variations in Earth's mantle and crust. *Earth and Planetary Science Letters* 398, 127–140.

Dauphas, N., van Zuilen, M., Busigny, V., Lepland, A., Wadhwa, M. and Janney, P. E. (2007b) Iron isotope, major and trace element characterization of early Archean supracrustal rocks from SW Greenland. *Geochimica et Cosmochimica Acta* 71, 4745–4770.

Davis, D. W., Sutcliffe, R. H. and Trowell, N. F. (1988) Geochronological constraints on the tectonic evolution of a late Archean greenstone belt, Wabigoon Subprovince, Northwest Ontario. *Precambrian Research* 39, 171–191.

Dupeyron, J., Decraene, M.-N., Marin-Carbonne, J. and Busigny, V. (2023) Formation pathways of Precambrian sedimentary pyrite: Insights from in situ Fe isotopes. *Earth and Planetary Science Letters* 609, 118070.

Fabre, S., Nédélec, A., Poitrasson, F., Strauss, H., Thomazo, C. and Nogueira, A. (2011) Iron and sulphur isotopes from the Carajás mining province (Pará, Brazil): Implications for ocean and atmospheric oxidation across the Archean–Proterozoic transition. *Chemical Geology* 289, 124–139.

Ferry, J. M. (1981) Petrology of graphitic sulfide-rich schists from South-central Maine: An example of desulfidation during prograde regional metamorphism. *American Mineralogist* 66, 908–930.

Foden, J., Sossi, P. A. and Nebel, O. (2018) Controls on the iron isotopic composition of global arc magmas. *Earth and Planetary Science Letters* 494, 190–201.

Foden, J., Sossi, P. A. and Wawryk, C. M. (2015) Fe isotopes and the contrasting petrogenesis of A-, I-, and S-type granite. *Lithos* 212–215, 32–44.

Forshaw, J. B. and Pattison, D. R. M. (2022) Major-element geochemistry of pelites. *Geology* 51, 39–43.

Frost, B. R., Barnes, C. G., Collins, W. J., Arculus, R. J., Ellis, D. J. and Frost, C. D. (2001) A geochemical classification for granitic rocks. *Journal of Petrology* 42, 2033–2048.

Frost, C. D., von Blanckenburg, F., Schoenberg, R., Frost, B. R. and Swapp, S. M. (2007) Preservation of Fe isotope heterogeneities during diagenesis and metamorphism of banded iron formation. *Contributions to Mineralogy and Petrology* 153, 211–235.

Galić, A., Mason, P. R., Mogollón, J. M., Wolthers, M., Vroon, P. Z. and Whitehouse, M. J. (2017) Pyrite in a sulfate-poor Paleoarchean basin was derived predominantly from elemental sulfur.*Chemical Geology* 449, 135–146.

Guidotti, C. V. and Dyar, M. D. (1991) Ferric iron in metamorphic biotite and its petrologic and crystallochemical implications. *American Mineralogist* 76, 161–175.

Guilbaud, R., Butler, I. B. and Ellam, R. M. (2011) Abiotic pyrite formation produces a large Fe isotope fractionation. *Science* 332, 1548–1551.

Guiraud, M., Powell, R. and Rebay, G. (2001) H_2O in metamorphism and unexpected behaviour in the preservation of metamorphic mineral assemblages. *Journal of Metamorphic Geology* 19, 445–454.

He, Y., Wu, H., Ke, S., Liu, S.-A. and Wang, Q. (2017) Iron isotopic compositions of adakitic and non-adakitic granitic magmas: Magma compositional control and subtle residual garnet effect. *Geochimica et Cosmochimica Acta* 203, 89–102.

Heard, A. and Dauphas, N. (2019) Archean–Paleoproterozoic pyrite and iron formation Fe isotope and sedimentary S isotope records.

Heard, A. W. and Dauphas, N. (2020) Constraints on the coevolution of oxic and sulfidic ocean iron sinks from Archean–Paleoproterozoic iron isotope records.*Geology* 48, 358–362.

Heard, A. W., Dauphas, N., Guilbaud, R., Rouxel, O. J., Butler, I. B., Nie, N. X. and Bekker, A. (2020) Triple iron isotope constraints on the role of ocean iron sinks in early atmospheric oxygenation. *Science* 370, 446–449.

Heimann, A., Beard, B. L. and Johnson, C. M. (2008) The role of volatile exsolution and sub-solidus fluid/rock interactions in producing high $^{56}Fe/^{54}Fe$ ratios in siliceous igneous rocks.*Geochimica et Cosmochimica Acta* 72, 4379–4396.

Hermann, J., Zheng, Y.-F. and Rubatto, D. (2013) Deep fluids in subducted continental crust.*Elements* 9, 281–287.

Hofmann, A., Bekker, A., Rouxel, O., Rumble, D. and Master, S. (2009) Multiple sulphur and iron isotope composition of detrital pyrite in Archean sedimentary rocks: A new tool for provenance analysis.*Earth and Planetary Science Letters* 286, 436–445.

Holland, T. J. B. and Powell, R. (2011) An improved and extended internally consistent thermodynamic dataset for phases of petrological interest. *Journal of Metamorphic Geology* 29, 333–383.

Holland, T. and Powell, R. (2003) Activity–composition relations for phases in petrological calculations: An asymmetric multicomponent formulation. *Contributions to Mineralogy and Petrology* 145, 492–501.

Hyslop, E. V., Valley, J. W., Johnson, C. M. and Beard, B. L. (2008) The effects of metamorphism on O and Fe isotope compositions in the Biwabik Iron Formation, northern Minnesota. *Contributions to Mineralogy and Petrology* 155, 313–328.

Johnson, C. M. and Beard, B. L. (2005) Biogeochemical cycling of iron isotopes. *Science* 309, 1025–1027.

Johnson, C. M., Beard, B. L., Beukes, N. J., Klein, C. and O'Leary, J. M. (2003) Ancient geochemical cycling in the Earth as inferred from Fe isotope studies of banded iron formations from the Transvaal Craton. *Contributions to Mineralogy and Petrology* 144, 523–547.

Johnson, C. M., Beard, B. L., Klein, C., Beukes, N. J. and Roden, E. E. (2008) Iron isotopes constrain biologic and abiologic processes in banded iron formation genesis. *Geochimica et Cosmochimica Acta* 72, 151–169.

Johnson, C. M., Beard, B. L., Roden, E. E., Newman, D. K. and Nealson, K. H. (2004) Isotopic constraints on biogeochemical cycling of Fe. *Reviews in Mineralogy and Geochemistry* 55, 359–408.

Khomenko, V. M., Langer, K. and Geiger, C. A. (2001) Structural locations of the iron ions in cordierite: A spectroscopic study.*Contributions to Mineralogy and Petrology* 141, 381–396.

Klimm, K., Kohn, S. C. and Botcharnikov, R. E. (2012) The dissolution mechanism of sulphur in hydrous silicate melts. II: Solubility and speciation of sulphur as a function of fO_2. *Chemical Geology* 322–323, 250–267.

Kress, V. C. and Carmichael, I. S. E. (1991) The compressibility of silicate liquids containing Fe_2O_3 and the effect of composition, temperature, oxygen fugacity and pressure on their redox states.*Contributions to Mineralogy and Petrology* 108, 82–92.

Le Breton, N. and Thompson, A. B. (1988) Fluid-absent (dehydration) melting of biotite in metapelites in the early stages of crustal anatexis.*Contributions to Mineralogy and Petrology* 99, 226–237.

Lewis, M. J., Bucholz, C. E. and Jagoutz, O. E. (2021) Evidence for polybaric fractional crystallization in a continental arc: Hidden Lakes mafic complex, Sierra Nevada Batholith. *Contributions to Mineralogy and Petrology* 176, 90.

Liang, W., Huang, J., Zhang, G. and Huang, F. (2022) Iron isotopic fractionation during eclogite anatexis and adakitic melt evolution.*Contributions to Mineralogy and Petrology* 177, 33.

Liebmann, J., Spencer, C. J., Kirkland, C. L., Bucholz, C. E., Xia, X.-P., Martin, L., Kitchen, N. and Shumlyanskyy, L. (2021) Coupling sulfur and oxygen isotope ratios in sediment melts across the Archean–Proterozoic transition. *Geochimica et Cosmochimica Acta* 307, 242–257.

Liou, P., Wang, Z., Mitchell, R. N., Doucet, L. S., Li, M., Guo, J. and Zhai, M. (2022) Fe isotopic evidence that "high pressure" TTGs formed at low pressure.*Earth and Planetary Science Letters* 592, 117645.

Ma, H.-Z., Chen, Y.-X., Zhou, K., Gao, P., Zheng, Y.-F., Zha, X.-P., Xia, X.-P., Zhao, Z.-F. and Huang, F. (2022) The effect of crystal fractionation on the geochemical composition of syn-exhumation magmas: Implication for high δ^{56}Fe granites.*Geochimica et Cosmochimica Acta* 332, 156–185.

Marin-Carbonne, J., Busigny, V., Miot, J., Rollion-Bard, C., Muller, E., Drabon, N., Jacob, D., Pont, S., Robyr, M., Bontognali, T. R. R., François, C., Reynaud, S., Van Zuilen, M. and Philippot, P. (2020) In situ Fe and S isotope analyses in pyrite

from the 3.2 Ga Mendon Formation (Barberton Greenstone Belt, South Africa): Evidence for early microbial iron reduction.*Geobiology* 18, 306–325.

Marin-Carbonne, J., Rollion-Bard, C., Bekker, A., Rouxel, O., Agangi, A., Cavalazzi, B., Wohlgemuth-Ueberwasser, C. C., Hofmann, A. and McKeegan, K. D. (2014) Coupled Fe and S isotope variations in pyrite nodules from Archean shale.*Earth and Planetary Science Letters* 392, 67–79.

Matthews, A., Morgans-Bell, H. S., Emmanuel, S., Jenkyns, H. C., Erel, Y. and Halicz, L. (2004) Controls on iron-isotope fractionation in organic-rich sediments (Kimmeridge Clay, Upper Jurassic, Southern England).*Geochimica et Cosmochimica Acta* 68, 3107–3123.

Nabelek, P. I. (2020) Petrogenesis of leucogranites in collisional orogens.*Geological Society of London Special Publication* 491, 179–207.

Nie, N. X., Dauphas, N., Alp, E. E., Zeng, H., Sio, C. K., Hu, J. Y., Chen, X., Aarons, S. M., Zhang, Z., Tian, H., Wang, D., Prissel, K. B., Greer, J., Bi, W., Hu, M. Y., Zhao, J., Shahar, A., Roskosz, M., Teng, F., Krawczynski, M. J., Heck, P. R. and Spear, F. S. (2021) Iron, magnesium, and titanium isotopic fractionations between garnet, ilmenite, fayalite, biotite, and tourmaline: Results from NRIXS, ab initio calculations, and mineral separates. *Geochimica et Cosmochimica Acta* 302, 18–45.

O'Neill, H. St. C., Berry, A. J. and Mallmann, G. (2018) The oxidation state of iron in mid-ocean ridge basaltic (MORB) glasses: Implications for their petrogenesis and oxygen fugacities. *Earth and Planetary Science Letters* 504, 152–162.

Ostrander, C. M., Severmann, S., Gordon, G. W., Kendall, B., Lyons, T. W., Zheng, W., Roy, M. and Anbar, A. D. (2022) Significance of ^{56}Fe depletions in late-Archean shales and pyrite.*Geochimica et Cosmochimica Acta* 316, 87–104.

Paiste, K., Fike, D. A., Kirsimäe, K., Jones, C. and Lepland, A. (2022) Testing the global significance of the sulfur isotope record of the ca. 2.0 Ga Zaonega Formation: A micro-scale S isotope investigation.*Geochimica et Cosmochimica Acta* 331, 86–104.

Patiño Douce, A. E. and Beard, J. S. (1995) Dehydration-melting of biotite gneiss and quartz amphibolite from 3 to 15 kbar. *Journal of Petrology* 36, 707–738.

Patiño Douce, A. E. and Harris, N. (1998) Experimental constraints on Himalayan anatexis. *Journal of Petrology* 39, 689–710.

Planavsky, N., Rouxel, O. J., Bekker, A., Hofmann, A., Little, C. T. S. and Lyons, T. W. (2012) Iron isotope composition of some Archean and Proterozoic iron formations.*Geochimica et Cosmochimica Acta* 80, 158–169.

Poitrasson, F. and Freydier, R. (2005) Heavy iron isotope composition of granites determined by high resolution MC-ICP-MS. *Chemical Geology* 222, 132–147.

Polyakov, V. B., Clayton, R. N., Horita, J. and Mineev, S. D. (2007) Equilibrium iron isotope fractionation factors of minerals: Reevaluation from NRIXS and Mössbauer spectroscopy. *Geochimica et Cosmochimica Acta* 71, 3833–3846.

Richards, J. P. (2011) Magmatic to hydrothermal metal fluxes in convergent and collided margins.*Ore Geology Reviews* 40, 1–26.

Rolison, J. M., Stirling, C. H., Middag, R., Gault-Ringold, M., George, E. and Rijkenberg, M. J. A. (2018) Iron isotope fractionation during pyrite formation in a sulfidic Precambrian ocean analogue.*Earth and Planetary Science Letters* 488, 1–13.

Roskosz, M., Dauphas, N., Hu, J., Hu, M. Y., Neuville, D. R., Brown, D., Bi, W., Nie, N. X., Zhao, J. and Alp, E. E. (2022) Structural, redox and isotopic behaviors of iron in geological silicate glasses: A NRIXS study of Lamb–Mössbauer factors and force constants.*Geochimica et Cosmochimica Acta* 321, 184–205.

Roskosz, M., Sio, C. K. I., Dauphas, N., Bi, W., Tissot, F. L. H., Hu, M. Y., Zhao, J. and Alp, E. E. (2015) Spinel–olivine–pyroxene equilibrium iron isotopic fractionation and applications to natural peridotites.*Geochimica et Cosmochimica Acta* 169, 184–199.

Rouxel, O. J., Bekker, A. and Edwards, K. J. (2005) Iron isotope constraints on the Archean and Paleoproterozoic ocean redox state.*Science* 307, 1088–1091.

Schauble, E. A. (2004)mApplying stable isotope fractionation theory to new systems.*Reviews in Mineralogy and Geochemistry* 55, 65–111.

Schuessler, J. A., Schoenberg, R. and Sigmarsson, O. (2009) Iron and lithium isotope systematics of the Hekla volcano, Iceland – Evidence for Fe isotope fractionation during magma differentiation. *Chemical Geology* 258, 78–91.

Simon, A. C., Pettke, T., Candela, P. A., Piccoli, P. M. and Heinrich, C. A. (2004) Magnetite solubility and iron transport in magmatic-hydrothermal environments.*Geochimica et Cosmochimica Acta* 68, 4905–4914.

Stevens, G. and Clemens, J. (1993) Fluid-absent melting and the roles of fluids in the lithosphere: A slanted summary? *Chemical Geology* 108, 1–17.

Slotznick, S. P., Eiler, J. M. and Fischer, W. W. (2018) The effects of metamorphism on iron mineralogy and the iron speciation redox proxy. *Geochimica et Cosmochimica Acta* 224, 96–115.

Sossi, P. A., Foden, J. D. and Halverson, G. P. (2012) Redox-controlled iron isotope fractionation during magmatic differentiation: An example from the Red Hill intrusion, S. Tasmania. *Contributions to Mineralogy and Petrology* 164, 757–772.

Sossi, P. A., Nebel, O. and Foden, J. (2016) Iron isotope systematics in planetary reservoirs. *Earth and Planetary Science Letters* 452, 295–308.

Spear, F. S. (1993) Metamorphic phase equilibria and pressure–temperature–time paths. *Mineralogical Society of America Monograph*, 352–356.

Spear, F. S., Kohn, M. J. and Cheney, J. T. (1999) P–T paths from anatectic pelites. *Contributions to Mineralogy and Petrology* 134, 17–32.

Sylvester, P. J. (1998) Post-collisional strongly peraluminous granites.*Lithos* 45, 29–44.

Taylor, P. D. P., Maeck, R. and De Bièvre, P. (1992) Determination of the absolute isotopic composition and atomic weight of natural iron. *International Journal of Mass Spectrometry and Ion Processes* 121, 111–125.

Telus, M., Dauphas, N., Moynier, F., Tissot, F. L. H., Teng, F. Z., Nabelek, P. I., Craddock, P. R. and Groat, L. A. (2012) Iron, zinc, magnesium and uranium isotopic fractionation during continental crust differentiation: The tale from migmatites, granitoids, and pegmatites.*Geochimica et Cosmochimica Acta* 97, 247–265.

Teng, F.-Z., Dauphas, N., Huang, S. and Marty, B. (2013) Iron isotopic systematics of oceanic basalts. *Geochimica et Cosmochimica Acta* 107, 12–26.

Terry, R. D. and Chilingar, G. V. (1955) Summary of "Concerning some additional aids in studying sedimentary formations," by M. S. Shvetsov. *Journal of Sedimentary Research* 25, 229–234.

Thompson, A. B. (1982) Dehydration melting of pelitic rocks and the generation of H_2O-undersaturated granitic liquids. *American Journal of Science* 282, 1567–1595.

Tomkins, A. G. (2010) Windows of metamorphic sulfur liberation in the crust: Implications for gold deposit genesis. *Geochimica et Cosmochimica Acta* 74, 3246–3259.

Urey, H. C. (1947) The thermodynamic properties of isotopic substances.*Journal of the Chemical Society*, 562.

Valley, J. W. (1986) Stable isotopes in high-temperature geological processes. In: Valley, J. W., Taylor, H. P. and O'Neil, J. R. (eds.) *Stable Isotopes in High Temperature Geological Processes*. De Gruyter. pp. 445–490.

Wang, S.-J., Li, S.-G., Chen, L.-J., He, Y.-S., An, S.-C. and Shen, J. (2013) Geochronology and geochemistry of leucosomes in the North Dabie Terrane, East China: Implications for post-UHPM crustal melting during exhumation. *Contributions to Mineralogy and Petrology* 165, 1009–1029.

Wang, Y., Zhu, X., Tang, C., Mao, J. and Chang, Z. (2021) Discriminating between magmatic- and magmatic-hydrothermal ore deposits using Fe isotopes. *Ore Geology Reviews* 130, 103946.

Warr, L. N. (2021) IMA–CNMNC approved mineral symbols. *Mineralogical Magazine* 85, 291–320.

Wawryk, C. M. and Foden, J. D. (2015) Fe-isotope fractionation in magmatic-hydrothermal mineral deposits: A case study from the Renison Sn–W deposit, Tasmania. *Geochimica et Cosmochimica Acta* 150, 285–298.

White, R. W., Powell, R., Holland, T. J. B. and Worley, B. (2000) The effect of TiO_2 and Fe_2O_3 on metapelitic assemblages at greenschist and amphibolite facies: Mineral equilibria calculations in the system K_2O–FeO–MgO–Al_2O_3–SiO_2–H_2O–TiO_2–Fe_2O_3. *Journal of Metamorphic Geology* 18, 497–511.

White, R. W., Powell, R. and Clarke, G. L. (2002) The interpretation of reaction textures in Fe-rich metapelitic granulites of the Musgrave Block, central Australia: Constraints from mineral equilibria calculations. *Journal of Metamorphic Geology* 20, 41–55.

White, R. W., Powell, R., Holland, T. J. B., Johnson, T. E. and Green, E. C. R. (2014a) New mineral activity–composition relations for thermodynamic calculations in metapelitic systems. *Journal of Metamorphic Geology* 32, 261–286.

White, R. W., Powell, R. and Johnson, T. E. (2014b) The effect of Mn on mineral stability in metapelites revisited: New a–x relations for manganese-bearing minerals. *Journal of Metamorphic Geology* 32, 809–828.

Whitehouse, M. J. and Fedo, C. M. (2007) Microscale heterogeneity of Fe isotopes in >3.71 Ga banded iron formation from the Isua Greenstone Belt, southwest

Greenland.*Geology* 35, 719–722.

Xu, L.-J., He, Y., Wang, S.-J., Wu, H. and Li, S. (2017) Iron isotope fractionation during crustal anatexis: Constraints from migmatites from the Dabie orogen, Central China. *Lithos* 284–285, 171–179.

Yamaguchi, K. E., Johnson, C. M., Beard, B. L. and Ohmoto, H. (2005)Biogeochemical cycling of iron in the Archean–Paleoproterozoic Earth: Constraints from iron isotope variations in sedimentary rocks from the Kaapvaal and Pilbara Cratons. *Chemical Geology* 218, 135–169.

Yardley, B. W. and Bodnar, R. J. (2014) Fluids in the continental crust.*Geochemical Perspectives* 3, 1–2.

Yardley, B. W. D. (2005) Metal concentrations in crustal fluids and their relationship to ore formation.*Economic Geology* 100, 613–632.

Yardley, B. W. D. (2013) The chemical composition of metasomatic fluids in the crust. In: Harlov, D. E. and Austrheim, H. (eds.) *Metasomatism and the Chemical Transformation of Rock*. Springer. pp. 17–51.

Yoshiya, K., Nishizawa, M., Sawaki, Y., Ueno, Y., Komiya, T., Yamada, K., Yoshida, N., Hirata, T., Wada, H. and Maruyama, S. (2012) In situ iron isotope analyses of pyrite and organic carbon isotope ratios in the Fortescue Group: Metabolic variations of a Late Archean ecosystem. *Precambrian Research* 212–213, 169–193.

Yoshiya, K., Sawaki, Y., Hirata, T., Maruyama, S. and Komiya, T. (2015a) In situ iron isotope analysis of pyrites in ∼3.7 Ga sedimentary protoliths from the Isua supracrustal belt, southern West Greenland. *Chemical Geology* 401, 126–139.

Yoshiya, K., Sawaki, Y., Shibuya, T., Yamamoto, S., Komiya, T., Hirata, T. and Maruyama, S. (2015b) In situ iron isotope analyses of pyrites from 3.5 to 3.2 Ga sedimentary rocks of the Barberton Greenstone Belt, Kaapvaal Craton.*Chemical Geology* 403, 58–73.

Zajacz, Z., Halter, W. E., Pettke, T. and Guillong, M. (2008) Determination of fluid/melt partition coefficients by LA-ICP-MS analysis of coexisting fluid and silicate melt inclusions: Controls on element partitioning. *Geochimica et Cosmochimica Acta* 72, 2169–2197.

Zhang, Z. J., Dauphas, N., Johnson, A. C., Aarons, S. M., Bennett, V. C., Nutman, A. P., MacLennan, S. and Schoene, B. (2023) Titanium and iron isotopic records of

granitoid crust production in diverse Archean cratons. *Earth and Planetary Science Letters* 620, 118342.

TABLES

Table 2.1: Force constants for Fe-carrying phases.

Phase	Force constant (N/m)	Method	Reference
Silicate melt	$\left[199 + \frac{41}{1+e^{34-\mathrm{SiO_2}}}\right] \times \left(1 - \frac{\mathrm{Fe^{3+}}}{\Sigma\mathrm{Fe}}\right) \times 351 \times \left(\frac{\mathrm{Fe^{3+}}}{\Sigma\mathrm{Fe}}\right)$	NRIXS	*Dauphas et al.* (2014)
Biotite (Annite)	$188 + 59.4 \times \left(\frac{\mathrm{Fe^{3+}}}{\Sigma\mathrm{Fe}}\right)$	NRIXS	*Nie et al.* (2021)
Garnet (Almandine)	110	NRIXS	*Nie et al.* (2021)
Cordierite	188	–	Same as biotite with no $\mathrm{Fe^{3+}}/\Sigma\mathrm{Fe}^{*}$
Ilmenite	$133 \times \left(1 - \frac{\mathrm{Fe^{3+}}}{\Sigma\mathrm{Fe}}\right) \times 244 \times \left(\frac{\mathrm{Fe^{3+}}}{\Sigma\mathrm{Fe}}\right)$	NRIXS	*Nie et al.* (2021)
Spinel	$196 + 104 \times \left(\frac{\mathrm{Fe^{3+}}}{\Sigma\mathrm{Fe}}\right)$	NRIXS	*Roskosz et al.* (2015)
Orthopyroxene	177	NRIXS	*Dauphas et al.* (2012)

Table 2.2: Iron isotope compositions of granites, metapelites, sulfides, and geostandards.

Lithology	**Sample**	**GLB / Metamorphic Zone**	**n**	δ^{56}Fe			δ^{57}Fe		
				Value	95% c.i.	2 SE	Value	95% c.i.	2 SE
	SP-16-34	GLB-5	8	0.187	0.031	0.016	0.266	0.044	0.017
	SP-16-33	GLB-5	5	0.111	0.018	0.009	0.183	0.034	0.024
	F11-4	GLB-3	8	0.233	0.031	0.021	0.349	0.044	0.039
	SP-16-27	GLB-3	8	0.116	0.031	0.018	0.182	0.044	0.026
	SP-16-29	GLB-3	7	0.179	0.040	0.019	0.261	0.058	0.023
Granites	SP-16-19	GLB-1	6	0.175	0.038	0.020	0.273	0.066	0.033
	SP-16-20a	GLB-1	5	0.202	0.023	0.019	0.293	0.048	0.035
	E19-8	GLB-1	9	0.158	0.037	0.019	0.244	0.053	0.030
	SP-16-23	Inclusion-rich zone in GLB-1	6	0.194	0.038	0.021	0.295	0.066	0.030
	SP-16-22	Inclusion-rich zone in GLB-1	6	0.315	0.038	0.013	0.476	0.066	0.028
	SP-16-24	Inclusion-rich zone in GLB-1	7	0.236	0.019	0.013	0.349	0.031	0.018

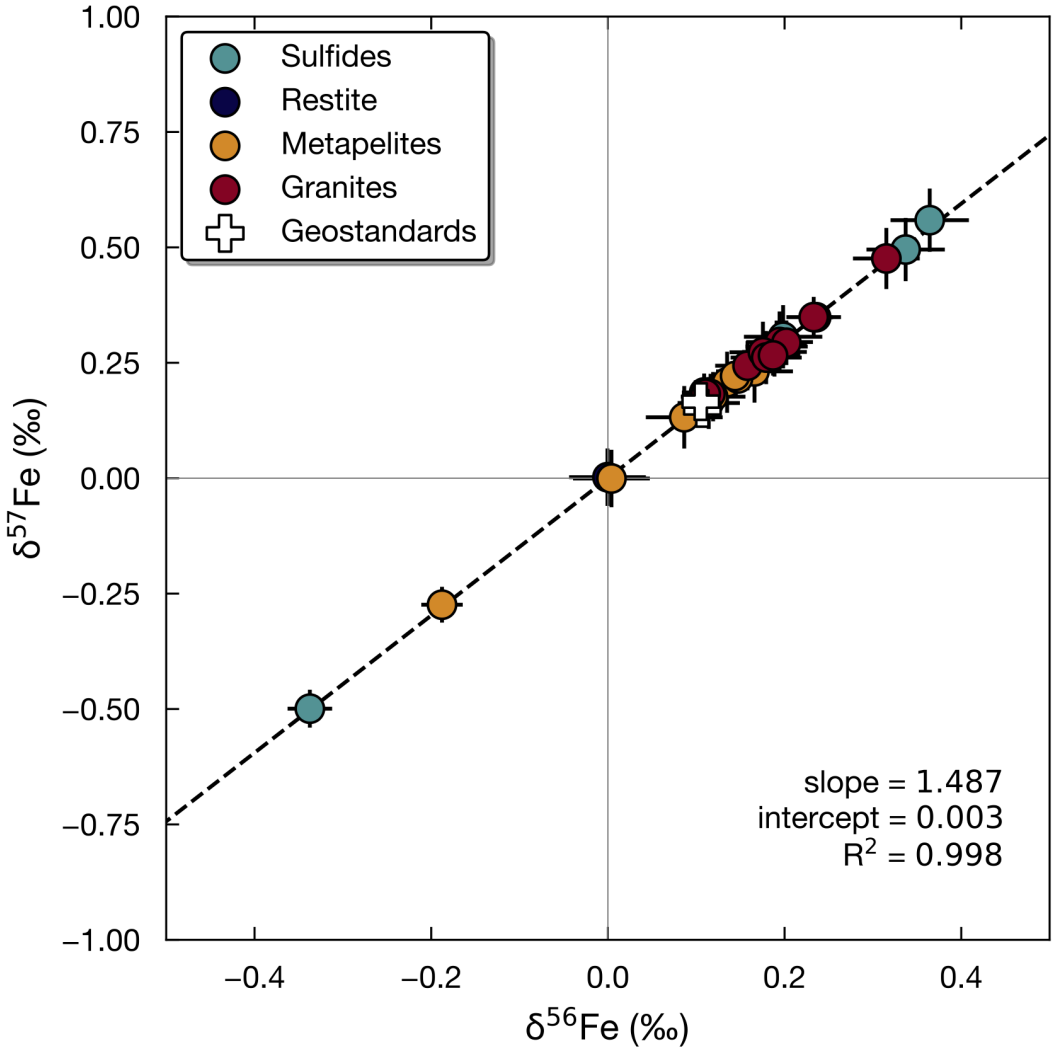
Continued on next page

Lithology	**Sample**	**GLB / Metamorphic Zone**	**n**	δ^{56}Fe			δ^{57}Fe		
				Value	95% c.i.	2 SE	Value	95% c.i.	2 SE
Meta-sedimentary rocks	SP-18-34	Sillimanite – K-feldspar	6	0.144	0.017	0.012	0.221	0.026	0.028
	SP-16-16	Sillimanite – K-feldspar	9	0.119	0.037	0.019	0.177	0.053	0.032
	SP-16-43	Sillimanite	7	0.191	0.035	0.023	0.285	0.056	0.035
	SP-16-44	Sillimanite	9	0.189	0.037	0.012	0.274	0.053	0.020
	SP-16-11	Garnet	5	-0.188	0.023	0.008	-0.274	0.039	0.012
	SP-18-27	Garnet	7	0.114	0.035	0.011	0.163	0.056	0.013
	SP-18-26	Garnet	6	0.004	0.043	0.016	-0.001	0.062	0.027
	SP-16-37	Andalusite	6	0.147	0.018	0.010	0.216	0.032	0.017
	SP-18-8	Biotite-Chlorite	6	0.135	0.038	0.012	0.208	0.066	0.019
	SP-18-6	Biotite-Chlorite	9	0.086	0.044	0.008	0.132	0.068	0.009
	SP-18-5	Biotite-Chlorite	9	0.166	0.044	0.017	0.231	0.068	0.028
Restite	SP-16-30	Inclusion in GLB-3	6	0.000	0.043	0.016	0.002	0.062	0.039
Sulfides	SP-18-26	Garnet	8	0.364	0.044	0.020	0.559	0.069	0.040
	SP-18-27	Garnet	8	0.337	0.044	0.018	0.495	0.069	0.027
	SP-16-16	Sillimanite – K-feldspar	8	0.198	0.044	0.056	0.306	0.069	0.029
	SP-16-20a	GLB-1	8	0.109	0.025	0.021	0.186	0.041	0.043
	SP-16-11	Garnet	8	-0.337	0.025	0.019	-0.499	0.041	0.040

Type	**Sample**	δ^{56}Fe			δ^{57}Fe		
		Value	2 SE	ref.	Value	2 SE	ref.
Geostandards	AGV-2	0.107	0.002	0.105 ± 0.011 ‰	0.151	0.010	0.146 ± 0.016 ‰
	BHVO-1	0.105	0.004	0.105 ± 0.008 ‰	0.166	0.009	0.161 ± 0.012 ‰

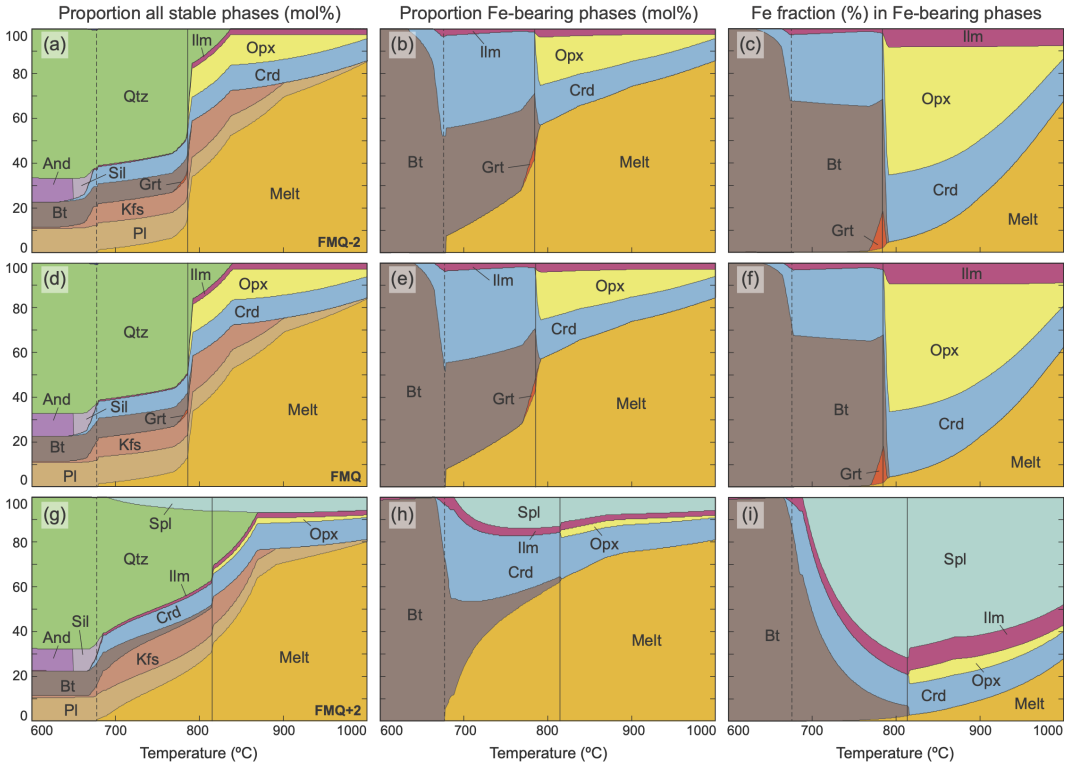
SUPPLEMENTARY MATERIAL

Fe isotopes and variable hydration state of the system



Supplementary Figure S2.1: Fe isotope compositions of all samples and geostandards in three-isotope space (δ^{57}Fe vs. δ^{56}Fe). The data plot on a mass-dependent fractionation line with slope 1.487 and intercept 0.003.

Modeling under minimally water-saturated conditions at the solidus means the rock is fully hydrated, with only a small amount of free water present in the system at the onset of partial melting (*Mayne et al.*, 2020). This approach assumes that volatiles are lost from the system during progressive burial and metamorphism, leading to limited pore fluid presence by the time partial melting starts. As such, most melt generated under this approximation results from fluid-absent melting, with only a negligible amount produced by fluid-present melting just above the wet solidus. This agrees with the observation that most granitic magmas produced by partial



Supplementary Figure S2.2: Phase equilibrium modeling results for a metapelite with the composition of sample SP-16-16. The calculations were done at a constant pressure of 0.3 GPa, ranging from 600°C to 1000°C under three different oxygen fugacity conditions: FMQ-2 (a-c), FMQ (d-f), and FMQ+2 (g-i). Panels in the column to the left display the modal proportions in mol% for all the equilibrium phases in the system, the middle column shows the modal proportion in mol% for Fe-bearing phases only, and the column to the right displays the fraction of the total amount of iron in the system that each Fe-bearing phase contains. The vertical dashed line marks the position of the solidus, and the solid line indicates the appearance of orthopyroxene in the mineral assemblage.

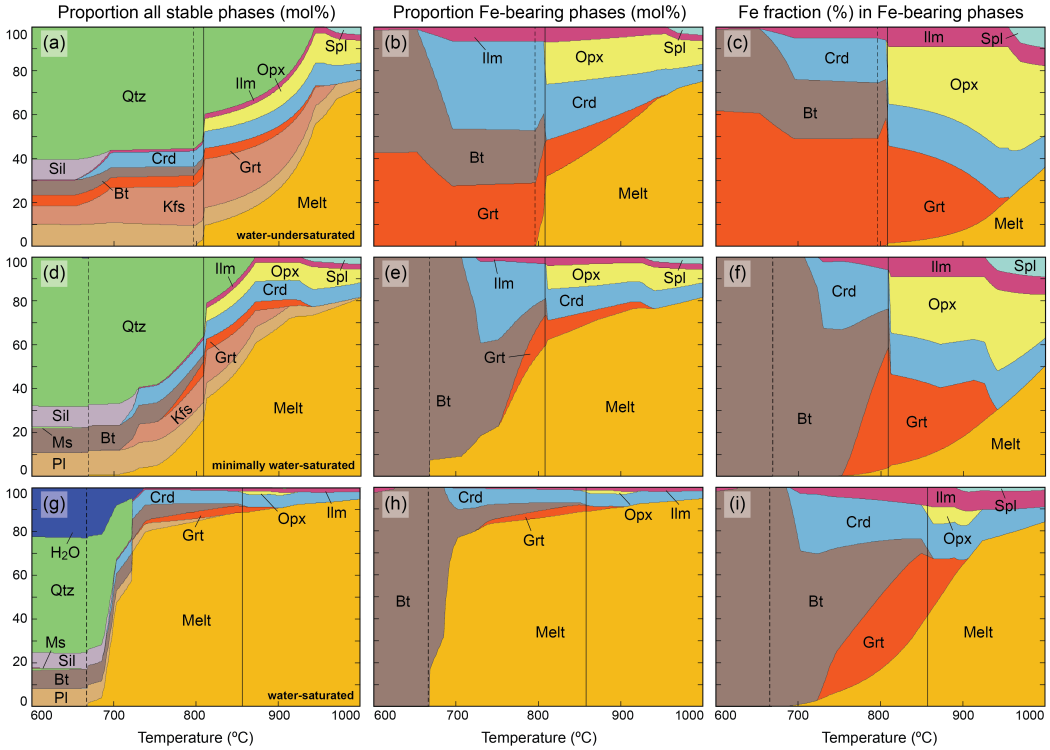
melting of crustal rocks likely result from fluid-absent melting reactions (*Stevens and Clemens*, 1993; *Clemens et al.*, 2020).

Partial melting under minimally saturated water conditions is intermediate between two cases: water-undersaturated and water-excess melting conditions. In the first case, we consider water-undersaturated melting to occur when the H_2O content of the system is lower than required to minimally saturate the solidus, leading to fluid-absent melting. Here, the granite solidus varies between the wet and dry solidus, where the solidus location depends on the initial amount of H_2O. Incongruent melting reactions produce peritectic phases in the residue, such as garnet, cordierite, spinel, and orthopyroxene (*Clemens et al.*, 2020; *Johnson et al.*, 2021). By contrast,

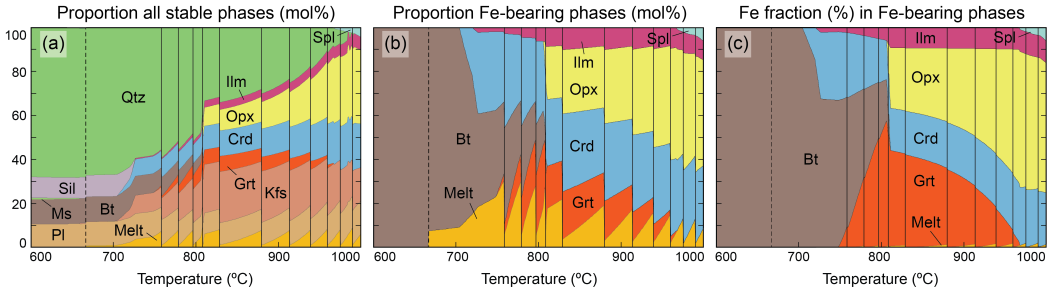
in the water-excess scenario, partial melting is considered to occur in the presence of significant amount of free aqueous fluid, meaning the system contains significantly more water than hydrous minerals can accommodate (*Weinberg and Hasalová*, 2015). This situation can occur due to infiltration of externally derived fluids into the system, where intergranular diffusion is fast enough to allow fluids to equilibrate with the surrounding rock before being expelled (*Weinberg and Hasalová*, 2015). While the mechanisms of water influx and equilibration during anatexis are unclear, there is general agreement that this process is not dominant for producing granitic rocks (*Stevens and Clemens*, 1993; *Clemens and Watkins*, 2001; *Clemens*, 2003; *Clemens et al*., 2020). However, partial melting under water-excess conditions has been shown to be important for generating granitic magmas in some migmatites (*Weinberg and Hasalová*, 2015; *Clemens et al*., 2020). The proportion of melt produced by the reaction Qtz + Pl ± Kfs + H_2O = Melt depends on the amount water present (or introduced) during partial melting, as added H_2O will dissolve into the melt, increasing the melt fraction (*Weinberg and Hasalová, 2015*).

The amount of water in the system significantly controls phase stability and melt production during anatexis and may therefore influence the Fe isotope composition of produced melts. To investigate this, we estimated the equilibrium Fe isotope composition of melts produced under water-undersaturated and water-excess conditions at the solidus. For water-undersaturated conditions, the initial H_2O content was set to 90% of the H_2O content required for minimal water saturation, whereas for water-excess conditions, the initial H_2O content of the system was set to 5 wt.%. In both cases, pressure conditions were set to 0.4 GPa, and fO_2 was constrained by the FMQ buffer (Figure S3).

Significant differences in phase stability are predicted for the water-undersaturated and water-saturated melting models relative to minimally water-saturated conditions. In the first case, the 10% reduction in the amount of water required to minimally saturate the solidus increases the solidus temperature to ~798 °C (Figure S3a). The abundance of biotite at subsolidus conditions is reduced to ~5 mol.%. Biotite dehydration melting occurs across a reduced temperature range (~798-810 °C), before being quickly consumed by the melt + orthopyroxene producing reaction. The stability fields of K-feldspar, garnet, and cordierite extend to temperatures well below the solidus (Figure S3a). In contrast, under water-saturated conditions, partial melting starts at ~669 °C, initially producing less than 5 mol.% melt through the reaction Qtz + Pl + H_2O = Melt. Then, at ~685 °C, biotite, sillimanite, quartz,



Supplementary Figure S2.3: Phase equilibrium modeling results for a metapelite with the composition of sample SP-16-16. The calculations were run at a constant pressure of 0.4 GPa, oxygen fugacity constrained by the FMQ buffer, and temperatures ranging from 600°C to 1000°C. We considered melting conditions including water undersaturated (a-c), with the initial H_2O content was set to 90% of the H_2O content required for minimal water saturation at the solidus; minimally water-saturated (d-f), with ~0.5 mol% free H_2O at the solidus; and water-saturated (g-i), with 5 wt.% in the system. Panels in the column to the left display the modal proportions in mol% for all the equilibrium phases in the system, the middle column shows the modal proportion in mol% for Fe-bearing phases only, and the column to the right displays the fraction of the total amount of iron in the system that each Fe-bearing phase contains. The vertical dashed line marks the position of the solidus, and the solid line marks the biotite-out and orthopyroxene-in transition.

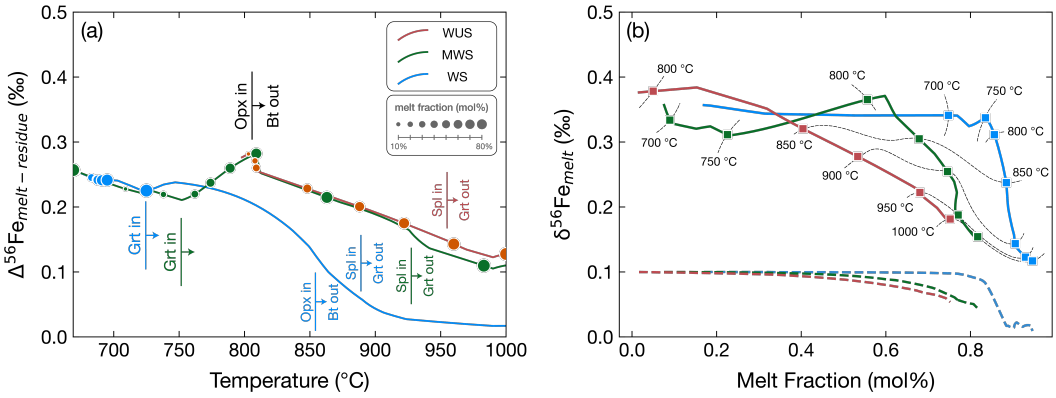


Supplementary Figure S2.4: Phase equilibrium modeling results for a metapelite with the composition of sample SP-16-16 assuming melt extraction. The calculations were run at a constant pressure of 0.4 GPa, oxygen fugacity constrained by the FMQ buffer, and temperatures ranging from 600°C to 1000°C. The initial water content was set to minimally water-saturated conditions at the solidus. The vertical dashed line marks the position of the solidus, and the solid lines mark melt loss events (MLE). Each MLE was considered to occur when the proportion of melt in the system exceeded 7 vol.% (Rosenberg and Handy, 2005). At this melt threshold, the system composition was updated to reflect melt extraction, leaving behind a residue in equilibrium with ~1 vol.% melt. The panel to the left displays the modal proportions in mol% for all the equilibrium phases in the system, the middle panel shows the modal proportion in mol% for Fe-bearing phases only, and the panel to the right displays the fraction of the total amount of iron in the system that each Fe-bearing phase contains.

and H_2O react to produce cordierite and significant melt (~60 mol.%) until quartz is exhausted at ~720 °C (Figure S3g). At this point, the melt-producing reaction generates garnet and consumes plagioclase. Biotite is completely consumed between ~850-860 °C when orthopyroxene becomes stable, producing ~88 mol.% melt at this point (Figure S3g).

The predicted Fe isotope fractionation between magmas produced by water- undersaturated melting and their complementary solid is nearly identical to that estimated for minimally water-saturated conditions (Figure S5a). Accordingly, at equivalent temperatures, the $\delta^{56}Fe_{melt}$ for water-undersaturated conditions remains similar to that of minimally water-saturated melting, even though melt fractions are significantly higher for the latter (Figure S5b). This results from Fe being incorporated into the melt in similar ratios, with Fe distributed in similar proportions among the residual iron-bearing phases (Figure S3c). This means that SPGs produced under water-undersaturated conditions may have Fe isotope compositions similar to those formed from fully hydrated protoliths. For the GLB in particular, and most other SPGs, water-undersaturated melting may not have played a role in generating the parent magmas. Partial melts produced under water-undersaturated solidus conditions

would have K_2O/Na_2O ratios much higher than those seen in most SPGs (*Chappell and White*, 1992; *Sylvester*, 1998; *Bucholz and Spencer*, 2019). Additionally, the absence of orthopyroxene in associated migmatites and restitic lithologies of the Zealand unit indicates partial melting likely started closer to the wet solidus.



Supplementary Figure S2.5: (a) Predicted equilibrium iron isotope fractionation between granitic melts and complementary residues produced by partial melting of metapelite SP-16-16 at 0.4 GPa, FMQ oxygen fugacity conditions, and temperatures between the solidus and 1000 °C. Circles with variable sizes represent melt fractions varying from 10% to 80%. Vertical lines mark the approximate temperature of orthopyroxene stability and biotite exhaustion. (b) Predicted δ^{56}Fe values for the melt (solid lines) and the residue (dashed lines), with $\delta^{56}Fe_{source}$ of 0.1 ‰. Squares mark different temperature conditions. In both panels, the colors represent melting at different hydration conditions: water-undersaturated (WUS; orange), minimally water-saturated (MWS; green), and water-saturated (WS; blue).

On the other hand, the Fe isotope composition of magmas produced under water-saturated conditions is maximum and relatively constant up to the temperature at which water is completely dissolved into the melt, depending on the initial water content considered. These predicted $\delta^{56}Fe_{melt}$ values are similar to the maximum values predicted for minimally water-saturated conditions (Figure S5a). After this point, both $\delta^{56}Fe_{melt}$ and $\Delta^{56}Fe_{melt-residue}$ decrease as the iron fraction stored in the melt progressively increases during biotite breakdown. These melts tend to have higher FeO contents than melts produced with lower initial water contents (Figure S3i). For example, between 750 °C and 800 °C, the calculated FeO_T contents of melts produced under water-saturated conditions vary between ~1.1 and ~2.4 wt.%, on an anhydrous basis, whereas those produced under minimally saturated-water conditions vary from 0.6 to 1.4 wt.% FeO_T. The median FeO_T of Archean-Proterozoic SPGs, also normalized to an anhydrous composition, is 1.0 wt.%, with an interquartile range (IQR) of 0.6 – 1.5 wt.% (*Bucholz and Spencer*,

2019). This implies that if SPGs were produced by water-fluxed melting, rather than minimally water-saturated conditions, they likely formed at temperatures close to the wet solidus., which is usually expected for anatectic migmatites rather than large granitic sources (*Stevens and Clemens*, 1993; *Clemens and Watkins*, 2001; *Clemens*, 2003; *Clemens et al.*, 2020). Alternatively, significant Fe loss may occur during magma crystallization and fluid release.

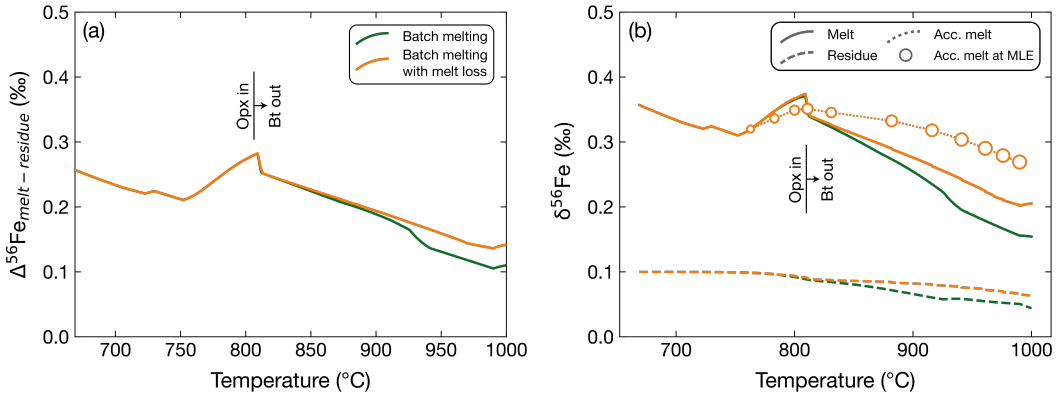
Although significant changes in phase stability can occur due to varying H_2O contents in the protolith, the maximum Fe isotope fractionation between the produced melts and complementary solid phases is expected to be similar across different water contents. Greater isotopic fractionation is observed at temperatures closer to the solidus and decreases as the fraction of iron in the melt increases relative to the total iron budget. Therefore, at equivalent temperatures, partial melts formed from more hydrated protoliths would represent larger melt fractions with higher FeO contents, which would generally have lower $\delta^{56}Fe_{melt}$. However, the variation in $\delta^{56}Fe_{melt}$ for melts produced under different water contents is relatively minor and close to the analytical precision (Figure S5b). For instance, at 800 °C, the predicted $\delta^{56}Fe_{melt}$ for melts produced under water-undersaturated, minimally water-saturated, and water-saturated conditions are 0.38, 0.37, and 0.31 ‰ (Figure S5b), respectively, assuming a protolith source with δ^{56}Fe of 0.1 ‰. Based on predicted melt compositions, minimally water-saturated conditions at the solidus seem to be the most reasonable modeling scenario for the generation of SPG granites in terms of major element and isotopic composition.

Phase equilibrium modeling and equilibrium isotopic fractionation with melt loss

In addition to batch melting (i.e., melts equilibrated in a closed system), partial melting simulations were also conducted considering changes in the bulk composition of the system due to periodic melt extraction (Figure S4). The initial model setup is the same as that of the run at 0.4 GPa and fO_2 conditions constrained by the FMQ oxygen buffer, with minimally water-saturated conditions at the solidus. A melt loss event (MLE) was considered to occur each time the melt fraction reached ~7 vol.% (*Rosenberg and Handy*, 2005). At this melt threshold, the system composition was updated to reflect melt extraction, leaving behind a residue in equilibrium with ~1 vol.% melt. Iron isotopic fractionation was calculated as described in Section 4.5 in the main text, with the system δ^{56}Fe composition recalculated after each MLE.

Melt extraction leads to progressive dehydration of the system, which results in reduced fertility after each MLE. Therefore, compared to batch melting, the total amount of melt produced when melt extraction occurs is predicted to be lower (Figure S4a). Moreover, because low melt fractions are higher in SiO_2 and lower in FeO and MgO, the fraction of iron in the instantaneous melts generated with melt extraction is significantly lower than that of melts produced via batch melting (Figure S4c). However, the distribution of iron in the residual phases is relatively similar in both cases.

The predicted iron isotope fractionation between instantaneous melts and residues produced during partial melting with continuous melt loss is almost identical to that estimated for simple batch melting (Figure S6a). However, small differences in $\delta^{56}Fe_{melt}$ values (< 0.05 ‰) are estimated at temperatures above biotite dehydration melting, primarily due to higher silica contents in the melt. Likewise, the progressive hybridization of melts extracted at each MLE during biotite dehydration melting would result in iron isotope compositions indistinguishable from those of batch melts (Figure S6b). However, at higher temperatures, the differences in δ^{56}Fe between batch and aggregated melts become more pronounced, with isotopically heavier hybrid melts resulting from the progressive shrinking of the system (Figure S6b). The accumulated melts are more strongly influenced by the initial melt batches, as the melts extracted during later MLEs represent progressively smaller melt fractions relative to the initial size of the system (Figure S6b). Thus, the isotopic composition of aggregated melts produced before and after biotite dehydration melting is predicted to remain relatively uniform across the entire temperature range considered.



Supplementary Figure S2.6: Equilibrium isotopic fractionation considering batch melting (green) and compositional changes in the system due to melt loss events (MLE) when the melt volume in the system reached 7% (orange). Calculations were done for partial melting of metapelite SP-16-16 at 0.4 GPa, FMQ oxygen fugacity conditions, and temperatures between the solidus and 1000 °C. (a) Predicted equilibrium iron isotope fractionation between granitic melts and complementary residues (b) Predicted δ^{56}Fe values for the melt (solid lines) and the residue (dashed lines), with $\delta^{56}Fe_{source}$ of 0.1 ‰. Circles represent different melt loss events (MLE), with sizes proportional to the accumulated melt fraction extracted from the system after each MLE. In both panels, vertical lines mark the approximate temperature of orthopyroxene stability and biotite exhaustion.

Fluid-melt fractionation during fluid exsolution

Let us consider a system where fluid and melt are in chemical equilibrium at temperatures above the solidus. The fractionation factors between the fluid and melt ($\Delta^{56}Fe_{fluid-melt}$) can be calculated from reduced partition function ratios (β-factors). For fluids, fractionation factors can be approximated from the expression:

$$1000 \times \ln \beta_{\text{melt}} \left(\frac{^{56}\text{Fe}}{^{54}\text{Fe}} \right) = \frac{A_1}{T^2} \times \frac{A_2}{T^4} \times \frac{A_3}{T^6}$$

where A_1, A_2, and A_3 are coefficients of the polynomial expansion of β equilibrium fractionation factors taken from *Dauphas et al.* (2017), and T is the temperature in Kelvin. For the melt, the fractionation factor is expressed in terms of the mean force constant of iron bonds (F):

$$1000 \times \ln \beta_{\text{melt}} \left(\frac{^{56}\text{Fe}}{^{54}\text{Fe}} \right) = 2853 \times \frac{F}{T^2}$$

where F (N/m) for Fe^{2+} is given by the expression (from *Dauphas et al.*, 2014):

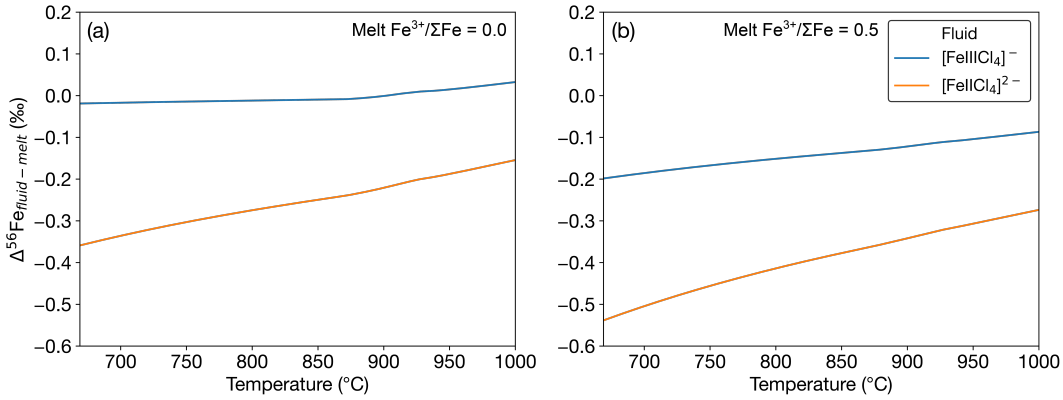
$$F = 199 + \frac{41}{1 + e^{\,31 - \mathrm{SiO_2}/2}}$$

where SiO_2 is the silica content of the magma in weight percent. For Fe^{3+}, $F = 351$ N/m.

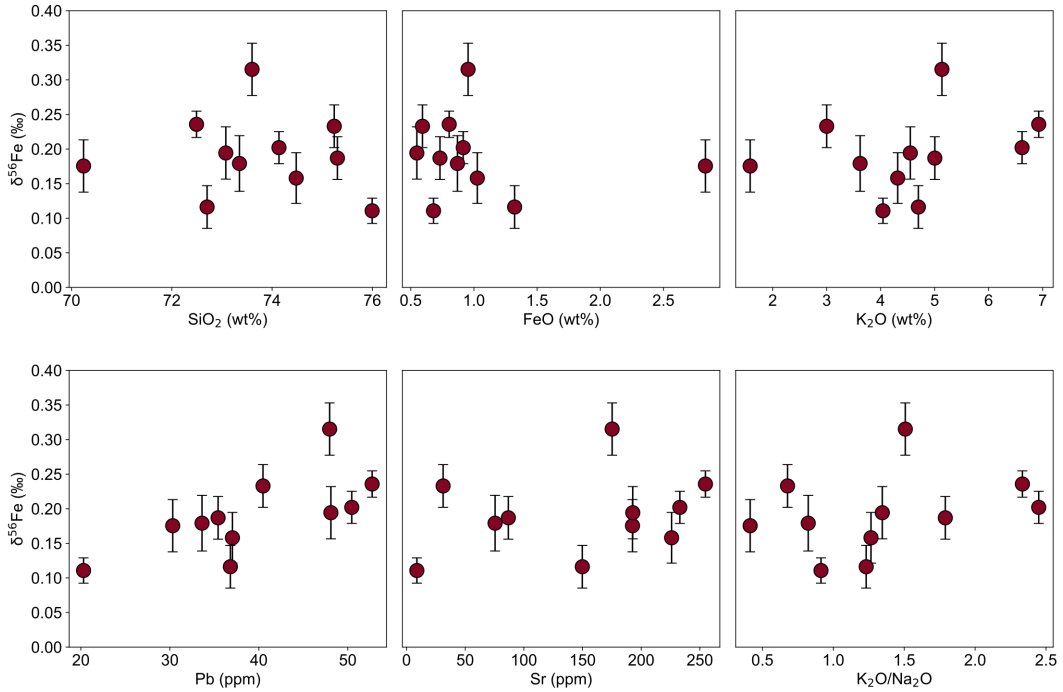
$$\Delta^{56}\mathrm{Fe}_{\mathrm{fluid-melt}} = \delta^{56}\mathrm{Fe}_{\mathrm{fluid}} - \delta^{56}\mathrm{Fe}_{\mathrm{melt}} = 1000 \times \ln \beta_{\mathrm{fluid}} - 1000 \times \ln \beta_{\mathrm{melt}}$$

We consider the fluid to be iron-bearing chlorides (i.e., $[Fe(III)Cl_4]^-$ and $[Fe(II)Cl_4]^{2-}$), and the melt phase to have a granitic composition. For simplicity, we assume that the SiO_2 composition of the melt is that of the partial melting model for SP-16-16 at 0.4 GPa and an oxygen fugacity buffered at FMQ. However, for this example, we ignore the estimated $Fe^{3+}/\Sigma Fe$ ratios for the melt from the model and consider only two cases: $Fe^{3+}/\Sigma Fe = 0$ and $Fe^{3+}/\Sigma Fe = 0.5$.

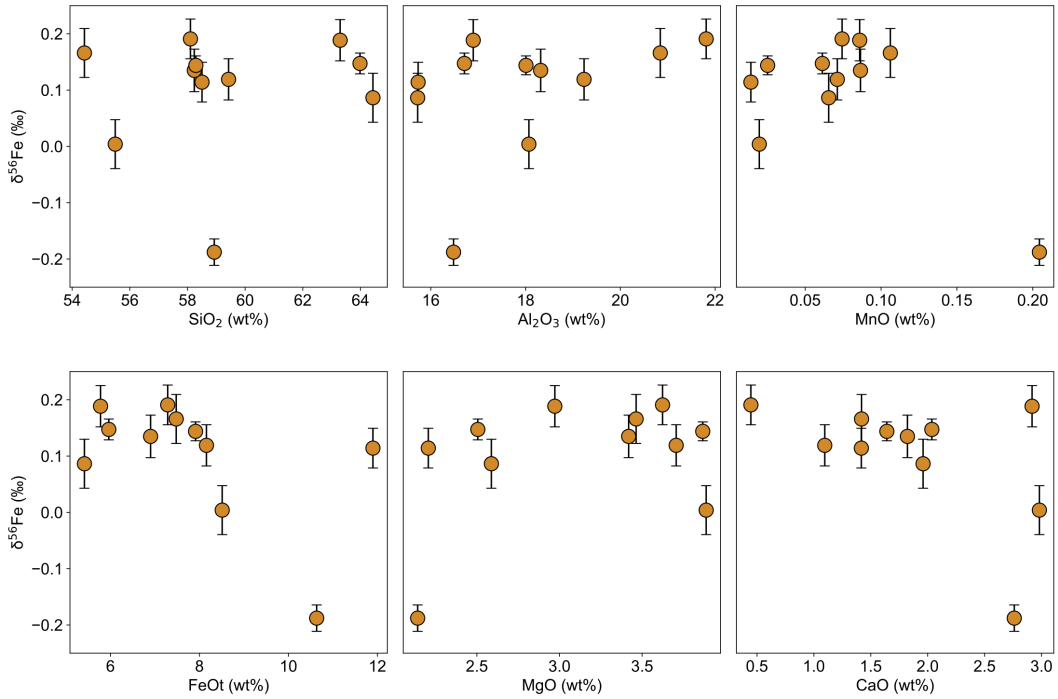
Figures S7a and S7b show estimated $\Delta^{56}\mathrm{Fe}_{\mathrm{fluid-melt}}$ values between 669 °C (solidus) and 1000 °C for melt compositions with $Fe^{3+}/\Sigma Fe = 0$ and $Fe^{3+}/\Sigma Fe = 0.5$, respectively. In general, fractionation between the fluid and the melt decreases with increasing temperature. Regardless of the oxidation state of the magma, the iron isotope composition of the melt at temperatures relevant to biotite dehydration melting (i.e., < 820 °C) is heavier than that of the fluid, with minimal fractionation between $[Fe(III)Cl_4]^-$ fluid and a melt containing no ferric iron. However, iron in magmatic–hydrothermal systems is mainly carried by fluids as ferrous chlorides (*Chou and Eugster*, 1977; *Simon et al.*, 2004), for which more negative $\Delta^{56}\mathrm{Fe}_{\mathrm{fluid-melt}}$ values are expected. Thus, if significant exsolution of iron-rich fluids occurs during magma crystallization, the iron isotope composition of the magma would shift toward higher $\delta^{56}\mathrm{Fe}_{\mathrm{melt}}$ values, a process suggested in earlier studies of iron isotopes in granitic magmas (*Poitrasson and Freydier*, 2005; *Heimann et al.*, 2008).



Supplementary Figure S2.7: Estimated $\Delta^{56}Fe_{fluid-melt}$ values between 669 °C (solidus) and 1000 °C for melt compositions with $Fe^{3+}/\Sigma Fe = 0$ (a) and $Fe^{3+}/\Sigma Fe = 0.5$ (b). The fluids considered are iron-bearing chlorides: $[Fe(III)Cl_4]^-$ (blue) and $[Fe(II)Cl_4]^{2-}$ (orange). The melt is the same as that predicted by the partial melting model for SP-16-16 at 0.4 GPa and an oxygen fugacity buffered at FMQ. Fractionation factors were calculated from expressions for reduced partition function ratios (β-factors) taken from *Dauphas et al.* (2017) for the fluids and *Dauphas et al.* (2014) for the melt.



Supplementary Figure S2.8: Iron isotope composition of metasedimentary samples from the Zealand unit versus sample geochemistry.



Supplementary Figure S2.9: Iron isotope composition of SPG samples from the GLB versus whole-rock chemistry.

Additional References

Bucholz, C. E., Biasi, J. A., Beaudry, P. and Ono, S. (2020) Sulfur isotope behavior during metamorphism and anatexis of Archean sedimentary rocks: A case study from the Ghost Lake batholith, Ontario, Canada. *Earth Planet. Sci. Lett.* **549**, 116494.

Bucholz, C. E. and Spencer, C. J. (2019) Strongly peraluminous granites across the Archean–Proterozoic transition. *J. Petrol.* **60**, 1299–1348.

Chappell, B. W. and White, A. J. R. (1992) I- and S-type granites in the Lachlan Fold Belt. *Earth Environ. Sci. Trans. R. Soc. Edinb.* **83**, 1–26.

Chou, I.-M. and Eugster, H. (1977) Solubility of magnetite in supercritical chloride solutions. *Am. J. Sci.* **277**, 1296–1314.

Clemens, J. D. (2003) S-type granitic magmas—petrogenetic issues, models and evidence. *Earth-Sci. Rev.* **61**, 1–18.

Clemens, J. D., Stevens, G. and Bryan, S. E. (2020) Conditions during the formation of granitic magmas by crustal melting—hot or cold; drenched, damp or dry? *Earth-Sci. Rev.* **200**, 102982.

Clemens, J. D. and Watkins, J. (2001) The fluid regime of high-temperature metamorphism during granitoid magma genesis. *Contrib. Mineral. Petrol.* **140**, 600–606.

Dauphas, N., John, S. G. and Rouxel, O. (2017) Iron isotope systematics. *Rev. Mineral. Geochem.* **82**, 415–510.

Dauphas, N., Roskosz, M., Alp, E. E., Neuville, D. R., Hu, M. Y., Sio, C. K., Tissot, F. L. H., Zhao, J., Tissandier, L., Médard, E. and Cordier, C. (2014) Magma redox and structural controls on iron isotope variations in Earth's mantle and crust. *Earth Planet. Sci. Lett.* **398**, 127–140.

Heimann, A., Beard, B. L. and Johnson, C. M. (2008) The role of volatile exsolution and sub-solidus fluid/rock interactions in producing high $^{56}Fe/^{54}Fe$ ratios in siliceous igneous rocks. *Geochim. Cosmochim. Acta* **72**, 4379–4396.

Johnson, T., Yakymchuk, C. and Brown, M. (2021) Crustal melting and suprasolidus phase equilibria: From first principles to the state-of-the-art. *Earth-Sci. Rev.* **221**, 103778.

Mayne, M. J., Stevens, G. and Moyen, J.-F. (2020) A phase equilibrium investigation of selected source controls on the composition of melt batches generated by sequential melting of an average metapelite. *Geol. Soc. Lond. Spec. Publ.* **491**, 223–241.

Poitrasson, F. and Freydier, R. (2005) Heavy iron isotope composition of granites determined by high-resolution MC-ICP-MS. *Chem. Geol.* **222**, 132–147.

Rosenberg, C. L. and Handy, M. R. (2005) Experimental deformation of partially melted granite revisited: Implications for the continental crust. *J. Metamorph. Geol.* **23**, 19–28.

Simon, A. C., Pettke, T., Candela, P. A., Piccoli, P. M. and Heinrich, C. A. (2004) Magnetite solubility and iron transport in magmatic-hydrothermal environments. *Geochim. Cosmochim. Acta* **68**, 4905–4914.

Stevens, G. and Clemens, J. (1993) Fluid-absent melting and the roles of fluids in the lithosphere: A slanted summary? *Chem. Geol.* **108**, 1–17.

Sylvester, P. J. (1998) Post-collisional strongly peraluminous granites. *Lithos* **45**, 29–44.

Weinberg, R. F. and Hasalová, P. (2015) Water-fluxed melting of the continental crust: A review. *Lithos* **212–215**, 158–188.

Chapter 3

TRIPLE-OXYGEN ISOTOPES IN GRANITIC MAGMAS REVEAL MAJOR SHIFTS IN EARTH'S WEATHERING CONDITIONS THROUGH TIME

ABSTRACT

The geochemical signatures preserved in sedimentary rocks constitute Earth's primary archive of ancient surface environments and climate evolution. However, direct constraints on weathering conditions from individual sedimentary deposits remain temporally and spatially fragmented and may be modified by diagenesis or local depositional processes. Triple-oxygen-isotope signatures preserved in granites and migmatites formed by partial melting of sedimentary protoliths provide a complementary archive. Because such melts integrate material from large volumes of sedimentary crust, their isotopic compositions can approximate the average weathering signature of broad source regions, preserving a lithology-integrated record of ancient surface weathering environments. By analyzing garnet hosted in these rocks and inverting its triple oxygen isotope composition through phase-equilibrium modeling, we reconstruct weathering temperatures and meteoric water compositions from the Mesozoic back to the Neoarchean. Our results reveal four distinct climate states linked to atmospheric oxidation, glaciation, and supercontinent cycles. Most notably, we find highly variable Archean weathering temperatures that reach near-freezing values, indicating that glacial conditions have existed on Earth since at least 2.7 Ga. This is followed by cooler, more stable Paleoproterozoic conditions after the Huronian glaciations; conspicuously warm mid-Proterozoic climates; and moderate post-Cryogenian Phanerozoic temperatures, consistent with independent paleoclimate reconstructions. We demonstrate that strongly peraluminous lithologies provide robust records of ancient weathering environments and that continental assembly played a fundamental role in regulating Earth's long-term climate.

Sedimentary rocks represent one of the most prominent archives of Earth's surface environment. Their mineralogical constituents form through mechanical, chemical, and biological processes and preserve direct evidence of major shifts in surface con-

ditions, including changes in atmospheric composition, ocean redox state, global climate, and biological activity (e.g., *Nesbitt et al.*, 1996; *Farquhar et al.*, 2000; *Konhauser et al.*, 2017). For example, clastic materials reveal information about the energy of their depositional environment and the mode of transport, whereas (bio)chemical minerals can potentially record temporal relationships or signatures imparted by the thermodynamic conditions of the environment during the sedimentation process. As a result, sedimentary rocks provide a window into deciphering paleoenvironmental conditions across geological history, with implications for understanding long-term connections between tectonics and planetary-scale systems such as the atmosphere, hydrosphere, and biosphere, and ultimately the conditions that allowed life to flourish and evolve.

Reconstructing past environmental conditions requires interrogating the sedimentary record through different lenses. For example, isotopic compositions preserved in chemical precipitates, such as carbonates, chert, and sulfides or sulfates, have been widely used as proxies for seawater temperatures, atmospheric composition changes, and global redox cycles (e.g., *Blake et al.*, 2010; *Isson and Rauzi*, 2024; *McGunnigle et al.*, 2022). Likewise, siliciclastic rocks, composed of detritus generated by mechanical erosion and chemical weathering, represent a composite record that preserves information about the depositional environment and the chemical conditions present during fluid-rock interaction. Thus, while the texture and mineral composition of bulk siliciclastic rocks are routinely used for provenance analysis and to infer depositional modes, the isotopic and geochemical signatures of the chemical weathering component (e.g., clay minerals) can be used to estimate meteoric water compositions and surface temperatures (e.g., *Bindeman et al.*, 2018, 2019; *Hofmann and Bindeman*, 2023).

However, precise constraints on surface and marine temperature conditions are difficult to infer for most of Earth's history. Existing sedimentary archives—including cherts, carbonates, iron formations, phosphates, and paleosols—often preserve only spatially limited conditions or specific temporal windows, leaving major uncertainties about how representative these records are of global climate conditions. Furthermore, some of these records are extremely sensitive to post-depositional processes that overprint their primary isotopic composition and obscure any record of surface conditions (*Marin-Carbonne et al.*, 2014). For example, it remains uncertain whether the isotopic signatures preserved in Archean cherts reflect primary surface environments or have been reset by diagenetic equilibration at burial temper-

atures (*Lowe et al.*, 2020; *Sengupta et al.*, 2020). Consequently, interpretations of Archean surface temperatures remain contradictory: some interpretations suggest surface temperatures as high as ~50–85 °C (e.g., *Knauth and Lowe*, 2003; *Lowe et al.*, 2020), while others indicate moderate temperature environments (< 40 °C) (*Hren et al.*, 2009).

Triple-oxygen isotopes in siliciclastic rocks provide a sensitive tracer of low-temperature water–rock interaction because clay minerals formed during chemical weathering inherit characteristic isotopic signatures that reflect the chemistry of meteoric waters involved in weathering reactions and the temperatures of formation (*Bindeman*, 2021). Although these signatures are generally retained after burial, diagenesis, and metamorphism (*Bindeman*, 2021; *Valley*, 1986; *Zheng et al.*, 2003), as in other sedimentary rocks, preserved siliciclastic sequences can be spatially heterogeneous, locally modified, and unevenly distributed through time, complicating efforts to extract coherent, large-scale climatic signals directly from them.

In contrast, strongly peraluminous granites (SPGs) and migmatites, formed through partial melting of sediments (anatexis), homogenize the composition of large volumes of their parental strata, effectively averaging chemical heterogeneities across individual beds or basins (*Bucholz and Spencer*, 2019). Garnet is a common product of anatexis, with an extremely slow oxygen diffusivity, allowing it to preserve equilibrium isotopic composition over long timescales and through secondary thermal events (*Scicchitano et al.*, 2022; *Chamberlain and Conrad*, 1991). As a result, garnets crystallizing from strongly peraluminous magmas retain the triple oxygen isotope compositions inherited from their sedimentary source rocks (protoliths) with minimal subsequent modification. Because the extent of isotopic fractionation between garnet and its source can be quantified via thermodynamic modeling (*Hernández-Montenegro et al.*, 2024; *Bucholz and Hernández-Montenegro*, 2025), garnet triple-oxygen isotope compositions provide a means to reconstruct those of sedimentary protoliths and, by extension, isotopic signatures reflecting the environments of weathering and sedimentation.

Here, we present triple oxygen isotope compositions of a spatially and temporally diverse suite of garnets hosted in strongly peraluminous granites and migmatites, with crystallization and protolith depositional ages ranging from the Mesozoic to the Neoarchean. We use phase-equilibrium modeling to quantify equilibrium fractionation between garnet and its sedimentary source during melting, using a compilation of siliciclastic sediments to approximate global-average protolith compositions at

the corresponding depositional times. We then combine these reconstructions with isotopic mass-balance relationships to isolate the triple oxygen isotope composition of the chemical weathering component—defined as a mixture of clays formed by the interaction of crustal materials with meteoric waters. From theoretical and experimental constraints on mineral–water triple oxygen isotope fractionation, we invert these compositions to obtain weathering temperatures and corresponding meteoric water oxygen isotopes (see Methods). This approach yields a lithology-integrated record of the weathering conditions existing before and during sediment deposition, capturing large-scale environmental signals often obscured in individual sedimentary successions.

Measured triple oxygen isotope Compositions

We analyzed triple oxygen isotope compositions of garnets from SPGs and migmatitic leucosomes formed by partial melting of sedimentary protoliths. The dataset comprises analyses from 66 samples spanning four major time intervals: Neoarchean, Paleoproterozoic (post-Huronian), early Neoproterozoic (pre-Cryogenian), and Phanerozoic. Samples were selected from well-characterized localities where petrologic and geochemical evidence indicates derivation from metasedimentary sources and where garnet crystallized in equilibrium with granitic melts. Because garnet has extremely low oxygen diffusivity, it preserves primary isotopic compositions even after high-temperature metamorphism and anatexis. A detailed description of sample localities, geological context, and selection criteria is provided in the Supplementary Methods.

Measured garnet triple oxygen isotope compositions were used to reconstruct the isotopic composition of the sedimentary protolith from which the granitic melts were derived. This reconstruction accounts for equilibrium oxygen-isotope fractionation between garnet and the bulk sedimentary source during partial melting, based on phase-equilibrium modeling of metasedimentary anatexis (Supplementary Methods). The resulting estimates represent lithology-integrated compositions of the siliciclastic sediment sources that supplied the melts.

We report oxygen isotope ratios normalized to the VSMOW standard, where $\delta^X\mathrm{O} = (R^{X/16}_{\mathrm{sample}}/R^{X/16}_{\mathrm{VSMOW}} - 1)\times 1000$, with $X = 17$ and 18. For triple oxygen isotope analysis, we use the linearized logarithmic notation, where $\delta'^X\mathrm{O} = 1000\ln(\delta^X\mathrm{O}/1000 + 1)$ and deviations from the terrestrial fractionation line are given by $\Delta'^{17}\mathrm{O} = \delta'^{17}\mathrm{O} - 0.528 \times \delta'^{18}\mathrm{O}$.

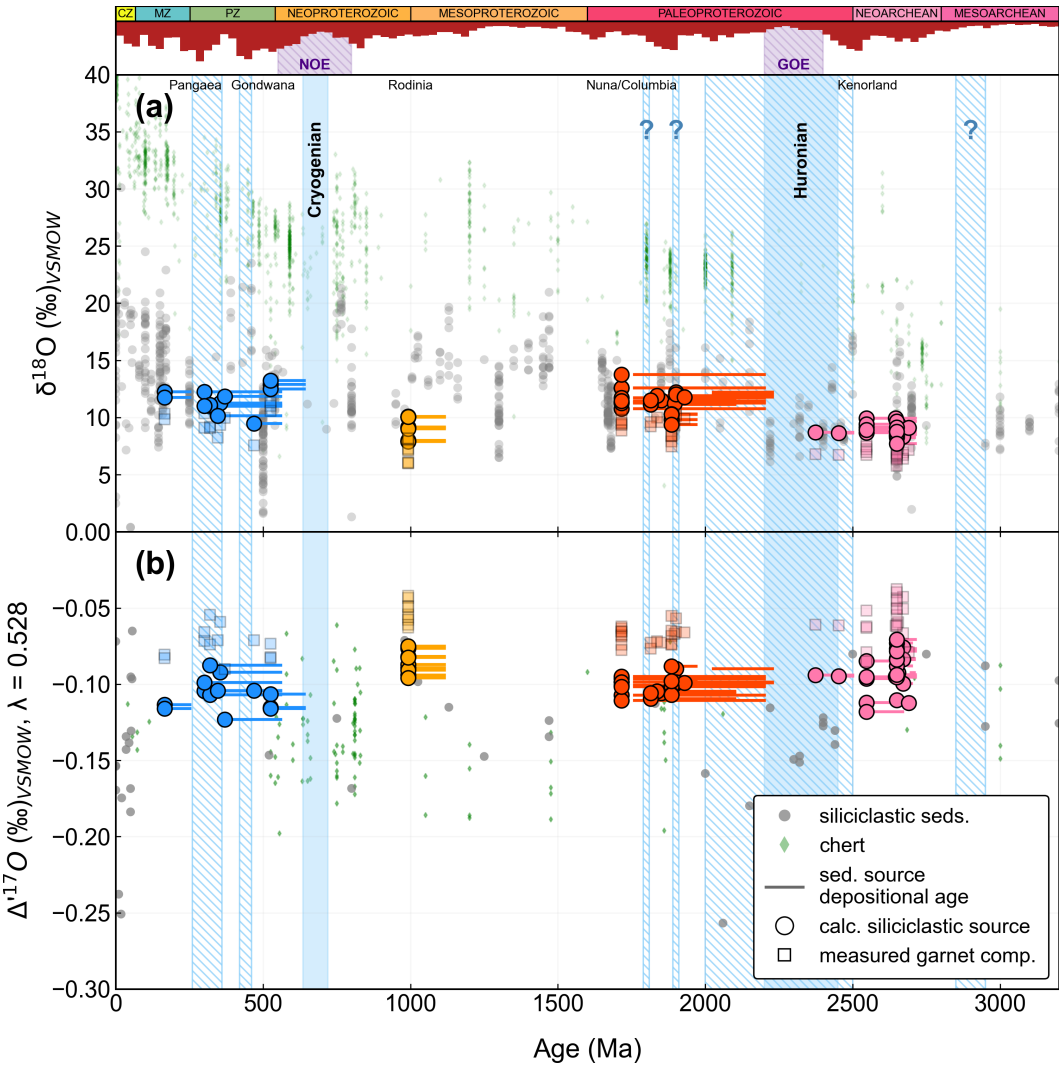


Figure 3.1: Isotopic compositions of granitic garnets and calculated bulk siliciclastic sediments through time. Values of δ'^{18}O and Δ'^{17}O values are shown in panels **(a)** and **(b)**, respectively. Larger colored circles represent calculated bulk protolith compositions from this study at their crystallization age, while the smaller colored squares represent the corresponding garnet measurements. Horizontal lines with same color as circles are interpreted ranges of depositional data for granites and migmatite source sediments. Grey circles are siliciclastic sediment compositions compiled from previous studies (*Bindeman et al.*, 2016, 2018; *Payne et al.*, 2015, and references therein) and green diamonds are chert data (*Liljestrand et al.*, 2020; *Sengupta et al.*, 2020; *Zakharov et al.*, 2021; *Isson and Rauzi*, 2024, and references therein). Shaded blue regions mark the Huronian and Cryogenian glaciation periods, while hatched blue regions represent smaller or purported glacial periods. At the top, red bars represent bins of detrital zircon age populations from compiled data by *Roberts and Spencer* (2015), showing peaks at supercontinent cycles. Intervals for the GOE and NOE are also shown as hatched, purple intervals in the top panel.

Reconstructed triple oxygen isotope compositions of the sedimentary protoliths define four discrete age clusters in both δ'^{18}O and Δ'^{17}O space (Figure 3.1). Respectively, δ'^{18}O and Δ'^{17}O values range from ~ 9.5 to 13.2‰ and −0.123 to −0.087‰ for Phanerozoic samples; ~ 7.9 to 10.1‰ and −0.096 to −0.075‰ for early Neoproterozoic samples; ~ 9.4 to 13.7‰ and −0.111 to −0.088‰ for Paleoproterozoic post-Huronian samples; and ~ 8.2 to 9.9‰ and −0.118 to −0.071‰ for Neoarchean samples. Within each age group, reconstructed source compositions fall within the ranges defined by published siliciclastic sediments, whereas chert data extend to higher δ'^{18}O and lower Δ'^{17}O values (Figure 3.1). Our estimates for sedimentary protolith compositions, however, occupy a narrower field than the published siliciclastic datasets, reflecting the homogenization of mixed sediment sources during metamorphism and partial melting.

The corresponding weathering-product compositions form distinct clusters in triple oxygen isotope space (Figure 3.2). These clusters fall at lower Δ'^{17}O and higher δ'^{18}O values than measured garnet and calculated sedimentary-source compositions. In general, these groups overlap arrays of clay–water fractionation curves originating from the global meteoric water line, which are functions of temperature, and provide the basis for the quantitative inversion of weathering conditions (Figure 3.2).

Weathering Temperatures and δ'^{18}O of Meteoric Waters

Numerical solutions for weathering temperatures obtained from the triple oxygen isotope inversion (see Extended Methods) are shown in Figure 3.2. Neoarchean samples formed before the Great Oxidation Event (GOE) display the widest range of reconstructed temperatures, from ~ 2 °C to ~ 43 °C. By contrast, Paleoproterozoic samples with protoliths deposited following the GOE define a lower-temperature field from ~ 3 to ~ 17 °C, while those preceding the Neoproterozoic Oxygenation Event (NOE) form a higher-temperature cluster of ~ 14–41 °C. Lastly, Phanerozoic samples derived from post-Cryogenian protoliths span ~ 2–27 °C. Published siliciclastic sediment temperatures plotted in Figure 3.3 (grey circles) overlap with, but extend beyond, the ranges reconstructed here from the garnet-bearing magmatic samples.

By construction, the estimated weathering-water compositions fall along the meteoric water line of *Luz and Barkan* (2010), with an excess Δ'^{17}O ($\gamma = 0.033$), which is a parameter that reflects the effect of emerged land on precipitation. The choice of γ defines the Δ'^{17}O composition of the weathering waters, but it does not affect

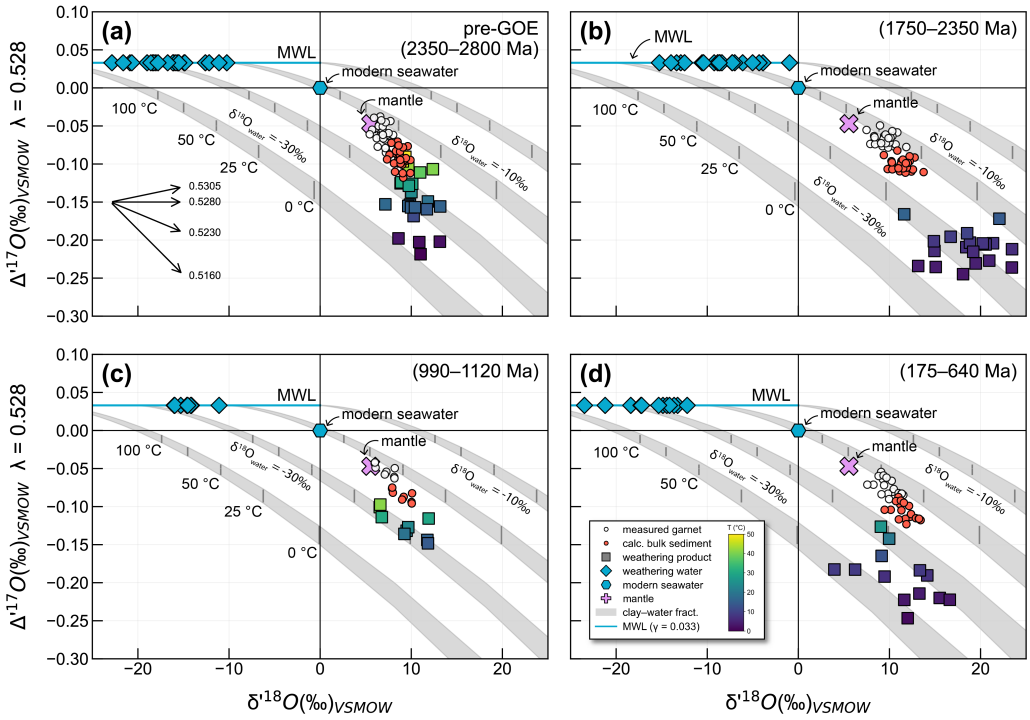


Figure 3.2: Isotopic compositions of granitic garnets and calculated bulk siliciclastic sediments in triple oxygen isotope space for pre-GOE **(a)**, post-Huronian glaciation **(b)**, pre-NOE **(c)**, and post-cryogenian data **(d)**. δ'^{18}O relative to the Vienna Standard Mean Ocean Water (VSMOW) and Δ'^{17}O values with a reference $\lambda = 0.528$ are shown on the x and y axis, respectively. The arrows in panel (a) indicate the effects of different choices of the mass law exponent. Grey curves represent fractionation lines between water and weathering products at fixed $\delta'^{18}O_{water}$ of -30, -20, -10, and 0 ‰, with curve thickness representing the uncertainty in the A and B fractionation parameters due to variability in the sedimentary record (see Extended Methods). The red data points are calculated isotopic composition for the bulk siliciclastic source, estimated from garnet triple oxygen isotope measurements (white circles). Estimated weathering products (squares) are colored by calculated weathering temperature. Blue diamonds represent estimated compositions for corresponding weathering waters, computing with the meteoric water line (MWL) of *Luz and Barkan* (2010). Mantle and modern seawater compositions are represented by the purple filled cross (×) and the teal hexagon symbols, respectively.

inverted temperature or δ'^{18}O values.

Our estimated values form age-specific ranges in δ'^{18}O that differ among the four groups. Neoarchean (pre-GOE) values range from ~ −19.8 to −8.6‰, while Paleoproterozoic (post-GOE) samples span ~ −14.8 to +1.5‰. Early Neoproterozoic (pre-NOE) samples cluster between ~ −16.0 and −11.1‰, whereas Phanerozoic (post-NOE) samples extend to the most negative values in the dataset, ranging from ~ −25.3 to −10.9‰.

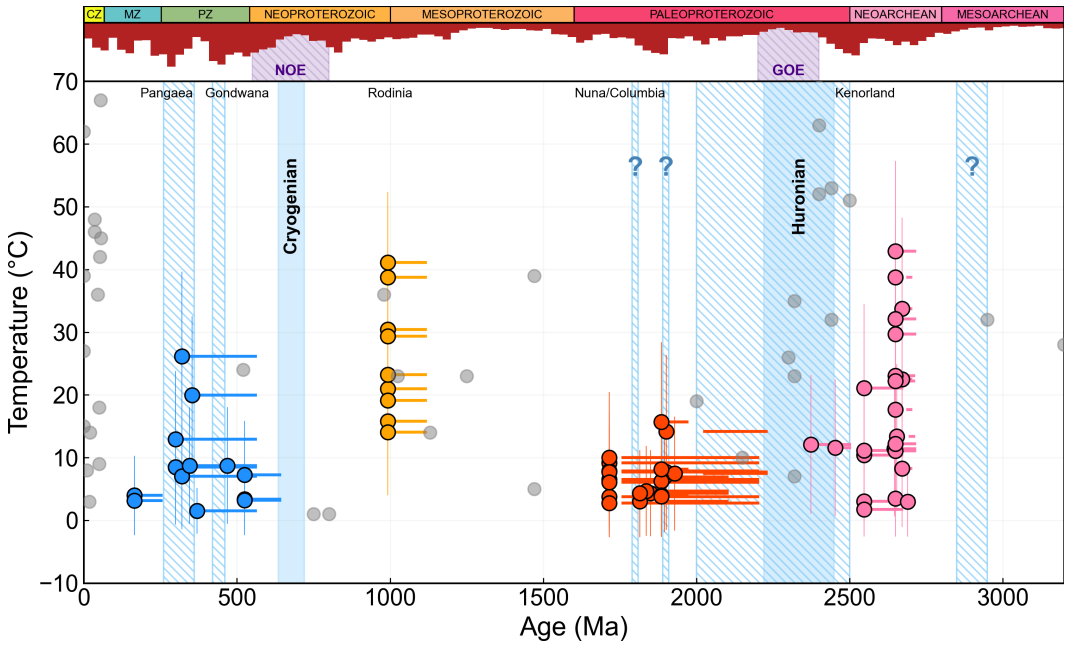


Figure 3.3: Calculated weathering temperatures through time. Colored circles are data from this study. The associated horizontal lines with the same color as circles represent the corresponding range of depositional ages for granite and migmatite source sediments. Grey circles are siliciclastic sediments with calculated weathering temperatures from *Bindeman et al.* (2018). Shaded blue regions mark the Huronian and Cryogenian glaciation periods, while hatched blue areas represent smaller or purported glacial periods. At the top, red bars represent bins of detrital zircon age populations from compiled data by *Roberts and Spencer* (2015), showing peaks at supercontinent cycles. Intervals for the GOE and NOE are also shown as hatched, purple intervals in the top panel.

Preservation of Primary Weathering Signatures

The validity of this paleoclimate reconstruction relies on the premise that the triple oxygen isotope composition of garnet in SPGs and migmatites faithfully records the integrated composition of its sedimentary source, corrected for high-temperature fractionation. Several lines of evidence suggest that these signatures are primary

and robust against magmatic or metamorphic overprinting.

First, the slow diffusion of oxygen in garnet effectively precludes significant isotopic resetting after crystallization. Under typical crustal conditions, the closure temperature for oxygen diffusion in garnet exceeds peak metamorphic temperatures (*Scicchitano et al.*, 2022), such that the isotopic composition acquired during growth is effectively locked in. Accordingly, garnet oxygen isotope compositions are known to faithfully record crystallization conditions (e.g., *Chamberlain and Conrad*, 1991; *Kohn et al.*, 1993). Because bulk-rock oxygen isotope compositions are generally conserved during prograde metamorphism of sedimentary rocks (*Bindeman*, 2021; *Valley*, 1986; *Zheng et al.*, 2003), garnet formed in isotopic equilibrium with its host rock should preserve the isotopic signature of the sedimentary protolith.

Second, the isotopic fractionation associated with partial melting and crystallization at high temperatures ($> 650\,^{\circ}\mathrm{C}$) is small and predictable. Phase-equilibrium modeling shows that the equilibrium fractionation between garnet and the sedimentary source of strongly peraluminous melts ($\Delta^{18}O_{\text{grt-melt}}$) is systematically small and insensitive to modest variations in bulk composition (Supplementary Figure S3.2). Crucially, the measured triple oxygen isotope compositions of our garnet suite do not define the shallow slope expected for high-temperature equilibrium fractionation ($\theta \approx 0.527 - 0.529$), but instead fall along a trend with a significantly lower slope ($\theta \approx 0.5232$; Figure 3.2), similar to theoretical values for fractionation between clay and water at low temperatures (*Ibarra et al.*, 2022; *Schauble and Young*, 2021). Consequently, the large range of $\delta'^{18}O$ and $\Delta'^{17}O$ values observed in our dataset cannot be generated by magmatic differentiation or variable melting temperatures, and must therefore reflect inheritance from low-temperature surface processes.

The Archean Climate Conundrum

The most striking feature of our record is the pronounced variability and low-temperature excursions observed in the Neoarchean (pre-GOE) dataset. Our reconstructed weathering temperatures range from $\sim 2\,^{\circ}\mathrm{C}$ to $\sim 43\,^{\circ}\mathrm{C}$, potentially indicating substantial spatial and temporal variability in surface conditions prior to atmospheric oxygenation. This variability is difficult to reconcile with interpretations based on chert oxygen isotopes that invoke uniformly high ocean temperatures of 55–85 °C (e.g., *Knauth and Lowe*, 2003; *Lowe et al.*, 2020; *McGunnigle et al.*, 2022), which would only be possible if the Archean seawater $\delta^{18}O$ was significantly depleted (*Ibarra et al.*, 2022; *Herwartz et al.*, 2021).

The coexistence of cool and warm weathering environments implies that the late Archean climate system sustained broad thermal gradients. The cold end of our reconstructed range ($\sim 2\,^{\circ}C$) requires weathering in high-latitude or high-altitude regions. While direct glacial deposits are not preserved in the sedimentary successions interpreted as the source of the Archean SPGs studied here, the detection of near-freezing weathering temperatures indicates that the climate system was cool enough to support cryogenic conditions in the continental hinterland. This interpretation is consistent with the occurrence of glacial diamictites in other Archean successions—such as the ca. 2.9 Ga Pongola and Witwatersrand Supergroups in the Kaapvaal Craton, South Africa—which demonstrate that the Archean Earth was fundamentally capable of sustaining surface ice (*Hofmann and Bindeman*, 2023; *de Wit and Furnes*, 2016). Conversely, the upper end of the range ($\sim 43\,^{\circ}C$) is consistent with persistent low-latitude warmth potentially maintained by a CO_2 and CH_4-rich greenhouse atmosphere (*Krissansen-Totton et al.*, 2018).

These findings offer a nuanced perspective on the Faint Young Sun paradox debate (*Sagan and Chyba*, 1997; *Rosing et al.*, 2010; *Goldblatt and Zahnle*, 2011). Alternatively to a uniformly hot ocean compensating for reduced solar luminosity ($\sim$ 75–80% of modern), or a hard snowball state, our results indicate a dynamic climate system capable of sustaining both temperate and cryogenic conditions. This implies that greenhouse forcing—likely dominated by elevated CO_2 and CH_4 (*Catling and Zahnle*, 2020)—was sufficient to prevent runaway Snowball Earth conditions, but not strong enough to impose persistently extreme surface temperatures.

Secular Evolution of Weathering Regimes

Following the Archean, our record reveals a fundamental reorganization of the surface climate system that aligns with major transitions in atmospheric chemistry and continental assembly (Figure 3.3).

Post-Huronian Stabilization in the Paleoproterozoic: Reconstructed weathering temperatures for protoliths deposited after the Great Oxidation Event (GOE) and the Huronian glaciations (3–17 °C) are both lower and more homogeneous than those recorded in Neoarchean rocks. The interpreted depositional interval for the protoliths of our samples spans the Rhyacian and Orosirian periods (ca. 2.2–1.8 Ga), following the termination of the Huronian glaciations. Our data, however, point to the establishment of a sustained, cool climatic baseline rather than a return to strongly greenhouse conditions. While widespread glacial deposits are not characteristic of

this period, discrete evidence supports the persistence of cold conditions well after the main Huronian pulse. Notable examples include the Serra Sul diamictite in Brazil (ca. 2.0-2.5 Ga; *Araújo and Nogueira*, 2019), low-latitude glaciofluvial features in the Kimberley Basin, Western Australia (ca. 1.8 Ga; *Williams*, 2005), and periglacial evidence in Central Sweden (ca. 1.9 Ga; *Kuipers et al.*, 2013). These records are consistent with our reconstructed temperatures and indicate that the post-GOE Earth remained fundamentally capable of sustaining ice. We suggest that the rise of atmospheric O_2 and the collapse of the Archean methane greenhouse fundamentally shifted Earth's radiative balance. Furthermore, the onset of vigorous oxidative weathering on the continents by ca. 2.15 Ga would have enhanced the silicate weathering feedback (*Scott et al.*, 2008), establishing a buffered climate state regulated by increasingly extensive and stable continents.

A Greenhouse-Biased Supercontinent in the Mesoproterozoic: Early Neoproterozoic migmatite leucosomes from the Northern Andes yield elevated weathering temperatures of $\sim$ 14–41 °C, indicating a warm surface environment prior to the Cryogenian. These samples are derived from a Northern Andean inlier of the Amazonian Craton (Colombia) associated with the Putumayo–Grenvillian orogeny, with protolith depositional ages constrained to ca. 1.1–1.0 Ga (*Ibañez–Mejia et al.*, 2020). The reconstructed temperatures are consistent with paleogeographic reconstructions placing the Amazonian Craton at low-to-mid latitudes during the assembly of Rodinia (*Li et al.*, 2008).

This interval corresponds to the latter stages of the "Boring Billion," a period characterized by the long-lived stability of the Nuna/Rodinia supercontinent system and a nutrient-limited ocean. We propose that the concentration of continental mass within the stable interior of Rodinia, together with low erosion rates, reduced the efficiency of global silicate weathering. Such a tectonic configuration would have sustained elevated atmospheric CO_2 and relatively low O_2 levels, contributing to a greenhouse-biased climate state (*Planavsky et al.*, 2014). While these results support regional warmth consistent with a low-latitude position during Rodinia assembly, the limited spatial coverage of these samples precludes robust extrapolation to global climatic conditions, particularly given the likely presence of high-latitude continental regions during Rodinia's reorganization.

A Dynamic Phanerozoic Climate Regime: Phanerozoic samples deposited after the Cryogenian glaciations record moderate weathering temperatures spanning $\sim$ 2–27 °C, consistent with the range of global surface temperatures inferred from inde-

pendent paleoclimate proxies and climate models (*Judd et al.*, 2024). This interval follows both the Neoproterozoic Oxygenation Event (NOE) and the termination of Snowball Earth glaciations—two transitions that fundamentally reorganized the ocean–atmosphere system and intensified continental weathering (*Campbell and Squire*, 2010; *Och and Shields-Zhou*, 2012).

The broad range of reconstructed temperatures may reflect substantial geographic variability in sedimentary source regions, including differences in latitude and altitude. Alternatively, it may indicate a climate system capable of larger-amplitude variability than that inferred for the mid-Proterozoic. Such variability is consistent with a more dynamic coupling among atmospheric CO_2, biological productivity, seafloor alteration, and continental weathering under elevated O_2 levels. Our results capture this increased dynamism, including alternations between glacial and temperate weathering regimes during the early to mid-Phanerozoic.

A New Lithologic Archive of Ancient Weathering

By extracting triple oxygen isotope signatures from garnet formed during the partial melting of sedimentary rocks, our approach yields a lithology-integrated reconstruction of surface weathering conditions that complements and extends traditional paleoclimate archives. Unlike siliciclastic strata, which preserve spatially localized records and are susceptible to diagenetic overprinting, sediment-derived granitic magmas homogenize large sediment volumes and retain their integrated isotopic signatures through crustal processing and time. Consequently, strongly peraluminous granites and anatectic migmatites constitute a stable archive that can be leveraged to interrogate ancient weathering processes, atmospheric composition, and climate states.

More broadly, this methodology establishes for the first time a general framework for reconstructing ancient meteoric water compositions and weathering temperatures from sediment-derived magmatic systems. These results highlight the capacity of triple-oxygen isotopes in granitic minerals to resolve long-standing questions about Earth's climate evolution through deep time, including the origin of mid-Proterozoic warmth, the magnitude and spatial structure of Archean climate variability, and the coupling among supercontinent cycles, weathering rates, and atmospheric oxygenation.

METHODS

Oxygen isotope measurements

Triple oxygen isotope ratios were measured at the Terrestrial Biogeochemistry and Paleoclimatology Laboratory (Brown University), following established protocols (*Havel et al.*, 2025). Oxygen isotope compositions are reported relative to Vienna Standard Mean Ocean Water (VSMOW) using both conventional (δ) and linearized (δ') notation, with deviations from mass-dependent fractionation expressed as $\Delta'^{17}O$ relative to a reference slope $\lambda = 0.528$.

Analyses were performed using ~1.5–3.5 mg hand-picked garnet grains from strongly peraluminous granites and leucosomes hosted in anatectic metapelites. Oxygen was released from the samples via laser fluorination, followed by multi-stage purification in liquid-nitrogen traps to remove condensable waste gases. Purified oxygen was then analyzed for oxygen isotopes using a Thermo Scientific 253 Plus isotope ratio mass spectrometer. Each sample unknown was analyzed in multiple reference–sample cycles under identical conditions to reference materials. Analyses whose measured bellows pressure deviated by more than 2σ from the robust linear regression of bellows pressure on sample weight (Figure S3.1) were interpreted as reflecting incomplete fluorination or a gas-handling anomaly and were excluded from further data reduction.

The Gore Mountain garnet standard (UWG-2) was measured at the beginning and end of each analytical session and used to define a time-dependent correction for instrumental drift in $\delta^{18}O$ and $\delta^{17}O$. Within-run analytical precision (1σ), based on pooled UWG-2 replicates ($n_{sess} = 45$; $n_{repl} = 342$), was ±0.0121,‰ and ±0.0118,‰ for $\delta^{18}O$ and $\delta^{17}O$, respectively. Long-term external reproducibility was assessed from repeated analyses of the San Carlos olivine standard (SCO; $n_{sess} = 31$; $n_{repl} = 51$), yielding count-weighted one-sigma uncertainties of ±0.328,‰ for $\delta^{18}O$ and ±0.169,‰ for $\delta^{17}O$.

The uncertainty on $\Delta'^{17}O$ is substantially smaller (±0.010,‰): session-to-session instrumental drift shifts $\delta'^{17}O$ and $\delta'^{18}O$ nearly proportionally, so that the two terms in $\Delta'^{17}O = \delta'^{17}O - 0.528, \delta'^{18}O$ nearly cancel under error propagation, greatly reducing the propagated variance relative to either individual isotope ratio. Measured $\Delta'^{17}O$ values for SCO were indistinguishable from the accepted reference composition (*Sharp and Wostbrock*, 2021). The uncertainties estimated for SCO are adopted for all unknown samples in this study. A complete description of the analytical methods is provided in the Supplementary Information.

Weathering product modeling and isotope mass balance

Bulk siliciclastic sediment compositions were compiled from the Sedimentary Geochemistry and Paleoenvironments Project (*Farrell et al.*, 2021) and published datasets of Archean and Proterozoic sedimentary rocks (the full dataset is provided in a CaltechDATA Repository: *Hernández-Montenegro*, 2026). Mean whole rock compositions and dispersion statistics (range and standard deviation) were computed for sediments with depositional ages comprising four groups: before the GEO (pre-GOE), between the GOE and the NOE (pre-NOE), and after the NOE (post-NOE). These statistics were used to unmix siliciclastic compositions into end-member components, including quartz, feldspar, and clays (illite, smectite, chlorite, and kaolinite), using a Monte Carlo–based non-negative least-squares inversion.

From the resulting phase proportions, we derived mass balance equations for the isotopic contribution of the clastic component (quartz and feldspar) and the weathering product from clay minerals (wp) to the measured bulk siliciclastic isotopic composition (see Reconstruction of the source isotopic composition section). We also derived temperature-dependent wp–water oxygen isotope fractionation expressions for composite weathering products, assuming oxygen-weighted combinations of mineral-specific fractionation curves from experimental and theoretical calibrations (i.e., *Savin and Lee*, 1988; *Zheng*, 1993; *Sharp et al.*, 2016).

Weathering temperatures were determined by inverting a temperature solution that simultaneously satisfies the mass balance-estimated values for $\delta'^{18}O$, $\delta'^{17}O$, and $\Delta'^{17}O$ of the calculated weathering products and equilibrium triple-oxygen isotope relationships as a function of temperature (*Pack and Herwartz*, 2014; *Dauphas and Schauble*, 2016). Corresponding meteoric water $\delta'^{18}O$, $\delta'^{17}O$, and $\Delta'^{17}O$ values were then calculated using the inferred temperatures and mineral–water fractionation factors, assuming the reference meteoric water line of *Luz and Barkan* (2010).

Uncertainties in mineral proportions, wp–water fractionation parameters, and detrital mineral isotope compositions were propagated in our inversion algorithm by running 10^6 Monte Carlo iterations for each sample. Reported temperature values represent Monte Carlo means with 1σ uncertainties. A detailed description of the temperature inversion algorithm is given in the Supplementary Information.

Reconstruction of the source isotopic composition

Measured garnet oxygen isotope compositions were converted to bulk sedimentary source compositions using temperature-dependent garnet–source fractionation fac-

tors derived from phase equilibrium modeling (see Phase equilibrium modeling section). The fractionation factors adopted were the mean $\Delta_{grt-source}$ at dehydration melting temperatures for the average siliciclastic rock compositions considered for each time interval (*i.e.*, pre-GOE, post-GOE, pre-NOE, and post-NOE). Note that variability in $\Delta_{grt-source}$ across this temperature range is < 0.1 ‰ for any given protolith composition. Moreover, the extent of $\Delta_{grt-source}$ among different protoliths is relatively uniform, ranging from -1.93 to -2.16 ‰. Oxygen isotope fractionation during prograde metamorphism was assumed to be negligible, as shown in previous studies (e.g., *Valley*, 1986; *Zheng et al.*, 2003; *Bindeman*, 2021).

Phase equilibrium modeling

Phase equilibrium calculations were performed using `Theriak-Domino` (*de Capitani and Petrakakis*, 2010) to quantify mineral assemblages and oxygen isotope fractionation during partial melting of metasedimentary rocks (*Bucholz and Hernández-Montenegro*, 2025). Calculations were conducted in the MnNKCFMASHTO system at 0.75 GPa and 600–1000 °C under minimally water-saturated conditions, using the thermodynamic dataset of *Holland and Powell* (2011) and published activity–composition models appropriate for metapelites (*White et al.*, 2014b,a). Model outputs were used to derive $\Delta_{grt-source}$ and to evaluate equilibrium oxygen isotope partitioning among phases (*Vho et al.*, 2019). Full thermodynamic details are provided in the Supplementary Information and model outputs are included in *Hernández-Montenegro* (2026).

References

Araújo, R., and A. Nogueira, Serra Sul diamictite of the Carajás Basin (Brazil): A Paleoproterozoic glaciation on the Amazonian craton, *Geology*, *47*(12), 1166–1170, doi:10.1130/G46923.1, 2019.

Bindeman, I. N., Triple Oxygen Isotopes in Evolving Continental Crust, Granites, and Clastic Sediments, *Reviews in Mineralogy and Geochemistry*, *86*(1), 241–290, doi:10.2138/rmg.2021.86.08, 2021.

Bindeman, I. N., A. Bekker, and D. O. Zakharov, Oxygen isotope perspective on crustal evolution on early Earth: A record of Precambrian shales with emphasis on Paleoproterozoic glaciations and Great Oxygenation Event, *Earth and Planetary Science Letters*, *437*, 101–113, doi:10.1016/j.epsl.2015.12.029, 2016.

Bindeman, I. N., D. O. Zakharov, J. Palandri, N. D. Greber, N. Dauphas, G. J. Retallack, A. Hofmann, J. S. Lackey, and A. Bekker, Rapid emergence of subaerial

landmasses and onset of a modern hydrologic cycle 2.5 billion years ago, *Nature*, *557*(7706), 545–548, doi:10.1038/s41586-018-0131-1, 2018.

Bindeman, I. N., G. Bayon, and J. Palandri, Triple oxygen isotope investigation of fine-grained sediments from major world's rivers: Insights into weathering processes and global fluxes into the hydrosphere, *Earth and Planetary Science Letters*, *528*, 115,851, doi:10.1016/j.epsl.2019.115851, 2019.

Blake, R. E., S. J. Chang, and A. Lepland, Phosphate oxygen isotopic evidence for a temperate and biologically active Archaean ocean, *Nature*, *464*(7291), 1029–1032, doi:10.1038/nature08952, 2010.

Bucholz, C. E., and J. D. Hernández-Montenegro, Temporal variation in oxygen isotopes of peraluminous granites derived from sedimentary sources, *Lithos*, *492–493*, 107,864, doi:10.1016/j.lithos.2024.107864, 2025.

Bucholz, C. E., and C. J. Spencer, Strongly Peraluminous Granites across the Archean–Proterozoic Transition, *Journal of Petrology*, *60*(7), 1299–1348, doi:10.1093/petrology/egz033, 2019.

Campbell, I. H., and R. J. Squire, The mountains that triggered the Late Neoproterozoic increase in oxygen: The Second Great Oxidation Event, *Geochimica et Cosmochimica Acta*, *74*(15), 4187–4206, doi:10.1016/j.gca.2010.04.064, 2010.

Catling, D. C., and K. J. Zahnle, The Archean atmosphere, *Science Advances*, *6*(9), eaax1420, doi:10.1126/sciadv.aax1420, 2020.

Chamberlain, C. P., and M. E. Conrad, Oxygen Isotope Zoning in Garnet, *Science*, *254*(5030), 403–406, doi:10.1126/science.254.5030.403, 1991.

Dauphas, N., and E. A. Schauble, Mass Fractionation Laws, Mass-Independent Effects, and Isotopic Anomalies, *Annual Review of Earth and Planetary Sciences*, *44*(1), 709–783, doi:10.1146/annurev-earth-060115-012157, 2016.

de Capitani, C., and K. Petrakakis, The computation of equilibrium assemblage diagrams with Theriak/Domino software, *American Mineralogist*, *95*(7), 1006–1016, 2010.

de Wit, M. J., and H. Furnes, 3.5-Ga hydrothermal fields and diamictites in the Barberton Greenstone Belt—Paleoarchean crust in cold environments, *Science Advances*, *2*(2), e1500,368, doi:10.1126/sciadv.1500368, 2016.

Farquhar, J., H. Bao, and M. Thiemens, Atmospheric Influence of Earth's Earliest Sulfur Cycle, *Science*, *289*(5480), 756–758, doi:10.1126/science.289.5480.756, 2000.

Farrell, Ú. C., et al., The sedimentary geochemistry and paleoenvironments project, *Geobiology*, *19*(6), 545–556, 2021.

Goldblatt, C., and K. J. Zahnle, Faint young Sun paradox remains, *Nature*, *474*(7349), E1–E1, doi:10.1038/nature09961, 2011.

Havel, R., D. E. Ibarra, R. Bartoschewitz, and G. Budde, Interrogating leaching procedures of meteorites for triple oxygen isotope analyses, *Meteoritics & Planetary Science*, *60*(10), 2311–2333, doi:10.1111/maps.70039, 2025.

Hernández-Montenegro, J. D., C. E. Bucholz, E. S. Sosa, M. A. Kipp, and F. L. H. Tissot, Iron isotope fractionation during partial melting of metapelites and the generation of strongly peraluminous granites, *Geochimica et Cosmochimica Acta*, *380*, 112–130, doi:10.1016/j.gca.2024.07.016, 2024.

Hernández-Montenegro, J. D., As on earth, so on mars: Magmatic records of planetary evolution. supporting information, doi:10.22002/04fbj-4g807, 2026.

Herwartz, D., A. Pack, and T. J. Nagel, A CO2 greenhouse efficiently warmed the early Earth and decreased seawater 18O/16O before the onset of plate tectonics, *Proceedings of the National Academy of Sciences*, *118*(23), e2023617,118, doi:10.1073/pnas.2023617118, 2021.

Hofmann, A., and I. N. Bindeman, Earth's first glaciation at 2.9 Ga revealed by triple oxygen isotopes, *Geochemical Perspectives Letters*, *26*(26), 20–24, 2023.

Holland, T. J. B., and R. Powell, An improved and extended internally consistent thermodynamic dataset for phases of petrological interest, involving a new equation of state for solids, *Journal of Metamorphic Geology*, *29*(3), 333–383, doi:10.1111/j.1525-1314.2010.00923.x, 2011.

Hren, M. T., M. M. Tice, and C. P. Chamberlain, Oxygen and hydrogen isotope evidence for a temperate climate 3.42 billion years ago, *Nature*, *462*(7270), 205–208, doi:10.1038/nature08518, 2009.

Ibañez–Mejia, M., J. Gómez, and D. Mateus–Zabala, The Putumayo orogen of Amazonia: A synthesis, *The geology of Colombia, Volume 1 Proterozoic-Paleozoic*, 2020.

Ibarra, D. E., A. G. Yanchilina, M. K. Lloyd, K. A. Methner, C. P. Chamberlain, R. Yam, A. Shemesh, and D. A. Stolper, Triple oxygen isotope systematics of diagenetic recrystallization of diatom opal-A to opal-CT to microquartz in deep sea sediments, *Geochimica et Cosmochimica Acta*, *320*, 304–323, doi:10.1016/j.gca.2021.11.027, 2022.

Isson, T., and S. Rauzi, Oxygen isotope ensemble reveals Earth's seawater, temperature, and carbon cycle history, *Science*, *383*(6683), 666–670, doi:10.1126/science.adg1366, 2024.

Judd, E. J., J. E. Tierney, D. J. Lunt, I. P. Montañez, B. T. Huber, S. L. Wing, and P. J. Valdes, A 485-million-year history of Earth's surface temperature, *Science*, *385*(6715), eadk3705, doi:10.1126/science.adk3705, 2024.

Knauth, L. P., and D. R. Lowe, High Archean climatic temperature inferred from oxygen isotope geochemistry of cherts in the 3.5 Ga Swaziland Supergroup, South Africa, *Geological Society of America Bulletin*, *115*(5), 566–580, 2003.

Kohn, M. J., J. W. Valley, D. Elsenheimer, and M. J. Spicuzza, O isotope zoning in garnet and staurolite: Evidence for closed-system mineral growth during regional metamorphism, *American Mineralogist*, *78*(9-10), 988–1001, 1993.

Konhauser, K. O., et al., Iron formations: A global record of Neoarchaean to Palaeoproterozoic environmental history, *Earth-Science Reviews*, *172*, 140–177, doi:10.1016/j.earscirev.2017.06.012, 2017.

Krissansen-Totton, J., G. N. Arney, and D. C. Catling, Constraining the climate and ocean pH of the early Earth with a geological carbon cycle model, *Proceedings of the National Academy of Sciences*, *115*(16), 4105–4110, doi:10.1073/pnas.1721296115, 2018.

Kuipers, G., F. F. Beunk, and F. M. van der Wateren, Periglacial evidence for a 1.91–1.89 Ga old glacial period at low latitude, Central Sweden, *Geology Today*, *29*(6), 218–221, doi:10.1111/gto.12027, 2013.

Li, Z. X., et al., Assembly, configuration, and break-up history of Rodinia: A synthesis, *Precambrian Research*, *160*(1), 179–210, doi:10.1016/j.precamres.2007.04.021, 2008.

Liljestrand, F. L., A. H. Knoll, N. J. Tosca, P. A. Cohen, F. A. Macdonald, Y. Peng, and D. T. Johnston, The triple oxygen isotope composition of Precambrian chert, *Earth and Planetary Science Letters*, *537*, 116,167, doi:10.1016/j.epsl.2020.116167, 2020.

Lowe, D. R., D. E. Ibarra, N. Drabon, and C. P. Chamberlain, Constraints on surface temperature 3.4 billion years ago based on triple oxygen isotopes of cherts from the Barberton Greenstone Belt, South Africa, and the problem of sample selection, *American Journal of Science*, *320*(9), 790–814, 2020.

Luz, B., and E. Barkan, Variations of 17O/16O and 18O/16O in meteoric waters, *Geochimica et Cosmochimica Acta*, *74*(22), 6276–6286, doi:10.1016/j.gca.2010.08.016, 2010.

Marin-Carbonne, J., F. Robert, and M. Chaussidon, The silicon and oxygen isotope compositions of Precambrian cherts: A record of oceanic paleo-temperatures?, *Precambrian Research*, *247*, 223–234, doi:10.1016/j.precamres.2014.03.016, 2014.

McGunnigle, J., E. Cano, Z. Sharp, K. Muehlenbachs, D. Cole, M. Hardman, T. Stachel, and D. Pearson, Triple oxygen isotope evidence for a hot Archean ocean, *Geology*, *50*(9), 991–995, doi:10.1130/G50230.1, 2022.

Nesbitt, H. W., G. M. Young, S. M. McLennan, and R. R. Keays, Effects of Chemical Weathering and Sorting on the Petrogenesis of Siliciclastic Sediments, with Implications for Provenance Studies, *The Journal of Geology*, *104*(5), 525–542, doi:10.1086/629850, 1996.

Och, L. M., and G. A. Shields-Zhou, The Neoproterozoic oxygenation event: Environmental perturbations and biogeochemical cycling, *Earth-Science Reviews*, *110*(1), 26–57, doi:10.1016/j.earscirev.2011.09.004, 2012.

Pack, A., and D. Herwartz, The triple oxygen isotope composition of the Earth mantle and understanding ΔO17 variations in terrestrial rocks and minerals, *Earth and Planetary Science Letters*, *390*, 138–145, doi:10.1016/j.epsl.2014.01.017, 2014.

Payne, J. L., M. Hand, N. J. Pearson, K. M. Barovich, and D. J. McInerney, Crustal thickening and clay: Controls on O isotope variation in global magmatism and siliciclastic sedimentary rocks, *Earth and Planetary Science Letters*, *412*, 70–76, doi:10.1016/j.epsl.2014.12.037, 2015.

Planavsky, N. J., C. T. Reinhard, X. Wang, D. Thomson, P. McGoldrick, R. H. Rainbird, T. Johnson, W. W. Fischer, and T. W. Lyons, Low Mid-Proterozoic atmospheric oxygen levels and the delayed rise of animals, *science*, *346*(6209), 635–638, 2014.

Roberts, N. M. W., and C. J. Spencer, The zircon archive of continent formation through time, *Geological Society, London, Special Publications*, *389*(1), 197 LP – 225, 2015.

Rosing, M. T., D. K. Bird, N. H. Sleep, and C. J. Bjerrum, No climate paradox under the faint early Sun, *Nature*, *464*(7289), 744–747, doi:10.1038/nature08955, 2010.

Sagan, C., and C. Chyba, The Early Faint Sun Paradox: Organic Shielding of Ultraviolet-Labile Greenhouse Gases, *Science*, *276*(5316), 1217–1221, doi:10.1126/science.276.5316.1217, 1997.

Savin, SM., and M. Lee, Isotopic studies of phyllosilicates, *Reviews in Mineralogy and Geochemistry*, *19*(1), 189–223, 1988.

Schauble, E. A., and E. D. Young, Mass Dependence of Equilibrium Oxygen Isotope Fractionation in Carbonate, Nitrate, Oxide, Perchlorate, Phosphate, Silicate, and Sulfate Minerals, *Reviews in Mineralogy and Geochemistry*, *86*(1), 137–178, doi:10.2138/rmg.2021.86.04, 2021.

Scicchitano, M. R., et al., Oxygen diffusion in garnet: Experimental calibration and implications for timescales of metamorphic processes and retention of primary O isotopic signatures, *American Mineralogist*, *107*(7), 1425–1441, doi:10.2138/am-2022-7970, 2022.

Scott, C., T. W. Lyons, A. Bekker, Y.-a. Shen, S. W. Poulton, X.-l. Chu, and A. D. Anbar, Tracing the stepwise oxygenation of the Proterozoic ocean, *Nature*, *452*(7186), 456–459, 2008.

Sengupta, S., S. T. M. Peters, J. Reitner, J.-P. Duda, and A. Pack, Triple oxygen isotopes of cherts through time, *Chemical Geology*, *554*, 119,789, doi:10.1016/j.chemgeo.2020.119789, 2020.

Sharp, Z. D., and J. A. Wostbrock, Standardization for the Triple Oxygen Isotope System: Waters, Silicates, Carbonates, Air, and Sulfates, *Reviews in Mineralogy and Geochemistry*, *86*(1), 179–196, doi:10.2138/rmg.2021.86.05, 2021.

Sharp, Z. D., J. A. Gibbons, O. Maltsev, V. Atudorei, A. Pack, S. Sengupta, E. L. Shock, and L. P. Knauth, A calibration of the triple oxygen isotope fractionation in the SiO2–H2O system and applications to natural samples, *Geochimica et Cosmochimica Acta*, *186*, 105–119, doi:10.1016/j.gca.2016.04.047, 2016.

Valley, J. W., Stable isotope geochemistry of metamorphic rocks, *Reviews in Mineralogy and Geochemistry*, *16*(1), 445–489, 1986.

Vho, A., P. Lanari, and D. Rubatto, An Internally-Consistent Database for Oxygen Isotope Fractionation Between Minerals, *Journal of Petrology*, *60*(11), 2101–2129, doi:10.1093/petrology/egaa001, 2019.

White, R. W., R. Powell, T. J. B. Holland, T. E. Johnson, and E. C. R. Green, New mineral activity–composition relations for thermodynamic calculations in metapelitic systems, *Journal of Metamorphic Geology*, *32*(3), 261–286, 2014a.

White, R. W., R. Powell, and T. E. Johnson, The effect of Mn on mineral stability in metapelites revisited: New a–x relations for manganese-bearing minerals, *Journal of Metamorphic Geology*, *32*(8), 809–828, 2014b.

Williams, G. E., Subglacial meltwater channels and glaciofluvial deposits in the Kimberley Basin, Western Australia: 1.8 Ga low-latitude glaciation coeval with continental assembly, *Journal of the Geological Society*, *162*(1), 111–124, doi:10.1144/0016-764903-157, 2005.

Zakharov, D. O., J. Marin-Carbonne, J. Alleon, and I. N. Bindeman, Triple Oxygen Isotope Trend Recorded by Precambrian Cherts: A Perspective from Combined Bulk and in situ Secondary Ion Probe Measurements, *Reviews in Mineralogy and Geochemistry*, *86*(1), 323–365, doi:10.2138/rmg.2021.86.10, 2021.

Zheng, Y.-F., Calculation of oxygen isotope fractionation in hydroxyl-bearing silicates, *Earth and Planetary Science Letters*, *120*(3), 247–263, doi:10.1016/0012-821X(93)90243-3, 1993.

Zheng, Y.-F., B. Fu, B. Gong, and L. Li, Stable isotope geochemistry of ultrahigh pressure metamorphic rocks from the Dabie–Sulu orogen in China: Implications

for geodynamics and fluid regime, *Earth-Science Reviews*, *62*(1), 105–161, doi: 10.1016/S0012-8252(02)00133-2, 2003.

SUPPLEMENTARY MATERIAL: TRIPLE-OXYGEN ISOTOPES IN GRANITIC MAGMAS REVEAL MAJOR SHIFTS IN EARTH'S WEATHERING CONDITIONS THROUGH TIME

SUPPLEMENTARY METHODS

S1. SAMPLE DESCRIPTION

In this work, we studied peraluminous to strongly peraluminous granitic samples from both large scale igneous bodies (batholiths) and centimeter- to meter-scale leucosomes from migmatitic rocks produced by partial melting of metasedimentary rocks. We selected samples containing garnet crystals interpreted to have formed in equilibrium with a granitic melt, including peritectic garnets incorporated into the melt during leucosome segregation and magmatic garnets crystallized in equilibrium with the host melt. We specifically target garnet as it is known to have an extremely low oxygen diffusivity and preserve original isotopic signatures even after high temperature homogenization (*Scicchitano et al.*, 2022; *Chamberlain and Conrad*, 1991; *Valley*, 1986). Below, we provide a general description and geological context for each locality.

Volcan Mountain, Peninsular Ranges (San Diego County, California, USA)

Two garnet-bearing leucocratic granite samples (VM24-02, -04) were collected at Volcan Mountain in the Peninsular Ranges, California. These rocks are part of the ~165 Ma strongly peraluminous Harper Creek suite (*Shaw et al.*, 2003). The Harper Creek suite consists of tonalite to granodiorite plutons and anatectic migmatites schist and gneiss with a metasedimentary protolith (*Shaw et al.*, 2003). Field and petrographic relations indicate that Harper Creek rocks originated predominantly through high degrees of partial melting of the Julian Schist, a heterogeneous sequence of quartzofeldspathic, pelitic, and calc-silicate metasedimentary rocks deposited in turbiditic environments (*Germinario*, 1993). Based on regional stratigraphic constraints and detrital zircon data, the likely depositional age for the Julian Schist spans from the Triassic to Early Jurassic (250–175 Ma) (*Germinario*, 1993; *Shaw et al.*, 2003).

Hercynian Orogeny, Spanish Central System (Spain)

Two garnet samples from peraluminous leucosomes in migmatitic rocks from the Toledo Anatectic Complex in Central Spain were analyzed (G-1 and G-4). The

migmatization age for the Toledo Anatectic Complex has been interpreted to range from ~317-330 Ma (*Bea et al.*, 2006; *Castiñeiras et al.*, 2008), recording a period of large-scale crustal anatexis during the late Hercynian orogeny.

Sample G-114912 is a xenolith of a lower crust felsic granulite formed in equilibrium with peraluminous magmas. Geochemical evidence suggests that this type of lower crust felsic granulites, hosted in ultrabasic dikes intruding the Hercynian basement of Central Spain, are associated to late-Hercynian peraluminous magmatism derived from sedimentary protoliths with minimal mantle contribution (*Villaseca et al.*, 1999). We also analyzed one sample from the Hoyo de Pinares pluton (G-94726), a granitoid intrusion emplaced at shallow crustal levels in the eastern Spanish Central System. Zircon U–Pb ages for this unit yields an age of 299 ± 1.8 Ma, indicating crystallization after the main Hercynian deformation stage. (*Orejana et al.*, 2012; *Villaseca et al.*, 2012).

Based on detrital zircon populations, the protolith of the peraluminous Hercynian plutons, as well as that of related pelitic and psammitic migmatites, is interpreted to have maximum depositional ages of 560 Ma, indicating Neoproterozoic sedimentation with West African craton provenance (*Villaseca et al.*, 1998; *Castiñeiras et al.*, 2008).

Sierras Pampeanas and Famatinian Belt (Argentina)

Seven garnet-bearing samples from the Sierras Pampeanas and the adjacent Famatinian belt were examined. Sample VIN-203 derives from the Vinquis Intrusive Complex (Andaluca Unit), which comprises weakly peraluminous granitic plutons emplaced during the early Carboniferous between 346 ± 3 Ma and 342 ± 3 Ma (*Morales Cámera et al.*, 2022). Sample ANI-400 was collected from the La Costa pluton of the Anillaco unit, dated at 354 ± 5 Ma (*Alasino et al.*, 2010; *Dahlquist et al.*, 2018, 2021). Sample GRA-CB is sourced from the Cura Brochero granite within the Achala Intrusive Complex, which records Late Devonian crustal melting between 379–359 Ma (*Morales Cámera et al.*, 2020). Sample ASP-401 corresponds to the Peñón Rosado granite (469 ± 4 Ma) of the Famatinian belt, representing Ordovician S-type magmatism (*Dahlquist et al.*, 2007).

In addition, we studied garnet grains extracted from leucosomes samples associated with the Juan XXIII diatexite of the San Carlos migmatitic massif (DIA-J23-2, -B, -LEU). These migmatitic rocks record early Cambrian crustal anatexis, constrained indirectly by nearby peraluminous intrusions yielding ages of 529–523 Ma (*Escayola*

et al., 2007). Taken together, these units document recurrent episodes of deep crustal melting from the early Cambrian through the Carboniferous, derived from broadly Neoproterozoic metasedimentary basements along the proto-Andean margin (*Rapela et al.*, 2016; *Escayola et al.*, 2007; *Dahlquist et al.*, 2021).

Florencia Migmatites, Northern Andes (Colombia)

Nine garnet samples extracted from leucosomes in migmatitic samples from northwestern South America (GZN-25, -48, -49, -64, -65, -75, -77, -81, -84). The samples were collected from the Florencia Migmatites unit within the Garzón Massif in the Colombian Andes. They consist of metatexites and diatexites derived from sedimentary protoliths. Zircon U-Pb ages in rocks from this unit indicate an age of 992 ± 5 Ma, interpreted as the timing of peak granulite-facies metamorphism and associated anatexis during the Putumayo (Grenvillian) orogeny (*Ibanez-Mejia et al.*, 2011; *Ibañez–Mejia et al.*, 2020). Similarly, detrital zircon data constrain maximum depositional ages of the sedimentary protolith to 1115 ± 4 Ma (*Ibanez-Mejia et al.*, 2011; *Ibañez–Mejia et al.*, 2020).

Harney Peak Granite, Trans-Hudson Orogen (USA)

Eight garnet-bearing samples from the Harney Peak Granite were selected for this study (HP-43A, 44A, 46A; SD-18-11, -14, -15, -16, -18). The Harney Peak Granite, and associated satellite intrusions, is a strongly peraluminous unit exposed in the Black Hills of South Dakota (*Bucholz and Spencer*, 2019), with an interpreted crystallization age of 1715 ± 3 Ma (*Redden et al.*, 1990). Petrologic and geochemical evidence indicates that the inner portions of the granite formed predominantly through high degrees of partial melting of immature Archean metasedimentary sources in the lower crust, whereas the outer zones, which include the garnet-bearing granites analyzed here, were generated by partial melting of a Proterozoic sedimentary source (*Nabelek et al.*, 1992). The depositional age of the sedimentary protolith supplying these outer-zone magmas is interpreted to lie between ~2100 and 1880 Ma (*Bucholz and Spencer*, 2019).

Svecofennian Granite–Migmatite Zone (Finland)

Five samples corresponding to garnet-bearing leucosomes from the late Svecofennian granite–migmatite zone were studied (17-FIN-02, 01B, 05B, 06A, 06B). U-Pb zircon geochronology indicates crystallization ages ranging from 1815 ± 16 to 1896 ± 26 Ma (*Liebmann et al.*, 2021b), following arc accretion, crustal thickening, and migmatization at ca. 1910-1870 Ma (*Bucholz and Spencer*, 2019). The rocks

from the late Svecofennian granite–migmatite zone record partial melting of pelitic to psammitic sedimentary protoliths deposited prior to Svecofennian orogenesis, likely between ~2000 and 1900 Ma (*Bucholz and Spencer*, 2019). Detrital zircon spectra indicate strong inheritance from local supracrustal sedimentary sources (*Ehlers et al.*, 1993; *Bucholz and Spencer*, 2019).

Hepburn Intrusive Suite, Wopmay Orogen (Canada)

Five samples from the ca. 1885 Ma Hepburn intrusive suite were selected for analysis (SAB-81-L54, -S55, -65, -V27, -Z29B). This unit represents a major Paleoproterozoic magmatic episode within the Wopmay Orogen along the western margin of the Slave Craton (*Hoffman and Bowring*, 1984; *Lalonde*, 1989; *Bucholz and Spencer*, 2019), intruding sedimentary successions of the Coronation Supergroup deposited in a back-arc basin between ~2100 to ~1900 Ma (*Bowring and Grotzinger*, 1992; *Lalonde*, 1989). Although mantle-derived magmatism contributed to the thermal and magmatic evolution of the system, the granitoid rocks largely reflect partial melting and extensive assimilation of supracrustal sedimentary rocks within the back-arc basin during orogenesis. The predominance of peraluminous compositions and widespread evidence for interaction with sedimentary host rocks indicate that crustal recycling of supracrustal material was the dominant control on magma genesis (*Bucholz and Spencer*, 2019).

Jining and Daqingshan–Wulashan complexes, North China Craton (Inner Mongolia, China)

We analyzed five samples from strongly peraluminous granites from the North China Craton. Samples 18-IM-10B, -11B, and 12B were collected from the Jining Complex and have crystallization ages of ca. 1901-1929 Ma (*Liebmann et al.*, 2021a). The Jining Complex forms part of the Paleoproterozoic Khondalite Belt in the western block of the North China Craton. The rocks in this unit are dominated by high-grade metasedimentary rocks interpreted as metamorphosed pelitic to psammitic sediments deposited between ca. 2000 and 1960 Ma (*Li et al.*, 2011; *Wang et al.*, 2011). These sediments were derived from Archean to early Paleoproterozoic continental sources and subsequently metamorphosed to granulite facies during continental collision from ca. ~1950 to ~1920 Ma (*Li et al.*, 2011). The garnet-bearing peraluminous granite samples studied here represent partial melts generated during crustal thickening.

Similarly, two samples from strongly peraluminous granites in the Daqingshan –

Wulashan Complex were studied (18-IM-20 and -23D). The two samples display crystallization ages of 2374 and 2453 Ma (*Liebmann et al.*, 2021a). As in the Jining Complex, the migmatites and peraluminous granites in this region are interpreted to be derived from a sedimentary protolith deposited after 2500 Ma and before ~2400-2450 Ma (*Dong et al.*, 2014).

South Pass granites, Wyoming Province (USA)

Five garnet-bearing granite samples from the South Pass granite suite within the Wyoming Craton were analyzed (WY-18-4, -5, -10, -11, -12). The South Pass granite crystallized at 2.55 Ga during late Neoarchean crustal reworking of the Wyoming Province. Evidence from geochemical data indicates that the granite was derived from a psammitic or pelitic metasedimentary source, producing strongly peraluminous magmas during regional crustal thickening (*Bucholz and Spencer*, 2019). The protolith of the South Pass granites corresponds to metasedimentary rocks from the South Pass supracrustal belt, with an interpreted depositional age of ca. 2670 Ma (*Frost et al.*, 2006).

Superior Craton (Canada, USA)

Sixteen samples from different localities in the Superior Craton were included in our analysis. These samples include garnet-bearing strongly peraluminous granites from the Treelined Lake Complex - English River Subprovince, Ontario (SP-17-33, -36); the Armstrong Highway section - Quetico Subprovince (SP-17-13); the Georgia Lake batholith - Quetico Subprovince (SP-17-26); the Medicine Lake stock - Sioux Lookout Terrane (SP-17-37, -38, -39); the Sharpe Lake batholith - English River Subprovince (SP-17-52); the Allison Lake batholith - English River Subprovince (SP-17-74, -76, -82); the Ghost Lake batholith - Sioux Lookout Terrane (SP-16-33); the Sturgeon Lake granite - Quetico Subprovince (SP-16-46, -51, -52); the Wenasaga Lake batholith - Quetico Subprovince (SP-17-43). These granites display crystallization ages that range from ~2646 to 2690 Ma (*Bucholz and Spencer*, 2019). Overall, the occurrence of strongly peraluminous magmatism in the Superior Province is associated with partial melting of pelitic to psammitic metasedimentary rocks during craton stabilization, whose protolith was likely deposited between ~2750 and 2700 Ma (*Bucholz and Spencer*, 2019; *Hrabi and Cruden*, 2006; *Davis et al.*, 1988; *Breaks and Moore*, 1992).

S2. OXYGEN ISOTOPES

A. Oxygen isotope notation

All oxygen isotope data are reported relative to Vienna Standard Mean Ocean Water (VSMOW) using both conventional δ notation and linearized notation (δ').

$$\delta^n\mathrm{O} = 10^3\left(\frac{\left(\frac{^n\mathrm{O}}{^{16}\mathrm{O}}\right)_{\mathrm{sample}}}{\left(\frac{^n\mathrm{O}}{^{16}\mathrm{O}}\right)_{\mathrm{VSMOW}}} - 1\right), \qquad n = 17, 18. \tag{S3.1}$$

$$\delta'^n\mathrm{O} = 10^3\ \ln\left(\frac{\delta^n\mathrm{O}}{1000} + 1\right), \qquad n = 17, 18. \tag{S3.2}$$

Deviations from a reference mass-dependent fractionation line are expressed using the triple-oxygen isotope parameter $\Delta'^{17}\mathrm{O}$, defined relative to a reference slope $\lambda = 0.528$, unless otherwise noted:

$$\Delta'^{17}\mathrm{O} = \delta'^{17}\mathrm{O} - \lambda\,\delta'^{18}\mathrm{O}. \tag{S3.3}$$

B. Oxygen isotope measurements

Triple oxygen isotope ratios were determined by laser fluorination in the Terrestrial Biogeochemistry and Paleoclimatology Laboratory at Brown University, following the analytical protocol described in detail by *Havel et al.* (2025).

Analyses were conducted on 1.5–3.5 mg hand-picked garnet grains separated from strongly peraluminous granites and leucosomes hosted in anatectic metapelites. During each daily analytical session, four to six sample aliquots were loaded into individual pits of a nickel sample holder (Ni 201), together with comparable aliquots of San Carlos olivine (SCO) and Gore Mountain garnet (UWG–2), which served as reference materials (*Valley et al.*, 1995; *Sharp and Wostbrock*, 2021). The sample holder was transferred to a stainless steel fluorination chamber. The chamber was evacuated to high vacuum ($\sim 10^{-6}$ mbar) and pumped for at least 8 hours prior to analysis to remove adsorbed atmospheric moisture.

Oxygen was released from samples by infrared laser heating in the presence of $\sim$80 Torr BrF_5. Fluorination was performed in multiple short heating steps to ensure quantitative oxygen extraction. Released oxygen was cryogenically purified using a series of liquid-nitrogen traps to remove condensable waste gases. The resulting O_2

was passed through a 5 Å molecular sieve held at cryogenic temperature while non-condensable waste products were evacuated. Following controlled thermal release, the purified O_2 was transferred to a frozen secondary 5 Å molecular sieve using an ultra-high-purity helium carrier gas, with residual contaminants removed using a gas chromatography column. After removal of the helium carrier gas, purified O_2 was introduced into the mass spectrometer sample bellows by thawing the molecular sieve over ~5–6 minutes.

Isotopic analyses were performed using a Thermo Scientific 253 Plus isotope ratio mass spectrometer configured for triple oxygen isotope measurements in dual-inlet mode, with ion beams monitored at m/z 32, 33, 34, 35, and 36. Each unknown sample was analyzed in 3–5 blocks of 10 reference–sample–reference comparison cycles, with an integration time of 26 s per cycle. Reference materials were measured daily under identical analytical conditions. For each analytical session, SCO was measured once (typically 1–2 blocks), whereas UWG–2 was analyzed at both the beginning (3 blocks) and end (9–18 blocks) of the session. Analyses whose measured bellows pressure deviated by more than 2σ from the regression line were interpreted as reflecting incomplete fluorination or a gas-handling anomaly and were excluded from further data reduction (Figure S3.1).

Repeated analyses of reference materials were used to quantify analytical precision, accuracy, and long-term reproducibility. Analyses with $|\Delta\delta^{18}\mathrm{O}| > 1.0$,‰ offset from accepted values were excluded as outliers. UWG-2 garnet was measured routinely at the beginning and end of each analytical session and used to define a time-dependent correction for instrumental drift in $\delta^{18}\mathrm{O}$ and $\delta^{17}\mathrm{O}$. Typical within-analysis repeatability (1σ), determined from pooled replicate statistics of UWG-2 analyses ($n_{\mathrm{sess}} = 45$; $n_{\mathrm{repl}} = 342$), was ±0.0121,‰ for $\delta^{18}\mathrm{O}$ and ±0.0118,‰ for $\delta^{17}\mathrm{O}$.

San Carlos olivine (SCO) was processed as an unknown to independently assess analytical accuracy and long-term external reproducibility. Because SCO is not used in the normalization procedure, its session-to-session scatter reflects the true post-correction residual uncertainty applicable to unknown samples. SCO analyses reproduced accepted reference values within uncertainty, with small count-weighted mean offsets of −0.362,‰ for $\delta^{18}\mathrm{O}$ and −0.180,‰ for $\delta^{17}\mathrm{O}$ ($n_{\mathrm{sess}} = 31$; $n_{\mathrm{repl}} = 51$). Long-term external reproducibility, defined by the count-weighted standard deviation of SCO session means, was ±0.328,‰ (1σ) for $\delta^{18}\mathrm{O}$ and ±0.169,‰ for $\delta^{17}\mathrm{O}$. For reference, the analogous count-weighted scatter of UWG-2 — which

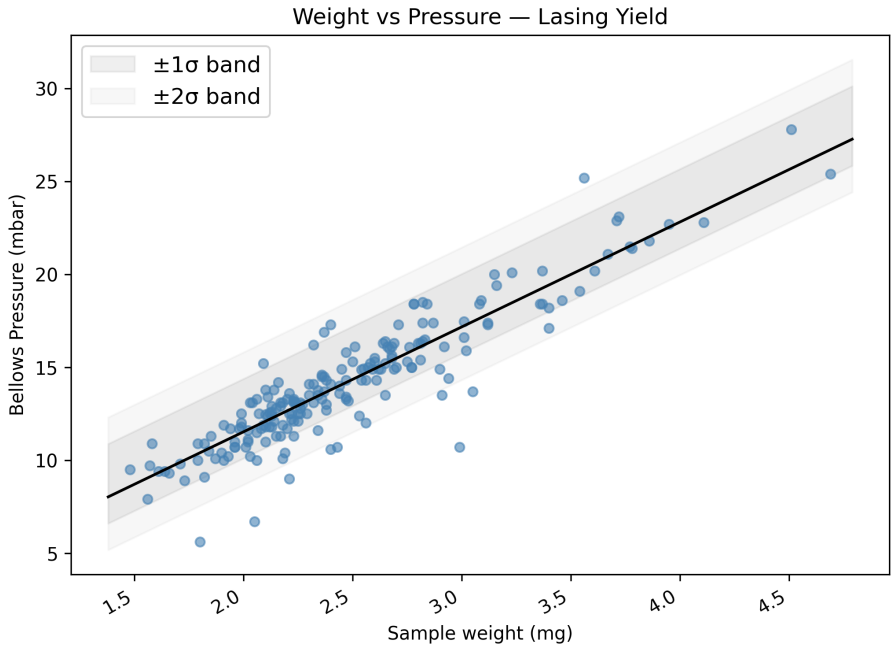


Figure S3.1: Measured bellows pressure (mbar) as a function of sample weight (mg) for all analyses in this study. The solid line is the best fit linear regression model. Shaded bands mark $\pm 1\sigma$ and $\pm 2\sigma$ prediction intervals. Analyses lying outside the $\pm 2\sigma$ band may indicate incomplete fluorination, a gas-handling leak, or other analytical problems, and were excluded from the final data reduction.

characterizes the magnitude of raw instrumental drift prior to normalization rather than post-correction residuals — was ±0.303,‰ for δ^{18}O and ±0.155,‰ for δ^{17}O ($n_{\text{sess}} = 45$; $n_{\text{repl}} = 342$).

Triple oxygen isotope performance was evaluated using Δ'^{17}O. SCO analyses yielded a count-weighted mean Δ'^{17}O of −0.0534,‰, indistinguishable from the accepted reference composition (*Sharp and Wostbrock*, 2021), with a long-term count-weighted external reproducibility of ±0.010,‰ (1σ; $n_{\text{sess}} = 31$). This value is adopted as the uncertainty on Δ'^{17}O for unknown samples throughout this study. Although the external reproducibilities on δ^{18}O and δ^{17}O are large (~0.17–0.33,‰), the Δ'^{17}O uncertainty is substantially smaller because δ'^{17}O and δ'^{18}O co-vary nearly proportionally from session to session ($r \approx 0.999$), reflecting mass-dependent in-

strumental drift. Under standard error propagation,

$$\sigma^2(\Delta'^{17}\mathrm{O}) = \sigma^2(\delta'^{17}\mathrm{O}) + 0.528^2, \sigma^2(\delta'^{18}\mathrm{O}) - 2 \times 0.528, \mathrm{cov}(\delta'^{17}\mathrm{O}, , \delta'^{18}\mathrm{O}); \tag{S3.4}$$

the large positive covariance term nearly cancels the individual variance contributions, yielding $\sigma(\Delta'^{17}\mathrm{O}) \ll \sigma(\delta'^{17}\mathrm{O})$.

C. Calculation of weathering products

Unmixing of mineral components from siliciclastic sediment data compilation

Bulk major-element compositions of siliciclastic sediments were compiled from the SGP database and supplemented with Archean–Proterozoic datasets not included in SGP. Only samples with complete major oxide analyses (SiO_2, Al_2O_3, FeO, MgO, CaO, Na_2O, K_2O) were retained. Oxide concentrations were converted and normalized to molar abundances for subsequent processing.

To quantify the distribution of detrital and weathering-derived minerals through time, bulk compositions were unmixed into contributions from a library of mineral endmembers (quartz, K-feldspar, plagioclase, kaolinite, illite, chlorite, smectite). For each Monte Carlo composition $\mathbf{y}^{(k)}$, we solved for the mineral fractions $\mathbf{x}^{(k)}$ under the constraints that all fractions are non-negative and sum to unity:

$$\mathbf{A}\mathbf{x}^{(k)} \approx \mathbf{y}^{(k)}, \qquad x_i^{(k)} \geq 0, \ \sum_i x_i^{(k)} = 1,$$

where $\mathbf{A}$ is the matrix of mineral oxide compositions. A projected-gradient non-negative least-squares algorithm was used to obtain a stable solution for each Monte Carlo draw.

For every mineral i, the oxygen content per gram was computed from its oxide stoichiometry. Oxygen-normalized mineral fractions were therefore:

$$X_i^{\mathrm{O},(k)} = \frac{x_i^{(k)} O_i}{\sum_j x_j^{(k)} O_j},$$

and represent the fraction of the whole-rock oxygen inventory residing in each phase. These values are used throughout the isotope mass balance, because oxygen—not mineral mass—is conserved in triple-oxygen mixing.

Mineral–water fractionation for weathering products

Only clay minerals are considered to participate in isotopic exchange with surface waters during surface weathering. Mineral–water oxygen-isotope fractionation for clay minerals is conventionally expressed as a function of temperature as a polynomial of the form:

$$10^3 \ln \alpha_{18} = \frac{A}{T^2} + \frac{B}{T}, \qquad T \text{ in Kelvin}, \tag{S3.5}$$

where the parameters A and B are mineral-specific constants derived from experimental or theoretical calibrations.

We assume that the composite weathering product in siliciclastic rocks follows the same functional form. Accordingly, we obtained the temperature-dependent fractionation factor for the weathering product relative to water as a linear combination of the endmember mineral fractionation curves weighted by their oxygen-normalized proportions, X_i^{O}:

$$\left(10^3 \ln \alpha_{18}\right)_{\mathrm{wp-H_2O}} = \sum_{i \in \mathrm{wp}} X_i^{\mathrm{O}} \left(\frac{A_i}{T^2} + \frac{B_i}{T}\right), \tag{S3.6}$$

where the set of contributing minerals consists of kaolinite, smectite, illite, and chlorite (*Savin and Lee*, 1988; *Zheng*, 1993; *Sharp et al.*, 2016). The ensemble of draws provides the mean and standard deviation of the A and B parameters for wp-H_2O fractionation for each geologic time window considered.

Isotopic mass balance for weathering products

Bulk siliciclastic sediments were assumed to consist of feldspar, detrital quartz, and clay minerals. Let the fraction of each of these components be:

$$x_{\mathrm{fps}},\ x_{\mathrm{qtz}},\ x_{\mathrm{clay}}, \qquad x_{\mathrm{fps}} + x_{\mathrm{qtz}} + x_{\mathrm{clay}} = 1.$$

The $\delta'^{18}\mathrm{O}$ of the weathering product is:

$$\delta'^{18}\mathrm{O}_{\mathrm{wp}} = \frac{\delta'^{18}\mathrm{O}_{\mathrm{bulk}} - x_{\mathrm{fps}}\, \delta'^{18}\mathrm{O}_{\mathrm{fps}} - x_{\mathrm{qtz}}\, \delta'^{18}\mathrm{O}_{\mathrm{qtz}}}{x_{\mathrm{clay}}}. \tag{S3.7}$$

To account for the uncertainty in feldspar and detrital quartz in our temperature inversion algorithm, for each Monte Carlo run, we draw $\delta'^{18}O$ quartz taken from magmatic rocks from *Bindeman* (2021) (i.e., 10.5 ± 2.04‰) and feldspar (assumed

to be the same as Archean TTGs) from *Rumble et al.* (2013) (i.e., 6.74 ± 0.78‰). The corresponding $\delta'^{17}O$ values for each $\delta'^{18}O$ draw were estimated using fixed slopes (0.524 for quartz; 0.532 for feldspar) and intercepts (-0.020 for quartz; -0.082 for feldspar) estimated from the source dataset:

$$\delta'^{17}\mathrm{O}_{\mathrm{fps}} = m_{\mathrm{fps}}\,\delta'^{18}\mathrm{O}_{\mathrm{fps}} + b_{\mathrm{fps}}, \tag{S3.8}$$

$$\delta'^{17}\mathrm{O}_{\mathrm{qtz}} = m_{\mathrm{qtz}}\,\delta'^{18}\mathrm{O}_{\mathrm{qtz}} + b_{\mathrm{qtz}}. \tag{S3.9}$$

The resulting weathering product triple-oxygen composition is

$$\Delta'^{17}\mathrm{O}_{\mathrm{wp}} = \delta'^{17}\mathrm{O}_{\mathrm{wp}} - \lambda_{\mathrm{ref}}\,\delta'^{18}\mathrm{O}_{\mathrm{wp}}, \qquad \lambda_{\mathrm{ref}} = 0.528. \tag{S3.10}$$

D. Triple-oxygen composition of the sedimentary protolith

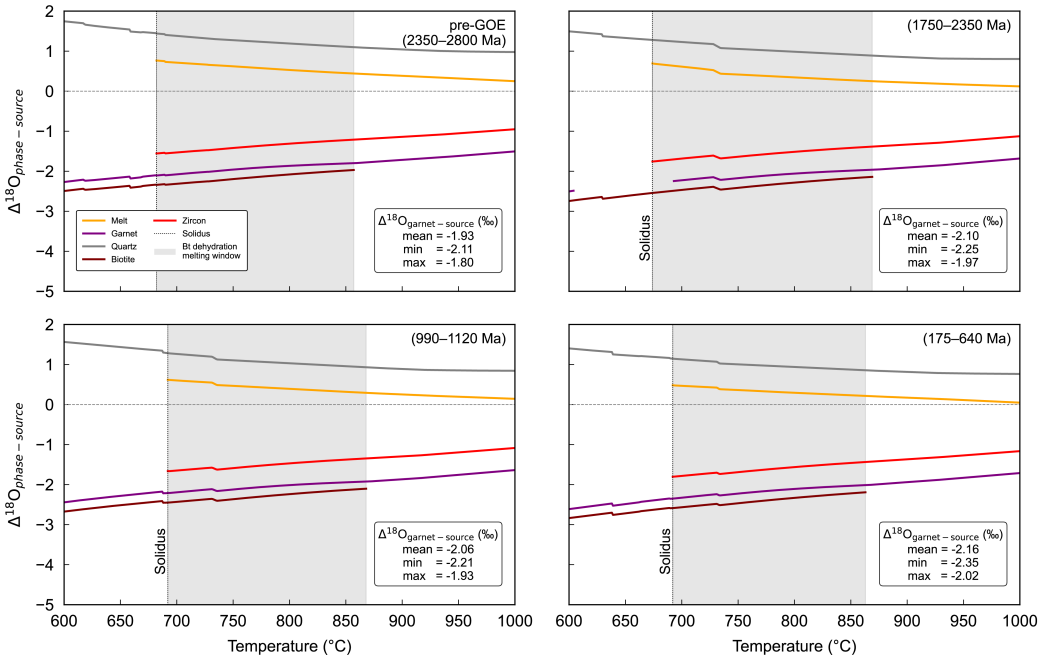


Figure S3.2: Modeled Δ^{18}O fractionation between phases produced during anatexis and sedimentary protoliths. The protolith compositions correspond to mean siliciclastic sediments within depositional ages interpreted for the samples in our dataset: pre-GOE **(a)**, post-Huronian glaciation **(b)**, pre-NOE **(c)**, and post-cryogenian data **(d)**. Equilibrium isotope fractionation is calculated following a similar approach as *Bucholz and Hernández-Montenegro* (2025), using the database of *Vho et al.* (2019).

Measured isotopic compositions for garnet were converted to an estimated bulk metasedimentary source composition using fractionation factors obtained from

phase equilibria modeling for $\delta'^{18}O$ (see Section S2). A fractionation factor between garnet and the source protolith ($\Delta_{grt-source}$) during anatexis was obtained as the average fractionation between the solidus (680 °C) and the field of biotite dehydration (870 °C), yielding values of -1.93 ‰, -2.10 ‰, -2.06 ‰, and -2.16 ‰, for time intervals considered (Supplementary Figure S3.2). This temperature range represents the field of dehydration melting, where most strongly peraluminous melts are inferred to generate (*Bucholz*, 2025).

The $\delta'^{17}O$ values for modeled garnet compositions were determined from linear regression of our garnet triple isotope measurements:

$$\delta'^{17}O_{grt} = m\,\delta'^{18}O_{grt} + b$$

where $m = 0.5232$ and $b = -0.024$ ($r^2 = 0.99$).

Consequently, the compositions of $\delta'^{18}O$ and $\delta'^{17}O$ for the sedimentary source of the SPG melts were obtained as:

$$\delta'^{18}O_{bulk} = \delta'^{18}O_{grt} + \Delta_{grt-source}, \tag{S3.11}$$

$$\delta'^{17}O_{bulk} = \delta'^{17}O_{grt} + (m\Delta_{grt-source} + b). \tag{S3.12}$$

And:

$$\Delta'^{17}O_{bulk} = \delta'^{17}O_{bulk} - 0.528\,\delta'^{18}O_{bulk}. \tag{S3.13}$$

We also considered that oxygen-isotope fractionation during metamorphism was negligible, as shown in previous studies (e.g., *Bindeman*, 2021; *Valley*, 1986; *Zheng et al.*, 2003).

E. Temperature inversion from triple-oxygen isotopes

In equilibrium mass-dependent fractionation, oxygen isotope ratios are related by:

$$\alpha_{17} = \alpha_{18}^{\theta}, \tag{S3.14}$$

where α_{17} and α_{18} are the fractionation factors for $^{17}O/^{16}O$ and $^{18}O/^{16}O$, respectively, and θ describes the mass dependence of fractionation (*Dauphas and Schauble*, 2016).

Using the definition of linearized isotope notation, this relationship can be written

as:

$$\delta'^{17}\mathrm{O} = \theta\,\delta'^{18}\mathrm{O}. \tag{S3.15}$$

Thus, θ is defined as the slope of equilibrium fractionation trajectories in δ'^{17}O–δ'^{18}O space:

$$\theta = \frac{d\,\delta'^{17}\mathrm{O}}{d\,\delta'^{18}\mathrm{O}}. \tag{S3.16}$$

Experimental and theoretical studies show that θ can be parameterized as a temperature-dependent function:

$$\theta(T) = 0.5305 - \frac{s}{T}, \qquad s = 2.24, \tag{S3.17}$$

where T is the temperature in Kelvin and the parameter s is appropriate for the clay–water system (*Pack and Herwartz*, 2014).

Modeled triple-oxygen fractionation for the weathering product is then:

$$\Delta'^{17}\mathrm{O}_{\mathrm{wp}}(T) = \left(10^3 \ln \alpha_{18}(T)\right) \left[\theta(T) - \lambda_{\mathrm{ref}}\right]. \tag{S3.18}$$

The weathering temperature T can therefore be obtained by minimizing the misfit between solutions for equation S3.18 and equation S3.10:

$$T = \arg\min_{T} \left[\Delta'^{17}\mathrm{O}_{\mathrm{wp}}(T) - \Delta'^{17}\mathrm{O}_{\mathrm{wp,obs}}\right]^2. \tag{S3.19}$$

where the temperature in equation S3.18 is obtained from a grid search from −10 to 300 °C, which ensures stable convergence of the algorithm.

F. Reconstruction of δ'^{18}O, δ'^{17}O, and Δ'^{17}O compositions of weathering waters

Once a solution for T was found, the water δ'^{18}O composition was estimated as follows:

$$\delta'^{18}\mathrm{O}_{\mathrm{water}} = \delta'^{18}\mathrm{O}_{\mathrm{wp}} - \left(10^3 \ln \alpha_{18}(T)\right). \tag{S3.20}$$

The meteoric-water line (MWL) is normally expressed as:

$$\delta'^{17}\mathrm{O}_{\mathrm{water}} = \lambda_{\mathrm{MWL}}\,\delta'^{18}\mathrm{O}_{\mathrm{water}} + \gamma_{\mathrm{MWL}}, \tag{S3.21}$$

with $\lambda_{\mathrm{MWL}} = 0.528$ and $\gamma_{\mathrm{MWL}} = 0.033$ (*Luz and Barkan*, 2010), unless otherwise specified.

The final triple-oxygen value of the weathering water was obtained as:

$$\Delta'^{17}O_{water} = \delta'^{17}O_{water} - \lambda_{ref}\,\delta'^{18}O_{water} \tag{S3.22}$$

G. Monte-Carlo uncertainty propagation

A total of $N = 10^5$ Monte Carlo iterations were performed to ensure convergence of the calculated means and associated uncertainties. Each iteration samples uncertainties in:

- mineral abundances and oxygen fractions,
- mineral–water fractionation parameters (A, B),
- feldspar and quartz $\delta'^{18}O$.

For each run, we computed:

$$T,\ \delta'^{18}O_{wp},\ \delta'^{17}O_{wp},\ \Delta'^{17}O_{wp},\ \delta'^{18}O_{water},\ \delta'^{17}O_{water},\ \Delta'^{17}O_{water}.$$

Reported values represent Monte-Carlo means and 1σ uncertainties.

S3. PHASE EQUILIBRIUM MODELING

A. Phase equilibrium calculations

Phase equilibrium modeling was performed to estimate mineral and melt proportions, as well as bulk and phase-specific compositions, during partial melting of metasedimentary rocks. Calculations were conducted using the software `Theriak-Domino` (*de Capitani and Petrakakis*, 2010). We considered the compositional system MnO – Na_2O – K_2O – CaO – FeO – MgO – Al_2O_3 – SiO_2 – H_2O – TiO_2 –O_2 (MnNKCFMASHTO), appropriate for modeling anatexis of metapelitic rocks (*White et al.*, 2014b).

All thermodynamic calculations used the internally-consistent dataset of *Holland and Powell* (2011) together with published activity–composition (*a–x*) models for the major solid-solution phases involved in partial melting of metapelites: biotite (Bt), garnet (Grt), cordierite (Crd), orthopyroxene (Opx), and staurolite (St) (*White et al.*, 2014b); white mica (Ms) and silicate melt (Melt) (*White et al.*, 2014a); ilmenite–hematite (Ilm–Hem) (*White et al.*, 2000); spinel–magnetite (Spl–Mag)

(*White et al.*, 2002); plagioclase (Pl) and K-feldspar (Kfs) (*Holland and Powell*, 2003); and epidote (Ep) (*Holland and Powell*, 2011). Pure phases considered include quartz (Qtz), rutile (Rt), titanite (Ttn), sillimanite (Sil), andalusite (And), kyanite (Ky), and an H_2O fluid. Mineral abbreviations follow *Warr* (2021).

Calculations were performed at 0.75 GPa and temperatures between 600 and 1000°C. Partial melting was modeled under minimally water-saturated conditions (i.e., <0.5 mol% H_2O at the solidus), which avoids unconstrained increases in melt productivity associated with fluid-present melting. We also considered an initial $Fe^{+3}/\Sigma Fe$ ratio of 0.2, which is close to the average value for metapelitic rocks (*Forshaw and Pattison*, 2021).

B. Equilibrium oxygen-isotope fractionation

Results from phase equilibrium modeling were used to compute temperature-dependent oxygen isotope fractionation among all stable phases during anatexis using a similar approach as that implemented in *Bucholz and Hernández-Montenegro* (2025). Fractionation between quartz and any pure phase j was calculated following *Vho et al.* (2019):

$$10^3 \ln \alpha_{\mathrm{qtz}-j} = \left(\frac{A_{\mathrm{qtz}-j}}{T^2}\right) + \left(\frac{B_{\mathrm{qtz}-j}}{T}\right) + C_{\mathrm{qtz}-j}, \tag{S3.23}$$

where T is the temperature in Kelvin, and A, B, and C are endmember-specific coefficients. Because

$$10^3 \ln \alpha_{\mathrm{qtz}-j} \approx \Delta^{18}\mathrm{O}_{\mathrm{qtz}-j} = \delta'^{18}\mathrm{O}_{\mathrm{qtz}} - \delta'^{18}\mathrm{O}_j,$$

equation S3.23 provides the temperature-dependent difference in $\delta'^{18}O$ between quartz and phase j.

For any solid solution s, the bulk quartz–s fractionation was approximated as the oxygen-weighted sum of its k endmembers:

$$\delta'^{18}\mathrm{O}_{\mathrm{qtz}} - \delta'^{18}\mathrm{O}_s \approx \sum_k \left[\left(\frac{A_{\mathrm{qtz}-k}}{T^2} + \frac{B_{\mathrm{qtz}-k}}{T} + C_{\mathrm{qtz}-k}\right) X_{k,s} \frac{N_{k,s}}{N_s}\right], \tag{S3.24}$$

where $X_{k,s}$ is the mole fraction of endmember k in s, $N_{k,s}$ is the oxygen fraction contributed by endmember k, and N_s is the total oxygen fraction of the solid solution.

Because the melt phase is described in the a–x model using fictive endmembers not present in the isotopic database, its oxygen isotope fractionation was calculated by treating the melt as a normative mixture of minerals, using its mineral-normative composition (in mol.%) as the set of $X_{k,s}$ terms. Biotite, cordierite, and staurolite were treated as pure phases because several of their thermodynamic endmembers are absent from the fractionation database. For endmembers missing from the database, we adopted coefficients from structurally and compositionally analogous species or used averaged values when appropriate.

A complete list of solid-solution endmembers and their assigned A, B, and C coefficients is provided in Supplementary Table S1. Fractionation parameters for pure phases appear in Supplementary Table S2.

With Δ^{18}O values established for all minerals relative to quartz, the δ^{18}O of each phase at a given T was obtained assuming closed-system behavior and bulk oxygen-isotope mass balance:

$$p^i_{\text{eff}} = \frac{X^i_{\text{O}}\, p^i_{\text{molar}}}{\sum_n X^n_{\text{O}}\, p^n_{\text{molar}}}, \tag{S3.25}$$

where X^i_{O} is the oxygen fraction of phase i, p^i_{molar} its molar proportion, and the sum is over all stable phases at that P–T condition. These oxygen-effective proportions were used to distribute the bulk-rock δ^{18}O among the mineral assemblage.

SUPPLEMENTARY TABLES

Table S1. Endmember definitions and assumed equivalent mineral endmembers.

Solution	Endmember in a–x model	Formula	Endmember in O frac. database	A	B	C
Melt	qL	Si_4O_8	Quartz	0	0	0
	abL	$NaAlSi_3O_8$	Albite	0.33	0.53	0
	kspL	$KAlSi_3O_8$	Orthoclase	0.19	1.08	0
	anL	$CaAl_2Si_2O_8$	Anorthite	0.71	1.13	0
	silL	$Al_2Si_1.6O_8$	Corundum	2.98	5.54	0
	foL	$Mg_2Si_2O_8$	Forsterite	1.50	2.84	0
	faL	$Fe_4Si_2O_8$	Fayalite	1.20	3.03	0
	h_2oL	H_2O	Olivine	1.35	2.94	0
			Diopside	1.03	1.74	0
Biotite	phl	$KMg_3AlSi_3O_{11}(OH)_2$	Biotite	0.90	2.67	0
	ann	$KFe_3AlSi_3O_{11}(OH)_2$	Biotite	0.90	2.67	0
	fbi	$KMg_2Fe(III)Al_2Si_2O_{11}(OH)_2$	Biotite	0.90	2.67	0
	mnbi	$KMn_3AlSi_3O_{11}(OH)_2$	Biotite	0.90	2.67	0
	obi	$KMg_2FeAlSi_3O_{11}(OH)_2$	Biotite	0.90	2.67	0
	east	$KMg_2Al_3Si_2O_{11}(OH)_2$	Biotite	0.90	2.67	0

Table S1 (continued). Endmember definitions and assumed equivalent mineral endmembers.

Solution	Endmember in a–x model	Formula	Endmember in O frac. database	A	B	C
Cordierite	crd	$Mg_2Al_4Si_5O_{18}$	Cordierite	0.66	1.58	0
	hcrd	$Mg_2Al_4Si_5O_{17}(OH)_2$	Cordierite	0.66	1.58	0
	fcrd	$Fe_2Al_4Si_5O_{18}$	Cordierite	0.66	1.58	0
	mncrd	$Mn_2Al_4Si_5O_{18}$	Cordierite	0.66	1.58	0
Garnet	alm	$Fe_3Al_2Si_3O_{12}$	Almandine	1.29	1.98	0
	gr	$Ca_3Al_2Si_3O_{12}$	Grossular	1.37	1.91	0
	kho	$Mg_3Fe(III)_2Si_3O_{12}$	Andradite	1.17	2.35	0
	py	$Mg_3Al_2Si_3O_{12}$	Pyrope	1.18	2.39	0
	spss	$Mn_3Al_2Si_3O_{12}$	Spessartine	1.29	2.04	0
Feldspar	abh	$NaAlSi_3O_8$	Albite	0.33	0.53	0
	an	$CaAl_2Si_2O_8$	Anorthite	0.71	1.13	0
	san	$KAlSi_3O_8$	Orthoclase	0.19	1.08	0
Epidote	cz	$Ca_2Al_3Si_3O_{12}(OH)$	Zoisite	0.81	1.82	0
	ep	$Ca_2Fe(III)Al_2Si_3O_{12}(OH)$	Epidote	0.57	2.23	0
	fep	$Ca_2Fe(II)_2Al_2Si_3O_{12}(OH)$	Epidote	0.57	2.23	0

Table S1 (continued). Endmember definitions and assumed equivalent mineral endmembers.

Solution	Endmember in a–x model	Formula	Endmember in O frac. database	A	B	C
Muscovite	cel	$KMgAlSi_4O_{10}(OH)_2$	Glauconite	0.84	1.82	0
	fcel	$KFeAlSi_4O_{10}(OH)_2$	Glauconite	0.84	1.82	0
	fmu	$KFe(III)Al_2Si_3O_{10}(OH)_2$	Muscovite	0.85	1.06	0
	ma	$CaAl_4Si_2O_{10}(OH)_2$	Margarite	0.51	2.06	0
	pa	$NaAl_3Si_3O_{10}(OH)_2$	Paragonite	0.62	1.55	0
Orthopyroxene	en	$Mg_2Si_2O_6$	Enstatite	0.76	2.23	0
	fm	$MgFeSi_2O_6$	Hypersthene	0.74	2.19	0
	fopx	$MgFe(III)AlSiO_6$	Hypersthene	0.74	2.19	0
	fs	$Fe_2Si_2O_6$	Ferrosilite	0.72	2.15	0
	mgts	$MgAl_2SiO_6$	Enstatite	0.76	2.23	0
	mnopx	$Mn_2Si_2O_6$	Ferrosilite	0.72	2.15	0
Spinel	herc	$FeAl_2O_4$	Hercinite	3.05	4.81	0
	mt	$FeFe(III)_2O_4$	Magnetite	2.34	4.00	0
	sp	$MgAl_2O_4$	Spinel	3.25	4.85	0
	usp	Fe_2TiO_4	Ulvospinel	2.46	4.27	0

Table S1 (continued). Endmember definitions and assumed equivalent mineral endmembers.

Solution	Endmember in a–x model	Formula	Endmember in O frac. database	A	B	C
Ilmenite	dilm	$FeTiO_3$	Ilmenite	2.37	4.17	0
	geik	$MgTiO_3$	Geikielite	2.49	4.32	0
	hem	Fe_2O_3	Hematite	1.32	5.86	0
	oilm	$FeTiO_3$	Ilmenite	2.37	4.17	0
	pnt	$MnTiO_3$	Ilmenite	2.37	4.17	0
Staurolite	fst	$Fe_4Al_{18}Si_{7.5}O_{44}(OH)_4$	Staurolite	0.46	2.25	0
	mnst	$Mn_4Al_{18}Si_{7.5}O_{44}(OH)_4$	Staurolite	0.46	2.25	0
	mst	$Mg_4Al_{18}Si_{7.5}O_{44}(OH)_4$	Staurolite	0.46	2.25	0
	msto	$Mg_4Fe(III)_2Al_{16}Si_{7.5}O_{44}(OH)_4$	Staurolite	0.46	2.25	0

Table S2. Coefficients for pure phases.

Pure phase	A	B	C
Quartz	0	0	0
Rutile	1.50	3.68	0
Titanite	1.05	2.41	0
Sillimanite	0.06	1.91	0
Andalusite	0.33	1.72	0
Kyanite	0.40	1.87	0
H_2O	4.11	−3.39	0

Table S3: Triple oxygen isotope compositions of S-type granites, leucosomes, and diatexites analyzed in this study.

Sample	Location	Rock type	Age (Ma)	n	$\delta^{18}O$ (‰)	$\delta^{17}O$ (‰)	$\delta'^{18}O$ (‰)	$\delta'^{17}O$ (‰)	$\Delta'^{17}O$ (‰)
VM24-02	Peninsular Range	Granite	165	3	10.393	5.393	10.339	5.378	-0.081
VM24-04	Peninsular Range	Granite	165	2	9.895	5.129	9.847	5.116	-0.083
G-1	Variscan, Hercynian orogeny	Leucosome	320	3	9.126	4.754	9.085	4.742	-0.054
VIN-203	Sierras Pampeanas	Granite	346	3	8.278	4.291	8.244	4.282	-0.071
ANI-400	Sierras Pampeanas	Granite	354	3	9.397	4.891	9.353	4.879	-0.059
GRA-CB	Sierras Pampeanas	Granite	370	3	10.008	5.181	9.958	5.168	-0.090
ASP-401	Sierras Pampeanas	Granite	469	3	7.598	3.933	7.569	3.925	-0.071
DIA-J23-2	Sierras Pampeanas	Diatexite	525	3	11.062	5.743	11.001	5.726	-0.082
DIA-J23-LEU	Sierras Pampeanas	Leucosome	525	5	11.392	5.915	11.328	5.898	-0.083
GZN-84	Garzon Massif, Colombia	Leucosome	992	3	8.190	4.253	8.157	4.244	-0.063
GZN-81	Garzon Massif, Colombia	Leucosome	992	3	8.222	4.283	8.188	4.274	-0.050
GZN-77	Garzon Massif, Colombia	Leucosome	992	2	7.122	3.696	7.097	3.690	-0.058

Continued on next page

Table S3 – *continued*

Sample	Location	Rock type	Age (Ma)	*n*	$\delta^{18}O$ (‰)	$\delta^{17}O$ (‰)	$\delta'^{18}O$ (‰)	$\delta'^{17}O$ (‰)	$\Delta'^{17}O$ (‰)
GZN-75	Garzon Massif, Colombia	Leucosome	992	3	7.297	3.792	7.271	3.785	-0.054
GZN-65	Garzon Massif, Colombia	Leucosome	992	3	8.163	4.241	8.130	4.232	-0.061
GZN-64	Garzon Massif, Colombia	Leucosome	992	3	7.222	3.750	7.196	3.743	-0.056
GZN-49	Garzon Massif, Colombia	Leucosome	992	3	6.032	3.138	6.014	3.133	-0.042
GZN-48	Garzon Massif, Colombia	Leucosome	992	3	6.100	3.167	6.081	3.162	-0.049
GZN-25	Garzon Massif, Colombia	Leucosome	992	2	6.010	3.125	5.992	3.120	-0.043
HP-46A	Black Hills, South Dakota	Granite	1715	3	10.735	5.579	10.678	5.564	-0.074
SD-18-11	Black Hills, South Dakota	Granite	1715	10	11.917	6.197	11.847	6.177	-0.078
SD-18-14	Black Hills, South Dakota	Granite	1715	2	9.479	4.928	9.435	4.916	-0.065
SD-18-15	Black Hills, South Dakota	Granite	1715	5	9.473	4.926	9.428	4.914	-0.065
SD-18-18	Black Hills, South Dakota	Granite	1715	2	9.577	4.976	9.531	4.964	-0.069
17-FIN-06A	Finland	Leucosome	1815	3	9.272	4.808	9.229	4.797	-0.077
17-FIN-05B	Finland	Leucosome	1836	3	10.057	5.225	10.007	5.212	-0.072
17-FIN-01B	Finland	Leucosome	1850	3	9.652	5.012	9.606	4.999	-0.073

Continued on next page

Table S3 – *continued*

Sample	Location	Rock type	Age (Ma)	*n*	$\delta^{18}O$ (‰)	$\delta^{17}O$ (‰)	$\delta'^{18}O$ (‰)	$\delta'^{17}O$ (‰)	$\Delta'^{17}O$ (‰)
SAB-82-Z29B	Hepburn Batholith	Granite	1885	3	7.510	3.903	7.482	3.895	-0.055
SAB-82-V27	Hepburn Batholith	Granite	1885	3	8.398	4.360	8.363	4.351	-0.065
SAB-81-S55	Hepburn Batholith	Granite	1885	3	7.928	4.104	7.896	4.096	-0.074
SAB-81-L54A	Hepburn Batholith	Granite	1885	4	8.415	4.366	8.380	4.356	-0.068
SAB-81-S65	Hepburn Batholith	Granite	1885	3	8.453	4.380	8.418	4.371	-0.074
18-IM-10B	North China Craton	Granite	1901	3	10.361	5.400	10.308	5.386	-0.057
18-IM-11B	North China Craton	Granite	1901	3	10.169	5.291	10.118	5.277	-0.066
18-IM-12B	North China Craton	Granite	1929	3	9.947	5.173	9.898	5.160	-0.066
18-IM-23D	North China Craton	Granite	2453	5	6.738	3.491	6.715	3.485	-0.061
WY-18-10	Wyoming Craton	Granite	2547	3	8.031	4.153	7.999	4.145	-0.079
WY-18-11	Wyoming Craton	Granite	2547	4	6.761	3.512	6.738	3.506	-0.052
WY-18-12	Wyoming Craton	Granite	2547	3	7.242	3.732	7.216	3.725	-0.085
WY-18-4	Wyoming Craton	Granite	2547	2	7.499	3.889	7.471	3.882	-0.063
SP-17-33	Superior Province	Granite	2646	2	8.045	4.178	8.013	4.169	-0.062

Continued on next page

Table S3 – *continued*

Sample	Location	Rock type	Age (Ma)	*n*	$\delta^{18}O$ (‰)	$\delta^{17}O$ (‰)	$\delta'^{18}O$ (‰)	$\delta'^{17}O$ (‰)	$\Delta'^{17}O$ (‰)
SP-17-26	Superior Province	Granite	2650	2	6.514	3.394	6.493	3.389	-0.040
SP-17-82	Superior Province	Granite	2650	12	5.629	2.907	5.613	2.903	-0.061
SP-17-76	Superior Province	Granite	2650	2	6.849	3.548	6.826	3.542	-0.062
SP-17-74	Superior Province	Granite	2650	2	6.618	3.451	6.597	3.445	-0.038
SP-17-52	Superior Province	Granite	2650	2	7.223	3.762	7.197	3.755	-0.045
SP-17-13	Superior Province	Granite	2650	2	6.866	3.565	6.843	3.558	-0.055
SP-17-38	Superior Province	Granite	2650	2	6.899	3.586	6.875	3.579	-0.051
SP-17-37	Superior Province	Granite	2650	2	6.449	3.350	6.429	3.344	-0.050
SP-17-36	Superior Province	Granite	2650	2	7.745	4.038	7.715	4.030	-0.044
SP-17-39	Superior Province	Granite	2650	3	6.338	3.264	6.318	3.258	-0.077
SP-16-33	Superior Province	Granite	2654	2	7.541	3.915	7.513	3.907	-0.059
SP-16-51	Superior Province	Granite	2671	2	6.737	3.509	6.715	3.503	-0.043
SP-16-52	Superior Province	Granite	2671	21	6.074	3.160	6.055	3.155	-0.042
SP-16-46	Superior Province	Granite	2671	3	6.956	3.600	6.932	3.594	-0.066

Continued on next page

Table S3 – *continued*

Sample	Location	Rock type	Age (Ma)	n	$\delta^{18}O$ (‰)	$\delta^{17}O$ (‰)	$\delta'^{18}O$ (‰)	$\delta'^{17}O$ (‰)	$\Delta'^{17}O$ (‰)
SP-17-43	Superior Province	Granite	2690	3	7.187	3.709	7.162	3.702	-0.079

Reference material performance statistics (1σ):

Standard	n_{sess}	n_{repl}	$\delta^{18}O$ (‰)	$\delta^{17}O$ (‰)	$\delta'^{18}O$ (‰)	$\delta'^{17}O$ (‰)	$\Delta'^{17}O$ (‰)
UWG-2, within-analysis repeatability	45	342	±0.0121	±0.0118	±0.0121	±0.0118	—
UWG-2, external reproducibility (count-weighted)	45	342	±0.303	±0.155	±0.303	±0.155	—
SCO, external reproducibility (count-weighted)	31	51	±0.328	±0.169	±0.328	±0.169	±0.010

References

Alasino, P. H., J. A. Dahlquist, C. Galindo, C. Casquet, and J. Saavedra, Andalusite and Na-and Li-rich cordierite in the La Costa pluton, Sierras Pampeanas, Argentina: Textural and chemical evidence for a magmatic origin, *International Journal of Earth Sciences*, *99*(5), 1051–1065, 2010.

Bea, F., P. G. Montero, F. Gonzalez-Lodeiro, C. Talavera, J. F. Molina, J. H. Scarrow, M. J. Whitehouse, and T. Zinger, Zircon thermometry and U–Pb ion-microprobe dating of the gabbros and associated migmatites of the Variscan Toledo Anatectic Complex, Central Iberia, *Journal of the Geological Society*, *163*(5), 847–855, doi:10.1144/0016-76492005-143, 2006.

Bindeman, I. N., Triple Oxygen Isotopes in Evolving Continental Crust, Granites, and Clastic Sediments, *Reviews in Mineralogy and Geochemistry*, *86*(1), 241–290, doi:10.2138/rmg.2021.86.08, 2021.

Bowring, S. A., and J. P. Grotzinger, Implications of new chronostratigraphy for tectonic evolution of Wopmay orogen, northwest Canadian Shield, *American Journal of Science*, *292*(1), 1–20, 1992.

Breaks, F. W., and J. M. Moore, The Ghost Lake Batholith, Superior Province of northwestern Ontario; a fertile, S-type, peraluminous granite-rare-element pegmatite system, *The Canadian Mineralogist*, *30*(3), 835–875, 1992.

Bucholz, C. E., The diversity and origin of granites, in *Treatise on Geochemistry (Third Edition)*, edited by A. Anbar and D. Weis, pp. 153–202, Elsevier, Oxford, doi:10.1016/B978-0-323-99762-1.00006-1, 2025.

Bucholz, C. E., and J. D. Hernández-Montenegro, Temporal variation in oxygen isotopes of peraluminous granites derived from sedimentary sources, *Lithos*, *492–493*, 107,864, doi:10.1016/j.lithos.2024.107864, 2025.

Bucholz, C. E., and C. J. Spencer, Strongly Peraluminous Granites across the Archean–Proterozoic Transition, *Journal of Petrology*, *60*(7), 1299–1348, doi:10.1093/petrology/egz033, 2019.

Castiñeiras, P., C. Villaseca, L. Barbero, and C. Martín Romera, SHRIMP U–Pb zircon dating of anatexis in high-grade migmatite complexes of Central Spain: Implications in the Hercynian evolution of Central Iberia, *International Journal of Earth Sciences*, *97*(1), 35–50, doi:10.1007/s00531-006-0167-6, 2008.

Chamberlain, C. P., and M. E. Conrad, Oxygen Isotope Zoning in Garnet, *Science*, *254*(5030), 403–406, doi:10.1126/science.254.5030.403, 1991.

Dahlquist, J. A., C. Galindo, R. J. Pankhurst, C. W. Rapela, P. H. Alasino, J. Saavedra, and C. M. Fanning, Magmatic evolution of the Peñón Rosado granite: Petrogenesis of garnet-bearing granitoids, *Lithos*, *95*(3), 177–207, doi:10.1016/j.lithos.2006.07.010, 2007.

Dahlquist, J. A., P. H. Alasino, M. A. Basei, M. M. Morales Cámera, M. Macchioli Grande, and M. da Costa Campos Neto, Petrological, geochemical, isotopic, and geochronological constraints for the Late Devonian–Early Carboniferous magmatism in SW Gondwana (27–32 LS): An example of geodynamic switching, *International Journal of Earth Sciences*, *107*(7), 2575–2603, 2018.

Dahlquist, J. A., M. M. Morales Cámera, P. H. Alasino, R. J. Pankhurst, M. A. S. Basei, C. W. Rapela, J. A. Moreno, E. G. Baldo, and C. Galindo, A review of Devonian–Carboniferous magmatism in the central region of Argentina, pre-Andean margin of SW Gondwana, *Earth-Science Reviews*, *221*, 103,781, doi: 10.1016/j.earscirev.2021.103781, 2021.

Dauphas, N., and E. A. Schauble, Mass Fractionation Laws, Mass-Independent Effects, and Isotopic Anomalies, *Annual Review of Earth and Planetary Sciences*, *44*(1), 709–783, doi:10.1146/annurev-earth-060115-012157, 2016.

Davis, D. W., R. H. Sutcliffe, and N. F. Trowell, Geochronological constraints on the tectonic evolution of a late Archaean greenstone belt, Wabigoon Subprovince, Northwest Ontario, Canada, *Precambrian Research*, *39*(3), 171–191, doi:10. 1016/0301-9268(88)90041-1, 1988.

de Capitani, C., and K. Petrakakis, The computation of equilibrium assemblage diagrams with Theriak/Domino software, *American Mineralogist*, *95*(7), 1006–1016, 2010.

Dong, C., Y. Wan, S. A. Wilde, Z. Xu, M. Ma, H. Xie, and D. Liu, Earliest Paleoproterozoic supracrustal rocks in the North China Craton recognized from the Daqingshan area of the Khondalite Belt: Constraints on craton evolution, *Gondwana Research*, *25*(4), 1535–1553, doi:10.1016/j.gr.2013.05.021, 2014.

Ehlers, C., A. Lindroos, and O. Selonen, The late Svecofennian granite-migmatite zone of southern Finland—a belt of transpressive deformation and granite emplacement, *Precambrian Research*, *64*(1), 295–309, doi:10.1016/0301-9268(93) 90083-E, 1993.

Escayola, M. P., M. M. Pimentel, and R. Armstrong, Neoproterozoic backarc basin: Sensitive high-resolution ion microprobe U-Pb and Sm-Nd isotopic evidence from the Eastern Pampean Ranges, Argentina, *Geology*, *35*(6), 495–498, doi: 10.1130/G23549A.1, 2007.

Forshaw, J. B., and D. R. M. Pattison, Ferrous/ferric (Fe2+/Fe3+) partitioning among silicates in metapelites, *Contributions to Mineralogy and Petrology*, *176*(9), 63, doi:10.1007/s00410-021-01814-4, 2021.

Frost, C. D., B. L. Fruchey, K. R. Chamberlain, and B. Ronald Frost, Archean crustal growth by lateral accretion of juvenile supracrustal belts in the south-central Wyoming Province, *Canadian Journal of Earth Sciences*, *43*(10), 1533–1555, 2006.

Germinario, M., The early Mesozoic Julian Schist, Julian, California, in *The Prebatholithic Stratigraphy of Peninsular California*, edited by R. G. Gastil and R. H. Miller, p. 0, Geological Society of America, doi:10.1130/SPE279-p107, 1993.

Havel, R., D. E. Ibarra, R. Bartoschewitz, and G. Budde, Interrogating leaching procedures of meteorites for triple oxygen isotope analyses, *Meteoritics & Planetary Science*, *60*(10), 2311–2333, doi:10.1111/maps.70039, 2025.

Hoffman, P. F., and S. A. Bowring, Short-lived 1.9 ga continental margin and its destruction, wopmay orogen, northwest canada, *Geology*, *12*(2), 68–72, doi:10.1130/0091-7613(1984)12%3C68:SGCMAI%3E2.0.CO;2, 1984.

Holland, T., and R. Powell, Activity–composition relations for phases in petrological calculations: An asymmetric multicomponent formulation, *Contributions to Mineralogy and Petrology*, *145*(4), 492–501, doi:10.1007/s00410-003-0464-z, 2003.

Holland, T. J. B., and R. Powell, An improved and extended internally consistent thermodynamic dataset for phases of petrological interest, involving a new equation of state for solids, *Journal of Metamorphic Geology*, *29*(3), 333–383, doi:10.1111/j.1525-1314.2010.00923.x, 2011.

Hrabi, R. B., and A. R. Cruden, Structure of the Archean English River subprovince: Implications for the tectonic evolution of the western Superior Province, Canada, *Canadian Journal of Earth Sciences*, *43*(7), 947–966, doi:10.1139/e06-023, 2006.

Ibañez–Mejia, M., J. Gómez, and D. Mateus–Zabala, The Putumayo orogen of Amazonia: A synthesis, *The geology of Colombia, Volume 1 Proterozoic-Paleozoic*, 2020.

Ibanez-Mejia, M., J. Ruiz, V. A. Valencia, A. Cardona, G. E. Gehrels, and A. R. Mora, The Putumayo Orogen of Amazonia and its implications for Rodinia reconstructions: New U–Pb geochronological insights into the Proterozoic tectonic evolution of northwestern South America, *Precambrian Research*, *191*(1), 58–77, doi:10.1016/j.precamres.2011.09.005, 2011.

Lalonde, A. E., Hepburn intrusive suite: Peraluminous plutonism within a closing back-arc basin, Wopmay orogen, Canada, *Geology*, *17*(3), 261–264, doi:10.1130/0091-7613(1989)017<0261:HISPPW>2.3.CO;2, 1989.

Li, X.-P., Z. Yang, G. Zhao, R. Grapes, and J. Guo, Geochronology of khondalite-series rocks of the Jining Complex: Confirmation of depositional age and tectonometamorphic evolution of the North China craton, *International Geology Review*, *53*(10), 1194–1211, doi:10.1080/00206810903548984, 2011.

Liebmann, J., C. J. Spencer, C. L. Kirkland, C. Bucholz, X.-F. He, M. Santosh, X. P. Xia, L. Martin, and N. J. Evans, Emergence of continents above sea-level

influences sediment melt composition, *Terra Nova*, p. ter.12531, doi:10.1111/ter.12531, 2021a.

Liebmann, J., C. J. Spencer, C. L. Kirkland, C. E. Bucholz, X.-P. Xia, L. Martin, N. Kitchen, and L. Shumlyanskyy, Coupling sulfur and oxygen isotope ratios in sediment melts across the Archean-Proterozoic transition, *Geochimica et Cosmochimica Acta*, *307*, 242–257, doi:10.1016/j.gca.2021.05.045, 2021b.

Luz, B., and E. Barkan, Variations of 17O/16O and 18O/16O in meteoric waters, *Geochimica et Cosmochimica Acta*, *74*(22), 6276–6286, doi:10.1016/j.gca.2010.08.016, 2010.

Morales Cámera, M. M., J. A. Dahlquist, M. Garcia-Arias, J. A. Moreno, C. Galindo, M. A. Basei, and J. F. Molina, Petrogenesis of the F-rich peraluminous A-type granites: An example from the Devonian Achala batholith (Characato Suite), Sierras Pampeanas, Argentina, *Lithos*, *378*, 105,792, 2020.

Morales Cámera, M. M., J. A. Dahlquist, J. A. Moreno, P. S. Zandomeni, M. Garcia-Arias, and M. A. S. Basei, The Andaluca plutonic unit, Vinquis Intrusive Complex, Argentina: An assessment of mantle role in the genesis of Early Carboniferous weakly peraluminous A-type granites in the pre-Andean SW Gondwana margin, *Lithos*, *434–435*, 106,873, doi:10.1016/j.lithos.2022.106873, 2022.

Nabelek, P. I., C. Russ-Nabelek, and J. R. Denison, The generation and crystallization conditions of the Proterozoic Harney Peak Leucogranite, Black Hills, South Dakota, USA: Petrologic and geochemical constraints, *Contributions to Mineralogy and Petrology*, *110*(2), 173–191, doi:10.1007/BF00310737, 1992.

Orejana, D., C. Villaseca, P. Valverde-Vaquero, E. A. Belousova, and R. A. Armstrong, U–Pb geochronology and zircon composition of late Variscan S- and I-type granitoids from the Spanish Central System batholith, *International Journal of Earth Sciences*, *101*(7), 1789–1815, doi:10.1007/s00531-012-0750-y, 2012.

Pack, A., and D. Herwartz, The triple oxygen isotope composition of the Earth mantle and understanding ΔO17 variations in terrestrial rocks and minerals, *Earth and Planetary Science Letters*, *390*, 138–145, doi:10.1016/j.epsl.2014.01.017, 2014.

Rapela, C. W., S. O. Verdecchia, C. Casquet, R. J. Pankhurst, E. G. Baldo, C. Galindo, J. A. Murra, J. A. Dahlquist, and C. M. Fanning, Identifying Laurentian and SW Gondwana sources in the Neoproterozoic to Early Paleozoic metasedimentary rocks of the Sierras Pampeanas: Paleogeographic and tectonic implications, *Gondwana Research*, *32*, 193–212, doi:10.1016/j.gr.2015.02.010, 2016.

Redden, J. A., ZE. Peterman, RE. Zartman, E. DeWitt, JF. Lewry, and MR. Stauffer, U-Th-Pb geochronology and preliminary interpretation of Precambrian tectonic events in the Black Hills, South Dakota, *The Early Proterozoic Trans-Hudson Orogen of North America: Geological Association of Canada Special Paper*, *37*, 229–251, 1990.

Rumble, D., S. Bowring, T. Iizuka, T. Komiya, A. Lepland, M. T. Rosing, and Y. Ueno, The oxygen isotope composition of earth's oldest rocks and evidence of a terrestrial magma ocean, *Geochemistry, Geophysics, Geosystems*, *14*(6), 1929–1939, doi:10.1002/ggge.20128, 2013.

Savin, SM., and M. Lee, Isotopic studies of phyllosilicates, *Reviews in Mineralogy and Geochemistry*, *19*(1), 189–223, 1988.

Scicchitano, M. R., et al., Oxygen diffusion in garnet: Experimental calibration and implications for timescales of metamorphic processes and retention of primary O isotopic signatures, *American Mineralogist*, *107*(7), 1425–1441, doi:10.2138/am-2022-7970, 2022.

Sharp, Z. D., and J. A. Wostbrock, Standardization for the Triple Oxygen Isotope System: Waters, Silicates, Carbonates, Air, and Sulfates, *Reviews in Mineralogy and Geochemistry*, *86*(1), 179–196, doi:10.2138/rmg.2021.86.05, 2021.

Sharp, Z. D., J. A. Gibbons, O. Maltsev, V. Atudorei, A. Pack, S. Sengupta, E. L. Shock, and L. P. Knauth, A calibration of the triple oxygen isotope fractionation in the SiO2–H2O system and applications to natural samples, *Geochimica et Cosmochimica Acta*, *186*, 105–119, doi:10.1016/j.gca.2016.04.047, 2016.

Shaw, S. E., V. R. Todd, and M. Grove, Jurassic peraluminous gneissic granites in the axial zone of the Peninsular Ranges, southern California, in *Tectonic Evolution of Northwestern Mexico and the Southwestern USA*, edited by S. E. Johnson, S. R. Paterson, J. M. Fletcher, G. H. Girty, D. L. Kimbrough, and A. Martín-Barajas, p. 0, Geological Society of America, doi:10.1130/0-8137-2374-4.157, 2003.

Valley, J. W., Stable isotope geochemistry of metamorphic rocks, *Reviews in Mineralogy and Geochemistry*, *16*(1), 445–489, 1986.

Valley, J. W., N. Kitchen, M. J. Kohn, C. R. Niendorf, and M. J. Spicuzza, UWG-2, a garnet standard for oxygen isotope ratios: Strategies for high precision and accuracy with laser heating, *Geochimica et Cosmochimica Acta*, *59*(24), 5223–5231, doi:10.1016/0016-7037(95)00386-X, 1995.

Vho, A., P. Lanari, and D. Rubatto, An Internally-Consistent Database for Oxygen Isotope Fractionation Between Minerals, *Journal of Petrology*, *60*(11), 2101–2129, doi:10.1093/petrology/egaa001, 2019.

Villaseca, C., L. Barbero, and G. Rogers, Crustal origin of Hercynian peraluminous granitic batholiths of Central Spain: Petrological, geochemical and isotopic (Sr, Nd) constraints, *Lithos*, *43*(2), 55–79, doi:10.1016/S0024-4937(98)00002-4, 1998.

Villaseca, C., H. Downes, C. Pin, and L. Barbero, Nature and Composition of the Lower Continental Crust in Central Spain and the Granulite–Granite Linkage: Inferences from Granulitic Xenoliths, *Journal of Petrology*, *40*(10), 1465–1496, doi:10.1093/petroj/40.10.1465, 1999.

Villaseca, C., D. Orejana, and E. A. Belousova, Recycled metaigneous crustal sources for S- and I-type Variscan granitoids from the Spanish Central System batholith: Constraints from Hf isotope zircon composition, *Lithos*, *153*, 84–93, doi:10.1016/j.lithos.2012.03.024, 2012.

Wang, F., X.-P. Li, H. Chu, and G. Zhao, Petrology and metamorphism of khondalites from the Jining complex, North China craton, *International Geology Review*, *53*(2), 212–229, doi:10.1080/00206810903028144, 2011.

Warr, L. N., IMA–CNMNC approved mineral symbols, *Mineralogical Magazine*, *85*(3), 291–320, doi:10.1180/mgm.2021.43, 2021.

White, Powell, Holland, and Worley, The effect of TiO2 and Fe2O3 on metapelitic assemblages at greenschist and amphibolite facies conditions: Mineral equilibria calculations in the system K2O–FeO–MgO–Al2O3–SiO2–H2O–TiO2–Fe2O3, *Journal of Metamorphic Geology*, *18*(5), 497–511, doi:10.1046/j.1525-1314.2000.00269.x, 2000.

White, R. W., R. Powell, and G. L. Clarke, The interpretation of reaction textures in Fe-rich metapelitic granulites of the Musgrave Block, central Australia: Constraints from mineral equilibria calculations in the system K2O–FeO–MgO–Al2O3–SiO2–H2O–TiO2–Fe2O3, *Journal of Metamorphic Geology*, *20*(1), 41–55, doi:10.1046/j.0263-4929.2001.00349.x, 2002.

White, R. W., R. Powell, T. J. B. Holland, T. E. Johnson, and E. C. R. Green, New mineral activity–composition relations for thermodynamic calculations in metapelitic systems, *Journal of Metamorphic Geology*, *32*(3), 261–286, 2014a.

White, R. W., R. Powell, and T. E. Johnson, The effect of Mn on mineral stability in metapelites revisited: New a–x relations for manganese-bearing minerals, *Journal of Metamorphic Geology*, *32*(8), 809–828, 2014b.

Zheng, Y.-F., Calculation of oxygen isotope fractionation in hydroxyl-bearing silicates, *Earth and Planetary Science Letters*, *120*(3), 247–263, doi:10.1016/0012-821X(93)90243-3, 1993.

Zheng, Y.-F., B. Fu, B. Gong, and L. Li, Stable isotope geochemistry of ultrahigh pressure metamorphic rocks from the Dabie–Sulu orogen in China: Implications for geodynamics and fluid regime, *Earth-Science Reviews*, *62*(1), 105–161, doi:10.1016/S0012-8252(02)00133-2, 2003.

Chapter 4

ESTIMATING PRIMARY MAGMAS FROM MARS WITH PRIMARSMELT: IMPLICATIONS FOR THE PETROGENESIS OF SOME MARTIAN ROCKS AND THE THERMAL EVOLUTION OF MARS

Hernández-Montenegro, J. D., P. D. Asimow, and C. T. Herzberg, Estimating Primary Magmas From Mars With PRIMARSMELT: Implications for the Petrogenesis of Some Martian Rocks and the Thermal Evolution of Mars, *Journal of Geophysical Research: Planets*, *129*(11), e2024JE008,508, doi: 10.1029/2024JE008508,

Author contributions: J.D. Hernández-Montenegro developed the PRIMARSMELT modeling framework under the supervision of P.D. Asimow. J.D. Hernández-Montenegro performed the petrological modeling and thermal evolution analysis, and wrote the manuscript. P.D. Asimow and C.T. Herzberg contributed to conceptual development, interpretation of results, and manuscript revisions., 2024.

Abstract

Primary magmas form by partial melting in the mantle of a terrestrial planet and represent the starting material for building its crust. The compositions of primary magmas are critical for understanding the thermal history of planetary interiors, as they can be used to estimate mantle potential temperatures (T_P) and track changes in the conditions of mantle partial melting over time. Here, we introduce PRIMARSMELT, a new member of the PRIMELT software family, calibrated to estimate the composition of Martian primary magmas and their formation conditions. We applied PRIMARSMELT to a comprehensive database of basaltic compositions from Mars. Our results are consistent with their petrology, requiring olivine addition to restore fractionated compositions to their primary parents and olivine subtraction from cumulate rocks. Individual primary magma solutions provide insights into the petrogenesis of specific Martian meteorites, with implications for the near-primary nature of some primitive meteorites and the relationship between lithologies A and B in meteorite EETA 79001. Taken together, our results suggest nearly constant or potentially increasing mantle potential temperatures throughout the geo-

logical history of Mars. The average T_P for young shergottite meteorites is $\sim 1442 \pm 40\,^{\circ}\mathrm{C}$, similar to ambient mantle temperatures inferred from geophysical models. In contrast, older basaltic rocks record potential temperatures as low as $\sim 1320 \pm 48\,^{\circ}\mathrm{C}$ for igneous clasts in meteorites NWA 7034/7533. We suggest that, rather than plume-related magmatism, shergottite meteorites record ambient mantle temperatures, with the thermal evolution trend possibly resulting from inefficient heat loss, as expected for a planet in stagnant-lid mode.

1. Introduction

Primary magmas are critical to understanding the interiors of rocky bodies, as they represent the primitive material from which the crusts of terrestrial planets are derived (*O'Hara*, 1965; *Mckenzie and Bickle*, 1988). Primary magmas are melts produced during partial melting of the mantle, possibly aggregated, but before any subsequent evolution or differentiation (*O'Hara*, 1965). The pressure-temperature (*P-T*) conditions at which primary magmas form can be estimated from their major element chemistry. Their integrated composition should provide a reasonable estimate of the average initial composition of the crust, both locally and globally (*Herzberg and O'Hara*, 2002; *Herzberg and Asimow*, 2015), before processes such as intracrustal differentiation, delamination of lower crust, and erosion of upper crust begin to systematically modify that average (*Lee et al.*, 2008). From their composition, it is also possible to derive mantle potential temperatures (T_P, the temperature a parcel of mantle would have if it were brought adiabatically to the surface without melting, providing a measure of how hot or cold it is) and variations in the physicochemical conditions of mantle partial melting over time (*Herzberg and O'Hara*, 2002; *Herzberg and Asimow*, 2015). In particular, mantle potential temperatures derived from primary magmas have helped to constrain the thermal history of Earth (*Herzberg et al.*, 2010). However, the existence of primary magmas is essentially a hypothetical construct, as almost all mantle-derived melts experience some degree of magmatic differentiation before eruption or crustal emplacement. Processes such as fractional crystallization, accumulation of crystals in the melt, and assimilation of pre-existing crust are all likely to modify primary magma compositions to some extent.

Compared to Earth, the Martian crust has a much narrower compositional range, dominated by basaltic rocks that formed by extensive partial melting of the mantle and are thought to have had relatively simple crystallization histories (*McSween*

et al., 2009). The absence of plate tectonics and the early loss of water from the Martian mantle may have favored the generation and preservation of these rocks. However, Martian basalts still display considerable mineralogical and chemical diversity, suggesting variable degrees of differentiation and heterogeneity in the composition of their mantle sources (*Ehlmann and Edwards*, 2014; Schmidt et al., 2014). Such variability also implies that while some Martian basalts may closely resemble their primary magmas, most have likely been modified during cooling and crystallization (*Udry et al.*, 2014). Therefore, if our goal is to extract information about the conditions under which magmas were formed and the thermal state of the Martian mantle through time, a method to reconstruct primary magma compositions from Martian basalts is required.

Several computational methods have been successfully applied to estimate and investigate primary magmas on Earth. Some of these methods are based on forward modeling of mantle melting (*Mckenzie and Bickle*, 1988; *Niu and Batiza*, 1991; *Kinzler and Grove*, 1992; *Longhi*, 2002), inverse modeling of fractional crystallization (*Sato*, 1977; *Klein and Langmuir*, 1987; *Mckenzie and Bickle*, 1988; *Green et al., 2001*), or a combination of both processes (*Herzberg and O'Hara*, 2002; *Lee et al*., 2009; *Herzberg and Asimow*, 2015; *Brown Krein et al*., 2021). Some of these models limit their ambition to the interpretation of primitive basalts that have only fractionated olivine (*Lee et al.*, 2009; *Herzberg et al*., 2023), while some attempt to use the more common and less primitive multiply saturated lavas (*Langmuir et al*., 1992; *Brown Krein et al*., 2021). Moreover, thermodynamic packages such as MELTS and pMELTS (*Ghiorso and Sack*, 1995; *Asimow and Ghiorso*, 1998; *Ghiorso et al*., 2002), THERMOCALC (*Powell and Holland*, 1988), or Perple_X (*Connolly and Petrini*, 2002) have been widely used to simulate mantle melting and fractional crystallization of natural magmas. Most of these methods rely on experimental data available for magnesium-rich terrestrial compositions.

However, compared to the Earth, the composition of the Martian mantle is significantly more ferroan (Mg# = 75–79, with Mg# = $100 \times \mathrm{Mg}/(\mathrm{Mg} + \mathrm{Fe}^{2+})$ on a molar basis; *Dreibus and Wänke*, 1984; *Taylor*, 2013; *Khan et al*., 2018; *Yoshizaki and McDonough*, 2020) and so are the igneous products resulting from differentiation of Martian mantle-derived melts. This difference in composition influences the Fe^{2+}-Mg partitioning between the melt and minerals in equilibrium, with particular significance for olivine, which is dominant in the upper mantle and is both a residual phase and the first fractionated phase in most primitive terrestrial and Martian

magmas (*Roeder and Emslie*, 1970; *Toplis*, 2005; *Filiberto and Dasgupta*, 2011). Consequently, the systematics of partial melting and magmatic differentiation for erupted lavas from Mars and the Earth are different, and terrestrial models for primary magma calculations may yield inaccurate solutions when applied to Martian lithologies.

Some models for estimating the formation conditions of primary magmas have been specifically tailored for FeO-rich compositions comparable to Martian basalts. These models use either forward (e.g., MAGMARS; *Collinet et al*., 2021) or inverse (e.g., *Filiberto*, 2017; *Filiberto and Dasgupta*, 2011, 2015) modeling approaches. The former approach matches the composition of primitive basalts to that of a direct product of partial melting of the mantle, requiring the target composition to be a primary magma. On the other hand, the latter is a partial solution obtained by adding or subtracting olivine until its composition is in equilibrium with the estimated olivine composition of the Martian mantle residue, which may be an invalid solution if the mantle cannot produce a liquid complementary to that olivine composition.

Here, we present PRIMARSMELT, a recalibration and update of the PRIMELT3 model for terrestrial primary magmas (*Herzberg and Asimow*, 2015), customized for Mars. PRIMARSMELT addresses both the mantle melting and magmatic differentiation aspects of the primary magma problem and only returns a solution when

2. Model Description

2.1 PRIMARSMELT Algorithm

The algorithm implemented in PRIMARSMELT for primary magma calculations is based on PRIMELT-3P and earlier implementations of the PRIMELT family (*Herzberg et al*., 2007, 2023; *Herzberg and Asimow*, 2008, 2015). The logic underlying this algorithm is described in detail by *Herzberg & O'Hara* (2002) and is briefly summarized below. A schematic diagram of the method to find primary magma solutions with PRIMARSMELT is shown in Figure 1.

PRIMARSMELT takes as input the composition of a Martian igneous rock believed, based on its composition and texture, to have evolved only by olivine fractionation or by accumulation of olivine crystals. Liquids that have undergone olivine + clinopyroxene ± plagioclase fractionation cannot be easily inverted to primary magmas through this method without a significant increase in computational cost and

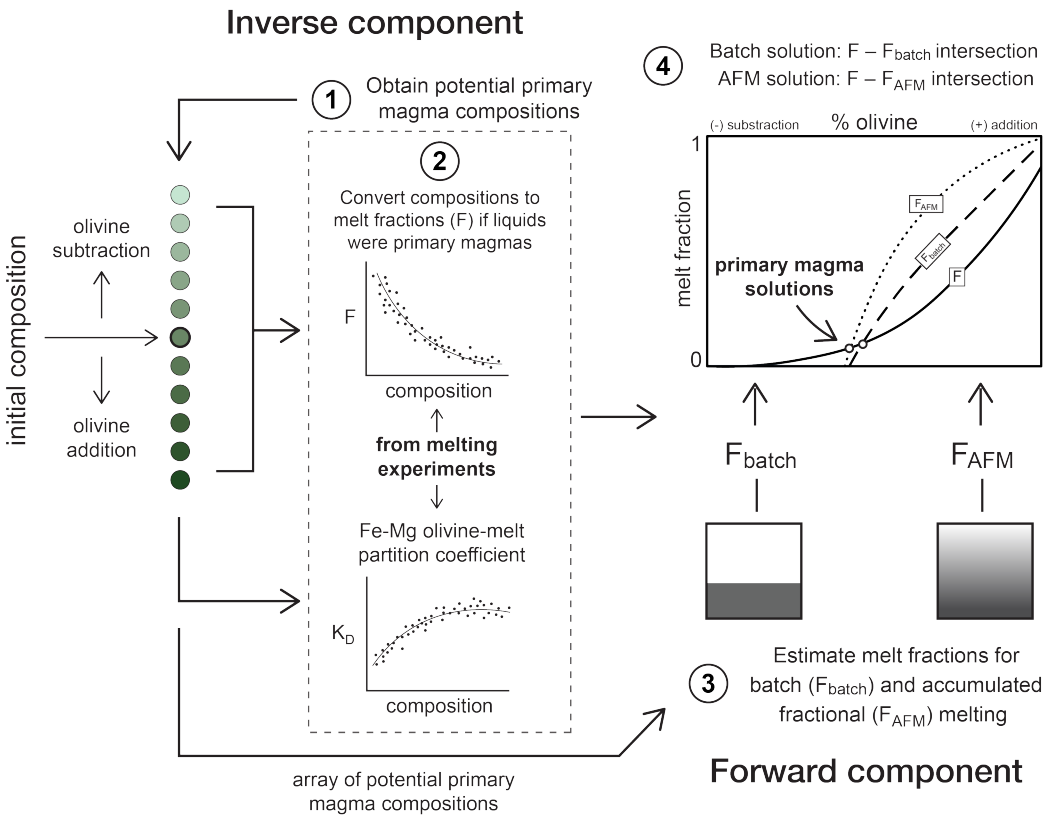


Figure 4.1: Schematic flow chart of the algorithm implemented in PRIMARSMELT to find primary magma solutions from the intersection of melt fractions derived from inverse and forward components.

uncertainty. Modeling fractionation of multiply saturated liquids requires knowledge of both the equilibrium composition and the fraction of all coexisting phases at given $P - T$ conditions. These phase equilibria calculations can be more efficiently accomplished by a Gibbs free energy minimization approach, similar to those implemented in software packages like pMELTS and Perple_X. However, such programs require thermodynamic databases and activity-composition models specific for Martian lithologies, which are currently lacking. PRIMARSMELT, calibrated specifically for Martian rocks, implements a more straightforward strategy that considers simple olivine-liquid equilibria. While this approach uses minimal computational resources, it requires relatively primitive liquid compositions that have only fractionated olivine.

Like previous versions of PRIMELT, PRIMARSMELT also includes filters to reject compositions likely to have fractionated pyroxene or to have been derived from exotic (pyroxenitic or volatile-rich) sources. From this initial composition, an array

of possible primary magma compositions is estimated by successively adding and subtracting equilibrium olivine in 0.1 wt.% increments. This corresponds to the inverse component of the model. The Fe-Mg olivine composition at each step is calculated using the distribution coefficient $K_D^{(Ol/Liq)}$ expression from *Toplis* (2005), which describes the equilibrium Fe^{2+}-Mg partitioning between olivine and melt as a function of the melt composition. The *Toplis* (2005) parameterization considers the pressure of olivine fractionation (P, which is a setting that may be chosen by the user), and the corresponding olivine–liquidus temperature ($T^{Ol/Liq}$). The remaining elements in olivine are determined using partition coefficient expressions from *Herzberg & O'Hara* (2002) for Ti, Al, Cr, Ca, and Mn and *Beattie et al.* (1991) for Ni.

If any potential solution from the array generated by the inverse component is a primary magma, then a solution for its composition and melt fraction produced by partial melting of the mantle must also exist. Melt compositions and corresponding melt fractions produced by mantle melting are calculated in the forward component of the model as discussed below in Section 2.3.1.

PRIMARSMELT yields a primary magma solution when the melt fractions estimated in the forward component intersect with one of the compositions in the inverse array. In an ideal case, both the batch melting and accumulated fractional melting models have their own solution in PRIMARSMELT. However, the algorithm may fail to find a solution for either model, a situation that may arise if the starting composition was not suitable (because it was not actually igneous, or was too chemically altered, or had fractionated phases other than olivine, etc.) or if the rock was derived from a source too distinct from the primitive Martian mantle (e.g., a pyroxenite, a volatile-rich peridotite, a strongly enriched or depleted peridotite, or an exotic magma ocean cumulate never homogenized to yield something akin to a bulk martian mantle composition).

2.2 Experimental dataset

A compilation of partial melting experiments was used to obtain expressions for F, for the FeO-MgO distribution coefficient between the liquid (Liq) and olivine (Ol) $K_D^{(Ol/Liq)}$, and for T_{Liq} as functions of the melt composition (see Supporting Information S1). In addition, expressions for the solidus and the batch melt fraction function in pressure-temperature space were derived from experimental data, allowing for estimation of the initial melting pressure (P_i). We selected partial melting

experiments with starting compositions similar to a primitive mantle composition for Mars with Mg# of ~75 (e.g., *Dreibus & Wänke*, 1984 – DW; *Lodders & Fegley*, 1997 – LF). The compiled data contains experiments from *Collinet et al.* (2015), *Collinet et al.* (2021), *Bertka & Holloway* (1994), *Matsukage et al.* (2013), *Ding et al.* (2020), and *Payré & Dasgupta* (2022), whose datasets are referred hereafter as C15, C21, BH94, M13, D20, and P22, respectively.

The direct partial melting experiments from C15 and C21 used DW as the starting composition. C15 includes twenty-five experiments conducted from 0.5 to 2.2 GPa at temperatures ranging from 1160 to 1550 °C, with melt fractions between 0.05 and 0.53. By contrast, the direct melting experiments in C21 were conducted at pressures between 2.4 and 2.66 GPa and temperatures of 1380 to 1470 °C, producing melt fractions between 0.05 and 0.30. C21 also includes reversal experiments that used mixtures of DW with liquid compositions obtained in previous runs as starting materials. These experiments were run at pressures of 1.0 and 2.6 GPa and temperatures between 1250 and 1410 °C, resulting in quenched experimental charges with large volume fractions of glass (i.e., 0.36-0.56), which allowed a test of the achievement of thermodynamic equilibrium in corresponding direct low melt fraction experiments (*Collinet et al.*, 2021).

The experiments from BH94 and M13 also had DW as the starting composition. BH94 gives four experiments at 1.5 GPa and temperatures from 1360 to 1550 °C, with melt fractions from 0.30 to 0.71. The M13 dataset is sixteen experiments at pressures from 1.0 to 4.5 GPa and temperatures from 1300 to 1750 °C, resulting in melt fractions between 0.14 and 0.89.

Most experimental runs in D20 used a starting material with the LF composition at pressures varying from 2 to 5 GPa at temperatures of 1250-1450 °C, which produced melt fractions between 0.08 and 0.38. This study also conducted experiments with starting compositions similar to LF but varying in Mg# and total alkalis to assess the effect of these variables on the solidus temperature. However, these experiments produced no measurements of a quenched liquid phase. The experiments from P22 used two starting compositions that only differed from LF in their P_2O_5 content: P_2O_5-free and 0.5 wt.% versus 0.2 wt.% in LF. These experiments were run at a constant pressure of 2 GPa and temperatures of 1210-1450 °C, yielding melt fractions from 0.07 to 0.28.

Except for M13, all the studies in the compiled dataset used graphite inner capsules placed in platinum outer capsules. This setup yields an average experimental oxygen

fugacity (fO_2) of ~IW +0.5 (*Médard et al.*, 2008), which is below the fayalite-magnetite-quartz (FMQ) buffer and consistent with several estimates of the prevalent fO_2 conditions of the Martian mantle (*Goodrich et al.*, 2003; *Herd*, 2003; *Nicklas et al.*, 2021). M13, by contrast, used a rhenium-platinum double capsule to reduce iron loss while maintaining fO_2 between FMQ and FMQ–3.

For the PRIMARSMELT calibration, the entire dataset was filtered to include only experiments conducted between 0.5 and 3.0 GPa, as the systematics of partial melting for garnet and plagioclase peridotite are likely described by expressions different from those describing melting of harzburgite and spinel peridotite (*Herzberg and Asimow*, 2015). For consistency, all experimental melt fractions and associated uncertainties due to variability in phase compositions and analytical uncertainty (σ_{comp}) were recalculated using the LIME mass balance algorithm in inverse log-ratio space (*Prissel et al.*, 2023). Experiments where the relative standard deviation of F due to compositional variability ($RSS = (100 \times \sigma_{\text{comp}})/F$) was higher than 20% were excluded from the dataset. In most cases, the excluded experimental runs coincided with those reported as anomalous in the original studies due to disequilibrium, significant iron loss, or considerable uncertainty in the quenched melt composition. In some cases, we utilized slightly different versions of this initial dataset, suited specifically for the variable being parameterized. For example, only direct partial melting experiments were considered for parameterization of the melt fraction, whereas both direct and reversal experimental melts were used to parameterize an expression for $K_D^{(\text{Ol/Liq})}$. Likewise, the fitting strategy for our liquid thermometer effectively removes datapoints that are systematically identified as outliers during iterative fitting of the dataset.

2.3 PRIMARSMELT components

2.3.1 Melt fraction estimation

Inverse component The melt fraction that a primary liquid represents can be approximated from experiments as a function of the melt composition and, independently, as a function of the temperature and pressure conditions at which the melt equilibrated. Melt fraction vs. melt composition is represented by:

$$F(AN) = \frac{1.57\, e^{0.227\, AN}}{32.9\, AN - 0.288} \tag{4.1}$$

where AN corresponds to the normalized anorthite coordinate in the Olivine–

Anorthite–Quartz (OL–AN–QTZ) plane projected from Diopside (*Herzberg and O'Hara*, 2002) (see Appendix A1). Melt fraction vs. pressure and temperature is given by:

$$\begin{aligned}(P,T) = &-1.91 - 8.63\times10^{-2}P + 1.77\times10^{-3}T \\ &- 8.88\times10^{-5}PT + 1.16\times10^{-2}P^2\end{aligned} \tag{4.2}$$

where P and T are the pressure and temperature conditions at which the liquid equilibrated in GPa and °C, respectively.

While Equation 1 is used in PRIMARSMELT to estimate the melt fraction corresponding to each liquid composition in the inverse array, the partial derivatives of Equation 2 allow estimates of the contribution of the experimental pressure and temperature uncertainty to the total uncertainty in F (σ_{total}):

$$\sigma_{\text{total}} = \sqrt{(\sigma_{P-T})^2 + \left(\sigma_{\text{comp}}\right)^2}; \qquad \sigma_{P-T} = \sqrt{\left(\frac{\partial F}{\partial P}\,\sigma_P\right)^2 + \left(\frac{\partial F}{\partial T}\,\sigma_T\right)^2}. \tag{4.3}$$

where σ_P and σ_T are assumed to be 0.1 GPa and 20 °C, respectively, and σ_{comp} for each experiment is obtained from the mass balance calculations. While piston–cylinder experiments usually report temperature uncertainties lower than 20 °C, we prefer a conservative choice that optimizes for χ^2_ν in the regression model.

Parameterization of Equation 1 was performed using weighted least squares with *AN* as the independent variable, which was calculated from experimental melt compositions. The basalt–peridotite reversal experiments from C21 were excluded as the melt fraction by volume in these experiments does not (by design) correspond to the quantity of melt produced by direct partial melting of the mantle source composition (*Kinzler and Grove*, 1992; *Collinet et al.*, 2021). A series of functional forms were explored before the final form of Equation 1 was selected; it was found to give the lowest error of all the four-parameter equations tested, and the correlations between parameter uncertainties became large for model forms with more than four parameters.

Figure 2 shows the results of the weighted least squares parameterization of Equation 1. Forty-eight experiments were considered in the regression, yielding R^2 and weighted-R^2 values that are both 0.95. The estimated reduced chi-squared parame-

ter (χ^2_ν) is 0.77, suggesting the model provides a relatively good fit to the data given its associated uncertainties. Overall, the fitted expression for F reproduces experimental melt fractions with a mean absolute error (MAE) of 0.027 (2.7 wt.%) and a root-mean-square error (RMSE) of 0.001. The uncertainty on F associated with Equation 1 is less than 0.03 (3 wt.%), resulting from typical two-sigma uncertainties on electron microprobe data propagating to uncertainties of ~0.005 on AN values.

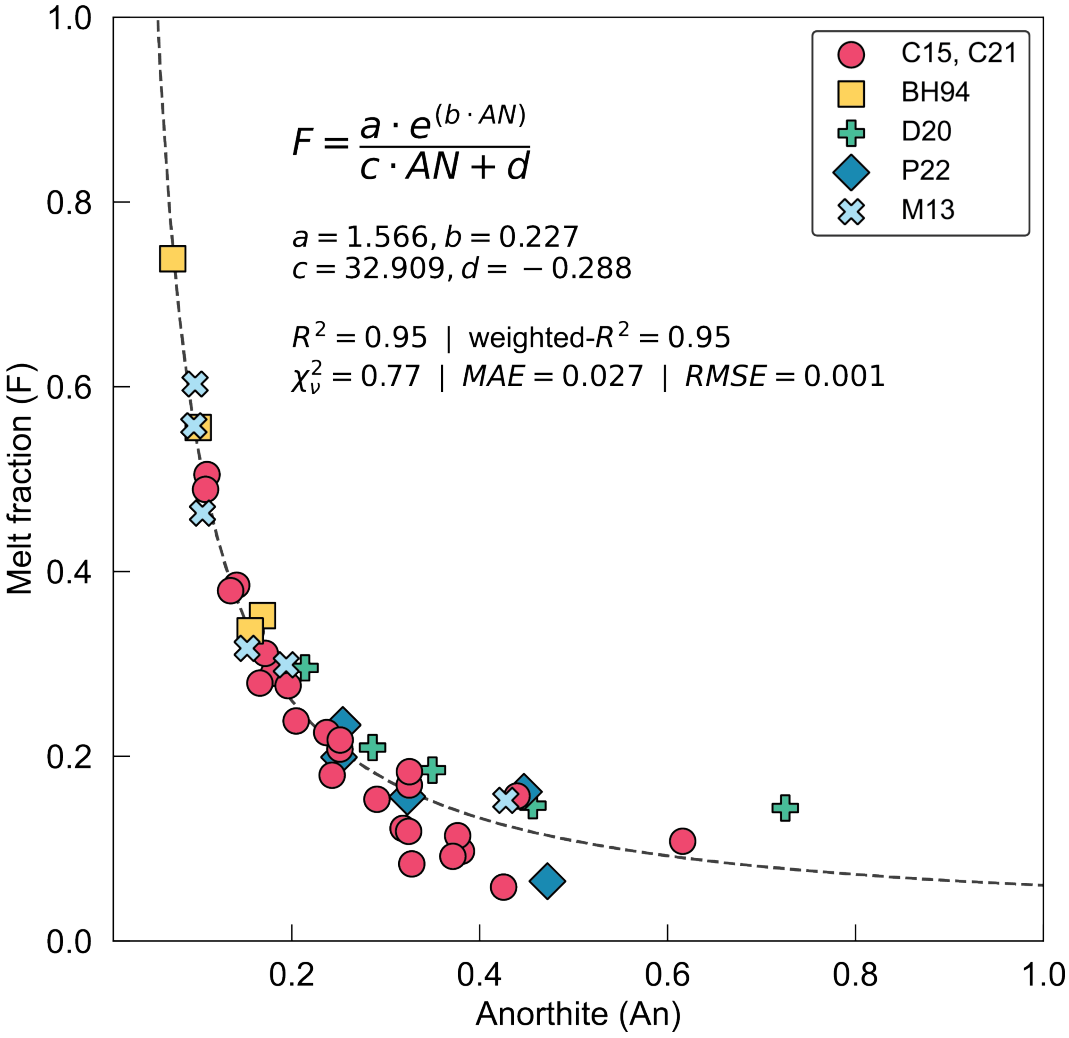


Figure 4.2: The regression of melt fraction against liquid composition fitted to the results of partial melting experiments on *Dreibus and Wanke* (1984) or *Lodders and Fegley* (1997) Martian mantle compositions. Data sources: C15 = *Collinet et al.* (2015); C21 = *Collinet et al.* (2021); BH94 = *Bertka and Holloway* (1994); D20 = *Ding et al.* (2020); P22 = *Payré and Dasgupta* (2022); M13 = *Matsukage* (2013).

Iterative fitting of Equation 2 provided values for the five coefficients, which allowed us to approximate the contribution of the uncertainty in the experimental P–T conditions (σ_P and σ_T) to the total uncertainty in F (σ_{total}). The estimated σ_{total} values

were then used to calculate weights as $1/\sigma_{\text{total}}$ in the regression of Equation 1 (see Appendix A2).

Forward component The melt fraction that a liquid would represent if it was produced by mantle partial melting can be obtained from its FeO and MgO contents by rearranging equations (22) and (23) in *Herzberg and O'Hara* (2002) according to the equation:

$$F_{\text{batch}} = \frac{(D_{\text{FeO}}\,\text{MgO}_{\text{Liq}} - \text{MgO}_0\,K_D^{\text{S/Liq}})}{(D_{\text{FeO}}\,\text{MgO}_{\text{Liq}} - \text{MgO}_{\text{L}}\,K_D^{\text{S/Liq}})} \tag{4.4}$$

where MgO_L and MgO_0 are the MgO contents of the liquid and the peridotite source in weight percent, D_{FeO} is the bulk distribution coefficient for FeO, which is the FeO content of the solid residue (S) divided by the FeO content of the liquid. $K_D^{\text{S/Liq}}$ is the FeO–MgO distribution coefficient for the solid residue and liquid defined as follows:

$$K_D^{\text{S/Liq}} = \frac{(\text{FeO/MgO})_{\text{S}}}{(\text{FeO/MgO})_{\text{Liq}}} \tag{4.5}$$

Herzberg and O'Hara (2002) showed that $K_D^{\text{S/Liq}}$ is nearly identical to $K_D^{\text{Ol/Liq}}$:

$$K_D^{\text{Ol/Liq}} = \frac{(\text{FeO/MgO})_{\text{Ol}}}{(\text{FeO/MgO})_{\text{Liq}}} \tag{4.6}$$

Therefore, it as an excellent approximation to write:

$$F_{\text{batch}} = \frac{D_{\text{FeO}}\,\text{MgO}_{\text{Liq}} - \text{MgO}_0\,K_D^{(\text{Ol/Liq})}}{D_{\text{FeO}}\,\text{MgO}_{\text{Liq}} - \text{MgO}_{\text{Liq}}\,K_D^{(\text{Ol/Liq})}} \tag{4.7}$$

This equation was used in the PRIMELT models calibrated for Earth (*Herzberg et al.*, 2007, 2023; *Herzberg and Asimow*, 2008, 2015) and we assume it is also appropriate for PRIMARSMELT. However, PRIMARSMELT uses $K_D^{(\text{Ol/Liq})}$ that has been recalibrated from experimental data for Mars compositions, and results are presented below in Section 2.3.4.

For any primary liquid with a specific content of MgO and FeO, the amount of melting needed to produce it for the case of accumulated fractional melting is always greater than or equal to that for batch melting (*Herzberg and O'Hara*, 2002).

From that work, *Herzberg and Asimow* (2008) determined that the melt fraction for accumulated fractional melting, F_{AFM}, can be derived from Equation 7 using the following relation:

$$F_{\mathrm{AFM}} = \left[\frac{0.98}{F_{\mathrm{batch}}} - 0.90\ (\ln F_{\mathrm{batch}})^2 + 0.07\ (\ln F_{\mathrm{batch}})^4 \right]^{-1} \tag{4.8}$$

As in previous calibrations of the PRIMELT algorithm, a primary magma composition for Mars is uniquely obtained along the inverse array when:

$$F(\mathrm{AN}) = F_{\mathrm{batch}}\ \&\ F(\mathrm{AN}) = F_{\mathrm{AFM}} \tag{4.9}$$

For batch melting and accumulated fractional melting, respectively.

2.3.2 An expression for the solidus

An expression for the solidus temperature as a function of pressure was obtained from partial melting experiments on the DW mantle composition. The solidus temperature was taken at each given pressure as the intercept of a linear fit to the available $T(F)$ data points. The resulting *P-T* pairs were then fitted to a second-order polynomial, yielding the following equation:

$$T_{\mathrm{solidus}} = 1038 + 154.1\,P - 8.589\,P^2 \qquad (R^2 = 0.99) \tag{4.10}$$

where T_{solidus} is in °C and P in GPa. For pressures between 0.5 and 3.0 GPa, Equation 10 yields temperatures nearly identical to the solidus expression of *Collinet et al*. (2015) but lower than those from the solidus expressions of *Filiberto and Dasgupta* (2011) and *Kiefer et al*. (2015), with average differences of ~4 °C, ~18 °C, and ~23 °C, respectively. For pressures between 3–5 GPa, our solidus expression is remarkably similar to that of *Filiberto and Dasgupta* (2011), which is constrained at 5 GPa by the experiments of Agee and Draper (2004). Our solidus may thus be extrapolated to 5 GPa, but careful interpretation of low-degree melt or AFM results in this pressure window is required as it is outside the calibration range of PRIMARSMELT and may involve melting of garnet peridotite, whose melt fractions and compositions may not be captured by the systematics of partial melting of spinel peridotite and harzburgite. For batch melting solutions in which the final pressure of melting is ≤3.0 GPa, though, the model is still valid because the melt is

considered to continuously re-equilibrate with the residue until the final pressure of melting.

2.3.3 Liquid thermometer and derivation of mantle potential temperatures

PRIMARSMELT requires an estimate of olivine–liquidus temperatures to calculate $K_D^{(\mathrm{Ol/Liq})}$ values in the inverse model and to derive mantle potential temperatures for primary magma solutions. A liquid thermometer in terms of MgO contents and P is preferred since the latter derivation is supported by the observation that MgO contents in wt.% remain approximately constant during adiabatic melting of the mantle. Thus, the liquid thermometer enables the calculation of MgO isopleths in P–T space and the initial melting pressure of a primary magma at the intersection between its MgO isopleth and the solidus.

PRIMARSMELT adopts a similar expression to that given in *Herzberg and Asimow* (2015; Equations 12–13) and used in PRIMELT3. This relationship describes temperature as a function of the MgO content in the liquid, with an additional term that accounts for the effect of pressure. We reformulated this thermometer using the experimental dataset for partial melting of Martian mantle compositions, leading to the following equation:

$$T^{(\mathrm{Ol/Liq})} = 1042 + 27.25\,\mathrm{MgO} - 0.3753\,\mathrm{MgO}^2 + 36.92\,P \qquad (R^2 = 0.90) \quad (4.11)$$

where $T^{(\mathrm{Ol/Liq})}$ is in °C, MgO in wt.%, and P in GPa. Equation 11 was obtained by ordinary least squares regression, as we considered all the experiments in the dataset to have a temperature uncertainty of 20 °C (1σ), taken as a conservative estimate for piston–cylinder experiments. The data used for fitting of Equation 11 is a reduced version of the original dataset and was obtained using a RANSAC algorithm, which removes suspect experiments showing a non-systematic relationship between temperature and MgO content of the liquid. Equation 11 captures experimental temperatures with an MAE of ~23 °C and an RMSE of ~30 °C. This MAE is only ~1 °C higher than that reported for the pressure-independent thermometer of *Collinet et al*. (2022). However, for the same set of experiments used in the calibration of Equation 11, the MAGMARS thermometer has an MAE of ~33 °C. Similarly, the thermometers from *Putirka* (2008) result in an MAE of ~28 °C for the pressure-dependent calibration and ~40 °C for the pressure-independent one. Notably, while

these thermometers are expressed in terms of several compositional variables, our calibration only requires the MgO content of the liquid and the equilibrium pressure of the primary magma. The error in T estimates with Equation 11 due to typical uncertainties on MgO contents from electron microprobe analysis (i.e., ~1.0 wt.%; 2σ) is less than ~25 °C.

PRIMARSMELT assumes that adiabatic decompression yields a series of liquids whose MgO contents remain approximately constant as pressure and temperature decrease and melt fraction increases. The convenience of this assumption is illustrated in Figure 3B, where MgO isopleths in P–T space from Equation 11 are nearly parallel to P–T paths predicted by pMELTS for isentropic decompression melting beginning at pressures of 1.5, 2.0, and 2.5 GPa. It can be argued that the accuracy of the pMELTS calibration for melting of Martian rocks is unproven, but pMELTS can still predict melt productivity and energy conservation within a thermodynamically consistent framework. For example, while the liquids produced with pMELTS tend to have MgO contents ~1 wt.% higher than those predicted by PRIMARSMELT, the position of the solidus at the modeled pressures is relatively close to the solidus of PRIMARSMELT.

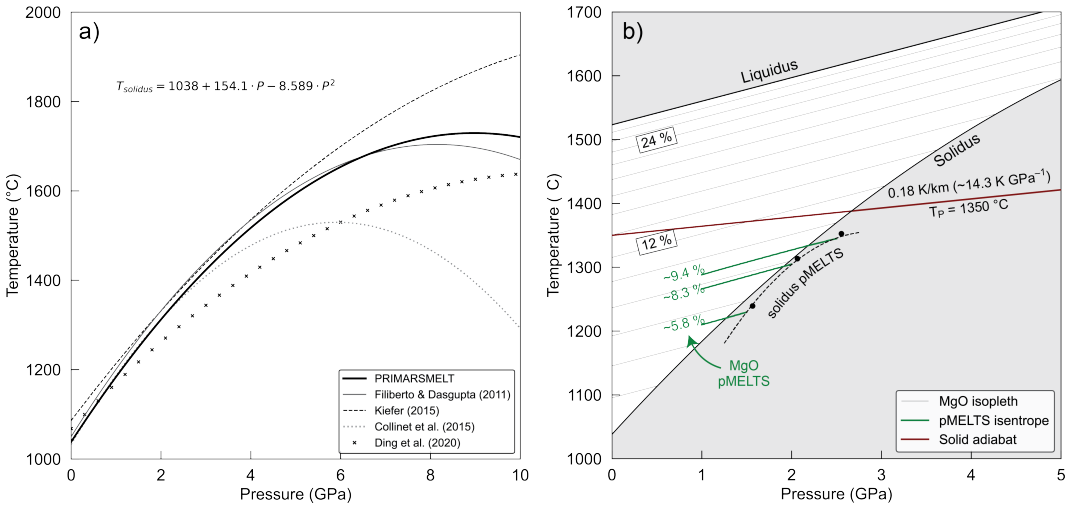


Figure 4.3: (a) Solidus expressions for the Martian mantle: thick black solid line, PRIMARSMELT (this study); gray solid line (*Filiberto & Dasgupta*, 2011), gray dashed line (*Kiefer*, 2015), gray dotted line (*Collinet et al.*, 2015), x-markers gray line (Ding et al., 2020). (b) Solidus and liquidus from PRIMARSMELT. MgO isopleths (gray lines) are approximately parallel to melting isentropes of the Martian mantle predicted by pMELTS (green lines). The red line is an example solid mantle adiabat with slope from *Kiefer* (2003), shown here projecting the temperature at the solidus to a mantle potential temperature of 1350 °C.

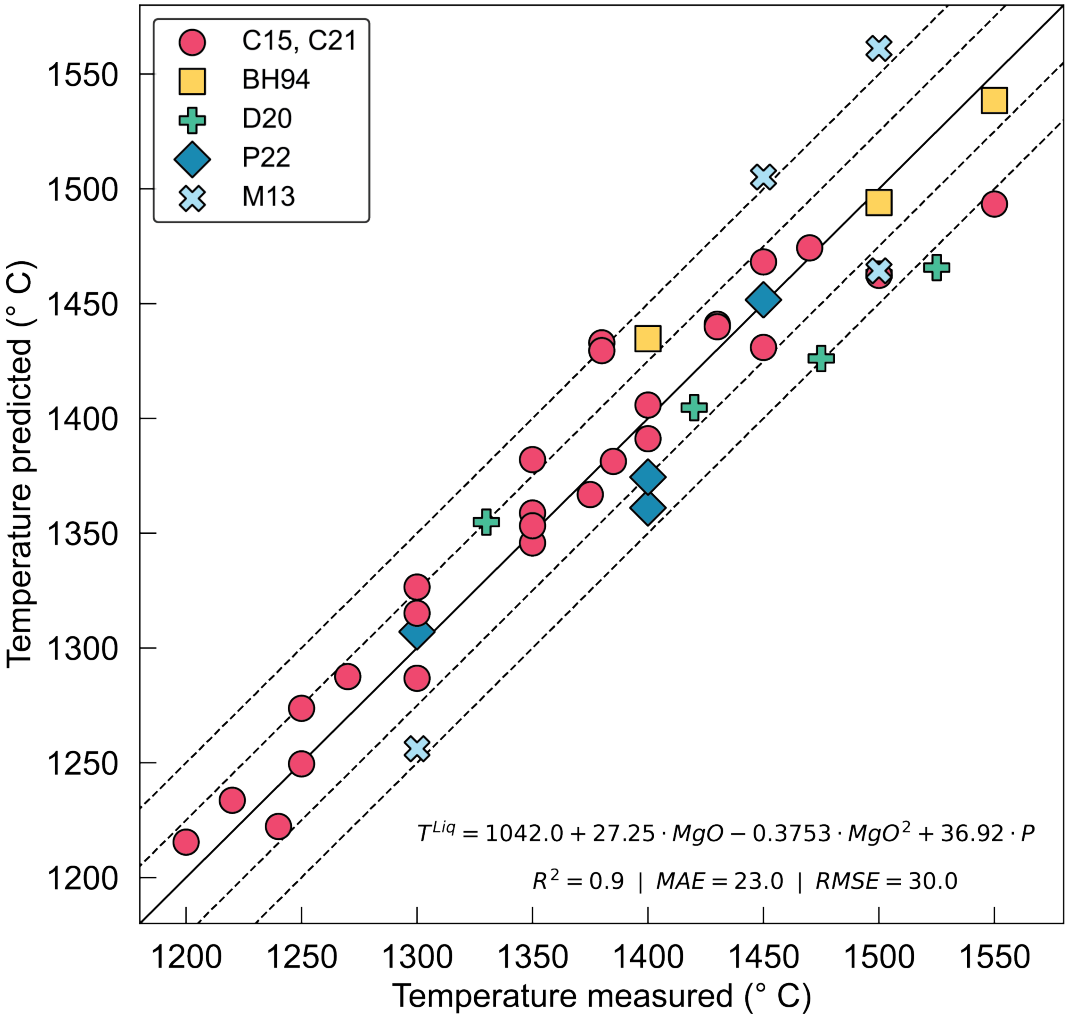


Figure 4.4: Liquid thermometer expressed in terms of MgO content of the liquid and pressure conditions at which the liquid equilibrated with residual Martian mantle assemblage.

The liquidus temperature can thus be calculated at the olivine fractionation pressure and projected along the corresponding MgO isopleth to find the initial melting pressure (P_i) at the intersection with the solidus. Thus, P_i can be conveniently reduced to a simple parameterization of MgO contents along the solidus line:

$$P_i = 8.189 \times 10^{-2} + 0.2134\,\mathrm{MgO} + 2.852 \times 10^{-3}\,\mathrm{MgO}^2 \tag{4.12}$$

The mantle potential temperature can be obtained by projecting the intersection between the solidus and the MgO isopleth to surface pressure following a solid-state adiabat, which for Mars is generally assumed as 0.18 K/km or ~14.3 K/GPa (*Kiefer*, 2003). The uncertainty on calculated mantle potential temperatures is equivalent to

the temperature uncertainty at the solidus due to MgO and P_i, which can be derived from Equations 11 and 12. Assuming a typical two-sigma error in MgO contents of ~1.0 wt.%, we estimate a T_P uncertainty of ~28 °C. Similarly, the uncertainty on P_i for MgO contents up to ~20 wt.% should be lower than ~0.5 GPa.

2.3.4 Olivine-liquid equilibrium

The compositions of olivine and liquid in equilibrium can be determined from the FeO–MgO distribution coefficient $K_D^{(\mathrm{Ol/Liq})}$, which is used here to calculate F_{batch}. From compiled data on partial melting of iron-rich mafic and ultramafic rocks, *Filiberto and Dasgupta* (2011) found that a $K_D^{(\mathrm{Ol/Liq})}$ of ~0.35 ± 0.01 is more appropriate to describe olivine–melt equilibrium conditions in Martian magmas than the typical value of 0.30 used for terrestrial basalts. However, the composition of the phases present in a system is controlled by its equilibrium state, which can be described in terms of constant *P–T* conditions and the compositional variables that define the system. PRIMARSMELT uses a parameterized expression for $K_D^{(\mathrm{Ol/Liq})}$ based on experimental melt compositions in the Mars melting database in equilibrium with olivine:

$$K_D^{(\mathrm{Ol/Liq})} = 0.24 + \frac{0.22}{1 + e^{-21\,(x-0.35)}} \tag{4.13}$$

where x is a compositional variable defined by the following function:

$$\begin{aligned} x = {} & -1.9 \times 10^{-3}\,\mathrm{SiO_2} - 1.7 \times 10^{-3}\,\mathrm{Al_2O_3} - 5.3 \times 10^{-2}\,\mathrm{Cr_2O_3} + 1.8 \times 10^{-2}\,\mathrm{FeO} \\ & - 3.4 \times 10^{-2}\,\mathrm{MgO} - 4.1 \times 10^{-3}\,\mathrm{CaO} + 0.025\,\mathrm{Mg\#} - 0.74 \end{aligned} \tag{4.14}$$

where the oxides in the liquid are in weight percent and Mg# is the molar ratio $100 \times \mathrm{Mg}/(\mathrm{Mg} + \mathrm{Fe})$ in the liquid.

Equation 13 defines a sigmoidal curve that fits $K_D^{(\mathrm{Ol/Liq})}$ values across the range of x observed in experiments and natural compositions of Martian magmas (Figure 5). The experimental data used for the regression of this expression included direct partial melting experiments from C15, C21, BH94, D20, P22, and M13, in addition to the reversal experiments of basalt–peridotite melting in C21. Because even small changes in FeO contents can lead to significant variations in $K_D^{(\mathrm{Ol/Liq})}$ values, only experiments with less than 5% Fe loss were considered (n = 42). In addition,

experimental $K_D^{(Ol/Liq)}$ values were calculated assuming a $Fe^{3+}/\Sigma Fe$ of 0.05, which is close to the expected ratio for experimental fO_2 conditions buffered at FMQ–2.

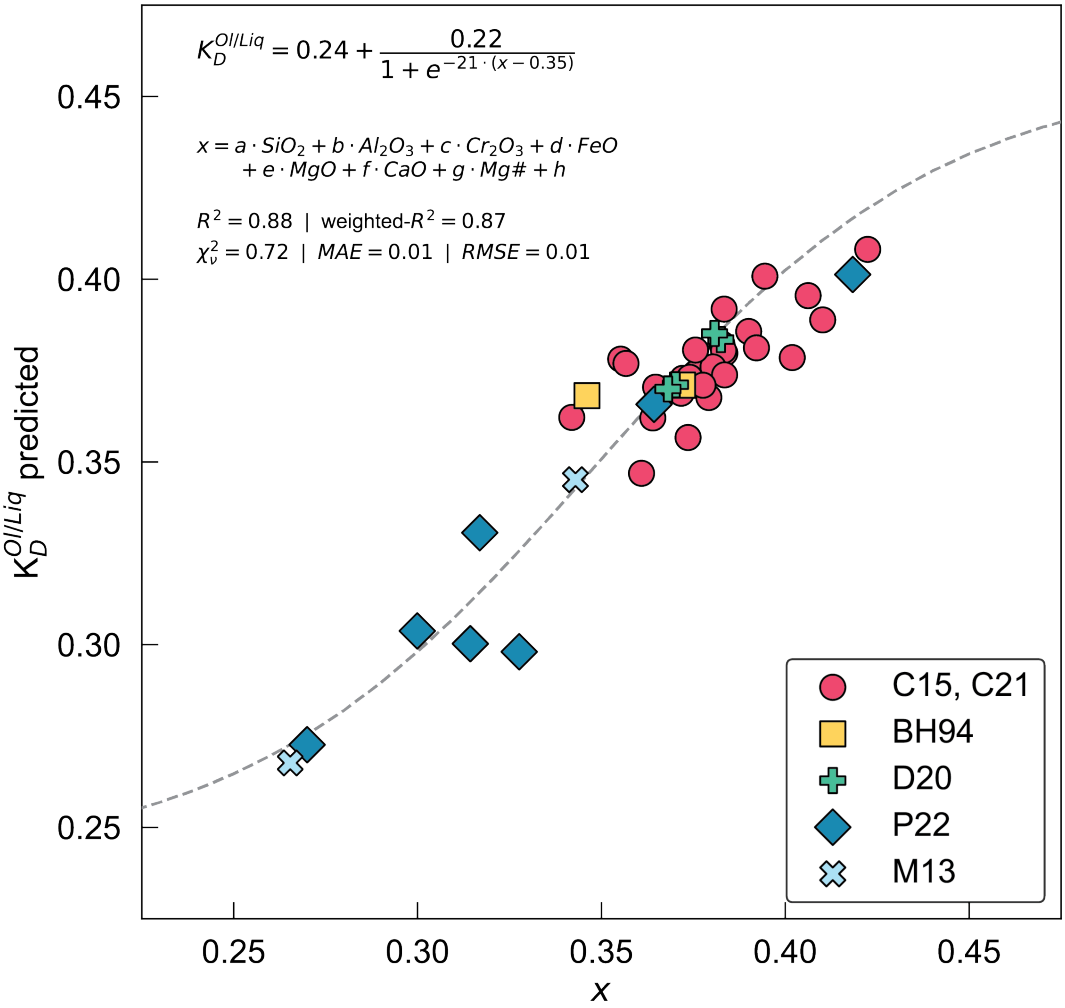


Figure 4.5: Parameterization of the Fe^{2+}–Mg distribution coefficient between olivine and liquid ($K_D^{Ol/Liq}$) for partial melting of the Martian mantle. The regressed expression is a function of the liquid composition (x) in terms of SiO_2, Al_2O_3, Cr_2O_3, FeO, MgO, CaO, and Mg#. The regression coefficients for x are: a = -1.9 × 10^{-3}, b = -1.7 × 10^{-3}, c = -5.3, × 10^{-2}, d = 1.8 × 10^{-2}, e = -3.4 × 10^{-2}, f = -4.1 × 10^{-3}, g = 0.025, h = -0.74.

Fitting of Equation 13 was performed using weighted least squares, where the weight of each data point was assumed as $1/\sigma_{K_D}$ and σ_{K_D} was estimated as:

$$\sigma_{K_D} = K_D^{(Ol/Liq)} \times \sqrt{\left(\frac{\sigma_{FeO}}{FeO}\right)^2_{Ol} + \left(\frac{\sigma_{MgO}}{MgO}\right)^2_{Ol} + \left(\frac{\sigma_{FeO}}{FeO}\right)^2_{Liq} + \left(\frac{\sigma_{MgO}}{MgO}\right)^2_{Liq}} \quad (4.15)$$

Our expression for $K_D^{(Ol/Liq)}$ provides a relatively good agreement between the model and the data, given the estimated uncertainties (Figure 5). Equations 13 and 14 predict $K_D^{(Ol/Liq)}$ values with an MAE of 0.009 and an RMSE of only 0.01. Again, as in *Herzberg and O'Hara* (2002) and previous versions of the PRIMELT algorithm, we assume that this parameterization of $K_D^{(Ol/Liq)}$ can be used in place of $K_D^{(S/Liq)}$ in the mass balance solution for melt fraction.

3. Using PRIMARSMELT

PRIMARSMELT is freely available for download as a Microsoft® Excel® macro-enabled workbook and as a Python-based graphical user interface (GUI). The input data for PRIMARSMELT consist of a list of sample names, major oxide compositions (wt.%), iron oxidation states (i.e., $Fe^{2+}/\Sigma Fe$), and olivine fractionation pressures (in bars) for one or more primitive Martian basalts. Because the PRIMARSMELT algorithm is primarily based on olivine–liquid equilibria, the input composition must contain data for FeO and MgO contents; otherwise, the calculations will fail. The user can modify the mantle composition by updating the source FeO and MgO contents from the default values (i.e., DW and LF). Loading samples for calculations is done by simply typing the data in the Excel version or selecting a text file in the GUI. Detailed instructions and input templates are provided with the Excel and GUI versions of PRIMARSMELT.

Once the data are loaded, PRIMARSMELT performs the necessary calculations for all the samples in the input file. The output is presented as two separate blocks, giving the batch and AFM solutions. In the GUI, the first three columns in each block correspond to the sample name (Name), warnings related to the input composition (i.e., *Warning: volatile-bearing source composition – VT*; *Warning: clinopyroxene fractionation – PX*), and whether a primary magma solution exists (Solution: Y or N). The columns %Ol, X_{Fo}, Mg#, and K_D give the amount of olivine addition (or subtraction if negative) required for the primary magma solution, the forsterite composition of the olivine in equilibrium with the primary magma, the Mg# of the primary magma, and the value of the Fe^{2+}–Mg distribution coefficient at the liquidus estimated from Toplis (2005) and used for olivine fractionation. Column P returns the (unmodified from the input) fractionation pressure, and T_{Liq} (°C) is the liquidus temperature at the fractionation pressure. Melt fractions are shown in columns F (Fe/Mg) for the batch solution and F_{AFM} for the accumulated fractional melting solution. The mantle potential temperature in °C and initial melting pressure in GPa are given in columns T_P (°C) and P_i (GPa). The remaining columns display

the primary magma composition in weight percent of major element oxides. For the Excel version of PRIMARSMELT, the outputs are the same as described for PRIMELT3-P (*Herzberg et al.*, 2023). It is noteworthy that some mismatch between the results of the Python and Excel versions of PRIMARSMELT may occur due to differences in the routines used to find the intersection between melt fractions for primary magma solutions. The majority of these discrepancies are subtle and result from interpolation between 1% increments of olivine addition/subtraction in Excel as opposed to the 0.1% increments used in Python. However, the Python GUI is often capable of identifying primary magma solutions in samples that the Excel version fails to detect.

4. Application to Martian rocks

4.1 The Mars igneous record

The known igneous record on Mars comprises rocks analyzed by exploration rovers on the surface and a suite of meteorites that have been recovered on Earth. Rocks from Gusev crater analyzed by the Spirit rover include basalts that crystallized from variably fractionated and alkaline magma compositions (*Filiberto*, 2017). The age of the lava flows that flooded Gusev crater is ~3.65 Ga, based on crater counting (*Greeley*, 2005). However, rocks from Gusev crater can be as old as the late Noachian (the Columbia Hills suite) or as young as the Hesperian sedimentary deposits partially filling the crater (*Grant et al.*, 2004).

The Curiosity rover, exploring the ~3.5–4.2 Ga Gale crater, has also analyzed several rocks whose origin is most likely igneous. These rocks include compositions that vary from basalts to evolved trachyandesites, felsic granodiorites, and quartz–diorites (*Schmidt et al.*, 2014; *Sautter et al.*, 2015; *Cousin et al.*, 2017; Edwards et al., 2017; Udry et al., 2018; Wu et al., 2021). The absolute age of these rocks is uncertain but can be bounded by the latest evidence of alluvial activity (~3.3 Ga; *Grant et al.*, 2014) and the exposure age of a mudstone rock on the crater's surface (~4.21 Ga; *Farley et al.*, 2014).

More recently, the Perseverance rover has analyzed several outcrops of igneous rocks in two lithological units on the floor of the ~3.9 Ga Jezero Crater. The Séítah formation is made of olivine-bearing rocks that resemble the composition and mineralogy of some Martian meteorites; it likely consists of igneous cumulates (*Farley et al.*, 2022; *Liu et al.*, 2022; *Beyssac et al.*, 2023). This unit may extend well beyond the crater as part of a regional olivine-bearing unit identified from interpretation

of orbital images (*Brown et al.*, 2020; *Farley et al.*, 2022). Overlying Séítah is the Máaz formation, which contains variably evolved basaltic rocks interpreted as lava flows that may or may not be related to Séítah (*Farley et al.*, 2022; *Liu et al.*, 2022; *Wiens et al.*, 2022; *Udry et al.*, 2023).

The only samples from Mars analyzed in the laboratory for chemical composition, mineralogy, and isotope ratios are meteorites derived from fragments of Martian crust ejected during impact events and transported to Earth (*Udry et al.*, 2020). Most of the Martian meteorites are probably of igneous origin and have been classified into four groups based on their petrological characteristics: shergottites, nakhlites, chassignites (or 'SNC'), and ALH 84001 (*Krot et al.*, 2014; *Udry et al.*, 2020). In addition, part of the igneous record from Mars is contained in polymict breccias, each of which includes different types of clasts that may be representative of the bulk composition of the crust (*Agee et al.*, 2013; *Humayun et al.*, 2013; *Santos et al.*, 2015; *Wittmann et al.*, 2015; *Udry et al.*, 2020).

Shergottites are the youngest (~150 Ma–2.4 Ga) and largest group (*Udry et al.*, 2020) and have been classified into basaltic, olivine-phyric, poikilitic (or lherzolitic), and gabbroic categories (*Krot et al.*, 2014; *Udry et al.*, 2020). Typically, basaltic shergottites have low Mg# and their mineralogy is dominated by olivine, clinopyroxene, and plagioclase, suggesting they crystallized from variably fractionated lavas. Olivine-phyric shergottites have porphyritic textures defined by olivine phenocrysts and later clinopyroxene and shocked plagioclase (maskelynite) (*Krot et al.*, 2014; *Udry et al.*, 2020). These rocks have been interpreted either as near-primary melts or liquids that accumulated olivine. Poikilitic shergottites, on the other hand, are cumulate rocks with high Mg# that commonly show olivine and chromite crystals enclosed by low-Ca pyroxene and may correspond to early products of magmatic fractionation from basaltic or olivine-phyric shergottite liquids (*Udry et al.*, 2020). Finally, gabbroic shergottites resemble basaltic shergottites but contain cumulate plagioclase and clinopyroxene and are considered to have crystallized at depth (*Udry et al.*, 2020).

Nakhlites, chassignites, and ALH 84001 are igneous cumulates that crystallized from evolved magmas (*Udry and Day*, 2018; *Udry et al.*, 2020). Nakhlites contain cumulus olivine, clinopyroxene, and minor mesostasis and plagioclase. Chassignites, by contrast, are dominated by olivine and contain crystallized melt inclusions as well as solid inclusions of chromite, interstitial orthopyroxene, and plagioclase. The crystallization and ejection ages of all these meteorites are very similar: ~1.3 Ga

and ~11 Ma, respectively. This and other similarities in composition and texture indicate that both groups were likely ejected from the same location on the Martian surface and may be genetically linked (*Udry et al.*, 2020). ALH 84001, an orthopyroxenite, is the only ancient Martian meteorite (~4 Ga) and forms a group unto itself. Although nakhlites and chassignites only represent ~10% of the Martian meteorites available (*Udry et al.*, 2020), similar rocks may be common on Mars, such as those exposed on the floor of Jezero crater.

The meteorite NWA 7034 is a polymict breccia containing different types of clasts. Igneous clasts in this meteorite (and paired meteorite NWA 7533) are the most abundant and have compositions that include basalt, basaltic andesite, and trachyandesite (*Humayun et al.*, 2013; *Santos et al.*, 2015). The clasts in these rocks cannot be related to each other by fractional or equilibrium crystallization processes and were likely formed from different igneous sources (*Santos et al.*, 2015). However, radiogenic ages from the matrix of NWA 7034 are similar to those from individual mineral clasts of igneous origin (~4.4 Ga; *McCubbin et al.*, 2016; *Nyquist et al.*, 2016), indicating that various igneous components in the rock crystallized at similar ancient ages and are therefore representative of the early Martian crust.

Compositions from basaltic and olivine-phyric shergottites, basaltic to trachyandesitic clasts from NWA 7034/7533, and basaltic rocks from Gusev, Gale, and Jezero craters can be used as input for estimation of primary magma compositions and mantle potential temperatures with PRIMARSMELT. Moreover, while the bulk compositions of nakhlites and chassignites only represent a snapshot of a crystallization path (*Udry and Day*, 2018; *Wu et al.*, 2021), their parental magmas may be traced back to primary magmas, assuming these cumulate rocks crystallized from fractionated liquids that were initially produced in the mantle. This assumption is consistent with a petrogenetic history requiring crystallization of nakhlites and chassignites from fractionated magmas to explain their cumulate texture, bulk composition, and mineral chemistry (*Udry and Day*, 2018). Thus, potential parental liquids for these meteorites can also be used to calculate their primary magmas and derive the temperatures of their mantle source. Notably, the parental magmas of nakhlites and chassignites, if accurately reconstructed, can fill the temporal gap between shergottites and older basaltic rocks from Gale and Gusev craters and the basaltic components in NWA 7034/7533. Likewise, estimates of the parental magma for olivine-phyric shergottites LAR 06319 and NWA 1068 may be more suitable for use with PRIMARSMELT than the actual bulk compositions of the meteorites.

The entire dataset with the compositions used for PRIMARSMELT calculations is given in Supporting Information S2.

4.2 PRIMARSMELT calculations

We applied PRIMARSMELT to the compilation of whole-rock compositions of Martian rocks described above and obtained a set of primary magma compositions, melt fractions, and mantle potential temperatures. All the calculations presented here were run using the GUI version of PRIMARSMELT. When necessary, bulk-rock compositions were modified from the original study to convert them into PRIMARSMELT format (i.e., elements as oxides expressed in weight percent). Also, when available, estimated primary $Fe^{2+}/\Sigma Fe$ ratios were considered in our calculations (e.g., *Schmidt et al*., 2013, 2014). Otherwise, we assumed an initial value of 0.95 for shergottite meteorites and 0.90 for rocks analyzed in-situ, consistent with overall higher oxygen fugacity estimated for Gusev and Gale crater basalts relative to the shergottites (e.g., *Herd et al*., 2002; *Schmidt et al*., 2013, 2014). These values are also similar to those inferred for Martian magmas, which reflect oxygen fugacity ~1–3 log units below the FMQ oxygen buffer (*Kress and Carmichael*, 1991; *Herd et al*., 2002; *Goodrich et al*., 2003; *Herd*, 2003; *Schmidt et al*., 2013, 2014; *Edwards et al*., 2017).

The results discussed herein were obtained using an olivine fractionation pressure of one bar for ease of comparison. This is equivalent to assuming that mantle partial melts produced at depth ascend to the surface before undergoing crystallization. However, increasing the fractionation pressure to ~1 GPa would result in T_P increases of less than 10 °C and minimal changes in the primary magma composition, at least for the simple case considered here where olivine is the only crystallizing phase.

4.2.1 Basaltic and olivine-phyric shergottites

PRIMARSMELT produces valid F_{AFM} solutions for all basaltic and olivine-phyric shergottites, while F_{batch} solutions for meteorites Los Angeles, NWA 6162, and LEW 88516 cannot be found. Several basaltic shergottites are suspected to have undergone clinopyroxene fractionation, as indicated by their low Mg# (< 40) and primary magma solutions requiring more than 40% olivine addition. Also, shergottites NWA 8656 and KG 002 (basaltic) and NWA 5990 (olivine-phyric) display warnings for carbonated peridotite melting, due to their high CaO and low SiO_2 contents.

F_{AFM} solutions for shergottites with the DW84 mantle composition correspond to melt fractions between ~0.14 and 0.58 and estimated T_P values between 1374 °C and 1547 °C, with an average of 1450 °C. These solutions predict, with high fidelity, olivine subtraction for olivine-phyric shergottites and olivine addition for basaltic shergottites (Figure 6), which is consistent with petrographic observations for these groups of meteorites (Udry et al., 2020 and references therein). To be clear, a solution indicating olivine subtraction means that the collected and measured rock contains accumulated olivine and is more MgO-rich than its predicted primary magma. On the other hand, a solution indicating olivine addition means that the collected and analyzed rock has experienced olivine fractionation and is less MgO-rich than its predicted primary magma. This is a very important test of the success of the method: the petrographic character was not used as input, only the bulk composition was used. If the method had instead concluded that basaltic shergottites had accumulated olivine and were more MgO-rich than their primary lavas, or conversely if the method were to find that olivine-phyric shergottites had fractionated olivine and were MgO-poor compared to their primary lavas, those would be considered serious failures. The primary magma solutions that require minor olivine addition or subtraction (e.g., < 5%) can be interpreted as primary to near-primary melts and belong, for the most part, to the olivine-phyric shergottites. By contrast, the basaltic shergottites require more than 5% olivine addition, reflecting variable degrees of differentiation within this group. The only exception is NWA 7042, whose primary magma solution requires ~6% olivine subtraction. This meteorite, however, has textural similarities with both basaltic and olivine-phyric groups and has been described as "petrographically intermediate" (*Kizovski et al.*, 2020).

On the other hand, calculated melt fractions for F_{batch} primary magma solutions range from ~0.15–0.73. The match between petrographic shergottite groups and whether the solutions require olivine addition or subtraction is not as evident for F_{batch} solutions as for F_{AFM} solutions. However, it is only within the group of olivine-phyric shergottites that primary magma solutions yield olivine subtraction. Moreover, for solutions with similar $T_P^{(\mathrm{Ol/Liq})}$, olivine addition/subtraction is systematically higher in basaltic shergottites compared to their olivine-phyric counterparts.

4.2.2 Igneous clasts in polymict breccias NWA 7034/7533

The calculated solutions for basaltic to trachyandesitic clasts in NWA 7034/7533 indicate that most fragments are relatively close to primary magmas. F_{AFM} and

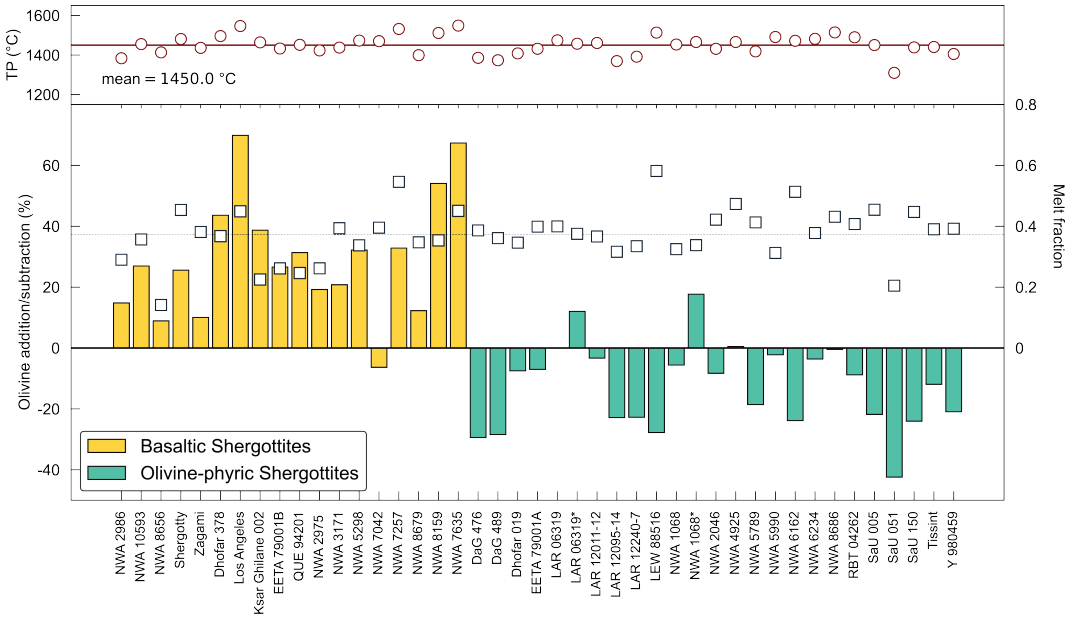


Figure 4.6: F_{AFM} primary magma solutions for all basaltic (yellow) and olivine-phyric shergottites (green) in our compiled database. Predicted mantle potential temperatures (T_P) are shown as circles in the top panel. The red horizontal line marks the average T_P. The amount of olivine addition/subtraction required for a successful primary magma solution is shown by the bars in the bottom panel (left-hand scale). Square markers indicate the FAFM predicted for each sample (right-hand scale). The dashed navy-blue horizontal line represents the average FAFM of all the shergottites. Compositions LAR 06319* and NWA 1068* are estimated parental magmas from *Balta et al.* (2013) and *Filiberto et al.* (2010).

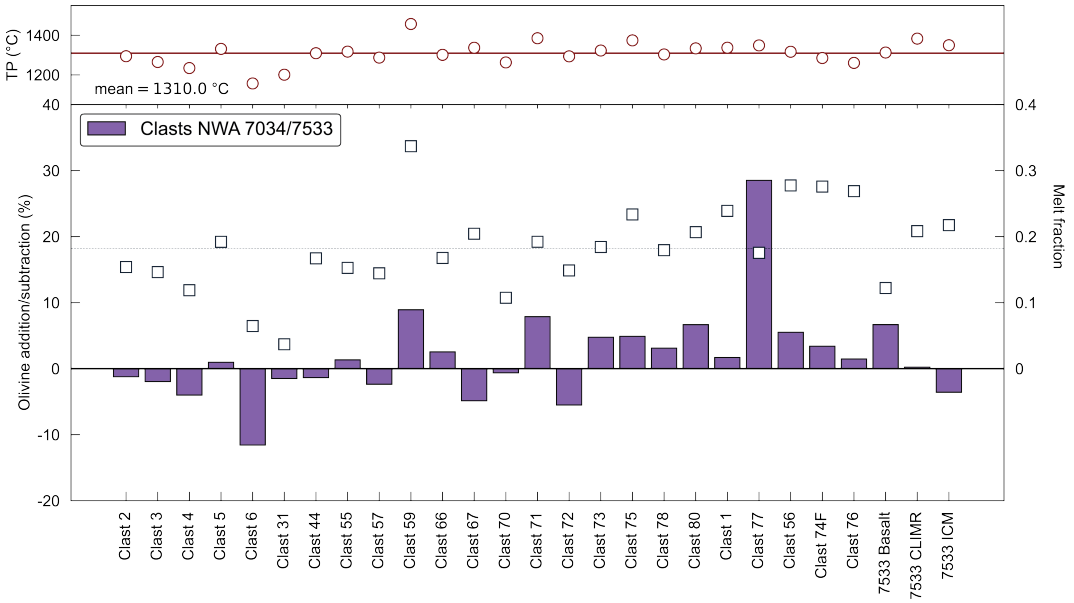


Figure 4.7: F_{AFM} primary magma solutions for all igneous clasts in NWA 7034/7533. Symbols as in Figure 6.

F_{batch} solutions indicate olivine addition or subtraction less than 10%. The estimated primary magmas have Mg# ~58 and are in equilibrium with ~Fo_{82} olivine. Moreover, the estimated melt fractions range from ~0.11 to 0.34, with F_{batch} solutions slightly higher than F_{AFM}. These melt fractions are produced at initial melting pressures of 1.6 to 4.0 GPa, with predicted T_P of 1235–1457 °C, averaging 1310 °C when all samples are considered and 1319 °C excluding clasts 6, 31, and 77 (whose compositions are flagged for melting of volatile-bearing source and clinopyroxene fractionation).

4.3 The parental magmas of chassignites

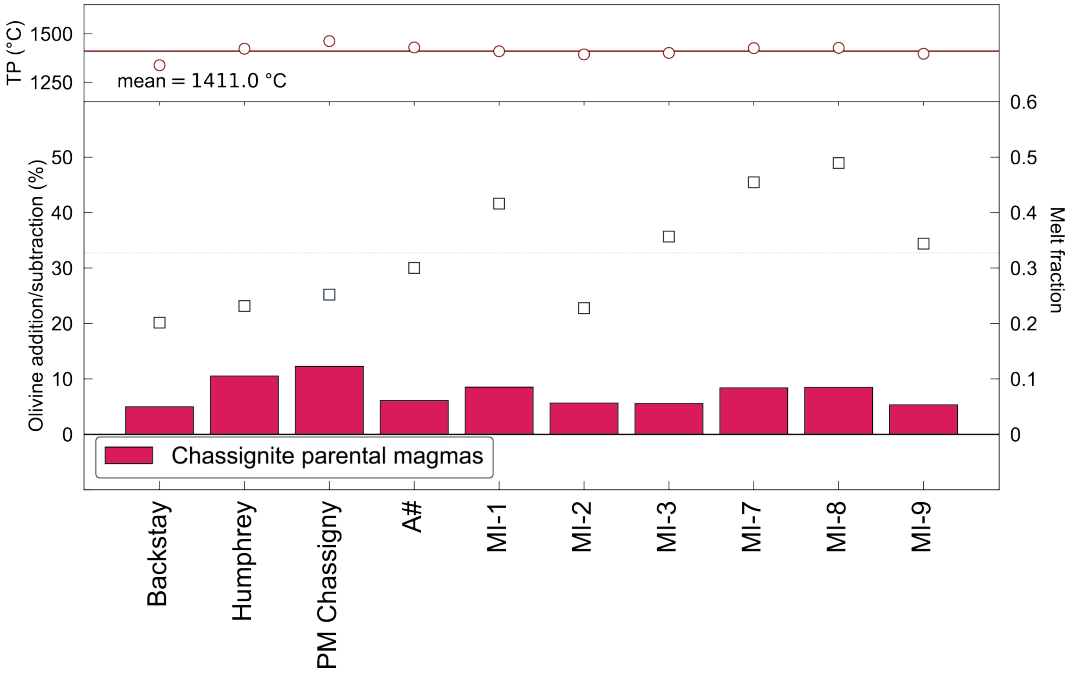


Figure 4.8: F_{AFM} primary magma solutions for proposed parental magmas of the chassignite meteorites: Backstay (*Nekvasil et al.*, 2009), Humphrey (*Filiberto*, 2008), PM Chassigny (*Johnson et al.*, 1991), A# (*He et al.*, 2013), MI-1–9 (*Wu et al.*, 2021). Symbols as in Figure 6.

We only considered parental magma compositions for the two most primitive chassignite meteorites, Chassigny and NWA 2737, containing Fo_{68} and Fo_{79} olivine, respectively. For the parental magma of Chassigny, we used the compositions of Gusev crater basalts Backstay and Humphrey. These rocks were proposed by *Filiberto* (2008) and *Nekvasil et al.* (2009), based on phase equilibrium experiments, as possible candidates for magmas that may have produced the mineral assemblage and olivine composition observed in Chassigny. On the other hand, the parental liquids for NWA 2737 used for PRIMARSMELT calculations are inferred compositions

from analysis of melt inclusions in olivine (*He et al.*, 2013; *Wu et al.*, 2021). The parental magmas of the ferroan chassignite NWA 8694 and the nakhlite meteorites are thought to be too evolved to have only fractionated olivine and were therefore excluded from our calculations (*Sautter et al.*, 2012; *Jambon et al.*, 2016; *Udry and Day*, 2018; *Hewins et al.*, 2020).

PRIMARSMELT finds valid solutions with no flags for primary magmas of the chassignite parental liquids. F_{AFM} and F_{batch} solutions yield mantle melt fractions of ~0.20–0.50, with solutions for the parental magmas of Chassigny corresponding to the lowest values. These parental liquids are relatively close to primary magma compositions, requiring between 5% and 11% olivine addition in all cases. Their estimated primary magmas have Mg# ~59–60 and are in equilibrium with Fo_{82}, in agreement with relatively minor magma differentiation prior to crystallization of the cumulate assemblages that formed the chassignites. The estimated initial melting pressures lie between 2.5 and 3.6 GPa, corresponding to T_P values of 1338–1439 °C, averaging 1411 °C.

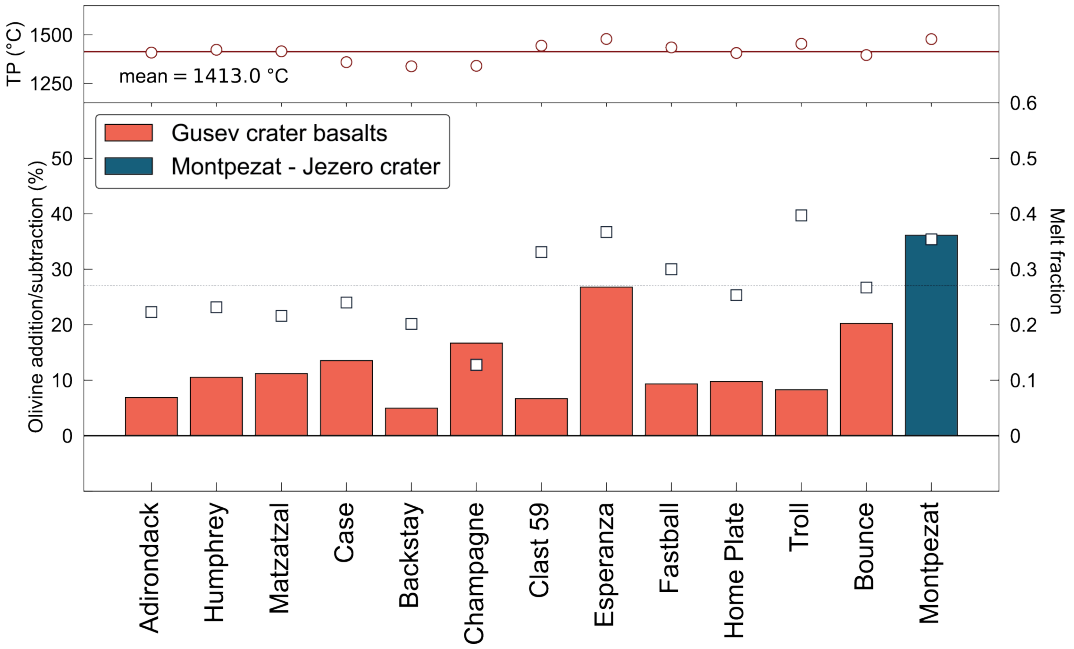


Figure 4.9: F_{AFM} primary magma solutions for basaltic rocks from the Gusev crater (orange) and basalt from the Jezero crater (Montpezat; dark blue). Symbols as in Figure 6.

4.4 In-situ measurements

Calculations using those rocks from Gusev, Gale, and Jezero craters that have been interpreted as igneous or near-igneous compositions (Stolper et al., 2013; Schmidt

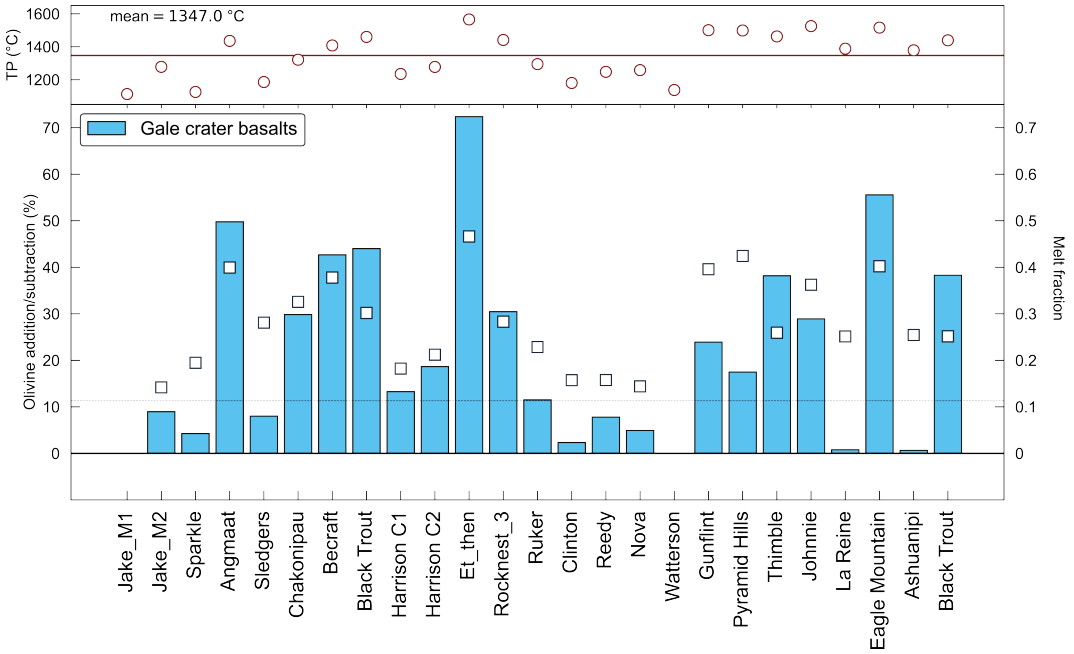


Figure 4.10: F_{AFM} primary magma solutions for basaltic rocks from Gale crater. Symbols as in Figure 6.

et al., 2014; Filiberto, 2017; Farley et al., 2022; Liu et al., 2022; Udry et al., 2023) are consistent with the fractionated nature of most basaltic lavas. PRIMARSMELT finds valid F_{AFM} and F_{batch} primary magma solutions for all the compositions except Jake_M1, for which an F_{AFM} solution could not be obtained. In general, all the solutions require variable degrees of olivine fractionation, but none of them require as much olivine fractionation as do the most fractionated basaltic shergottites. The F_{AFM} that these primary magmas represent are, on average, ~0.26 for the Gusev crater and Meridiani Planum and ~0.35 for Jezero crater. For Gale crater, F_{AFM} is ~0.17 for compositions from APXS and ~0.33 for ChemCam. In all cases, F_{batch} values are only marginally higher than F_{AFM}.

Among the rocks from Gusev crater and Meridiani Planum, the most evolved compositions are Esperanza, Bounce, and Champagne, requiring olivine addition of ~27%, 20%, and 17%, respectively, to obtain F_{AFM} solutions. Notably, the rest of the compositions from Gusev crater need less than 15% olivine addition, yielding T_P values within a range of 1338 °C to 1454 °C, significantly lower than previously inferred by Filiberto (2017), but in line with MAGMARS estimates for Adirondack basalts (Collinet et al., 2021).

The compositional data from Gale Crater include analyses from two instruments, APXS and ChemCam, which produce two distinct groups of results with PRI-

MARSMELT. Compositions from APXS have F_{AFM} solutions with less than 12% olivine addition, except *Et_then* and *Rocknest_3*, with ~72% and ~30%, respectively, which we excluded from further analysis due to possible clinopyroxene fractionation. These rocks yield primary magmas corresponding to T_P values of ~1180–1295 °C. By contrast, most analyses from ChemCam produce results with olivine addition spanning from 17% to 38% and T_P between 1439 °C and 1501 °C. Only the compositions corresponding to *Ashuanipi* and *La Reine* may represent primary to near-primary magmas with F_{AFM} of ~0.25 and T_P values of 1379–1388 °C, similar to primary magmas calculated for rocks from Gusev crater.

Finally, while a suite of variably evolved lavas has been analyzed from the Máaz formation in Jezero crater, only the most primitive composition (*Montpezat*; Mg# 35) was considered for calculations with PRIMARSMELT. The resulting primary magma for this composition requires ~36% olivine addition and is in equilibrium with Fo_{83}, significantly higher than olivine measured in the rock (Fo_{20}; Schmidt et al., 2022). This rock likely experienced significant olivine and pyroxene fractionation before achieving a ferroan composition in equilibrium with its olivine composition. Thus, the PRIMARSMELT solution cannot be representative of the primary magma composition for Montpezat.

5. Discussion

5.1 Primary to near-primary magma solutions for some olivine-phyric shergottites

Our PRIMARSMELT calculations produce primary to near-primary magma solutions for the olivine-phyric shergottites NWA 6234 and NWA 4925, in agreement with previous interpretations based on the geochemistry, mineralogy, and petrography of these rocks (*Gross et al., 2013*; *Peel et al.*, 2023). The estimated T_P values are 1482 °C and 1466 °C for NWA 6234 and NWA 4925, respectively. Furthermore, predicted olivine compositions in equilibrium with primary magmas with Mg# ~59–60 are Fo_{82}, which are close to the most forsteritic olivine compositions in both meteorites (i.e., Fo_{78} for NWA 6234 and Fo_{81} for NWA 4925). The somewhat larger difference between predicted olivine and measured olivine cores in NWA 6234 could be ascribed to relatively minor fractional crystallization of the primary magma, which has been proposed based on low Ni contents in the bulk rock and in olivine megacrysts (*Peel et al.*, 2023).

Paired meteorites LAR 06319 and LAR 12011–12, as well as NWA 1068, are also

found to be primary to near-primary magmas in equilibrium with olivine Fo_{81}–82. However, olivine cores from these rocks have compositions lower than Fo_{77} (*Basu Sarbadhikari et al.*, 2011; *Balta et al.*, 2013), suggesting that the primary magma may have experienced some olivine fractionation, followed by accumulation of olivine phenocrysts that nearly canceled out the compositional change (*Barrat et al.*, 2002; *Filiberto et al.*, 2010). Alternative solutions can be calculated using estimates of the parental magmas that correct for olivine accumulation following magma fractionation (e.g., *Balta et al.*, 2013; *Filiberto et al.*, 2010). With these parental magmas, PRIMARSMELT yields F_{AFM} primary magmas that require olivine addition of ~12% and ~18% for LAR 06319 and NWA 1068, respectively, with T_P values of 1457 °C and 1466 °C. Similar considerations apply to meteorites NWA 8686 and NWA 5990, which contain significantly more fayalitic olivine than that in equilibrium with their bulk composition. PRIMARSMELT predicts equilibrium olivine compositions of Fo_{83} for these meteorites, but their measured olivine cores are Fo_{52} for NWA 8686 and Fo_{59} for NWA 5990 (*Irving*, 2010; *Nicklas et al.*, 2022). This disparity may be related to entrainment of olivine formed from more fractionated magmas or assimilation of evolved crustal material (*Nicklas et al.*, 2022). Thus, neither NWA 8686 nor NWA 5990 can be used for primary magma calculations.

Meteorites Y–980459 and NWA 5789 are believed to represent mantle-derived compositions. The olivine in these rocks is in equilibrium with their bulk composition and has cores as primitive as Fo_{84}–85 (*Usui et al.*, 2008; *Gross et al.*, 2011). These olivine compositions are significantly more forsteritic than predicted with PRIMARSMELT for F_{AFM} solutions (~Fo_{80}) but close to those obtained for F_{batch} solutions (~Fo_{83}). For the F_{AFM} solutions, PRIMARSMELT predicts that Y–980459 and NWA 5789 accumulated ~20% olivine and yields T_P estimates of 1405 °C and 1418 °C, respectively. In contrast, the F_{batch} primary magmas necessitate ~10% olivine subtraction and have T_P values of 1461 °C for Y–980459 and 1471 °C for NWA 5789.

Because PRIMARSMELT requires an intersection between an olivine fractionation line and a melt fraction produced by partial melting of the source to find a primary magma solution, the compositions of Y–980459 and NWA 5789 can only yield near-primary magmas in equilibrium with Fo>80–83 if their mantle source has higher Mg#. For example, using the mantle composition from *Yoshizaki and McDonough* (2020; Mg# 79; YM) instead of DW results in F_{AFM} near-primary magmas in equilibrium with Fo_{86} at T_P values of 1521 °C and 1539 °C for Y–980459 and

NWA 5789, respectively. These estimates are within error of values inferred from experiments and constraints from mineral equilibria (differences of ~10–30 °C; *Musselwhite et al.*, 2006; *Gross et al.*, 2011; *Filiberto and Dasgupta*, 2015). By contrast, if these meteorites were produced by batch melting of this less FeO-rich source, they would represent fractionated compositions that lost ~11–14% olivine, and their primary magmas would be in equilibrium with Fo_{90} at mantle potential temperatures of ~1570–1578 °C.

5.2 Effects and implications of considering a more magnesian mantle source

Numerous studies have investigated the Martian mantle composition using data from Martian meteorites, remote sensing, and geophysical observations. These studies have inferred mantle compositions with Mg# values ranging from 75 to 86 (*Dreibus and Wänke*, 1984; *Sanloup et al.*, 1999; *Musselwhite et al.*, 2006; *Taylor*, 2013; *Khan et al.*, 2018, 2022; *Yoshizaki and McDonough*, 2020; *Collinet et al.*, 2023), likely indicating a compositionally heterogenous mantle in terms of Mg# (*Udry et al.*, 2020; *Collinet et al.*, 2023). The source composition is an important parameter in PRIMARSMELT calculations, as varying Mg# values of the source will impact model results. To assess the influence of considering a more MgO-rich source, we conducted primary magma calculations with PRIMARSMELT assuming the YM mantle source composition (Mg# 79). The results of these calculations are presented in Supporting Information S2 and Figures S1–S5 in Supporting Information S3.

One consequence of a higher Mg# mantle source in PRIMARSMELT is that the resulting primary magma for a particular rock will have a higher MgO content, assuming a successful solution is obtained. As a result, that primary magma will have higher T_P and P_i than a solution from a more FeO-rich mantle. This prediction likely holds true as long as the source Mg# remains relatively close to that of DW, as the model parameters that describe partial melting relationships may not change significantly. However, as the source deviates further from DW, different parameters and functional forms may better describe the systematics of partial melting (e.g., *Herzberg et al.*, 2023). This implies that higher MgO contents in primary magmas from MgO-rich mantle sources may not always correspond to higher mantle potential temperatures. For example, a primary magma with 10 wt.% MgO estimated with PRIMARSMELT yields a T_P of ~1335 °C, whereas the same T_P is predicted with PRIMELT3-P (*Herzberg et al.*, 2023) for a primary magma with 11.2 wt.% MgO, which assumes a source representative of the terrestrial mantle.

In addition to higher T_P values, an increase in the MgO content of a primary magma for a given rock also implies a different extent of olivine addition or subtraction to find a primary magma. For lithologies such as basaltic shergottites or basalts from Gusev and Gale craters, this implies even greater fractionation, as more olivine addition would be necessary to obtain a solution. Conversely, for rocks that accumulated olivine, like olivine-phyric shergottites, less olivine subtraction would be needed, potentially resulting in near-primary magma compositions for some lithologies (e.g., Y–980459 and NWA 5789, with source Mg# 79 for F_{AFM} solutions). However, assuming the same Mg# for the mantle source, some olivine-phyric shergottites would need to be interpreted as fractionated lavas (e.g., EETA 79001A, LAR 06319, Tissint), which is inconsistent with their cumulate nature.

Similarly, a more magnesian source will result in primary magmas in equilibrium with more forsteritic olivine. As demonstrated above, an increase in Mg# from 75 (DW) to 79 (YM) is necessary to explain the forsteritic olivine cores in meteorites Y–980459 and NWA 5789. However, the DW mantle composition is sufficient to predict Fo contents similar to those of olivine cores in meteorites NWA 6234 and NWA 4925, also interpreted as near-primary magmas. This requirement of different mantle sources to achieve primary magma solutions consistent with the olivine chemistry of olivine-phyric shergottites further supports the idea of a heterogenous Martian mantle.

While PRIMARSMELT can perform primary magma calculations using variable source compositions, the model parameters will remain the same as those calibrated using the DW/LF source (or a Mg# of ~75). Consequently, the uncertainty in all the calculated variables will increase to an unknown extent as the source departs significantly from this mantle composition. However, the agreement between F_{AFM} primary magma solutions for meteorites Y–980459 and NWA 5789 (assuming a mantle source with Mg# 79) and experimental/phase equilibria constraints suggests that PRIMARSMELT can yield successful results for source compositions beyond its original calibration.

5.3 The case of evolved basaltic shergottites

The application of PRIMARSMELT to highly evolved basaltic shergottites results in primary magma solutions that require significant olivine addition and are, in most cases, flagged for clinopyroxene fractionation (see Supporting Information S2). For example, the Los Angeles meteorite is a high-Al basalt formed by extensive frac-

tionation of a primary magma and relatively close to a liquid composition saturated in plagioclase and clinopyroxene (*Rubin et al.*, 2000; *Treiman and Filiberto*, 2015). PRIMARSMELT yields a F_{AFM} solution with ~70% olivine fractionation and a T_P of 1547 °C for Los Angeles. This solution is, however, unrealistic as PRIMARSMELT only considers olivine fractionation, whereas the Los Angeles liquid also fractionated clinopyroxene and plagioclase. This results in a liquid with higher MgO than the true primary magma, with the corresponding T_P representing only an upper limit of its actual value.

Zagami and Shergotty are also basaltic shergottites formed by olivine fractionation from a primary melt (*Stolper and McSween*, 1979). The fractions of olivine required to be added to find F_{AFM} solutions with the bulk compositions of Zagami and Shergotty are 10% and 25%, with T_P of 1436 °C and 1481 °C, respectively. While these solutions indicate Zagami and Shergotty are closer to primary magmas than Los Angeles, petrographic analysis and experiments indicate that their fractionation history cannot be explained by olivine fractionation only. Instead, the formation of Zagami and Shergotty may have also involved either fractionation or accumulation of variable amounts of pyroxene, so their bulk composition represents liquids plus cumulus phases (*Stolper and McSween*, 1979; *McCoy et al.*, 1992). We therefore interpret the T_P values obtained for these meteorites, which assume only olivine fractionation, as maximum estimates.

5.4 The origin of two distinct rocks in EETA 79001

EETA 79001 is a Martian meteorite consisting of two igneous lithologies separated by a gradational contact (*Goodrich*, 2003; *Van Niekerk et al.*, 2007). Understanding the relationship between these lithologies is crucial for deciphering magmatic and differentiation processes within the Martian crust. Lithology A is considered an olivine-phyric shergottite, with crystals of olivine, pyroxene, and Fe–Ti oxides (>1 mm) within a groundmass of mainly clinopyroxene and plagioclase (*McSween and Jarosewich*, 1983; *Goodrich*, 2003). The nature of most olivine crystals in lithology A—whether formed in equilibrium with the parental melt or as xenocrysts crystallizing from a different liquid—is debated (*McSween and Jarosewich*, 1983; *Herd et al.*, 2002; *Goodrich*, 2003; *Liu et al.*, 2013). Lithology B, by contrast, is an aphyric basaltic rock consisting of a groundmass comprising mostly clinopyroxene and plagioclase, more coarse-grained than the groundmass of lithology A (*McSween and Jarosewich*, 1983). Several models have been proposed for the relationship between lithologies A and B in EETA 79001, including magmatic differentiation

(*Goodrich*, 2003; *Van Niekerk et al*., 2007), magma mixing (*Wadhwa et al*., 1994), impact mixing (*Mittlefehldt et al*., 1999), formation of B as a xenolith within A (*Liu et al*., 2013), or the two lithologies representing different magma pulses (*McSween and Jarosewich*, 1983).

PRIMARSMELT can provide insights into the petrogenesis of lithologies A and B in EETA 79001. Using the bulk compositions for both lithologies from *Lodders* (1998) as an input, PRIMARSMELT calculates different F_{AFM} solutions, with melt fractions of 0.40 and 0.26 that require ~7% olivine subtraction and ~27% olivine addition for lithologies A and B, respectively. The primary magma composition for lithology B has higher SiO_2, Al_2O_3, and alkali contents than that of A, whereas the Mg# of both solutions is almost the same (i.e., ~58–59). This magma is predicted to be in equilibrium with Fo_{81}, as measured in the most magnesian olivine cores found in lithology A. More importantly, the estimated T_P and P_i of both lithologies are nearly identical, with values of ~1430 °C and 3.6 GPa, respectively. These results suggest that lithologies A and B may have originated at the same conditions from different batches of magma of the same mantle source, favoring either a xenolithic relationship between the two rocks or the interpretation that each rock formed from a separate magmatic pulse and followed a distinct crystallization path.

5.5 Comparison with MAGMARS

PRIMARSMELT and MAGMARS are programs designed to answer similar questions through different approaches. PRIMARSMELT is a model that implements both inverse and forward modeling approaches to estimate the primary magma composition of Martian basalts, along with their melt fraction and formation conditions. PRIMARSMELT implements a straightforward algorithm that finds a primary magma solution where the crystallization path of a specified rock composition—achieved through either fractionation or olivine accumulation—intersects the melt fraction that would be generated by partial melting of the Martian mantle. It assumes partial melting can occur through either batch or accumulated fractional melting. MAGMARS, on the other hand, is a forward model that can estimate the source composition and melting conditions for Martian basalts by simulating the near-fractional polybaric melting and batch melting of FeO-rich mantle compositions on Mars. It employs an iterative algorithm that adjusts for pressure, temperature, and source composition, aiming for an optimal match between model outputs and the target composition. Unlike PRIMARSMELT, MAGMARS requires primary to near-primary magma composition inputs to infer the source composition and

formation conditions.

Both models have been constructed from similar sets of partial melting experiments of the Martian mantle, although using different functional forms, fitting methods, and weighting strategies. The two models are calibrated with partial melting experiments of DW and LF. MAGMARS also incorporates partial melting experiments of the terrestrial mantle, assigning them the lowest weight in model fitting. This inclusion enables MAGMARS to explore more magnesian mantle sources with reduced uncertainty. PRIMARSMELT also allows for adjustments in the mantle source composition by setting specific MgO and FeO contents. However, the uncertainty of the model predictions increases to an unknown extent as the source departs from Mg# 75.

Despite their differences, both models achieve comparable accuracy in replicating the melt fractions and pressure–temperature conditions of the calibration experiments. However, discrepancies in the outcomes of the two models warrant careful analysis. For example, *Collinet et al.* (2023) estimate a mantle source with Mg# 85–86 to produce a melt with the composition of Y–980459. Their results give T_P of 1470–1520 °C for batch melting and 1440–1450 °C for polybaric fractional melting, and olivine addition ranging from 0–7%. In contrast, PRIMARSMELT cannot find a solution for Y–980459 with such a high-Mg# source. Instead, valid primary magma solutions in equilibrium with olivine close to the composition of measured olivine cores are found using sources with Mg# 79–80 (*Sanloup et al.*, 1999; *Yoshizaki and McDonough*, 2020). The F_{batch} solutions yield T_P of 1538–1570 °C, whereas the F_{AFM} solutions yield T_P of ~1521–1538 °C.

Similarly, MAGMARS yields a mantle source composition with Mg# 77 and T_P of 1390 ± 40 °C for the average composition of the Adirondack-class basalts considering near-fractional polybaric melting. Using the source composition given by MAGMARS in PRIMARSMELT, for the sake of comparison, the resulting AFM primary magma composition for the Adirondack-class basalts has a T_P of ~1490 ± 28 °C. This difference of ~100 °C results from substantially different accumulated melt fractions and requirements of olivine fractionation. PRIMARSMELT yields $F_{\text{AFM}} \sim 0.26$ with ~14 wt.% olivine fractionation, whereas the MAGMARS melt fraction is ~0.06–0.07, requiring only ~2.5 wt.% olivine fractionation. Experimental studies, however, have shown that the composition of Adirondack-class basalts is in equilibrium with olivine Fo < 75 (*Monders et al.*, 2007; *Filiberto et al.*, 2008), too Fe-rich to be in equilibrium with a Martian mantle with Mg# > 75, which

suggests these rocks have likely fractionated olivine. Moreover, partial melting experiments have shown that Adirondack-class basalts are similar to primary melts representing ~0.25 melting of DW (*Collinet et al*., 2015), consistent with the results from PRIMARSMELT.

5.6 The thermal evolution of Mars

An attempt to reconstruct the thermal history of a planet can be made by using igneous rocks to track changes in mantle potential temperatures through time (*Herzberg et al*., 2010). This can be accomplished for Mars by combining PRIMARSMELT solutions with geochronology data from the igneous record, which provides a convenient temporal distribution across its geologic history. The shergottite meteorites exhibit a range of crystallization ages from ~150 Ma to ~2.4 Ga (*Udry et al*., 2020), rocks from the chassignite group crystallized at ~1.34 Ga (*Nyquist et al*., 2001; *Udry and Day*, 2018), and the basaltic clasts in polymictic breccias NWA 7034/7533 formed ~4.4 Ga (*Humayun et al*., 2013; *Nyquist et al*., 2016; *Cassata et al*., 2018). Basalts from Gusev and Gale craters have unknown absolute ages of crystallization, but their time of formation is likely constrained to Hesperian to late pre-Noachian times (*Grant et al*., 2004, 2014; *Greeley*, 2005; *Farley et al*., 2014).

To assess the thermal evolution of the Martian mantle, we paired our primary magma calculations and estimates of T_P from PRIMARSMELT with known or estimated crystallization ages for Martian basalts. Our analysis only considered compositions within two standard deviations of mean Fe/Mn, Al/Ti, and K/Ti ratios, filtering out rocks that might have originated from mantle sources affected by extensive metasomatism. We also excluded primary magma solutions with warnings for clinopyroxene fractionation or melting of volatile-bearing peridotite. Moreover, only olivine-phyric shergottites with olivine cores Fo_{78} or higher were considered, as more fayalitic olivine was likely produced from fractionated liquids rather than primary melts. For LAR 06319 and NWA 1068, we used estimates of their parent liquids rather than their bulk-rock composition (*Filiberto et al*., 2010; *Balta et al*., 2013). Also, our T_P estimate for Y–980459 was calculated using a mantle source with Mg# 79 (i.e., *Yoshizaki and McDonough*, 2020) since cores of olivine megacrysts in this rock are more forsteritic than that in equilibrium with DW (*Usui et al.*, 2008).

Figure 11 shows resulting T_P values calculated with PRIMARSMELT against radio-

genic ages for Martian meteorites and inferred ranges of crystallization for Gusev and Gale crater basalts. The shergottite meteorites in our analysis span a period between 165 and 582 Ma and have T_P ranging from 1374–1532 °C, with an average of 1442 °C and a standard deviation (σ) from the mean of ~48 °C (n = 12). The parental magmas of the ~1.34 Ga chassignite meteorites yield a slightly lower average T_P than that of the shergottites—i.e., 1411 °C within a range of 1338–1462 °C (n = 10; $\sigma \approx$ 30 °C). These temperatures are remarkably similar to those obtained for Gusev crater (T_P average = 1410 °C; 1338–1478 °C; n = 10; $\sigma \approx$ 38 °C) and Gale crater basalts (T_P average = 1389 °C; 1248–1525 °C; n = 8; $\sigma \approx$ 100 °C), which may have crystallized in a period between the late pre-Noachian and the late Hesperian. The ~4.4 Ga igneous clasts in the polymict breccias NWA 7034/7533, on the other hand, display T_P values between 1235 °C and 1457 °C, with an average of 1320 °C (n = 23; $\sigma \approx$ 48 °C), which is lower than the values obtained for younger lithologies.

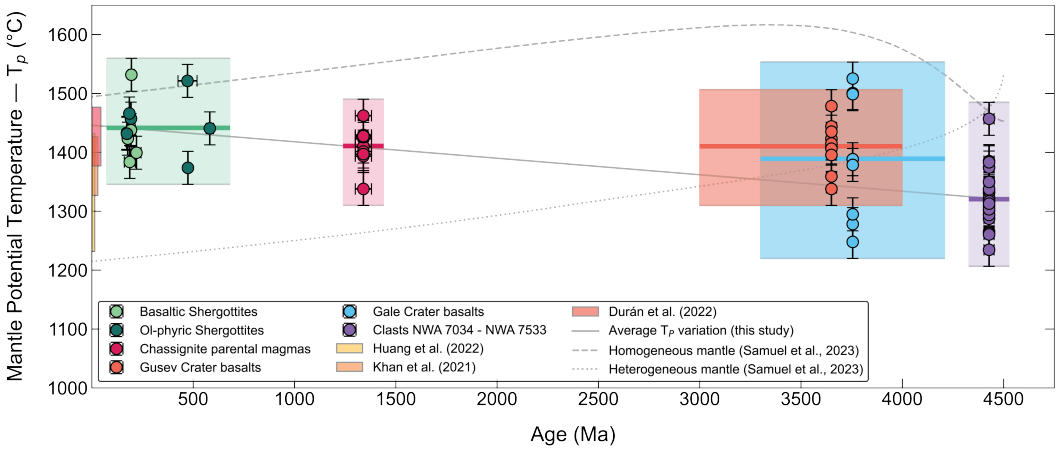


Figure 4.11: Estimated mantle potential temperatures for Martian basalts potentially derived from primary magmas versus their inferred crystallization age. Temperatures correspond to F_{AFM} solutions. Ages for basalts from Gusev (orange) and Gale (light blue) craters are shown as ranges inferred from geological interpretations, with a radiometric exposure age used in the case of Gale. The shaded regions denote the T_P ranges for each group. Colored boxes at the present day represent T_P estimates from inversion models of seismic data obtained by InSight. The solid gray line marks the overall T_P trend based on the results of this study. The gray dashed and dotted lines show modeled T_P estimates through time from *Samuel et al.* (2023) for a compositionally homogeneous mantle and for a mantle containing a basal, partially molten layer, respectively. Mantle potential temperatures from *Samuel et al.* (2023) were derived from uppermost-mantle temperatures together with lithospheric thickness plus the uppermost thermal boundary layer.

Our results for the average mantle potential temperature defined by Martian sher-

gottites are ~40–300 °C lower than the 1480–1745 °C values estimated by *iliberto* (2017) and *Filiberto and Dasgupta* (2015). *Collinet et al*. (2023) also determined a T_P of 1470–1520 °C (assuming batch melting) for meteorites Y–980459 and LAR 06319, nearly identical to our F_{AFM} solutions with a mantle source Mg# 79. In general, our range of T_P estimates for the shergottite meteorites agree with the modern-day ambient mantle temperatures that best match models of seismic data inversion from the InSight mission (i.e., *Khan et al*., 2021: ~1330–1430 °C; *Durán et al*., 2022: ~1380–1480 °C; *Huang et al*., 2022: ~1230–1430 °C; Figure 11). This similarity is evidence that the shergottite meteorites, or at least a subset of them, record ambient mantle conditions rather than plume-related magmatism or thermal anomalies, thus providing a reasonable estimate of the thermal state of the Martian mantle between 165 and 582 Ma. The combination of present-day T_P estimates with our results from shergottite meteorites shows that mantle potential temperatures on Mars have remained relatively constant for at least ~600 Ma, with an average T_P of 1442 ± 40 °C, higher than that estimated for Earth's mantle beneath mid-ocean ridges (i.e., 1350 ± 50 °C; *Herzberg et al*., 2007).

Relative to the estimated values from *Filiberto* (2017), the average T_P estimates from PRIMARSMELT for the basaltic rocks from Gusev and Gale craters, as well as clasts in polymict breccias NWA 7034/7533, are lower by ~50 °C. For the Adirondack-class basalts from Gusev crater, the discrepancy is significantly larger: we obtain T_P values of ~1408–1423 °C, whereas *Filiberto* (2017) estimated ~1522–1551 °C. Instead, our results are similar to those calculated with MAGMARS for the Adirondack-class rocks (i.e., 1390 ± 40 °C; *Collinet et al*., 2021). Likewise, the range of 1320–1520 °C for NWA 7034/7475/7533 predicted by *Collinet et al*. (2023) overlaps with our predicted values but appears higher than our average estimate for all the clasts in these meteorites (i.e., 1320 ± 48 °C). However, the results of *Collinet et al*. (2021; 2023) differ from ours in the mantle composition required (Mg# 77–81).

Together, our average T_P estimates exhibit a trend that suggests an increase of ~110 °C in mantle potential temperatures from ~4.4 Ga to 165 Ma. This trend is at odds with other studies concluding that the igneous record from Mars reflects a simple thermal history consistent with convective cooling of the mantle (*Baratoux et al*., 2011, 2013; *Filiberto and Dasgupta*, 2015; *Filiberto*, 2017). The previous conclusion relies on comparatively lower T_P for the Hesperian and Amazonian volcanic provinces (*Baratoux et al*., 2011; 2013) relative to higher T_P estimates for older basalts (*Filiberto and Dasgupta*, 2015; *Filiberto*, 2017). This interpretation is

challenged, however, by our consistently lower estimates for the T_P preserved in the igneous record from Mars compared to those of *Filiberto* (2017), which also imply that the primary magmas of some basaltic shergottites may record ambient mantle temperatures instead of plume-related magmatism. Furthermore, while the T_P values from *Baratoux et al.* (2011; 2013) are consistent with the relatively constant thermal history that we infer from our PRIMARSMELT calculations, their results from pMELTS may underestimate the actual mantle temperatures from which Hesperian and Amazonian volcanic provinces were derived. Partial melting simulations of DW with pMELTS have been shown to significantly overestimate FeO and underestimate SiO_2 contents of the generated liquids, even after empirical corrections are applied (*Balta and McSween Jr.*, 2013; *Collinet et al.*, 2015, 2021). Such discrepancies would result in pMELTS predicting mantle potential temperatures lower than their actual value for any target FeO and SiO_2 at a given melt fraction.

Hence, the possibility of a different thermal history on Mars cannot be ruled out. Inefficient heat loss may be a natural consequence of a stagnant-lid regime (*Batra and Foley*, 2022), leading to minimal mantle cooling or even the possibility that the Martian mantle has heated up over time, as has been proposed in studies of paleo-heat fluxes (*Ruiz et al.*, 2011; *Ruiz*, 2014). Indeed, some numerical models, geodynamic simulations, and convective scaling laws predict that, at least for specific time intervals, the mantle potential temperature of a planet can increase if the thermal lithosphere is thick, the abundance of radioactive elements in the upper mantle is large, or convection is slow due to high viscosity in a cold or dry mantle (*O'Neill et al.*, 2007; *Fraeman and Korenaga*, 2010; *Plesa et al.*, 2015; *Foley*, 2018; *Thiriet et al.*, 2019). The possibility of inefficient/delayed mantle cooling on Mars is especially interesting not only because it challenges the conventional idea of secular cooling of small planetary bodies like Mars (*Batra and Foley*, 2022; Stevenson, 2003), but also because it has implications for the volcanic and water degassing history of planetary interiors (*Stevenson*, 2003; *Fraeman and Korenaga*, 2010).

If models predicting secular mantle cooling on Mars are valid, then our results suggest that shergottite T_P estimates reflect formation in transient thermal anomalies. For example, while the average T_P calculated here for shergottite meteorites is similar to temperatures inferred from a thermal evolution model with a homogeneous mantle composition, this average estimate is >200 °C higher than predicted for a stratified mantle with a partially molten layer at the bottom (*Samuel et al.*, 2023). This stratified mantle model implies that ambient mantle temperatures in the last billion

years were likely too cold to produce shergottite parent magmas. Thus, shergottites might represent thermal anomalies, likely from hot spot magmatism linked to the partially molten layer. However, the present-day ambient mantle T_P predicted for this heterogeneous mantle model is lower than inferred by other studies also using InSight seismic data (*Khan et al.*, 2021; *Durán et al.*, 2022; *Huang et al.*, 2022).

5.7 Increase of initial melting pressure

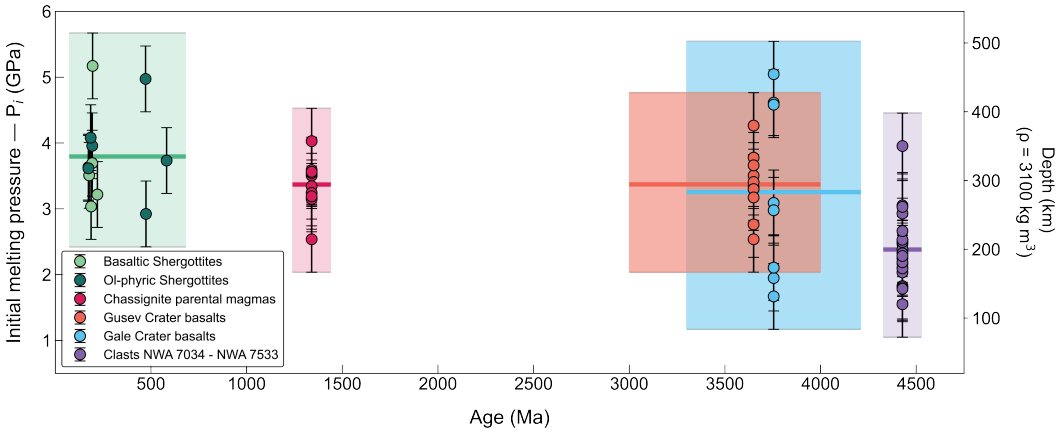


Figure 4.12: Estimated initial melting pressure (P_i) and depth of melting for Martian basalts potentially derived from primary magmas versus their inferred crystallization age. P_i values correspond to F_{AFM} solutions. Depths of melting recalculated from P_i assume an average lithospheric density of 3100 kg m^{-3}. Ages for basalts from Gusev (orange) and Gale (light blue) craters are shown as ranges inferred from geological interpretations, with a radiometric exposure age used for Gale.

The increasing trend in mantle potential temperature with time translates into an increase in average initial melting pressure. According to the initial pressure function calibrated above, this increase extends from ~ 2.4 GPa for clasts in NWA 7034/7533 to ~ 3.8 GPa for the shergottite meteorites. Assuming a mean lithospheric density of 3100 kg m^{-3}, this corresponds to an increase in initial melting depth from ~ 210 to 330 km. The average P_i for Gusev crater basalts and chassignite parental magmas are approximately the same (~ 3.4 GPa, ~ 290 km) and are very similar to that of the rocks from Gale crater (~ 3.3 GPa, ~ 280 km).

Collinet et al. (2023) obtained pressures for the shergottites of 1.6 ± 0.5 GPa (~ 140 km), interpreted as final pressures of equilibration with the mantle (P_f). These final pressures, however, were not particular to the shergottites but also relatively similar to values predicted for other compositions and mantle sources they considered. This implies that, while the base of the melting region in the mantle may have become deeper as the martian mantle warmed over time, the transition

zone between the convective and conductive layers may have remained relatively constant over time.

However, the expectation is that the final pressures of melt equilibration should match the thickness of the lithosphere, yet the estimated range of present-day lithospheric thickness inferred from seismic inversions is more similar to the initial melting depth we infer (i.e., ~ 200–450 km; Khan et al., 2018; *Durán et al.*, 2022). It may be that there are local variations in lithospheric thickness not resolved by the simple seismic models, which allow convective upwellings to reach shallower levels.

We note that the pressure difference between the onset and termination of decompression melting is expected to be positively correlated with extent of melting, other things being equal. In this context, the higher melt fractions predicted independently by PRIMARSMELT and MAGMARS for the younger lithologies are consistent with an increase in ΔP (P_i getting deeper, but P_f remaining roughly constant). This would also suggest that crustal production rates may have increased over time due to higher potential temperatures. However, an increasingly depleted (less fertile) mantle composition would change the relationship between ΔP and F_{AFM}. Evidence that these quantities have both increased may suggest a need for crustal recycling to maintain fertility in the Martian mantle and replenish the supply of radioactive elements at depth driving the system.

6. Conclusions

PRIMARSMELT is a new model for calculating primary magma compositions for Mars, with software implementations in Excel and Python. It implements an algorithm similar to that of the PRIMELT3-P model (and earlier versions) for terrestrial compositions (*Herzberg*, 2023). However, PRIMARSMELT has been specifically calibrated for Mars using available partial melting experiments of model Martian mantle compositions. PRIMARSMELT is intended to estimate primary magma compositions and corresponding melt fractions for basaltic Martian rocks that have only fractionated or accumulated olivine. PRIMARSMELT also uses an internal parameterization based on experimental liquid compositions to estimate *P–T* melting conditions in the source and mantle potential temperatures for primary magma solutions.

When applied to natural samples, PRIMARSMELT correctly identifies their most relevant petrographic features. Basaltic rocks interpreted to have crystallized from fractionated magmas are found to require olivine addition to obtain primary magma

solutions, whereas rocks interpreted to have accumulated olivine are found to require olivine subtraction. PRIMARSMELT can be used to determine the conditions under which rocks can be interpreted as primary to near-primary magmas. For example, meteorites Y–980459 and NWA 5789 can only represent primary magmas if their mantle source has Mg# $\sim$ 79. Furthermore, petrogenetic links between related rocks can be inferred from PRIMARSMELT results. For lithologies A and B in EETA 79001, two distinct primary solutions are obtained, which yield identical T_{P} and P_i conditions, suggesting that each rock represents a distinct liquid batch produced from the same mantle source.

Mantle potential temperature estimates derived from PRIMARSMELT for young shergottite meteorites suitable for primary magma calculations are considerably lower than previous estimates. Our results indicate an average T_{P} of $\sim 1442 \pm 40$°C for the shergottites, within the range of ambient mantle temperatures inferred from geophysical models. Older basaltic rocks from Gusev and Gale craters and clasts in polymict breccias NWA 7034/7533 also record potential temperatures $\sim$ 50°C lower than previously estimated. Together, our results can be interpreted to show nearly constant or potentially increasing mantle potential temperatures throughout Mars's geological history. This trend could be a natural consequence of inefficient heat loss, as expected for a planet in stagnant-lid mode.

References

Agee, C. B., & Draper, D. S. (2004). Experimental constraints on the origin of Martian meteorites and the composition of the Martian mantle. *Earth and Planetary Science Letters*, 224(3), 415–429.

Agee, C. B., Wilson, N. V., McCubbin, F. M., Ziegler, K., Polyak, V. J., Sharp, Z. D., et al. (2013). Unique meteorite from early Amazonian Mars: Water-rich basaltic breccia Northwest Africa 7034. *Science*, 339(6121), 780–785.

Asimow, P. D., & Ghiorso, M. S. (1998). Algorithmic modifications extending MELTS to calculate subsolidus phase relations. *American Mineralogist*, 83(9–10), 1127–1132.

Balta, J. B., & McSween Jr., H. Y. (2013). Application of the MELTS algorithm to Martian compositions and implications for magma crystallization. *Journal of Geophysical Research: Planets*, 118(12), 2502–2519.

Balta, J. B., Sanborn, M., McSween Jr., H. Y., & Wadhwa, M. (2013). Magmatic history and parental melt composition of olivine-phyric shergottite LAR 06319: Importance of magmatic degassing and olivine antecrysts in Martian magmatism. *Meteoritics & Planetary Science*, 48(8), 1359–1382.

Baratoux, D., Toplis, M. J., Monnereau, M., & Sautter, V. (2013). The petrological expression of early Mars volcanism. *Journal of Geophysical Research: Planets*, 118(1), 59–64.

Baratoux, D., Toplis, M. J., Monnereau, M., & Gasnault, O. (2011). Thermal history of Mars inferred from orbital geochemistry of volcanic provinces. *Nature*, 472(7343), 338–341.

Barrat, J. A., Jambon, A., Bohn, M., Gillet, P. h, Sautter, V., Göpel, C., et al. (2002). Petrology and chemistry of the Picritic Shergottite North West Africa 1068 (NWA 1068). *Geochimica et Cosmochimica Acta*, 66(19), 3505–3518.

Basu Sarbadhikari, A., Goodrich, C. A., Liu, Y., Day, J. M. D., & Taylor, L. A. (2011). Evidence for heterogeneous enriched shergottite mantle sources in Mars from olivine-hosted melt inclusions in Larkman Nunatak 06319. *Geochimica et Cosmochimica Acta*, 75(22), 6803–6820.

Batra, K., & Foley, B. (2022). Scaling laws for stagnant-lid convection with a buoyant crust. *Geophysical Journal International*, 228(1), 631–663.

Beattie, P., Ford, C., & Russell, D. (1991). Partition coefficients for olivine-melt and orthopyroxene-melt systems. *Contributions to Mineralogy and Petrology*, 109(2), 212–224.

Bertka, C. M., & Holloway, J. R. (1994). Anhydrous partial melting of an iron-rich mantle II: primary melt compositions at 15 kbar. *Contributions to Mineralogy and Petrology*, 115(3), 323–338.

Beyssac, O., Forni, O., Cousin, A., Udry, A., Kah, L. C., Mandon, L., et al. (2023). Petrological Traverse of the Olivine Cumulate Séítah Formation at Jezero Crater, Mars: A Perspective From SuperCam Onboard Perseverance. *Journal of Geophysical Research: Planets*, 128(7).

Brown, A. J., Viviano, C. E., & Goudge, T. A. (2020). Olivine-Carbonate Mineralogy of the Jezero Crater Region. *Journal of Geophysical Research: Planets*, 125(3).

Brown Krein, S., Molitor, Z. J., & Grove, T. L. (2021). ReversePetrogen: A Multiphase Dry Reverse Fractional Crystallization–Mantle Melting Thermobarometer Applied to 13,589 Mid-Ocean Ridge Basalt Glasses. *Journal of Geophysical Research: Solid Earth*, 126(8).

Cassata, W. S., Cohen, B. E., Mark, D. F., Trappitsch, R., Crow, C. A., Wimpenny, J., et al. (2018). Chronology of martian breccia NWA 7034 and the formation of the martian crustal dichotomy. *Science Advances*, 4(5).

Collinet, M., Médard, E., Charlier, B., Vander Auwera, J., & Grove, T. L. (2015). Melting of the primitive martian mantle at 0.5–2.2 GPa and the origin of basalts and alkaline rocks on Mars. *Earth and Planetary Science Letters*, 427, 83–94.

Collinet, M., Plesa, A., Grove, T. L., Schwinger, S., Ruedas, T., & Breuer, D. (2021). MAGMARS: A Melting Model for the Martian Mantle and FeO-Rich Peridotite. *Journal of Geophysical Research: Planets*, 126(12).

Collinet, M., Plesa, A.-C., Ruedas, T., Schwinger, S., & Breuer, D. (2023). The Temperature and Composition of the Mantle Sources of Martian Basalts. *Geophysical Research Letters*, 50(11).

Connolly, J. A. D., & Petrini, K. (2002). An automated strategy for calculation of phase diagram sections and retrieval of rock properties as a function of physical conditions. *Journal of Metamorphic Geology*, 20(7), 697–708.

Cousin, A., Sautter, V., Payré, V., Forni, O., Mangold, N., Gasnault, O., et al. (2017). Classification of igneous rocks analyzed by ChemCam at Gale crater, Mars. *Icarus*, 288, 265–283.

Dasgupta, R., & Hirschmann, M. M. (2007). Effect of variable carbonate concentration on the solidus of mantle peridotite. *American Mineralogist*, 92(2–3), 370–379.

Ding, S., Dasgupta, R., & Tsuno, K. (2020). The Solidus and Melt Productivity of Nominally Anhydrous Martian Mantle Constrained by New High Pressure–Temperature Experiments—Implications for Crustal Production and Mantle Source Evolution. *Journal of Geophysical Research: Planets*, 125(4).

Dreibus, G., & Wänke, H. (1984). Accretion of the Earth and the inner planets. In *Proceedings of the 27th International Geological Congress* (Vol. 11, pp. 1–20).

Durán, C., Khan, A., Ceylan, S., Zenhäusern, G., Stähler, S., Clinton, J. F., & Giardini, D. (2022). Seismology on Mars: An analysis of direct, reflected, and converted seismic body waves with implications for interior structure. *Physics of the Earth and Planetary Interiors*, 325, 106851.

Edwards, P. H., Bridges, J. C., Wiens, R., Anderson, R., Dyar, D., Fisk, M., et al. (2017). Basalt–trachybasalt samples in Gale Crater, Mars. *Meteoritics & Planetary Science*, 52(11), 2410–2931.

Ehlmann, B. L., & Edwards, C. S. (2014). Mineralogy of the Martian surface. *Annual Review of Earth and Planetary Sciences*, 42, 291–315.

Farley, K. A., Malespin, C., Mahaffy, P., Grotzinger, J. P., Vasconcelos, P. M., Milliken, R. E., et al. (2014). In Situ Radiometric and Exposure Age Dating of the Martian Surface. *Science*, 343(6169).

Farley, K. A., Stack, K. M., Shuster, D. L., Horgan, B. H. N., Hurowitz, J. A., Tarnas, J. D., et al. (2022). Aqueously altered igneous rocks sampled on the floor of Jezero crater, Mars. *Science*, 377(6614).

Filiberto, J. (2008). Experimental constraints on the parental liquid of the Chassigny meteorite: A possible link between the Chassigny meteorite and a Martian Gusev basalt. *Geochimica et Cosmochimica Acta*, 72(2), 690–701.

Filiberto, J., Treiman, A. H., & Le, L. (2008). Crystallization experiments on a Gusev Adirondack basalt composition. *Meteoritics & Planetary Science*, 43(7), 1137–1146.

Filiberto, J. (2017). Geochemistry of Martian basalts with constraints on magma genesis. *Chemical Geology*, 466, 1–14.

Filiberto, J., & Dasgupta, R. (2011). Fe^{2+}–Mg partitioning between olivine and basaltic melts: Applications to genesis of olivine-phyric shergottites and conditions of melting in the Martian interior. *Earth and Planetary Science Letters*, 304(3), 527–537.

Filiberto, J., & Dasgupta, R. (2015). Constraints on the depth and thermal vigor of melting in the Martian mantle. *Journal of Geophysical Research: Planets*, 120(1), 109–122.

Filiberto, J., Musselwhite, D. S., Gross, J., Burgess, K., Le, L., & Treiman, A. H. (2010). Experimental petrology, crystallization history, and parental magma characteristics of olivine-phyric shergottite NWA 1068: Implications for the petrogenesis of "enriched" olivine-phyric shergottites. *Meteoritics & Planetary Science*, 45(8), 1258–1270.

Foley, B. J. (2018). The dependence of planetary tectonics on mantle thermal state: applications to early Earth evolution. *Philosophical Transactions of the Royal Society A: Mathematical, Physical and Engineering Sciences*, 376(2132).

Fraeman, A. A., & Korenaga, J. (2010). The influence of mantle melting on the evolution of Mars. *Icarus*, 210(1), 43–57.

Ghiorso, M. S., & Sack, R. O. (1995). Chemical mass transfer in magmatic processes IV. A revised and internally consistent thermodynamic model for the interpolation and extrapolation of liquid–solid equilibria in magmatic systems at elevated temperatures and pressures. *Contributions to Mineralogy and Petrology*, 119(2–3), 197–212.

Ghiorso, M. S., Hirschmann, M. M., Reiners, P. W., & Kress, V. C. (2002). The pMELTS: A revision of MELTS for improved calculation of phase relations and major element partitioning related to partial melting of the mantle to 3 GPa. *Geochemistry, Geophysics, Geosystems*, 3(5), 1–35.

Goodrich, C. A. (2003). Petrogenesis of olivine-phyric shergottites Sayh al Uhaymir 005 and Elephant Moraine A79001 lithology A. *Geochimica et Cosmochimica Acta*, 67(19), 3735–3772.

Goodrich, C. A., Herd, C. D. K., & Taylor, L. A. (2003). Spinels and oxygen fugacity in olivine-phyric and lherzolitic shergottites. *Meteoritics & Planetary*

Science, 38(12), 1773–1792.

Grant, J. A., Arvidson, R., Bell, J. F., Cabrol, N. A., Carr, M. H., Christensen, P., et al. (2004). Surficial Deposits at Gusev Crater Along Spirit Rover Traverses. *Science*, 305(5685), 807–810.

Grant, J. A., Wilson, S. A., Mangold, N., Calef III, F., & Grotzinger, J. P. (2014). The timing of alluvial activity in Gale crater, Mars. *Geophysical Research Letters*, 41(4), 1142–1149.

Greeley, R., Foing, B. H., McSween Jr., H. Y., Neukum, G., Pinet, P., van Kan, M., et al. (2005). Fluid lava flows in Gusev crater, Mars. *Journal of Geophysical Research: Planets*, 110(E5).

Green, D. H., Falloon, T. J., Eggins, S. M., & Yaxley, G. M. (2001). Primary magmas and mantle temperatures. *European Journal of Mineralogy-Stuttgart*, 13(3), 437–452.

Gross, J., Treiman, A. H., Filiberto, J., & Herd, C. D. K. (2011). Primitive olivine-phyric shergottite NWA 5789: Petrography, mineral chemistry, and cooling history imply a magma similar to Yamato-980459. *Meteoritics & Planetary Science*, 46(1), 116–133.

Gross, J., Filiberto, J., Herd, C. D. K., Daswani, M. M., Schwenzer, S. P., & Treiman, A. H. (2013). Petrography, mineral chemistry, and crystallization history of olivine-phyric shergottite NWA 6234: A new melt composition. *Meteoritics & Planetary Science*, 48(5), 854–871.

He, Q., Xiao, L., Hsu, W., Balta, J. B., McSween, H. Y., & Liu, Y. (2013). The water content and parental magma of the second chassignite NWA 2737: Clues from trapped melt inclusions in olivine. *Meteoritics & Planetary Science*, 48(3), 474–492. https://doi.org/10.1111/maps.12073

Herd, C. D. K. (2003). The oxygen fugacity of olivine-phyric Martian basalts and the components within the mantle and crust of Mars. *Meteoritics & Planetary Science*, 38(12), 1793–1805. https://doi.org/10.1111/j.1945-5100.2003.tb00015.x

Herd, C. D. K., Schwandt, C. S., Jones, J. H., & Papike, J. J. (2002). An experimental and petrographic investigation of Elephant Moraine 79001 lithology A: Implications for its petrogenesis and the partitioning of chromium and vanadium in a martian basalt. *Meteoritics & Planetary Science*, 37(7), 987–1000. https://doi.org/10.1111/j.1945-5100.2002.tb00871.x

Herd, C. D. K., Borg, L. E., Jones, J. H., & Papike, J. J. (2002). Oxygen fugacity and geochemical variations in the Martian basalts: Implications for Martian basalt petrogenesis and the oxidation state of the upper mantle of Mars. *Geochimica et Cosmochimica Acta*, 66(11), 2025–2036. https://doi.org/10.1016/S0016-7037(02)00828-1

Hernández-Montenegro, J. D., Asimow, P. D., & Herzberg, C. (2024). PRIMARSMELT: Primary magma compositions for Mars (1.0). *CaltechDATA*. https://doi.org/10.22002/tt8tr-knd42

Herzberg, C., & Asimow, P. D. (2008). Petrology of some oceanic island basalts: PRIMELT2.XLS software for primary magma calculation. *Geochemistry, Geophysics, Geosystems*, 9(9). https://doi.org/10.1029/2008GC002057

Herzberg, C., & Asimow, P. D. (2015). PRIMELT3 MEGA.XLSM software for primary magma calculation: Peridotite primary magma MgO contents from the liquidus to the solidus. *Geochemistry, Geophysics, Geosystems*, 16(2), 563–578. https://doi.org/10.1002/2014GC005631

Herzberg, C., & O'Hara, M. J. (2002). Plume-Associated Ultramafic Magmas of Phanerozoic Age. *Journal of Petrology*, 43(10), 1857–1883. https://doi.org/10.1093/petrology/43.10.1857

Herzberg, C., Asimow, P. D., Arndt, N., Niu, Y., Lesher, C. M., Fitton, J. G., et al. (2007). Temperatures in ambient mantle and plumes: Constraints from basalts, picrites, and komatiites. *Geochemistry, Geophysics, Geosystems*, 8(2). https://doi.org/10.1029/2006GC001390

Herzberg, C. T., Asimow, P. D., & Hernández-Montenegro, J. D. (2023). The Meaning of Pressure for Primary Magmas: New Insights From PRIMELT3-P. *Geochemistry, Geophysics, Geosystems*, 24(1), e2022GC010657. https://doi.org/10.1029/2022GC010657

Herzberg, C., Condie, K., & Korenaga, J. (2010). Thermal history of the Earth and its petrological expression. *Earth and Planetary Science Letters*, 292(1–2), 79–88. https://doi.org/10.1016/j.epsl.2010.01.022

Hewins, R. H., Humayun, M., Barrat, J.-A., Zanda, B., Lorand, J.-P., Pont, S., et al. (2020). Northwest Africa 8694, a ferroan chassignite: Bridging the gap between nakhlites and chassignites. *Geochimica et Cosmochimica Acta*, 282, 201–226. https://doi.org/10.1016/j.gca.2020.05.021

Huang, Q., Schmerr, N. C., King, S. D., Kim, D., Rivoldini, A., Plesa, A.-C., et al. (2022). Seismic detection of a deep mantle discontinuity within Mars by

InSight. *Proceedings of the National Academy of Sciences*, 119(42), e2204474119. https://doi.org/10.1073/pnas.2204474119

Humayun, M., Nemchin, A., Zanda, B., Hewins, R. H., Grange, M., Kennedy, A., et al. (2013). Origin and age of the earliest Martian crust from meteorite NWA 7533. *Nature*, 503(7477), 513–516. https://doi.org/10.1038/nature12764

Irving, A. (2010). Olivine-bearing diabasic shergottite Northwest Africa 5990: Petrology and composition of a new type of depleted martian igneous rock (Vol. 1833). Presented at the *41th Lunar and Planetary Science Conference*, 2010.

Jambon, A., Sautter, V., Barrat, J.-A., Gattacceca, J., Rochette, P., Boudouma, O., et al. (2016). Northwest Africa 5790: Revisiting nakhlite petrogenesis. *Geochimica et Cosmochimica Acta*, 190, 191–212.

Johnson, M. C., Rutherford, M. J., & Hess, P. C. (1991). Chassigny petrogenesis: Melt compositions, intensive parameters and water contents of Martian (?) magmas. *Geochimica et Cosmochimica Acta*, 55(1), 349–366.

Khan, A., Liebske, C., Rozel, A., Rivoldini, A., Nimmo, F., Connolly, J. A. D., et al. (2018). A Geophysical Perspective on the Bulk Composition of Mars. *Journal of Geophysical Research: Planets*, 123(2), 575–611.

Khan, A., Sossi, P. A., Liebske, C., Rivoldini, A., & Giardini, D. (2022). Geophysical and cosmochemical evidence for a volatile-rich Mars. *Earth and Planetary Science Letters*, 578, 117330.

Khan, A., Ceylan, S., van Driel, M., Giardini, D., Lognonné, P., Samuel, H., et al. (2021). Upper mantle structure of Mars from InSight seismic data. *Science*, 373(6553), 434–438.

Kiefer, W. S. (2003). Melting in the martian mantle: Shergottite formation and implications for present-day mantle convection on Mars. *Meteoritics & Planetary Science*, 38(12), 1815–1832.

Kiefer, W. S., Filiberto, J., Sandu, C., & Li, Q. (2015). The effects of mantle composition on the peridotite solidus: Implications for the magmatic history of Mars. *Geochimica et Cosmochimica Acta*, 162, 247–258.

Kinzler, R. J., & Grove, T. L. (1992). Primary magmas of mid-ocean ridge basalts 1. Experiments and methods. *Journal of Geophysical Research: Solid Earth*, 97(B5), 6885–6906.

Kizovski, T. V., Izawa, M. R. M., Tait, K. T., Moser, D. E., Day, J. M. D., Hyde, B. C., et al. (2020). Petrogenesis, alteration, and shock history of intermediate shergottite Northwest Africa 7042: Evidence for hydrous magmatism on Mars? *Geochimica et Cosmochimica Acta*, 283, 103–123.

Klein, E. M., & Langmuir, C. H. (1987). Global correlations of ocean ridge basalt chemistry with axial depth and crustal thickness. *Journal of Geophysical Research*, 92(B8), 8089–8115.

Kress, V. C., & Carmichael, I. S. E. (1991). The compressibility of silicate liquids containing Fe_2O_3 and the effect of composition, temperature, oxygen fugacity and pressure on their redox states. *Contributions to Mineralogy and Petrology*, 108(1–2), 82–92. Krot, A. N., Keil, K., Scott, E. R. D., Goodrich, C. A., & Weisberg, M. K. (2014). Classification of Meteorites and Their Genetic Relationships. In H. D. Holland & K. K. Turekian (Eds.), *Treatise on Geochemistry* (Second Edition) (pp. 1–63). Oxford: Elsevier.

Langmuir, C. H., Klein, E. M., & Plank, T. (1992). Petrological systematics of mid-ocean ridge basalts: constraints on melt generation beneath ocean ridges. *GMS*, 71, 183–280.

Lee, C.-T. A., Luffi, P., Plank, T., Dalton, H., & Leeman, W. P. (2009). Constraints on the depths and temperatures of basaltic magma generation on Earth and other terrestrial planets using new thermobarometers for mafic magmas. *Earth and Planetary Science Letters*, 279(1–2), 20–33.

Liu, Y., Tice, M. M., Schmidt, M. E., Treiman, A. H., Kizovski, T. V., Hurowitz, J. A., et al. (2022). An olivine cumulate outcrop on the floor of Jezero crater, Mars. *Science*.

Liu, Y., Balta, J. B., Goodrich, C. A., McSween, H. Y., & Taylor, L. A. (2013). New constraints on the formation of shergottite Elephant Moraine 79001 lithology A. *Geochimica et Cosmochimica Acta*, 108, 1–20.

Lodders, K. (1998). A survey of shergottite, nakhlite and chassigny meteorites whole-rock compositions. *Meteoritics & Planetary Science*, 33(S4), A183–A190.

Lodders, K., & Fegley, B. (1997). An Oxygen Isotope Model for the Composition of Mars. *Icarus*, 126(2), 373–394.

Longhi, J. (2002). Some phase equilibrium systematics of lherzolite melting: I. *Geochemistry, Geophysics, Geosystems*, 3(3), 1–33.

Matsukage, K. N., Nagayo, Y., Whitaker, M. L., Takahashi, E., & Kawasaki, T. (2013). Melting of the Martian mantle from 1.0 to 4.5 GPa. *Journal of Mineralogical and Petrological Sciences*, 108(4), 201–214.

McCoy, T. J., Taylor, G. J., & Keil, K. (1992). Zagami: Product of a two-stage magmatic history. *Geochimica et Cosmochimica Acta*, 56(9), 3571–3582.

McCubbin, F. M., Boyce, J. W., Novák-Szabó, T., Santos, A. R., Tartèse, R., Muttik, N., et al. (2016). Geologic history of Martian regolith breccia Northwest Africa 7034: Evidence for hydrothermal activity and lithologic diversity in the Martian crust. *Journal of Geophysical Research: Planets*, 121(10), 2120–2149.

McKenzie, D., & Bickle, M. J. (1988). The volume and composition of melt generated by extension of the lithosphere. *Journal of Petrology*, 29(3), 625–679.

McSween, H. Y., & Jarosewich, E. (1983). Petrogenesis of the Elephant Moraine A79001 meteorite: Multiple magma pulses on the shergottite parent body. *Geochimica et Cosmochimica Acta*, 47(8), 1501–1513.

McSween, H. Y., Taylor, G. J., & Wyatt, M. B. (2009). Elemental Composition of the Martian Crust. *Science*, 324(5928), 736–739.

Médard, E., McCammon, C. A., Barr, J. A., & Grove, T. L. (2008). Oxygen fugacity, temperature reproducibility, and H_2O contents of nominally anhydrous piston-cylinder experiments using graphite capsules. *American Mineralogist*, 93(11–12), 1838–1844.

Mittlefehldt, D. W., Lindstrom, D. J., Lindstrom, M. M., & Martinez, R. R. (1999). An impact-melt origin for lithology A of martian meteorite Elephant Moraine A79001. *Meteoritics & Planetary Science*, 34(3), 357–367.

Monders, A. G., Médard, E., & Grove, T. L. (2007). Phase equilibrium investigations of the Adirondack class basalts from the Gusev plains, Gusev crater, Mars. *Meteoritics & Planetary Science*, 42(1), 131–148.

Musselwhite, D. S., Dalton, H. A., Kiefer, W. S., & Treiman, A. H. (2006). Experimental petrology of the basaltic shergottite Yamato-980459: Implications for the thermal structure of the Martian mantle. *Meteoritics & Planetary Science*, 41(9), 1271–1290.

Nekvasil, H., McCubbin, F. M., Harrington, A., Elardo, S., & Lindsley, D. H. (2009). Linking the Chassigny meteorite and the Martian surface rock Backstay: Insights

into igneous crustal differentiation processes on Mars. *Meteoritics & Planetary Science*, 44(6), 853–869.

Nicklas, R. W., Day, J. M. D., Vaci, Z., Udry, A., Liu, Y., & Tait, K. T. (2021). Uniform oxygen fugacity of shergottite mantle sources and an oxidized martian lithosphere. *Earth and Planetary Science Letters*, 564, 116876.

Nicklas, R. W., Day, J. M. D., Vaci, Z., & Udry, A. (2022). Petrogenesis of Northwest Africa 8686: A ferroan olivine-phyric shergottite. *Meteoritics & Planetary Science*, 57(5), 947–964.

Niu, Y., & Batiza, R. (1991). An empirical method for calculating melt compositions produced beneath mid-ocean ridges: Application for axis and off-axis (seamounts) melting. *Journal of Geophysical Research: Solid Earth*, 96(B13), 21753–21777.

Nyquist, L. E., Bogard, D. D., Shih, C.-Y., Greshake, A., Stöffler, D., & Eugster, O. (2001). Ages and Geologic Histories of Martian Meteorites. In R. Kallenbach, J. Geiss, & W. K. Hartmann (Eds.), *Chronology and Evolution of Mars* (pp. 105–164). Dordrecht: Springer Netherlands.

Nyquist, L. E., Shih, C.-Y., McCubbin, F. M., Santos, A. R., Shearer, C. K., Peng, Z. X., et al. (2016). Rb-Sr and Sm-Nd isotopic and REE studies of igneous components in the bulk matrix domain of Martian breccia Northwest Africa 7034. *Meteoritics & Planetary Science*, 51(3), 483–498.

O'Hara, M. J. (1965). Primary magmas and the origin of basalts. *Scottish Journal of Geology*, 1(1), 19–40.

O'Neill, C., Lenardic, A., Jellinek, A. M., & Kiefer, W. S. (2007). Melt propagation and volcanism in mantle convection simulations, with applications for Martian volcanic and atmospheric evolution. *Journal of Geophysical Research: Planets*, 112(E7).

Payré, V., & Dasgupta, R. (2022). Effects of phosphorus on partial melting of the Martian Mantle and compositions of the Martian Crust. *Geochimica et Cosmochimica Acta*, 327, 229–246.

Peel, C. J., Howarth, G. H., Day, J. M. D., le Roux, P., & Alard, O. (2023). Constraints on martian depleted shergottite volcanism from the petrogenesis of olivine-phyric shergottites NWA 2046 and NWA 4925. *Journal of African Earth Sciences*, 202, 104901.

Plesa, A.-C., Tosi, N., Grott, M., & Breuer, D. (2015). Thermal evolution and Urey ratio of Mars. *Journal of Geophysical Research: Planets*, 120(5), 995–1010.

Powell, R., & Holland, T. J. B. (1988). An internally consistent dataset with uncertainties and correlations: 3. Applications to geobarometry, worked examples and a computer program. *Journal of Metamorphic Geology*, 6(2), 173–204.

Prissel, K., Olive, J.-A., & Krawczynski, M. J. (2023). A Log-Ratio-Based Algorithm for Petrologic Mass-Balance Problems and Uncertainty Assessment. *Geochemistry, Geophysics, Geosystems*, 24(12), e2023GC011234.

Putirka, K. D. (2008). Thermometers and Barometers for Volcanic Systems. *Reviews in Mineralogy and Geochemistry*, 69(1), 61–120.

Roeder, P. L., & Emslie, R. F. (1970). Olivine-liquid equilibrium. *Contributions to Mineralogy and Petrology*, 29(4), 275–289.

Rubin, A. E., Warren, P. H., Greenwood, J. P., Verish, R. S., Leshin, L. A., Hervig, R. L., et al. (2000). Los Angeles: The most differentiated basaltic martian meteorite. *Geology*, 28(11), 1011–1014.

Ruiz, J. (2014). The early heat loss evolution of Mars and their implications for internal and environmental history. *Scientific Reports*, 4(1), 4338.

Ruiz, J., McGovern, P. J., Jiménez-Díaz, A., López, V., Williams, J.-P., Hahn, B. C., & Tejero, R. (2011). The thermal evolution of Mars as constrained by paleo-heat flows. *Icarus*, 215(2), 508–517.

Samuel, H., Drilleau, M., Rivoldini, A., Xu, Z., Huang, Q., Garcia, R. F., et al. (2023). Geophysical evidence for an enriched molten silicate layer above Mars's core. *Nature*, 622(7984), 712–717.

Sanloup, C., Jambon, A., & Gillet, P. (1999). A simple chondritic model of Mars. *Physics of the Earth and Planetary Interiors*, 112(1), 43–54.

Santos, A. R., Agee, C. B., McCubbin, F. M., Shearer, C. K., Burger, P. V., Tartese, R., & Anand, M. (2015). Petrology of igneous clasts in Northwest Africa 7034: Implications for the petrologic diversity of the Martian crust. *Geochimica et Cosmochimica Acta*, 157, 56–85.

Sato, H. (1977). Nickel content of basaltic magmas: identification of primary magmas and a measure of the degree of olivine fractionation. *Lithos*, 10(2), 113–120.

Sautter, V., Toplis, M. J., Wiens, R. C., Cousin, A., Fabre, C., Gasnault, O., et al. (2015). In situ evidence for continental crust on early Mars. *Nature Geoscience*, 8(8), 605–609.

Sautter, V., Toplis, M. J., Lorand, J.-P., & Macri, M. (2012). Melt inclusions in augite from the nakhlite meteorites: A reassessment of nakhlite parental melt and implications for petrogenesis. *Meteoritics & Planetary Science*, 47(3), 330–344.

Schmidt, M. E., Schrader, C. M., & McCoy, T. J. (2013). The primary fO_2 of basalts examined by the Spirit rover in Gusev Crater, Mars: Evidence for multiple redox states in the martian interior. *Earth and Planetary Science Letters*, 384, 198–208.

Schmidt, M. E., Campbell, J. L., Gellert, R., Perrett, G. M., Treiman, A. H., Blaney, D. L., et al. (2014). Geochemical diversity in first rocks examined by the Curiosity Rover in Gale Crater: Evidence for and significance of an alkali and volatile-rich igneous source. *Journal of Geophysical Research: Planets*, 119(1), 64–81.

Schmidt, M. E., Allwood, A., Brown, A. J., Christian, J., Clark, B. C., Debaille, V., et al. (2022). Highly Differentiated Lavas Examined by PIXL in Jezero Crater (Vol. 2022, pp. P52C–1553). Presented at the *AGU Fall Meeting Abstracts*.

Stevenson, D. J. (2003). Styles of mantle convection and their influence on planetary evolution. *Comptes Rendus - Geoscience*, 335(1), 99–111.

Stolper, E., & McSween, H. Y. (1979). Petrology and origin of the shergottite meteorites. *Geochimica et Cosmochimica Acta*, 43(9), 1475–1498.

Stolper, E. M., Baker, M. B., Newcombe, M. E., Schmidt, M. E., Treiman, A. H., Cousin, A., et al. (2013). The petrochemistry of Jake_M: A Martian mugearite. *Science*, 341(6153), 1239463.

Taylor, G. J. (2013). The bulk composition of Mars. *Geochemistry*, 73(4), 401–420.

Thiriet, M., Breuer, D., Michaut, C., & Plesa, A.-C. (2019). Scaling laws of convection for cooling planets in a stagnant lid regime. *Physics of the Earth and Planetary Interiors*, 286, 138–153.

Toplis, M. J. (2005). The thermodynamics of iron and magnesium partitioning between olivine and liquid: Criteria for assessing and predicting equilibrium in natural and experimental systems. *Contributions to Mineralogy and Petrology*, 149(1), 22–39.

Treiman, A. H., & Filiberto, J. (2015). Geochemical diversity of shergottite basalts: Mixing and fractionation, and their relation to Mars surface basalts. *Meteoritics & Planetary Science*, 50(4), 632–648.

Udry, A., Ostwald, A., Sautter, V., Cousin, A., Beyssac, O., Forni, O., et al. (2023). A Mars 2020 Perseverance SuperCam Perspective on the Igneous Nature of the Máaz Formation at Jezero Crater and Link With Séítah, Mars. *Journal of Geophysical Research: Planets*, 128(7).

Udry, A., & Day, J. M. D. (2018). 1.34 billion-year-old magmatism on Mars evaluated from the co-genetic nakhlite and chassignite meteorites. *Geochimica et Cosmochimica Acta*, 238, 292–315.

Udry, A., Balta, J. B., & McSween Jr, H. Y. (2014). Exploring fractionation models for Martian magmas. *Journal of Geophysical Research: Planets*, 119(1), 1–18.

Udry, A., Gazel, E., & McSween, H. Y. (2018). Formation of evolved rocks at Gale crater by crystal fractionation and implications for Mars crustal composition. *Journal of Geophysical Research: Planets*, 123(6), 1525–1540.

Udry, A., Howarth, G. H., Herd, C. D. K., Day, J. M. D., Lapen, T. J., & Filiberto, J. (2020). What Martian Meteorites Reveal About the Interior and Surface of Mars. *Journal of Geophysical Research: Planets*, 125(12).

Usui, T., McSween, H. Y., & Floss, C. (2008). Petrogenesis of olivine-phyric shergottite Yamato 980459, revisited. *Geochimica et Cosmochimica Acta*, 72(6), 1711–1730.

Van Niekerk, D., Goodrich, C. A., Taylor, G. J., & Keil, K. (2007). Characterization of the lithological contact in the shergottite EETA79001—A record of igneous differentiation processes on Mars. *Meteoritics & Planetary Science*, 42(10), 1751–1762.

Wadhwa, M., McSween, H. Y., & Crozaz, G. (1994). Petrogenesis of shergottite meteorites inferred from minor and trace element microdistributions. *Geochimica et Cosmochimica Acta*, 58(19), 4213–4229.

Wiens, R. C., Udry, A., Beyssac, O., Quantin-Nataf, C., Mangold, N., Cousin, A., et al. (2022). Compositionally and density stratified igneous terrain in Jezero crater, Mars. *Science Advances*, 8(34).

Wittmann, A., Korotev, R. L., Jolliff, B. L., Irving, A. J., Moser, D. E., Barker, I., & Rumble III, D. (2015). Petrography and composition of Martian regolith

breccia meteorite Northwest Africa 7475. *Meteoritics & Planetary Science*, 50(2), 326–352.

Wu, P., Gazel, E., Udry, A., Setera, J. B., & Ostwald, A. (2021). Melt inclusions in chassignite NWA 2737: A link between processes recorded in Martian meteorites and rocks at Gale crater. *Meteoritics & Planetary Science*, 56(7), 1328–1349.

Yoshizaki, T., & McDonough, W. F. (2020). The composition of Mars. *Geochimica et Cosmochimica Acta*, 273, 137–162.

SUPPLEMENTARY MATERIAL

A1. Definition of AN

Coordinates in the Olivine–Anorthite–Quartz plane projected from Diopside are calculated from mole percent oxide compositions (mole %) following (*Herzberg and O'Hara*, 2002). The three components are normalized to 1.

$$\begin{aligned} \mathrm{OL}' = &-1.5\,\mathrm{TiO_2} + 0.5\,(\mathrm{Al_2O_3} + \mathrm{Cr_2O_3} + \mathrm{FeO^*} + \mathrm{MnO} + \mathrm{MgO} \\ &- \mathrm{CaO} - \mathrm{Na_2O} + \mathrm{NiO}) + 3.0\,\mathrm{K_2O} \end{aligned}$$

$$\mathrm{AN}' = 1.0\,\mathrm{TiO_2} + 1.0\,\mathrm{Al_2O_3} + 1.0\,\mathrm{Cr_2O_3}$$

$$\begin{aligned} \mathrm{QTZ}' = &\ 1.0\,\mathrm{SiO_2} - 0.5\,(\mathrm{Al_2O_3} + \mathrm{Cr_2O_3} + \mathrm{FeO^*} + \mathrm{MnO} + \mathrm{MgO} + \mathrm{NiO}) \\ &- 1.5\,\mathrm{CaO} - 3.0\,(\mathrm{Na_2O} + \mathrm{K_2O}) \end{aligned}$$

$$\mathrm{OL} = \frac{\mathrm{OL}'}{\mathrm{OL}' + \mathrm{AN}' + \mathrm{QTZ}'}$$

$$\mathrm{AN} = \frac{\mathrm{AN}'}{\mathrm{OL}' + \mathrm{AN}' + \mathrm{QTZ}'}$$

$$\mathrm{QTZ} = \frac{\mathrm{QTZ}'}{\mathrm{OL}' + \mathrm{AN}' + \mathrm{QTZ}'}$$

A2. Method for estimation of regression uncertainty

Fitting of Equations 1 and 2 involved an iterative procedure that allowed to obtain total uncertainties for F, which were used to estimate regression weights as $1/\sigma$:

1. An initial fit for $F(P,T)$ was performed, yielding initial values for the regression coefficients.

2. The expression for $F(P,T)$ was used to obtain an initial estimate of uncertainties on F related to P and T, and the corresponding total uncertainty.

3. A refined expression for $F(P,T)$ was derived by weighted least squares, which was conducted iteratively by updating weights and regression coefficients until a constant value for each was reached.

4. An initial regression of Equation 1 was obtained by ordinary least squares, yielding initial values for the regression coefficients.

5. Equation 1 was refined using weighted least squares with initial estimates of regression coefficients from step 4, and weights from step 3.

A3. Warnings in PRIMARSMELT

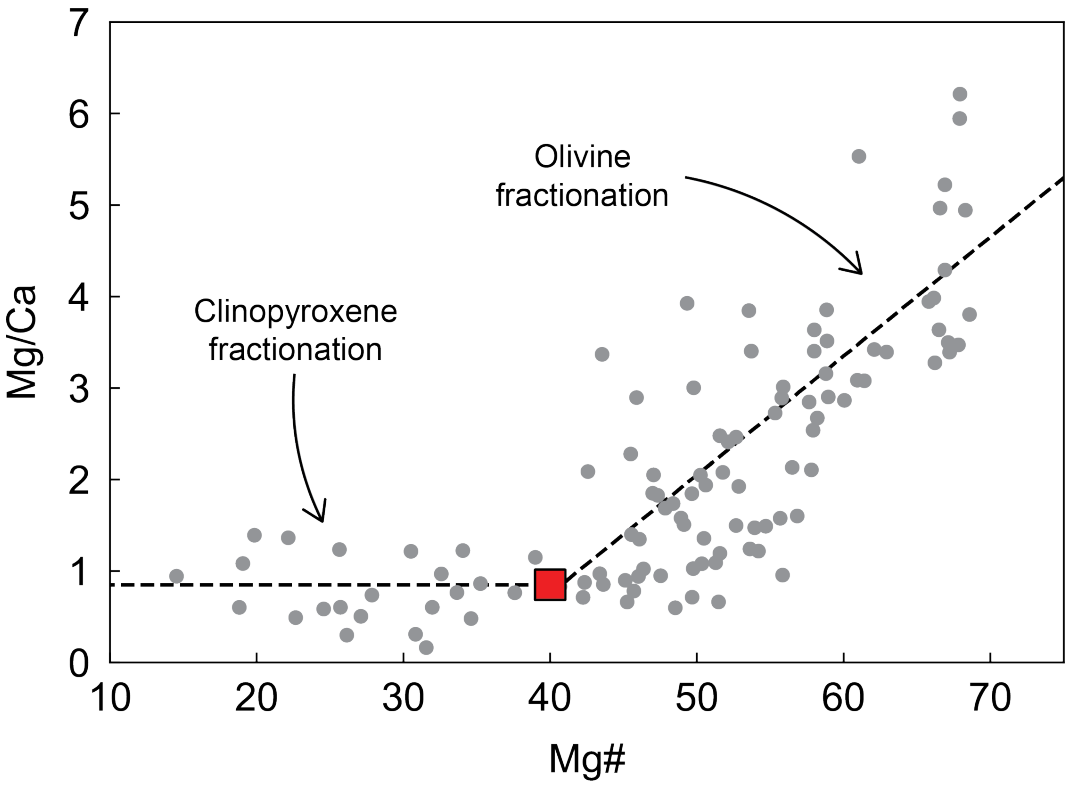


Figure S4A.1: Mg# vs. Mg/Ca diagram showing different trends due to olivine and clinopyroxene fractionation.

PRIMARSMELT alerts the user when the input composition suggests either partial melting of a volatile-bearing source or clinopyroxene fractionation. For melting of carbonated peridotite, the identification criteria are the same as in (*Herzberg & Asimow*, 2008) (their Equation 8), which is based on partial melting experiments with variable CO_2 contents (*Dasgupta*, 2007). Typically, low-degree partial melts from carbonate-bearing peridotite exhibit lower SiO_2 and higher CaO contents compared to those from anhydrous peridotite. Normalizing these liquids to a volatile-free basis can significantly increase their FeO and MgO contents, potentially leading to an overestimation of mantle temperatures.

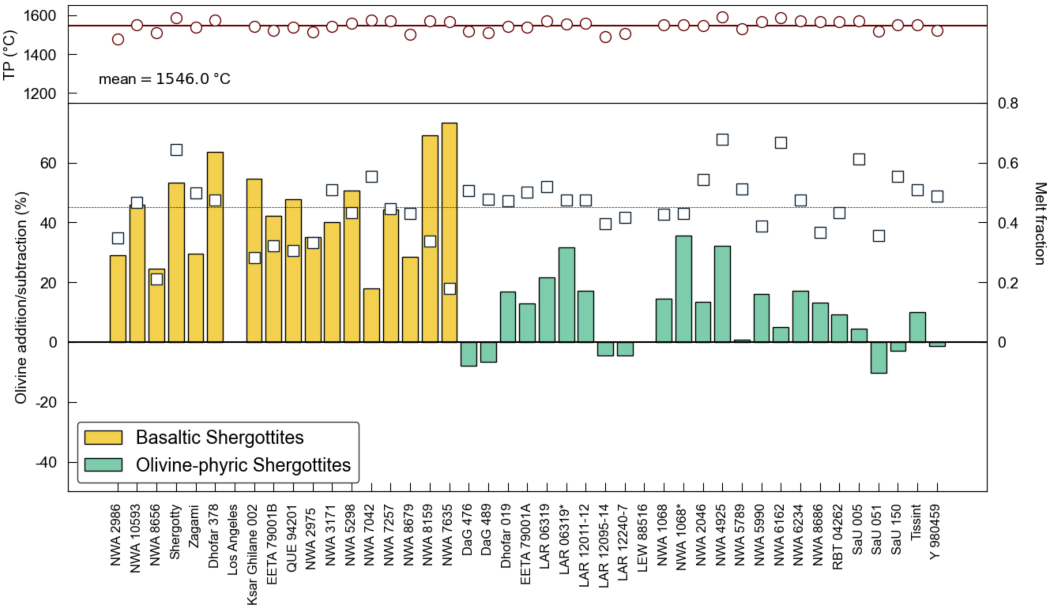
On the other hand, evolved compositions that may have experienced clinopyroxene fractionation appear to have Mg# values lower than 40. This relationship is illustrated in the Mg# versus Fe/Ca diagram in Figure A1, where all compiled Martian compositions are plotted. The breakpoint at Mg# $\sim$ 40 marks the shift from olivine

to clinopyroxene ± olivine fractionation. During olivine crystallization, Mg is removed from the liquid, reducing the Mg/Ca ratio. In contrast, augite crystallization removes Mg and Ca in a similar molar proportion, so that the liquid Mg/Ca ratio remains relatively constant.

A4. Additional figures

This Supporting Information corresponds to results of primary magma calculations with PRIMARSMELT assuming a less FeO-rich mantle source (YM; Mg# 79; *Yoshizaki and McDonough*, 2020). The output tables summarizing primary magma solutions produced by PRIMARSMELT are presented in Supporting Information S2.

Overall, assuming a more magnesian source results in primary magmas with higher MgO contents, corresponding to mantle potential temperatures ~90 °C higher than those produced when considering a mantle source with Mg# 75 (*Dreibus and Wänke*, 1984). These primary magma results would also represent higher initial pressures and melt fractions. Also, more olivine addition for fractionated basalts and less olivine subtraction are required to find a solution for a primary magma with higher MgO content. Consequently, except for some olivine-phyric shergottites, all the compositions in the database are seen by PRIMARSMELT as liquids that fractionated olivine when the YM mantle composition is assumed as the source.



Supplementary Figure S4.1: F_{AFM} primary magma solutions for all basaltic (yellow) and olivine-phyric shergottites (green) in our compiled database, assuming a mantle source with Mg# 79 (*Yoshizaki & McDonough*, 2020). Predicted mantle potential temperatures (T_P) are shown as circles in the top panel. The red horizontal line is the average T_P. The amount of olivine addition/subtraction required for a successful primary magma solution is shown by the bars in the bottom panel (left-hand scale). Square markers indicate the F_{AFM} predicted for each sample (right-hand scale). The dashed navy-blue horizontal line is the average F_{AFM} of all the shergottites. Compositions LAR 06319* and NWA 1068* are estimated parental magmas from *Balta et al.* (2013) and *Filiberto et al.* (2010).

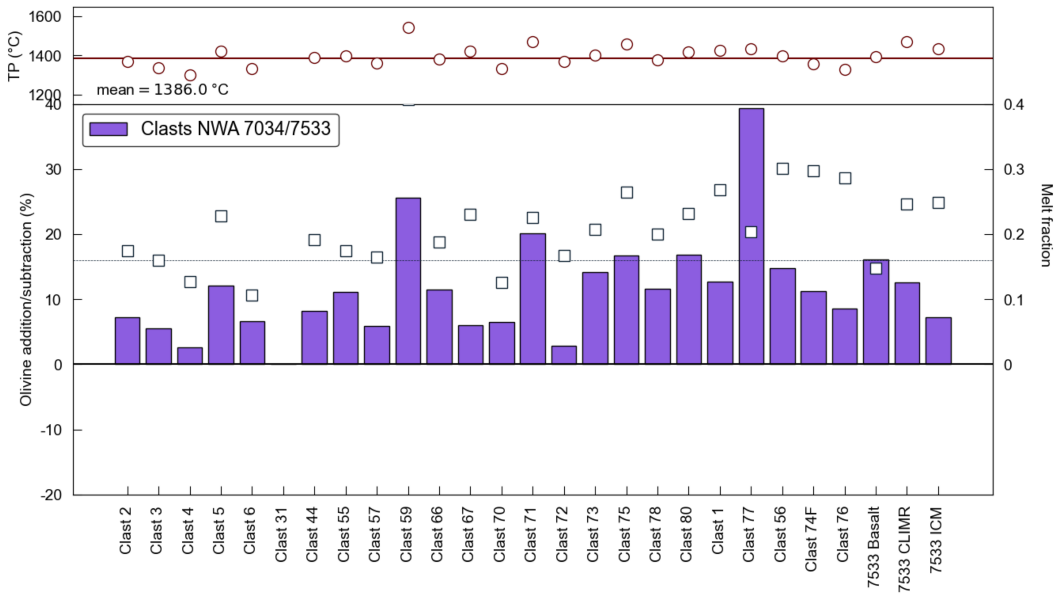
References for Supplemental Material

Balta, J. B., Sanborn, M., McSween Jr., H. Y., & Wadhwa, M. (2013). Magmatic history and parental melt composition of olivine-phyric shergottite LAR 06319: Importance of magmatic degassing and olivine antecrysts in Martian magmatism. *Meteoritics & Planetary Science*, 48(8), 1359–1382.

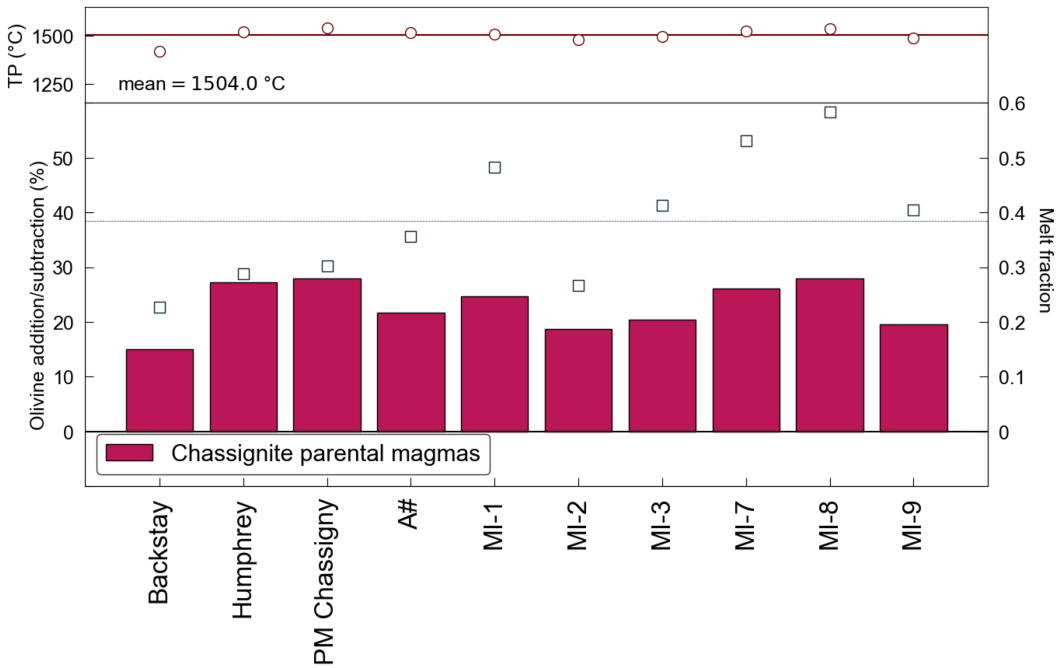
Barrat, J. A., Jambon, A., Bohn, M., Gillet, P. h, Sautter, V., Göpel, C., et al. (2002). Petrology and chemistry of the Picritic Shergottite North West Africa 1068 (NWA 1068). *Geochimica et Cosmochimica Acta*, 66(19), 3505–3518.

Basu Sarbadhikari, A., Day, J. M. D., Liu, Y., Rumble, D., & Taylor, L. A. (2009). Petrogenesis of olivine-phyric shergottite Larkman Nunatak 06319: Implications for enriched components in martian basalts. *Geochimica et Cosmochimica Acta*, 73(7), 2190–2214.

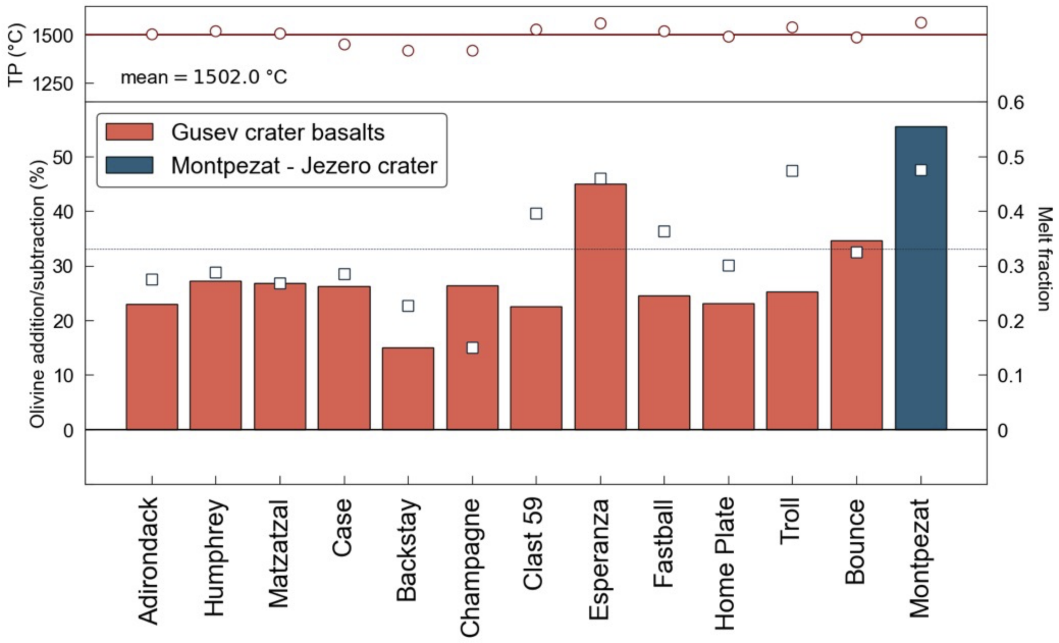
Bogard, D., Park, J., & Garrison, D. (2009). 39Ar–40Ar "ages" and origin of excess



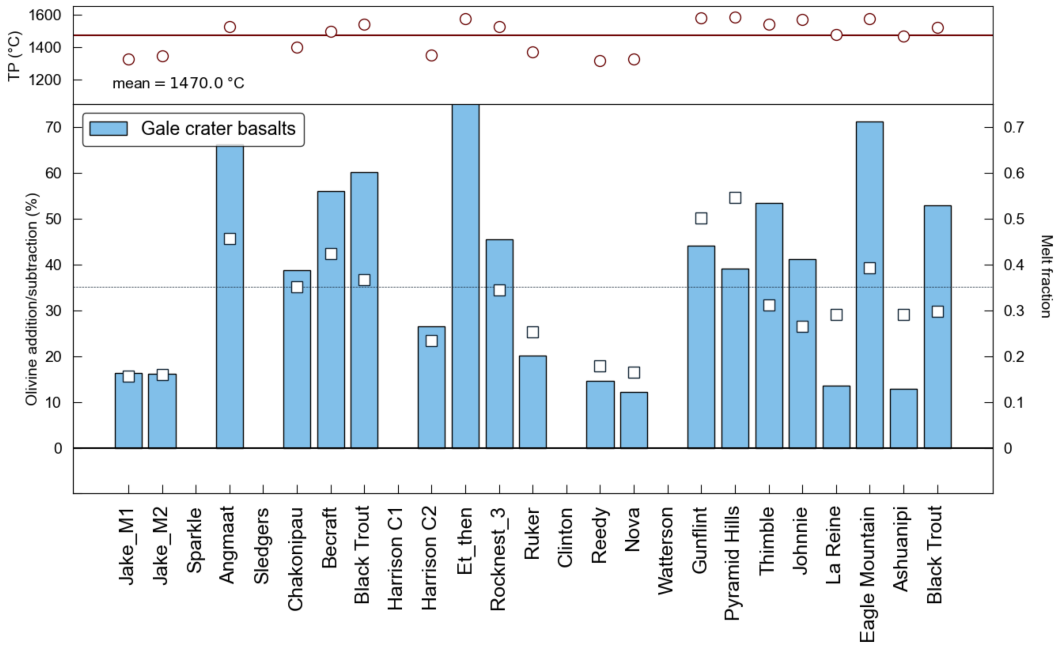
Supplementary Figure S4.2: F_{AFM} primary magma solutions for all igneous clasts in NWA 7034/7533, assuming a mantle source with Mg# 79 (*Yoshizaki & McDonough*, 2020). Symbols as in Figure S1.



Supplementary Figure S4.3: F_{AFM} primary magma solutions for proposed parental magmas of the chassignite meteorites: Backstay (*Nekvasil et al.*, 2009), Humphrey (*Filiberto*, 2008), PM Chassigny (*Johnson et al.*, 1991), A# (He et al., 2013), and MI-1–9 (Wu et al., 2021). Calculations assume a mantle source with Mg# 79 (*Yoshizaki & McDonough*, 2020). Symbols as in Figure S1.



Supplementary Figure S4.4: F_{AFM} primary magma solutions for basaltic rocks from the Gusev crater (orange) and basalt from the Jezero crater (Montpezat; dark blue). Calculations assume a mantle source with Mg# 79 (*Yoshizaki & McDonough*, 2020). Symbols as in Figure S1.



Supplementary Figure S4.5: F_{AFM} primary magma solutions for basaltic rocks from Gale crater, assuming a mantle source with Mg# 79 (*Yoshizaki & McDonough*, 2020). Symbols as in Figure S1.

40Ar in Martian shergottites. *Meteoritics & Planetary Science*, 44(6), 905–923.

Borg, L., Nyquist, L., Reese, Y., Wiesmann, H., Shih, C., Taylor, L., & Ivanova, M. (2001). The age of Dhofar 019 and its relationship to the other Martian meteorites. *Lunar Planet. Sci*, 32, 1144.

Borg, L. E., Nyquist, L. E., Taylor, L. A., Wiesmann, H., & Shih, C.-Y. (1997). Constraints on Martian differentiation processes from Rb–Sr and Sm–Nd isotopic analyses of the basaltic shergottite QUE 94201. *Geochimica et Cosmochimica Acta*, 61(22), 4915–4931.

Borg, L. E., Nyquist, L. E., Wiesmann, H., & Reese, Y. (2002). Constraints on the petrogenesis of Martian meteorites from the Rb–Sr and Sm–Nd isotopic systematics of the lherzolitic shergottites ALH77005 and LEW88516. *Geochimica et Cosmochimica Acta*, 66(11), 2037–2053.

Borg, L. E., Nyquist, L. E., Wiesmann, H., Shih, C.-Y., & Reese, Y. (2003). The age of Dar al Gani 476 and the differentiation history of the martian meteorites inferred from their radiogenic isotopic systematics. *Geochimica et Cosmochimica Acta*, 67(18), 3519–3536.

Darling, J. R., Moser, D. E., Barker, I. R., Tait, K. T., Chamberlain, K. R., Schmitt, A. K., & Hyde, B. C. (2016). Variable microstructural resp

Farley, K. A., Malespin, C., Mahaffy, P., Grotzinger, J. P., Vasconcelos, P. M., Milliken, R. E., et al. (2014). In Situ Radiometric and Exposure Age Dating of the Martian Surface. *Science*, 343(6169), 1247166.

Filiberto, J. (2017). Geochemistry of Martian basalts with constraints on magma genesis. *Chemical Geology*, 466, 1–14.

Filiberto, J., Musselwhite, D. S., Gross, J., Burgess, K., Le, L., & Treiman, A. H. (2010). Experimental petrology, crystallization history, and parental magma characteristics of olivine-phyric shergottite NWA 1068: Implications for the petrogenesis of “enriched” olivine-phyric shergottites. *Meteoritics & Planetary Science*, 45(8), 1258–1270.

Filiberto, J., Chin, E., Day, J. M. D., Franchi, I. A., Greenwood, R. C., Gross, J., et al. (2012). Geochemistry of intermediate olivine-phyric shergottite Northwest Africa 6234, with similarities to basaltic shergottite Northwest Africa 480 and olivine-phyric shergottite Northwest Africa 2990. *Meteoritics & Planetary Science*, 47(8), 1256–1273.

Gleason, J. D., Kring, D. A., Hill, D. H., & Boynton, W. V. (1997). Petrography and bulk chemistry of Martian lherzolite LEW88516. *Geochimica et Cosmochimica Acta*, 61(18), 4007–4014.

Goodrich, C. A. (2003). Petrogenesis of olivine-phyric shergottites Sayh al Uhaymir 005 and Elephant Moraine A79001 lithology A. *Geochimica et Cosmochimica Acta*, 67(19), 3735–3772.

Grant, J. A., Wilson, S. A., Mangold, N., Calef III, F., & Grotzinger, J. P. (2014). The timing of alluvial activity in Gale crater, Mars. *Geophysical Research Letters*, 41(4), 1142–1149.

Greeley, R., Foing, B. H., McSween Jr., H. Y., Neukum, G., Pinet, P., van Kan, M., et al. (2005). Fluid lava flows in Gusev crater, Mars. *Journal of Geophysical Research: Planets*, 110(E5).

Gross, J., Treiman, A. H., Filiberto, J., & Herd, C. D. K. (2011). Primitive olivine-phyric shergottite NWA 5789: Petrography, mineral chemistry, and cooling history imply a magma similar to Yamato-980459. *Meteoritics & Planetary Science*, 46(1), 116–133.

Gross, J., Filiberto, J., Herd, C. D. K., Daswani, M. M., Schwenzer, S. P., & Treiman, A. H. (2013). Petrography, mineral chemistry, and crystallization history of olivine-phyric shergottite NWA 6234: A new melt composition. *Meteoritics & Planetary Science*, 48(5), 854–871.

Grossman, J. N. (1999). The meteoritical bulletin, no. 83, 1999 July. *Meteoritics & Planetary Science*, 34(S4), A169–A186.

Grossman, J. N., & Zipfel, J. (2001). The meteoritical bulletin, no. 85, 2001 September. *Meteoritics & Planetary Science*, 36(S9), A293–A322.

Hays, N. R. (2011). Geochronology of Shergottite Meteorites: Using LA-MC-ICP-MS Analysis to Examine U-Th-Pb Systematics of Baddeleyites and Phosphates. Retrieved from http://hdl.handle.net/10150/202753

He, Q., Xiao, L., Hsu, W., Balta, J. B., McSween, H. Y., & Liu, Y. (2013). The water content and parental magma of the second chassignite NWA 2737: Clues from trapped melt inclusions in olivine. *Meteoritics & Planetary Science*, 48(3), 474–492. https://doi.org/10.1111/maps.12073

He, Q., Xiao, L., Balta, J. B., Baziotis, I. P., Hsu, W., & Guan, Y. (2015). Petrography and geochemistry of the enriched basaltic shergottite Northwest Africa 2975.

Meteoritics & Planetary Science, 50(12), 2024–2044.

Herd, C. D. K., Walton, E. L., Agee, C. B., Muttik, N., Ziegler, K., Shearer, C. K., et al. (2017). The Northwest Africa 8159 martian meteorite: Expanding the martian sample suite to the early Amazonian. *Geochimica et Cosmochimica Acta*, 218, 1–26. https://doi.org/10.1016/j.gca.2017.08.037

Humayun, M., Nemchin, A., Zanda, B., Hewins, R. H., Grange, M., Kennedy, A., et al. (2013). Origin and age of the earliest Martian crust from meteorite NWA 7533. *Nature*, 503(7477), 513–516.

Ikeda, Y., Kimura, M., Takeda, H., Shimoda, G., Kita, N. T., Morishita, Y., et al. (2006). Petrology of a new basaltic shergottite: Dhofar 378. *Antarctic Meteorite Research*, 19, 20–44.

Irving, A. (2010). Olivine-bearing diabasic shergottite Northwest Africa 5990: Petrology and composition of a new type of depleted martian igneous rock (Vol. 1833). Presented at the *41st Lunar and Planetary Science Conference*, 2010.

Kuehner, S. M., Irving, A. J., Herd, C. D. K., Gellissen, M., Lapen, T. J., & Rumble, D. (2011). Pristine Olivine-Phyric Shergottite Northwest Africa 6162: A Primitive Magma with Accumulated Crystals Derived from Depleted Martian Mantle, 1610. Presented at the *42nd Annual Lunar and Planetary Science Conference*.

Lapen, T. J., Righter, M., Andreasen, R., Irving, A. J., Satkoski, A. M., Beard, B. L., et al. (2017). Two billion years of magmatism recorded from a single Mars meteorite ejection site. *Science Advances*, 3(2), e1600922.

Liu, Y., Baziotis, I. P., Asimow, P. D., Bodnar, R. J., & Taylor, L. A. (2016). Mineral chemistry of the Tissint meteorite: Indications of two-stage crystallization in a closed system. *Meteoritics & Planetary Science*, 51(12), 2293–2315.

Llorca, J., Roszjar, J., Cartwright, J. A., Bischoff, A., Ott, U., Pack, A., et al. (2013). The Ksar Ghilane 002 shergottite—the 100th registered Martian meteorite fragment. *Meteoritics & Planetary Science*, 48(3), 493–513.

Lodders, K. (1998). A survey of shergottite, nakhlite and chassigny meteorites whole-rock compositions. *Meteoritics & Planetary Science*, 33(S4), A183–A190. https://doi.org/10.1111/j.1945-5100.1998.tb01331.x

Mandon, L., Quantin-Nataf, C., Thollot, P., Mangold, N., Lozac'h, L., Dromart, G., et al. (2020). Refining the age, emplacement and alteration scenarios

of the olivine-rich unit in the Nili Fossae region, Mars. *Icarus*, 336, 113436. https://doi.org/10.1016/j.icarus.2019.113436

Nekvasil, H., Filiberto, J., McCubbin, F. M., & Lindsley, D. H. (2007). Alkalic parental magmas for chassignites? *Meteoritics & Planetary Science*, 42(6), 979–992.

Nekvasil, H., McCubbin, F. M., Harrington, A., Elardo, S., & Lindsley, D. H. (2009). Linking the Chassigny meteorite and the Martian surface rock Backstay. *Meteoritics & Planetary Science*, 44(6), 853–869.

Nicklas, R. W., Day, J. M. D., Vaci, Z., & Udry, A. (2022). Petrogenesis of Northwest Africa 8686. *Meteoritics & Planetary Science*, 57(5), 947–964.

Nyquist, L., Reese, Y., Wiesmann, H., Shih, C.-Y., & Schwandt, C. (2000). Rubidium-strontium age of the Los Angeles shergottite. *Meteoritics & Planetary Science*, 35(Suppl.), A121.

Nyquist, L., Ikeda, Y., Shih, C.-Y., Reese, Y., Nakamura, N., & Takeda, H. (2006). Sm-Nd age and isotopic evidence for Dhofar 378. Presented at the *30th Symposium on Antarctic Meteorites*.

Nyquist, L. E., Bogard, D. D., Shih, C.-Y., Greshake, A., Stöffler, D., & Eugster, O. (2001). Ages and Geologic Histories of Martian Meteorites. In R. Kallenbach et al. (Eds.), *Chronology and Evolution of Mars* (pp. 105–164). Springer Netherlands.

Peel, C. J., Howarth, G. H., Day, J. M. D., le Roux, P., & Alard, O. (2023). Constraints on martian depleted shergottite volcanism. *Journal of African Earth Sciences*, 202, 104901.

Ramsey, S. R., Howarth, G. H., Udry, A., Gross, J., & Righter, K. (2021). Nickel–manganese variability in olivine. *Meteoritics & Planetary Science*, 56(8), 1597–1618.

Righter, M., Andreasen, R., & Lapen, T. (2015). Lu-Hf and Sm-Nd systematics of martian meteorites. Presented at the *46th Lunar and Planetary Science Conference*.

Rubin, A. E., Warren, P. H., Greenwood, J. P., Verish, R. S., Leshin, L. A., Hervig, R. L., et al. (2000). Los Angeles: The most differentiated basaltic martian meteorite. *Geology*, 28(11), 1011–1014.

Russell, S. S., Zipfel, J., Folco, L., Jones, R., Grady, M. M., McCoy, T., & Grossman, J. N. (2003). The Meteoritical Bulletin, No. 87. *Meteoritics & Planetary Science*,

38(S7), A189–A248.

Santos, A. R., Agee, C. B., McCubbin, F. M., Shearer, C. K., Burger, P. V., Tartese, R., & Anand, M. (2015). Igneous clasts in Northwest Africa 7034. *Geochimica et Cosmochimica Acta*, 157, 56–85.

Schmidt, M. E., Allwood, A., Brown, A. J., Christian, J., Clark, B. C., Debaille, V., et al. (2022). Highly differentiated lavas in Jezero Crater. Presented at the *AGU Fall Meeting Abstracts*.

Schulz, T., Povinec, P. P., Ferrière, L., Jull, A. T., Kováčik, A., Sýkora, I., et al. (2020). The history of the Tissint meteorite. *Meteoritics & Planetary Science*, 55(2), 294–311.

Shafer, J., Brandon, A., Lapen, T., Righter, M., Peslier, A., & Beard, B. (2010). Trace element systematics and Nd–Hf ages of LAR 06319. *Geochimica et Cosmochimica Acta*, 74(24), 7307–7328.

Shih, C., Nyquist, L., Wiesmann, H., & Barrat, J. (2003). NWA 1068 isotopic studies. Presented at the *34th Lunar and Planetary Science Conference*.

Shih, Chi-Yu, Nyquist, L. E., Wiesmann, H., Reese, Y., & Misawa, K. (2005). Yamato 980459 isotopic studies. *Antarctic Meteorite Research*, 18, 46–65.

Shih, C-Y, Nyquist, L., & Reese, Y. (2007). Isotopic Studies of SaU 094/005. Presented at the *Lunar and Planetary Science Conference*.

Shih, C-Y, Nyquist, L., Reese, Y., & Misawa, K. (2009). Isotopic studies of Yamato 984028. Presented at the *32nd Symposium on Antarctic Meteorites*.

Simon, J., Hickman-Lewis, K., Cohen, B., Mayhew, L., Shuster, D., Debaille, V., et al. (2023). Samples collected from Jezero Crater. *Journal of Geophysical Research: Planets*, 128(6).

Staddon, L. G., Darling, J. R., Schwarz, W. H., Stephen, N. R., Schuindt, S., Dunlop, J., & Tait, K. T. (2021). Dating martian mafic crust. *Geochimica et Cosmochimica Acta*, 315, 73–88.

Taylor, L., Nazarov, M., Shearer, C., McSween Jr, H., Cahill, J., Neal, C., et al. (2002). Martian meteorite Dhofar 019. *Meteoritics & Planetary Science*, 37(8), 1107–1128.

Udry, A., & Day, J. M. D. (2018). 1.34 billion-year-old magmatism on Mars. *Geochimica et Cosmochimica Acta*, 238, 292–315.

Usui, T., McSween, H. Y., & Floss, C. (2008). Yamato 980459, revisited. *Geochimica et Cosmochimica Acta*, 72(6), 1711–1730.

Usui, T., Sanborn, M., Wadhwa, M., & McSween Jr, H. Y. (2010). Robert Massif 04261 and 04262 meteorites. *Geochimica et Cosmochimica Acta*, 74(24), 7283–7306.

Walton, E. L., Spray, J. G., & Bartoschewitz, R. (2005). Sayh al Uhaymir 150. *Meteoritics & Planetary Science*, 40(8), 1195–1214.

Wu, P., Gazel, E., Udry, A., Setera, J. B., & Ostwald, A. (2021). Melt inclusions in chassignite NWA 2737. *Meteoritics & Planetary Science*, 56(7), 1328–1349.

Yang, S., Humayun, M., Jefferson, G., Fields, D., Righter, K., & Irving, A. (2013). Chemical composition of four shergottites. Presented at the *Lunar and Planetary Science Conference*.

Zhou, Q., Herd, C. D., Yin, Q.-Z., Li, X.-H., Wu, F.-Y., Li, Q.-L., et al. (2013). Geochronology of the Zagami meteorite. *Earth and Planetary Science Letters*, 374, 156–163.

Zipfel, J., Scherer, P., Spettel, B., Dreibus, G., & Schultz, L. (2000). Petrology and chemistry of Dar al Gani 476. *Meteoritics & Planetary Science*, 35(1), 95–106.

Chapter 5

ACTIVE MAGMATIC DEGASSING IS REQUIRED TO SUSTAIN LIQUID WATER IN THE MARTIAN CRUST

ABSTRACT

Seismic observations from NASA's InSight mission permit the presence of liquid water in the Martian mid-crust, yet the sources and longevity of such water reservoirs remain unconstrained. Here, we evaluate whether liquid water can persist under present-day Martian conditions by combining thermodynamic modeling of Martian magma crystallization with a physical model of fluid–rock interaction and permeability evolution. We show that primary Martian magmas containing modest initial water contents inevitably reach volatile saturation during differentiation at lower-crustal pressures, producing water-rich fluids during cooling and stalling. However, hydration reactions in the fractured mid-crust rapidly consume these fluids and progressively seal permeability. For values of initial porosity and reaction rates expected for hydrous alteration of mafic crust, permeability collapses on 10^3–10^5 year timescales—comparable to the cooling lifetimes of episodic magma chambers and far shorter than those required to sustain long-lived aquifers. Only extreme and likely unrealistic conditions permit permeability to persist for $\sim 10^6$ years. These results reconcile the seismic permissibility of mid-crustal fluids with independent constraints indicating a predominantly dry Martian crust and demonstrate that any present-day liquid water must be continuously supplied by active magmatic degassing.

1. Liquid water in the Martian mid-crust

The presence of liquid water within the Martian crust has profound implications for planetary evolution, habitability, and the fate of the early Martian hydrosphere. Orbital observations and geomorphological evidence indicate that large volumes of liquid water transiently existed on the Martian surface more than 3 billion years ago (*Carr and Head*, 2010). While much of this water was subsequently lost to space, sequestered in hydrous minerals, or stored as ice (*Scheller et al.*, 2021), the possibility that liquid reservoirs persist within the deep interior remains an open and compelling question.

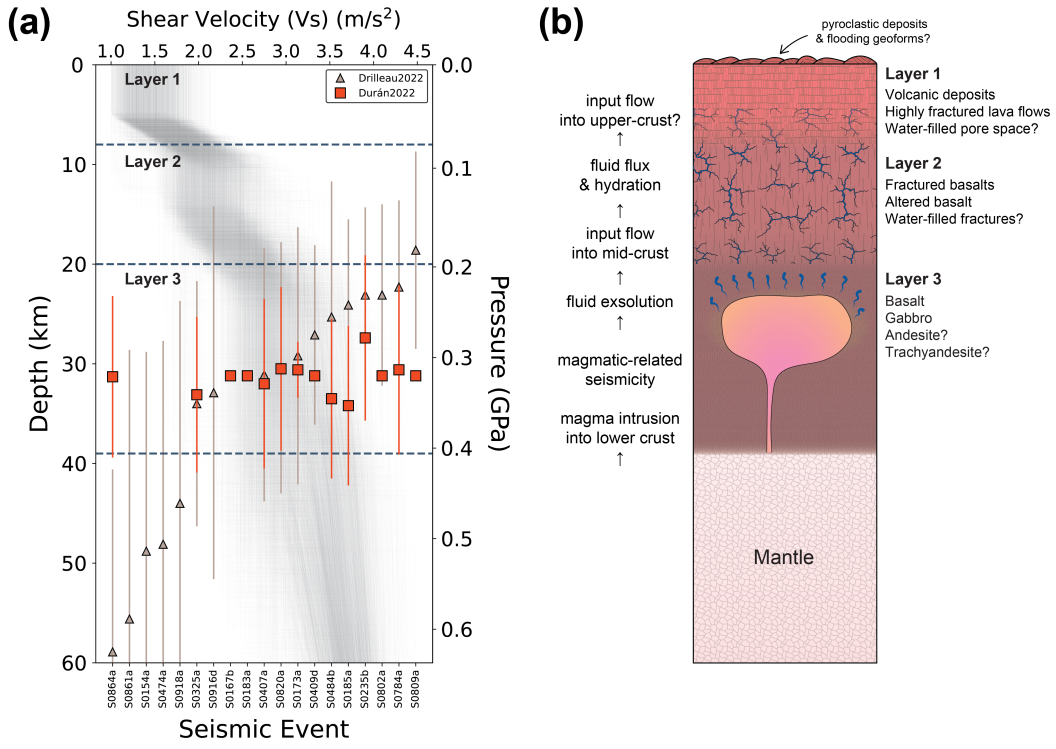


Figure 5.1: **(a)** Shear velocity, three-layer crustal structure of Mars at the InSight landing site from seismic inversion models by *Knapmeyer-Endrun et al.* (2021). Horizontal, dashed lines represent approximate transitions between the upper, mid, and lower crust. Markers correspond with marsquakes detected by InSight with estimated depths from *Drilleau et al.* (2022) (pale triangles) and *Durán et al.* (2022) (red squares). Depth-to-pressure conversion is based on density distribution from *Knapmeyer-Endrun et al.* (2025). **(b)** Schematic representation of our interpreted crustal profile beneath InSight's landing site.

Seismic data acquired by NASA's InSight mission have renewed interest in this problem by providing the first direct constraints on the physical structure of the Martian crust. Receiver function analyses and surface-wave inversions reveal a distinct velocity stratification beneath the landing site, interpreted as a three-layer crustal model (Figure 5.1, *Knapmeyer-Endrun et al.*, 2021; *Wieczorek et al.*, 2022; *Durán et al.*, 2022). The uppermost layer (Layer 1), extending to ~8 – 10 km depth, is characterized by low seismic velocities consistent with highly porous, fractured basaltic flows and impact ejecta. Beneath this lies a mid-crustal layer (Layer 2) extending to roughly 20 km depth, exhibiting higher velocities indicative of potentially fractured and altered igneous rocks (*Kilburn et al.*, 2022). This mid-crust layer is underlain by a denser lower crust above the Moho (Layer 3), which extends to ~40 km (*Knapmeyer-Endrun et al.*, 2021; *Wieczorek et al.*, 2022; *Durán*

et al., 2022).

Within this crustal framework, recent rock-physics models and laboratory experiments demonstrate that the observed seismic velocities and V_p/V_s ratios in the mid-crust can be reproduced by fractured igneous rocks containing liquid-filled cracks and significant hydrous alteration (Figure 5.1b, *Katayama and Akamatsu*, 2024; *Wright et al.*, 2024; *Manga and Wright*, 2021). These results indicate that liquid water is physically permissible under present-day Martian crustal conditions. At the same time, seismic interpretations are inherently non-unique: similar velocity structures may also arise from variations in dry crack geometry, lithological layering, or the presence of hydrous mineral phases such as chlorite or serpentine (*Jakosky*, 2025). Independent constraints from high-frequency seismogram analyses further indicate that seismic attenuation in the Martian crust is dominated by scattering rather than intrinsic absorption, a signature typically associated with heterogeneous but mostly dry crustal materials (*Menina et al.*, 2021, 2023). Taken together, these observations suggest that if liquid water is present in the Martian crust, it is likely confined to localized volumes rather than forming a regionally extensive aquifer.

Seismic constraints therefore permit—but do not uniquely require—the presence of liquid water in the Martian mid-crust. More importantly, they leave unresolved two fundamental questions relevant to habitability and future exploration: if liquid water is present in the mid-crust, what is its origin, and how long can it survive as a free fluid under current Martian conditions? Long-term sources of crustal water on Earth, including meteoric recharge and dehydration reactions associated with plate tectonics, do not operate on modern Mars (*McSween*, 2015). Likewise, ancient aquifers formed during early, wetter epochs are expected to be unstable over geological timescales, as low-temperature metamorphic hydration reactions progressively consume free water and incorporate it into structurally bound hydroxyl within minerals (*Scheller et al.*, 2022; *Palin et al.*, 2024). If liquid water exists today in the Martian mid-crust, it must therefore be supplied by an active process rather than preserved passively.

Here, we investigate whether magmatic activity provides such a source. By combining thermodynamic modeling of Martian magma evolution with a physical model of fluid–rock interaction, we evaluate whether magmatic processes can supply water to the crust and whether such water can persist under present-day Martian conditions.

2. Martian magmas inevitably reach volatile saturation

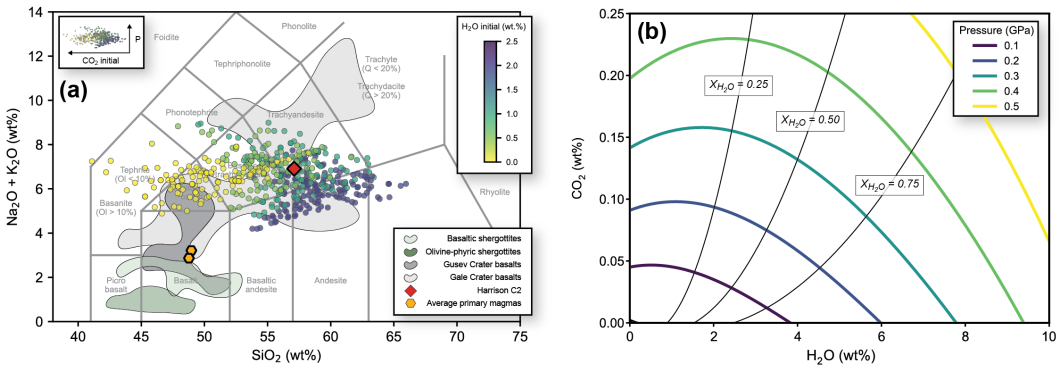


Figure 5.2: Volatile exsolution during cooling and crystallization of Martian primary magmas (*Hernández-Montenegro et al.*, 2024). **(a)** Total alkalis versus SiO_2 diagram. The colored circles represent modeled melt compositions at the point of volatile saturation during fractional crystallization of average primary magma composition from Mars (orange hexagons). The color of each circle scales with the initial H_2O content considered in the primary magma. Yellow circles correspond with either relatively dry or CO_2-rich primary magmas, clustering at low SiO_2 contents. Volatile-saturated intermediate magmas with compositions similar to those measured in Gale crater (light gray region) can be attained if primary magmas contain > 0.5 wt.% H_2O. The trachyandesite *Harrison C2* (red diamond – *Udry et al.*, 2018) is a natural example of these modeled intermediate compositions. **(b)** H_2O versus CO_2 (wt. %) diagram showing isopleths (thin black lines) and isobars (colored lines) of estimated volatile contents for fluid saturation of the *Harrison C2* composition at a near-liquidus temperature of 1000 °C.

Magmatic processes offer a potential mechanism for introducing water into the Martian crust (Figure 5.1b). Martian meteorites and in situ analyses indicate that Martian magmas are not completely dry, and even primitive compositions may contain pre-eruptive dissolved volatile contents of up to ~2 wt.% (*McSween et al.*, 2001; *McCubbin et al.*, 2012). Our modeling predicts that primary magmas with extremely dry or CO_2-rich compositions fail to reproduce magmatic evolution paths expected for Martian magmas based on the range of igneous compositions from *in situ* analysis and the meteorite record (Supplemental Figures **S1** and **S2**). In contrast, primary magmas containing on the order of tenths of a weight percent H_2O are consistent with mantle melting models and experimental constraints (*McCubbin et al.*, 2012, 2016; *Balta and McSween*, 2013).

As magmas cool and ascend, fractional crystallization produces melts that are progressively depleted in MgO and FeO while becoming enriched in SiO_2, incompatible elements, and volatile species, primarily H_2O and CO_2 (Supplemental Figures **S1** and **S2**). Thermodynamic modeling demonstrates that average compositions of

Martian primary magmas evolving along isobaric crystallization paths at pressures corresponding to the lower crust inevitably reach volatile saturation once they evolve to intermediate basaltic-andesite to trachyandesite compositions (Figure 5.2a). This behavior is consistent across a wide range of oxygen fugacities and initial volatile abundances consistent with Martian conditions.

The trachyandesite Harrison C2, analyzed by the Curiosity rover in Gale crater (*Udry et al.*, 2018), provides a natural example of such evolved Martian compositions (Figure 5.2a). At pressures corresponding to the top of the Martian lower crust, Harrison C2–like melts reach volatile saturation at temperatures of ~1000 °C, with dissolved water contents controlled by the depth of magma emplacement and reaching several weight percent at mid- to lower-crustal depths (Figure 5.2b). For magmas containing predominantly H_2O-rich fluids at depths of ~10–40 km, estimated water contents at the onset of volatile exsolution range from ~4 to 9 wt. % (Figure 5.2b).

Geophysical observations indicate that marsquakes cluster at depths of ~15 – 35 km (*Drilleau et al.*, 2022; *Durán et al.*, 2022), broadly corresponding to the extent of the lower crust (Figure 5.1a). As on Earth, Martian magmas are likely to stall at depths where significant density contrasts or rheological discontinuities are encountered (*Cashman et al.*, 2017). The transition between the lower and middle crust on Mars represents a favorable environment for magma stalling. At such depths, magmatic bodies are expected to continue cooling past their volatile saturation temperatures, becoming progressively enriched in volatiles and producing a sustained positive fluid flux into the surrounding crust. For example, cooling of a magma with the composition of Harrison C2 from 1000 to 700 °C, at rates expected for spherical magma bodies with radii ~ 1000˜5000 m, produces estimated water fluxes at the top of the intrusion of ~ 10^{-8} – 10^{-10} m s^{-1}.

3. Hydration reactions rapidly consume magmatic fluids

The fate of magmatically exsolved fluids depends on their interaction with the surrounding crust. To assess this process, we consider a simplified one-dimensional reactive-flow model in which fluids released at the top of a stalled magma body migrate upward through a fractured mid-crustal column (Figure 5.1b). As fluids move through the crust, they may escape upward or be consumed by hydration reactions that convert nominally anhydrous minerals into hydrous phases such as amphibole and phyllosilicates. The permeability of the crustal column also controls whether the exsolved fluid flows upwards or accumulates at the top of the intrusion

(*Annen and Burgisser*, 2021).

Hydration reactions exert two critical effects. First, they act as a chemical sink for water, removing free fluid from the system. Second, they progressively reduce permeability by clogging pore space and sealing fractures (*Kelemen and Hirth*, 2012; *Manga and Wright*, 2021). As permeability decreases, advective fluid transport becomes increasingly inefficient, further enhancing fluid retention and reaction. However, this effect is counteracted by a reduction in the reactivity of the rock surface as hydration proceeds (*Kelemen and Hirth*, 2012), lowering reaction rates as permeability declines.

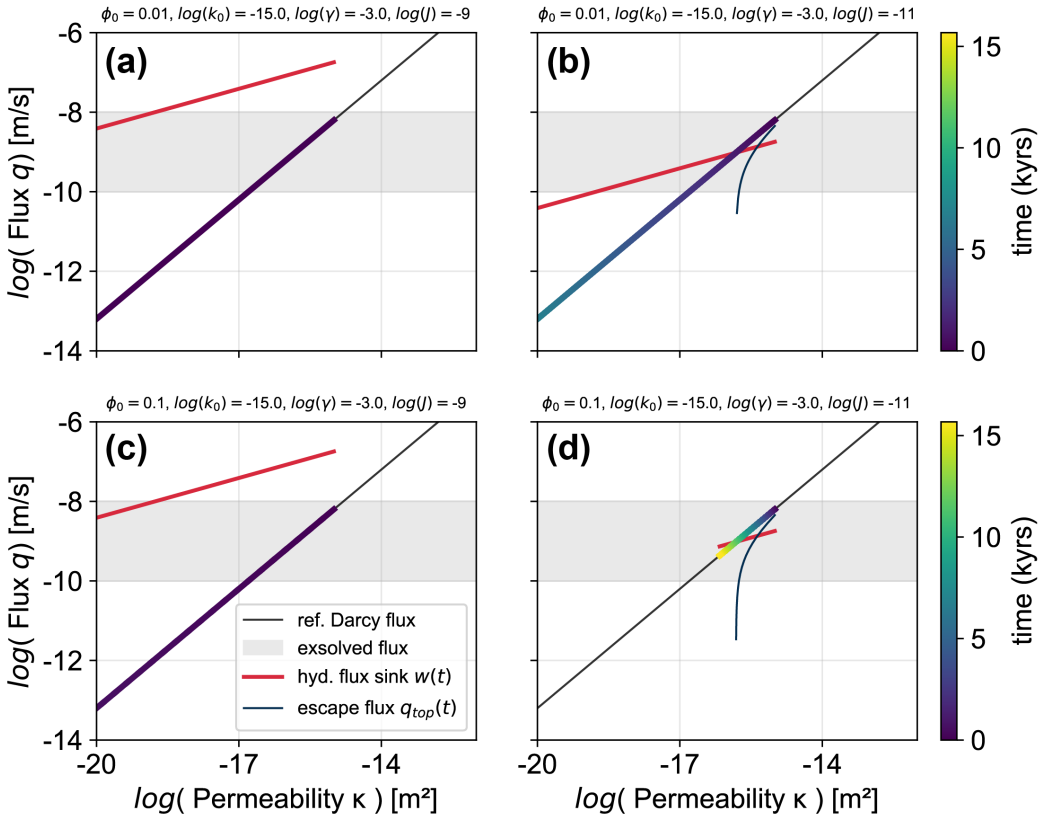


Figure 5.3: Evolution of permeability and fluid flux during the conductive cooling of a 5000 m magma body. Colored trajectories track permeability and Darcy flux over the cooling timescale of the intrusion for an initial permeability ($\kappa = 10^{-15}$) and volumetric mineral change due to hydration ($\gamma = 10^{-3}$ m^3 kg^{-1} H_2O). The models consider porosity (ϕ) values of 0.01 **(a - b)** and 0.1 **(b - d)** and rates of H_2O loss associated with hydration (J) between 10^{-9} **(a - c)** and 10^{-11} kg s^{-1} m^{-2} **(d)**. The shaded gray region represents average estimates of the volatile flux during magma cooling. Model results with different parameter choices are given in the Supplementary Information.

Rates of H_2O loss associated with hydration of mafic minerals during retrograde metamorphic reactions are on the order of 10^{-11} – 10^{-8} kg s^{-1} m^{-2} at temperatures between 200 to 400 °C (*Yardley et al.*, 2014; *Lamadrid et al.*, 2017). These hydration reactions are also accompanied by typical volumetric changes of $\sim 10^{-4}$ – 10^{-3} m^3 kg^{-1} H_2O. Our model results show that, for initial permeabilities ranging from 10^{-18} to 10^{-15} m^2, hydration reactions exert the dominant control on fluid fate (Figure 5.3a-d). Even when the initial Darcy flux through the column exceeds the hydration sink—for example, if the reactivity of the rock column is initially low—continued reaction ultimately drives the system toward sink-dominated behavior (Figure 5.3b,d). As a result, only a small fraction of magmatically exsolved fluid can migrate significant distances through the column before being consumed, and fluid escape is expected primarily during the earliest stages of system evolution. Even in cases where permeability is not fully lost during magmatic cooling—for example, if initial porosity is high and reactivity is low—hydration reactions eventually become dominant over advective flux (Figure 5.3d).

Compared to magmatic cooling timescales, which govern the duration of fluid supply to the crustal column, hydration-driven sealing consistently proceeds more rapidly (Figures 5.3 and 5.4). On Mars, the interface between the mid and lower crust roughly coincides with the depth limit at which long-lived magmatic intrusions can exist (*Chatterjee et al.*, 2025). Estimated cooling timescales for magmatic intrusions hosted in the Martian lower crust, neglecting magma recharge, range from thousands to hundreds of thousands of years depending on intrusion size and crustal thermal structure (e.g., radii of ∼1000–5000 m; T_0 = 1000 °C, T_f = 700 °C, $T_{\text{host rock}}$ = 400 °C). For most realistic porosities and reaction rates (*i.e.*, ϕ_0 ranging from 10^{-3} to 10^{-1}; J ranging from 10^{-11} and 10^{-9} kg s^{-1} m^{-2}), hydration reactions seal the fractured mid-crust on timescales of 10^1–10^5 years (Figure 5.4). Only a combination of exceptionally low reaction rates, small volumetric changes during hydration, high initial porosity and permeability, and strong loss of reactivity allows a permeable column to persist for more than 10^6 years (Figure 5.4c). Permeability collapse therefore occurs within the expected intrusion cooling lifetime, shutting down upward fluid transport well before long-lived hydrologic systems can develop.

Consequently, free liquid water can persist only transiently and locally within the Martian crust. The formation of large, long-lived aquifers in the mid-crust is physically implausible under present-day conditions. However, during the early stages of magma cooling—before permeability collapse is complete—some fluid

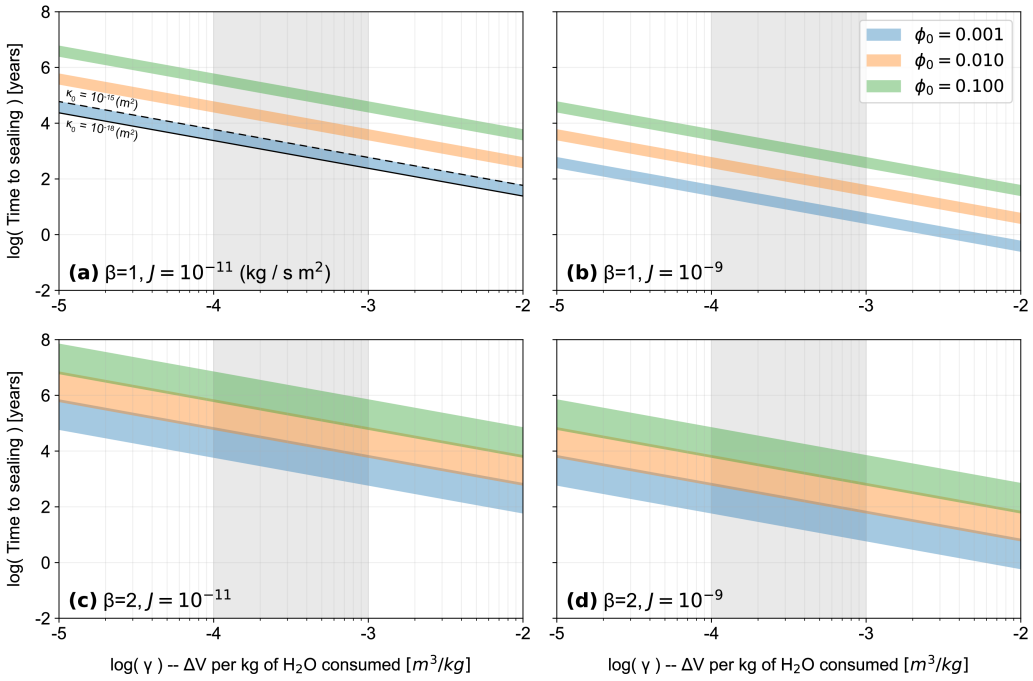


Figure 5.4: Estimated sealing time ($\kappa < 10^{-20}$ m^2) of the permeable column as a function of model parameters. Panels **(a)** and **(b)** correspond with a linear decrease in reactivity relative to porosity loss ($\beta = 1$) for J values of 10^{-11} and 10^{-9} kg s^{-1} m^{-2}, respectively. In panels **(c)** and **(d)**, the decrease in reactivity relative to porosity loss is quadratic ($\beta = 2$) for the same J values. Shaded regions represent initial porosity (ϕ_0) values of 0.001 (blue), 0.01 (orange), and 0.1 (green). The vertical width of each region is bounded by initial permeability values (κ_0) ranging 10^{-18} - 10^{-15} m^2. The shaded gray region overlaps with expected volumetric change ranges per kilogram of H_2O consumed during hydration reactions involving mafic minerals.

may escape hydration reactions in the mid-crust and migrate into colder upper crustal levels, where it may freeze or be incorporated into saline brines (*e.g.*, Figure 5.3b,d). Such escaping fluids may represent a potential source for liquid water inferred at different regions in the upper crust (e.g., *Knapmeyer-Endrun et al.*, 2025; *Sun et al.*, 2025), which could also be related to the aqueous floods inferred from remote sensing observations in the Cerberus Fossae region (*Burr et al.*, 2002).

4. Implications for present-day Mars

Taken together, these results reconcile the seismic permissibility of mid-crustal fluids with independent physical and geochemical constraints on their viability. Seismic observations indicate the presence of liquid water under specific assumptions about porosity, crack geometry, and saturation, but petrological and reactive-flow considerations show that such water cannot persist passively in the Martian crust. If liquid

water exists today in the mid-crust, it must therefore be generated continuously by an active process.

Intrusive magmatism provides the only mechanism consistent with these constraints. Martian magmas inevitably reach volatile saturation during differentiation and cooling, producing water-rich fluids at lower- to mid-crustal depths Figures 5.1 and 5.2. At the same time, hydration reactions rapidly consume those fluids and progressively reduce permeability, returning the crust to a predominantly dry state (Figures 5.3 and 5.4). This self-limiting cycle naturally explains why the Martian crust appears dry at regional scales while still permitting transient, localized fluid presence in regions where magmatic activity is ongoing, such as the geologically young Elysium Planitia province (*Horvath et al.*, 2021).

Moreover, two independent inferences from InSight data support the presence of present-day magmatic activity on Mars. First, marsquakes with characteristics consistent with magmatic or thermo-mechanical sources are clustered at depths overlapping the lower crust and spatially correlated with the Cerberus Fossae fracture system (Figure 5.1 *Stähler et al.*, 2022; *Horvath et al.*, 2021). This region also hosts evidence of recent pyroclastic eruptions (*Voigt et al.*, 2023), which most likely represent a surface manifestation of volatile-rich magmatism. Second, inferences of relatively low bulk average crustal densities can be explained by the presence of evolved magmas and alteration phases within the Martian crust (*Knapmeyer-Endrun et al.*, 2025; *Wieczorek et al.*, 2022; *Knapmeyer-Endrun et al.*, 2021). Together, these observations provide an independent geophysical context in which ongoing magmatic degassing is both plausible and expected.

Our results have implications for Martian seismicity, crustal evolution, and planetary habitability. Localized fluid release during magma cooling may facilitate brittle failure at mid-crustal depths, contributing to deep marsquakes. Although free liquid water is short-lived, repeated magmatic episodes over geological time could sustain episodic fluid availability, driving alteration and transient subsurface environments beneath the Martian surface.

References

Annen, C., and A. Burgisser, Modeling water exsolution from a growing and solidifying felsic magma body, *Lithos*, *402–403*, 105,799, doi:10.1016/j.lithos.2020.105799, 2021.

Balta, J. B., and H. Y. McSween, Jr., Water and the composition of Martian magmas,

Geology, *41*(10), 1115–1118, doi:10.1130/G34714.1, 2013.

Burr, D. M., A. S. McEwen, and S. E. H. Sakimoto, Recent aqueous floods from the Cerberus Fossae, Mars, *Geophysical Research Letters*, *29*(1), 13–1–13–4, doi:10.1029/2001GL013345, 2002.

Carr, M. H., and J. W. Head, Geologic history of Mars, *Earth and Planetary Science Letters*, *294*(3), 185–203, doi:10.1016/j.epsl.2009.06.042, 2010.

Cashman, K. V., R. S. J. Sparks, and J. D. Blundy, Vertically extensive and unstable magmatic systems: A unified view of igneous processes, *Science*, *355*(6331), eaag3055, doi:10.1126/science.aag3055, 2017.

Chatterjee, A. P., C. Huber, J. W. Head III, and O. Bachmann, Magma Chamber Longevity on Mars and Its Controls on Crustal Structure and Composition, *Journal of Geophysical Research: Planets*, *130*(4), e2024JE008,798, doi:10.1029/2024JE008798, 2025.

Drilleau, M., et al., Marsquake Locations and 1-D Seismic Models for Mars From InSight Data, *Journal of Geophysical Research: Planets*, *127*(9), e2021JE007,067, doi:10.1029/2021JE007067, 2022.

Durán, C., A. Khan, S. Ceylan, G. Zenhäusern, S. Stähler, J. F. Clinton, and D. Giardini, Seismology on Mars: An analysis of direct, reflected, and converted seismic body waves with implications for interior structure, *Physics of the Earth and Planetary Interiors*, *325*, 106,851, doi:10.1016/j.pepi.2022.106851, 2022.

Hernández-Montenegro, J. D., P. D. Asimow, and C. Herzberg, PRIMARSMELT: Primary magma compositions for Mars, doi:10.22002/w2ay2-dqs40, 2024.

Horvath, D. G., P. Moitra, C. W. Hamilton, R. A. Craddock, and J. C. Andrews-Hanna, Evidence for geologically recent explosive volcanism in Elysium Planitia, Mars, *Icarus*, *365*, 114,499, doi:10.1016/j.icarus.2021.114499, 2021.

Jakosky, B. M., Results from the inSight Mars mission do not require a water-saturated mid crust, *Proceedings of the National Academy of Sciences*, *122*(11), e2418978,122, doi:10.1073/pnas.2418978122, 2025.

Katayama, I., and Y. Akamatsu, Seismic discontinuity in the Martian crust possibly caused by water-filled cracks, *Geology*, *52*(12), 939–942, doi:10.1130/G52369.1, 2024.

Kelemen, P. B., and G. Hirth, Reaction-driven cracking during retrograde metamorphism: Olivine hydration and carbonation, *Earth and Planetary Science Letters*, *345–348*, 81–89, doi:10.1016/j.epsl.2012.06.018, 2012.

Kilburn, R., J. Dasent, V. Wright, and M. Manga, Lithology, Pore-Filling Media, and Pore Closure Depth Beneath InSight on Mars Inferred From Shear Wave Velocities, *Journal of Geophysical Research: Planets*, *127*(12), e2022JE007,539, doi:10.1029/2022JE007539, 2022.

Knapmeyer-Endrun, B., et al., Thickness and structure of the martian crust from InSight seismic data, *Science*, *373*(6553), 438–443, doi:10.1126/science.abf8966, 2021.

Knapmeyer-Endrun, B., et al., Porosity and hydrous alteration of the Martian crust from InSight seismic data, *Physics of the Earth and Planetary Interiors*, *366*, 107,383, doi:10.1016/j.pepi.2025.107383, 2025.

Lamadrid, H. M., J. D. Rimstidt, E. M. Schwarzenbach, F. Klein, S. Ulrich, A. Dolocan, and R. J. Bodnar, Effect of water activity on rates of serpentinization of olivine, *Nature Communications*, *8*(1), 16,107, doi:10.1038/ncomms16107, 2017.

Manga, M., and V. Wright, No Cryosphere-Confined Aquifer Below InSight on Mars, *Geophysical Research Letters*, *48*(8), e2021GL093,127, doi:10.1029/2021GL093127, 2021.

McCubbin, F. M., E. H. Hauri, S. M. Elardo, K. E. Vander Kaaden, J. Wang, and C. K. Shearer, Jr., Hydrous melting of the martian mantle produced both depleted and enriched shergottites, *Geology*, *40*(8), 683–686, doi:10.1130/G33242.1, 2012.

McCubbin, F. M., J. W. Boyce, P. Srinivasan, A. R. Santos, S. M. Elardo, J. Filiberto, A. Steele, and C. K. Shearer, Heterogeneous distribution of H2O in the Martian interior: Implications for the abundance of H2O in depleted and enriched mantle sources, *Meteoritics & Planetary Science*, *51*(11), 2036–2060, doi:10.1111/maps.12639, 2016.

McSween, H. Y., Petrology on Mars, *American Mineralogist*, *100*(11-12), 2380–2395, 2015.

McSween, H. Y., T. L. Grove, R. C. F. Lentz, J. C. Dann, A. H. Holzheid, L. R. Riciputi, and J. G. Ryan, Geochemical evidence for magmatic water within Mars from pyroxenes in the Shergotty meteorite, *Nature*, *409*(6819), 487–490, doi:10.1038/35054011, 2001.

Menina, S., et al., Energy Envelope and Attenuation Characteristics of High-Frequency (HF) and Very-High-Frequency (VF) Martian Events, *Bulletin of the Seismological Society of America*, *111*(6), 3016–3034, doi:10.1785/0120210127, 2021.

Menina, S., et al., Stratification of Heterogeneity in the Lithosphere of Mars From Envelope Modeling of Event S1222a and Near Impacts: Interpretation and Implications for Very-High-Frequency Events, *Geophysical Research Letters*, *50*(7), e2023GL103,202, doi:10.1029/2023GL103202, 2023.

Palin, R., J. Wade, and B. Dyck, Metamorphism in a wet Martian middle crust, *Proceedings of the National Academy of Sciences*, *121*(49), e2416680,121, doi:10.1073/pnas.2416680121, 2024.

Scheller, E. L., B. L. Ehlmann, R. Hu, D. J. Adams, and Y. L. Yung, Long-term drying of Mars by sequestration of ocean-scale volumes of water in the crust, *Science*, *372*(6537), 56–62, doi:10.1126/science.abc7717, 2021.

Scheller, E. L., et al., Aqueous alteration processes in Jezero crater, Mars—implications for organic geochemistry, *Science*, *378*(6624), 1105–1110, doi:10.1126/science.abo5204, 2022.

Stähler, S. C., et al., Tectonics of Cerberus Fossae unveiled by marsquakes, *Nature Astronomy*, *6*(12), 1376–1386, doi:10.1038/s41550-022-01803-y, 2022.

Sun, W., H. Tkalčić, M. G. Malusà, and Y. Pan, Seismic evidence of liquid water at the base of Mars' upper crust, *National Science Review*, *12*(6), nwaf166, doi:10.1093/nsr/nwaf166, 2025.

Udry, A., E. Gazel, and H. Y. McSween, Formation of evolved rocks at Gale crater by crystal fractionation and implications for Mars crustal composition, *Journal of Geophysical Research: Planets*, *123*(6), 1525–1540, doi:10.1029/2018JE005602, 2018.

Voigt, J. R. C., C. W. Hamilton, G. Steinbrügge, M. S. Christoffersen, S. Nerozzi, L. Kerber, J. W. Holt, and L. M. Carter, Revealing Elysium Planitia's Young Geologic History: Constraints on Lava Emplacement, Areas, and Volumes, *Journal of Geophysical Research: Planets*, *128*(12), e2023JE007,947, doi:10.1029/2023JE007947, 2023.

Wieczorek, M. A., et al., InSight Constraints on the Global Character of the Martian Crust, *Journal of Geophysical Research: Planets*, *127*(5), e2022JE007,298, doi:10.1029/2022JE007298, 2022.

Wright, V., M. Morzfeld, and M. Manga, Liquid water in the Martian mid-crust, *Proceedings of the National Academy of Sciences*, *121*(35), e2409983,121, doi:10.1073/pnas.2409983121, 2024.

Yardley, B. W. D., D. Rhede, and W. Heinrich, Rates of Retrograde Metamorphism and their Implications for the Rheology of the Crust: An Experimental Study, *Journal of Petrology*, *55*(3), 623–641, doi:10.1093/petrology/egu001, 2014.

SUPPLEMENTARY MATERIAL: ACTIVE MAGMATIC DEGASSING IS REQUIRED TO SUSTAIN LIQUID WATER IN THE MARTIAN CRUST

METHODS AND MATERIALS

S1. FRACTIONAL CRYSTALLIZATION MODELS

We used PRIMARSMELT (*Hernández-Montenegro et al.*, 2024) to calculate the average primary magma compositions of Martian basalts interpreted as products of crystallization of mantle-derived melts. We considered the mean compositions of primary magmas produced from partial melting of two mantle compositions: *i)* $Mg\# = 75$ from *Dreibus and Wänke* (1985, DW) and *ii)* $Mg\# = 79$ from *Yoshizaki and McDonough* (2020, YM). These two average compositions are also primary magma solutions, requiring only minimal olivine addition (< 1.0 wt. %).

Isobaric fractional crystallization calculations of the two primary magma compositions were conducted using rhyolite-MELTS v.1.2.0 (*Ghiorso and Gualda*, 2015; *Gualda et al.*, 2012), which uses the equation of state of *Duan and Zhang* (2006) for H_2O-CO_2 fluid. We considered the range of parameters summarized in Supplementary Table S5.1. The resulting liquid lines of descent (LLD) are shown in TAS space (SiO_2 versus Total alkalis [Na_2O + K_2O]) in Figures S5.1 and S5.2.

Table S5.1: Parameter space explored in model runs.

Parameter	Range / Value
P (GPa)	0.2–0.6 (every 0.05)
fO_2 (FMQ)	$-2, -1, 0$
H_2O_0	100, 1000, 5000, 10000, 20000
CO_{2_0}	0, 100, 200, 300, 400, 500

S2. MAGMA COOLING AND VOLUMETRIC FLUX OF EXSOLVED H_2O

Magma cooling rate

To approximate the flux of volatiles produced during magmatic cooling, we consider conductive heat loss from a spherical intrusion of radius R emplaced in an infinite host at fixed temperature T_∞ (*Turcotte and Schubert*, 2014). The magma is initially at uniform temperature T_0. Temperature evolution follows the diffusion equation in spherical symmetry:

$$\frac{\partial T}{\partial t} = \kappa \left[\frac{1}{r^2} \frac{\partial}{\partial r} \left(r^2 \frac{\partial T}{\partial r} \right) \right], \tag{S5.1}$$

where $\kappa = 10^{-6}\ \mathrm{m^2\ s^{-1}}$ is the thermal diffusivity. The initial and boundary conditions are $T(r, 0) = T_0$ and $T(R, t) = T_\infty$.

A dimensionless temperature can be defined as $\bar{\theta} = (\bar{T} - T_\infty)/(T_0 - T_\infty)$, where $\bar{T}$ is the volume-averaged magma temperature given by:

$$\bar{T}(t) = \frac{3}{R^3} \int_0^R T(r, t)\, r^2\, dr, \tag{S5.2}$$

From the solution for a sphere, Equation S5.2 yields:

$$\bar{\theta}(t) = \frac{6}{\pi^2} \sum_{n=1}^{\infty} \frac{1}{n^2} \exp\left(-n^2 \pi^2 \frac{\kappa t}{R^2} \right), \tag{S5.3}$$

which can be approximated by the first eigenmode as:

$$\bar{\theta}(t) \approx \frac{6}{\pi^2} \exp\left(-\pi^2 \frac{\kappa t}{R^2} \right) \tag{S5.4}$$

The time required for the magma body to cool to a target average temperature $\bar{T}$ can be calculated from Equation S5.4 as follows:

$$t_{\mathrm{cool}} \approx \frac{R^2}{\pi^2 \kappa} \ln\left[\frac{6}{\pi^2} \frac{T_0 - T_\infty}{\bar{T} - T_\infty} \right]. \tag{S5.5}$$

This defines a characteristic conductive cooling timescale,

$$\tau_c = \frac{R^2}{\pi^2 \kappa}. \tag{S5.6}$$

Over a temperature interval $\Delta T = T_{\mathrm{hi}} - T_{\mathrm{lo}}$, we define a representative mean cooling rate:

$$R_T \equiv \left| \frac{dT}{dt} \right| \approx \frac{\Delta T}{t_{\mathrm{cool}}}. \tag{S5.7}$$

Volatile exsolution flux estimation

Isobaric crystallization paths of the Harrison C2 trachyandesitic composition (*Udry et al.*, 2018) were simulated using rhyolite-MELTS v.1.2.0 (*Ghiorso and Gualda*, 2015; *Gualda et al.*, 2012). We calculated the average mass of the exsolved volatile phase across a temperature range from the liquidus T_{hi} = 1000 °C to T_{lo} = 700 °C (dM_f/dT), scaled to the total mass of the intrusion given by:

$$M_m = \rho_m \frac{4}{3} \pi R^3. \tag{S5.8}$$

The average volatile mass production rate (dM_f/dt) is then calculated as:

$$\frac{dM_f}{dt} = \frac{dM_f}{dT} \times R_T \qquad [\mathrm{kg\ s^{-1}}] \tag{S5.9}$$

Flux of exsolved volatiles

We assume that exsolved volatiles escape upward through the roof of the intrusion. For a spherical body, the roof area is taken as the upper hemisphere:

$$A_{\mathrm{roof}} = 2\pi R^2. \tag{S5.10}$$

The upward mass flux per unit area is therefore

$$j_m = \frac{dM_f/dt}{A_{\mathrm{roof}}} \qquad [\mathrm{kg\ s^{-1}\ m^{-2}}]. \tag{S5.11}$$

The corresponding volumetric flux is:

$$q = \frac{j_m}{\rho_f} = \frac{dM_f/dt}{\rho_f\, A_{\mathrm{roof}}} \qquad [\mathrm{m^3\ s^{-1}\ m^{-2}}]. \tag{S5.12}$$

where ρ_f is the density of the fluid.

In our calculations, we consider intrusions with radii ranging from 1000–5000 m and fluid density of 1000 kg $\mathrm{m^{-3}}$, resulting in volumetric fluxes between $\sim 10^{-10}$ and $\sim 10^{-8}$ $\mathrm{m^3\ s^{-1}\ m^{-2}}$.

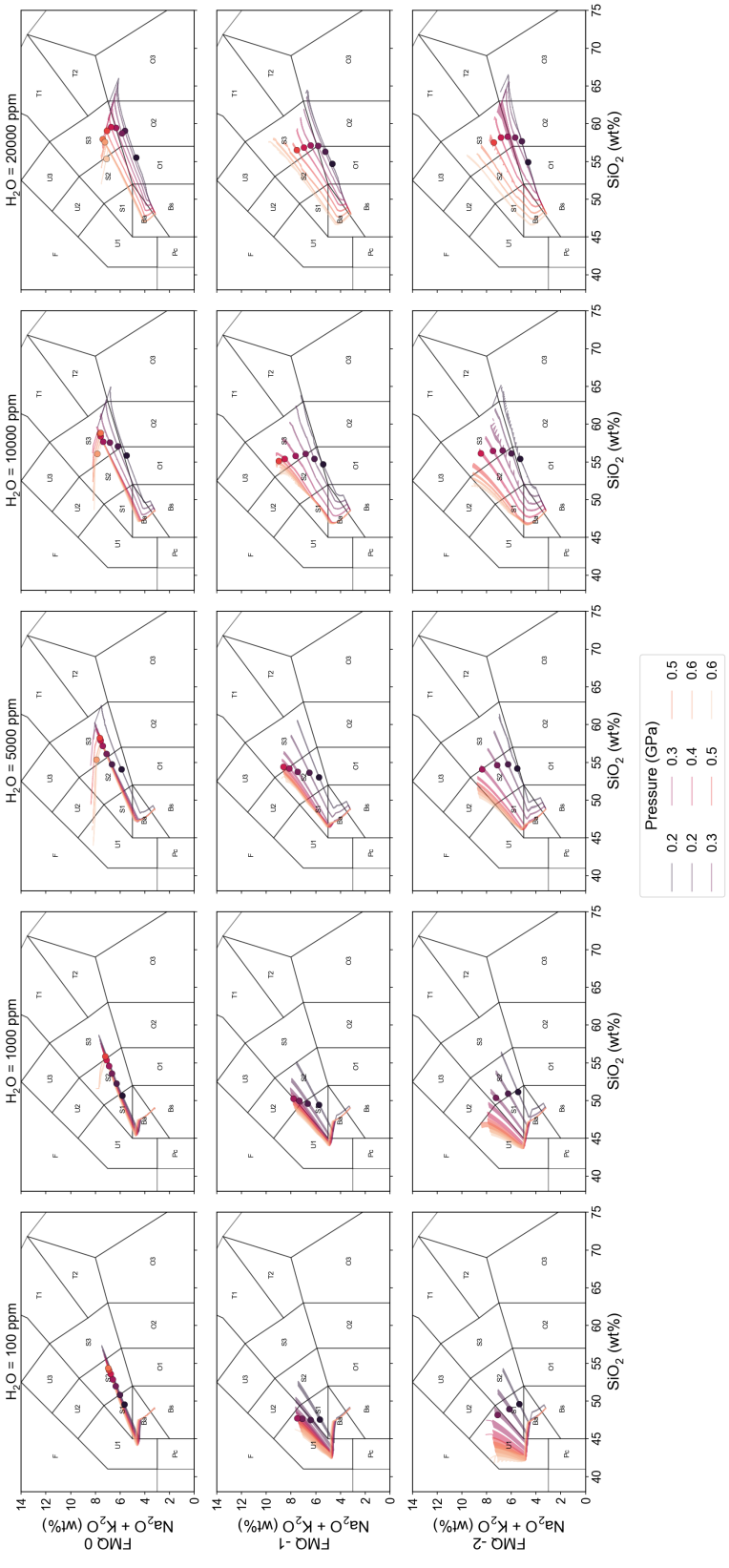


Figure S5.1: TAS diagram grid showing liquid lines of descent for melt compositions produced by fractional crystallization of an average primary magma generated by melting of the DW mantle composition for Mars. The initial H_2O content increases from left to right, and the oxygen fugacity (fO_2) relative to the Fayalite-Magnetite-Quartz buffer decreases from top to bottom. Each line color corresponds with crystallization pressures ranging 0.2-0.6 GPa and the thickness of each line results from variability in the CO_2 contents considered, which vary from 0 to 500 ppm.

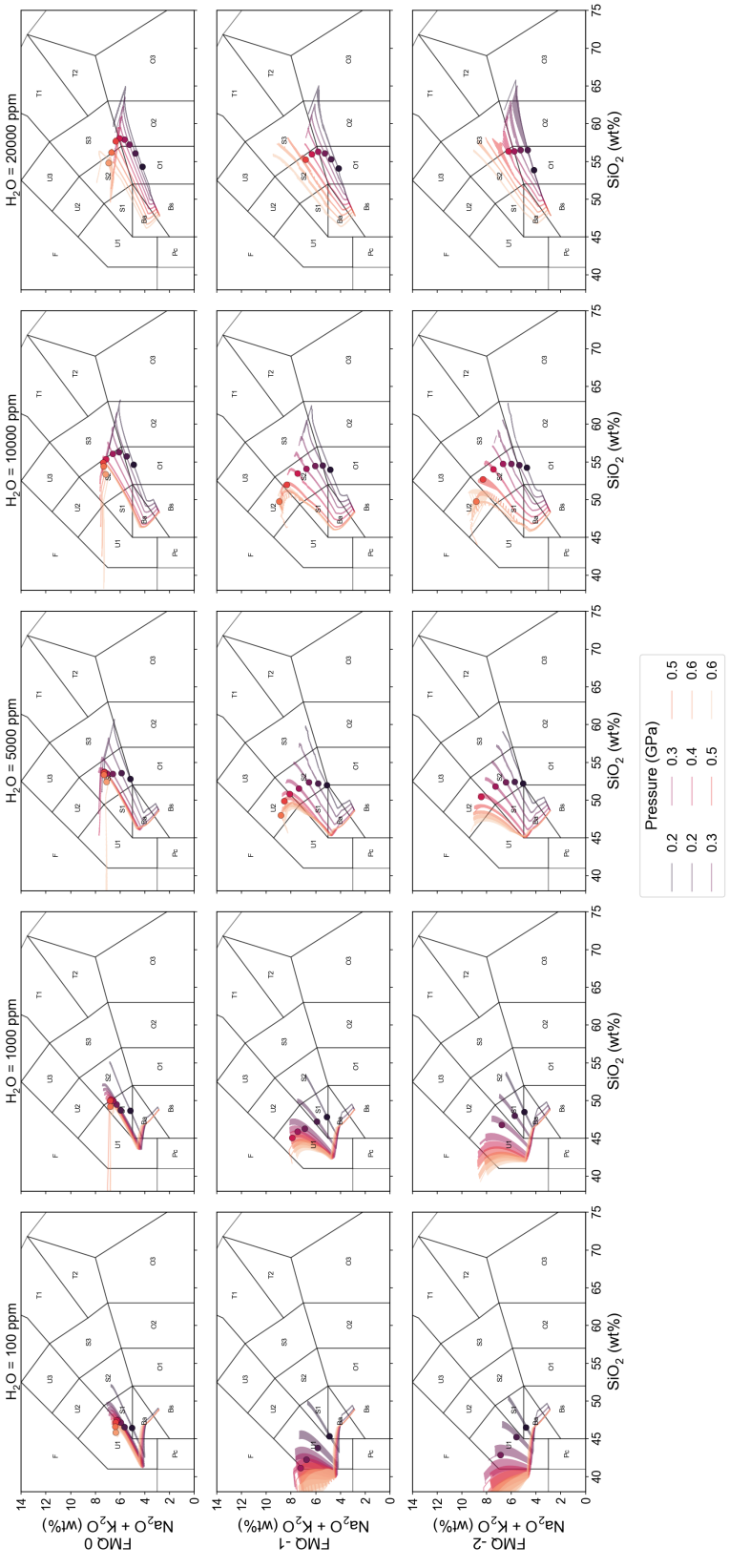


Figure S5.2: TAS diagram grid showing liquid lines of descent for melt compositions produced by fractional crystallization of an average primary magma generated by melting of the YM mantle composition for Mars. The initial H_2O content increases from left to right, and the oxygen fugacity (fO_2) relative to the Fayalite-Magnetite-Quartz buffer decreases from top to bottom. Each line color corresponds with crystallization pressures ranging 0.2-0.6 GPa and the thickness of each line results from variability in the CO_2 contents considered, which vary from 0 to 500 ppm.

S3. REACTIVE FLOW MODEL

We model one–dimensional vertical reactive fluid flow through a fractured crustal column of thickness L, extending from depth $z = 0$ (fluid source) to $z = L$ (upper boundary). The system represents fracture-dominated Darcy flow coupled to hydration reactions that consume fluid and modify porosity and permeability over time.

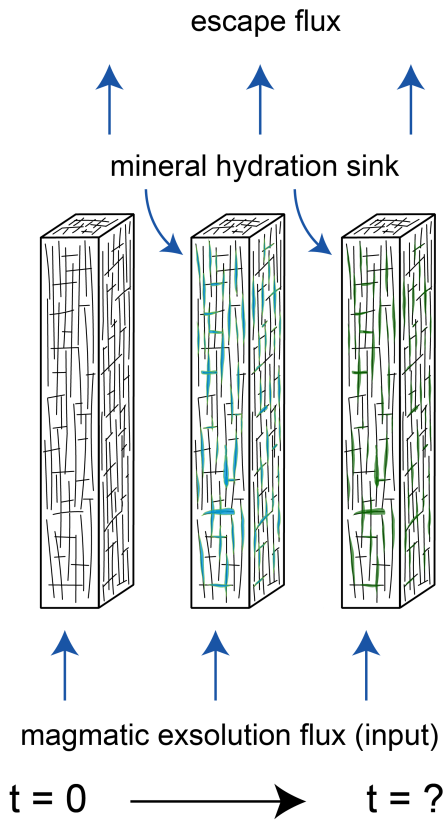


Figure S5.3: Schematic representation of a crustal column representative of the Martian mid-crust. Fluid flow occurs from bottom to top through a connected fracture network and is driven by buoyancy. Water is progressively consumed by hydration reactions at fracture walls, leading to a reduction in porosity and permeability through the addition of solid volume. Depending on the reaction rate and permeability at a given time, fluid may escape the mid-crust and migrate to the upper crust, where it could further react with the host rock, remain stored in the porous space, or eventually reach the surface.

Fluid Mass Balance

We assume single-phase aqueous fluid flow through a fracture network. Fluid mass conservation, including a volumetric sink due to hydration reactions, is written as:

$$\frac{\partial}{\partial t}\left(\rho_f \phi\right) + \frac{\partial}{\partial z}\left(\rho_f q\right) = -w(\phi), \tag{S5.13}$$

where ρ_f is the fluid density, ϕ is fracture porosity, q is the average Darcy flux across the column, and $w(\phi)$ is the volumetric mass consumption rate of aqueous fluid due to hydration reactions (kg m^{-3} s^{-1}).

Darcy Flow

Fluid flow through the crustal column is governed by Darcy's law (*Spear*, 1993; *Turcotte and Schubert*, 2014):

$$q(t) = \frac{k(\phi)}{\mu}\left(\rho_r - \rho_f\right) g, \tag{S5.14}$$

where $k(\phi)$ is permeability, μ is dynamic viscosity, ρ_r is host rock density, and g is gravitational acceleration on Mars (3.73 m s^{-2}). The driving force is the buoyancy contrast between rock and fluid; no other imposed pressure gradient is considered.

Reaction Rate and Hydration Sink

Hydration reactions consume water at mineral–fluid interfaces. We define the volumetric mass sink as a function of porosity to account for the progressive decrease in surface reactivity or passivation expected as porosity and permeability decay (*Kelemen and Hirth*, 2012).

$$w(\phi) = w_0 \left(\frac{\phi}{\phi_0}\right)^{\beta}, \tag{S5.15}$$

where w_0 is the volumetric mass consumption rate at a reference porosity, here taken as the initial porosity ϕ_0, and β is a sensitivity parameter that controls the change in reaction rate as porosity decreases.

The reference sink rate w_0 is derived from experimental rates of H_2O loss during reaction of aqueous fluid with exposed surfaces of mafic rocks and minerals (*Lamadrid et al.*, 2017; *Yardley et al.*, 2014):

$$w_0 = r_s S_v, \tag{S5.16}$$

where r_s is the mass consumption rate per unit area (kg m^{-2} s^{-1}), and $S_v = 2/d$ is the fracture surface area per unit volume for fracture spacing d (m^2 m^{-3}).

Porosity Evolution

Hydration reactions increase solid volume, reducing fracture porosity. Porosity evolution can be expressed as:

$$\frac{\partial \phi}{\partial t} = -\gamma\, w(\phi), \tag{S5.17}$$

where γ is the solid volume increase per unit mass of water consumed during hydration reactions (m^3 kg^{-1}). This formulation assumes locally isovolumetric bulk behavior, with solid volume growth accommodated by fracture closure.

Permeability–Porosity Relation

Because in our model fluid flow is fracture-dominated, permeability is related to porosity by a cubic-law scaling (*Steefel and Lasaga*, 1994; *Steefel et al.*, 2015; *Hommel et al.*, 2018):

$$k(\phi) = k_0 \left(\frac{\phi}{\phi_0} \right)^3, \tag{S5.18}$$

where k_0 is permeability at reference porosity ϕ_0. This relation captures the sensitivity of fracture permeability to aperture reduction during sealing.

Pore Velocity and Advective Timescale

The pore velocity is defined as

$$v(t) = \frac{q(t)}{\phi(t)}. \tag{S5.19}$$

The advective travel time from depth z to the top of the column is:

$$T_{\text{adv}}(z,t) = \int_z^L \frac{\phi(z',t)}{q(z',t)}\, dz' \tag{S5.20}$$

In our model, we consider an average initial porosity for the entire column, so Equation S5.20 can be simplified as:

$$T_{\mathrm{adv}} = \frac{\phi(t)}{q(t)}\, z \tag{S5.21}$$

This quantity evolves in time as both porosity and flux decrease due to reaction.

Closed-form porosity and permeability evolution

We consider a local porosity evolution law of the form

$$\frac{d\phi}{dt} = -\gamma\, w_0 \left(\frac{\phi}{\phi_0}\right)^{\beta}, \qquad \phi(0) = \phi_0, \tag{S5.22}$$

where ϕ is porosity, w_0 is the volumetric fluid mass consumption rate at reference porosity ϕ_0, γ is the solid volume increase per unit mass of water consumed, and β controls the sensitivity of reaction rate to porosity reduction. Permeability is related to porosity by a cubic-law scaling appropriate for fracture-dominated flow,

$$k(\phi) = k_0 \left(\frac{\phi}{\phi_0}\right)^{3}, \qquad k(0) = k_0. \tag{S5.23}$$

Defining

$$A \equiv \frac{\gamma w_0}{\phi_0^{\beta}}, \tag{S5.24}$$

the porosity evolution has different solutions, depending on the value of β:

For $\beta = 1$:

$$\phi(t) = \phi_0\, e^{-At} \tag{S5.25}$$

For $\beta \neq 1$:

$$\phi(t) = \left[\phi_0^{1-\beta} - (1-\beta)At\right]^{\frac{1}{1-\beta}} \tag{S5.26}$$

It follows that the permeability evolution is:

For all β:

$$k(t) = k_0 \left(\frac{\phi(t)}{\phi_0}\right)^{3} \tag{S5.27}$$

In particular, for $\beta = 1$:

$$k(t) = k_0\, e^{-3At}. \tag{S5.28}$$

Time to reach a target permeability: Given a target permeability value, the corresponding porosity is:

$$\phi_{\text{target}} = \phi_0 \left(\frac{k_{\text{target}}}{k_0} \right)^{1/3}. \tag{S5.29}$$

For $\beta = 1$, the time to reach k_{target} is:

$$t(k_{\text{target}}) = \frac{1}{3A} \ln\left(\frac{k_0}{k_{\text{target}}} \right) \tag{S5.30}$$

For $\beta \neq 1$:

$$t(k_{\text{target}}) = \frac{\phi_0^{1-\beta} - \phi_{\text{target}}^{1-\beta}}{(1-\beta)A}. \tag{S5.31}$$

Here, we consider that complete fracture sealing is achieved when a permeability of 10^{-20} m^2 is attained.

The parameter β represents the reduction of reactive capacity with porosity, $w(\phi) \propto \phi$. In fracture-controlled systems, progressive hydration and mineral growth reduce fracture aperture, connectivity, and accessible reactive surface area in proportion to the remaining open fracture volume (*Kelemen and Hirth*, 2012). However, the value of β is arbitrary, as the extent of reactive capacity loss with hydration is unknown. We consider values of $\beta = 1$ and $\beta = 2$, which provide reasonable cases of reaction shutoff during fracture sealing. In general, $\beta > 1$ would result in an extremely weak hydration sink, which means virtually no mineral alteration during fluid-rock interaction.

Characteristic Permeability Timescale

For $\beta = 1$, the porosity evolution equation admits an exponential solution,

$$\phi(t) = \phi_0 \exp\left(-\frac{\gamma w_0}{\phi_0} t \right), \tag{S5.32}$$

leading to exponential permeability decay,

$$k(t) = k_0 \exp\left(-\frac{3\gamma w_0}{\phi_0} t \right). \tag{S5.33}$$

The characteristic permeability decay timescale is therefore

$$\tau_k = \frac{1}{3}\frac{\phi_0}{\gamma w_0}. \tag{S5.34}$$

Comparison of τ_k with the advective timescale T_{adv} is useful to evaluate whether fluids escape the system before permeability collapse or are trapped by self-sealing of the fracture network.

References

Dreibus, G., and H. Wänke, Mars, a volatile-rich planet, *Meteoritics*, *20*, 367–381, 1985.

Duan, Z., and Z. Zhang, Equation of state of the H2O, CO2, and H2O–CO2 systems up to 10 GPa and 2573.15 K: Molecular dynamics simulations with ab initio potential surface, *Geochimica et cosmochimica acta*, *70*(9), 2311–2324, 2006.

Ghiorso, M. S., and G. A. Gualda, An H2O–CO2 mixed fluid saturation model compatible with rhyolite-MELTS, *Contributions to Mineralogy and Petrology*, *169*(6), 53, 2015.

Gualda, G. A., M. S. Ghiorso, R. V. Lemons, and T. L. Carley, Rhyolite-MELTS: A modified calibration of MELTS optimized for silica-rich, fluid-bearing magmatic systems, *Journal of Petrology*, *53*(5), 875–890, 2012.

Hernández-Montenegro, J. D., P. D. Asimow, and C. Herzberg, PRIMARSMELT: Primary magma compositions for Mars, doi:10.22002/w2ay2-dqs40, 2024.

Hommel, J., E. Coltman, and H. Class, Porosity–permeability relations for evolving pore space: A review with a focus on (bio-) geochemically altered porous media, *Transport in Porous Media*, *124*(2), 589–629, 2018.

Kelemen, P. B., and G. Hirth, Reaction-driven cracking during retrograde metamorphism: Olivine hydration and carbonation, *Earth and Planetary Science Letters*, *345–348*, 81–89, doi:10.1016/j.epsl.2012.06.018, 2012.

Lamadrid, H. M., J. D. Rimstidt, E. M. Schwarzenbach, F. Klein, S. Ulrich, A. Dolocan, and R. J. Bodnar, Effect of water activity on rates of serpentinization of olivine, *Nature Communications*, *8*(1), 16,107, doi:10.1038/ncomms16107, 2017.

Spear, F. S., Metamorphic phase equilibria and pressure-temperature-time paths, *Mineralogical Society of America Monograph*, pp. 352–356, 1993.

Steefel, C. I., and A. C. Lasaga, A coupled model for transport of multiple chemical species and kinetic precipitation/dissolution reactions with application to reactive

flow in single phase hydrothermal systems, *American Journal of science*, *294*(5), 529–592, 1994.

Steefel, C. I., et al., Reactive transport codes for subsurface environmental simulation, *Computational Geosciences*, *19*(3), 445–478, doi:10.1007/s10596-014-9443-x, 2015.

Turcotte, D., and G. Schubert, *Geodynamics*, Cambridge University Press, 2014.

Udry, A., E. Gazel, and H. Y. McSween, Formation of evolved rocks at Gale crater by crystal fractionation and implications for Mars crustal composition, *Journal of Geophysical Research: Planets*, *123*(6), 1525–1540, doi:10.1029/2018JE005602, 2018.

Yardley, B. W. D., D. Rhede, and W. Heinrich, Rates of Retrograde Metamorphism and their Implications for the Rheology of the Crust: An Experimental Study, *Journal of Petrology*, *55*(3), 623–641, doi:10.1093/petrology/egu001, 2014.

Yoshizaki, T., and W. F. McDonough, The composition of Mars, *Geochimica et Cosmochimica Acta*, *273*, 137–162, doi:10.1016/j.gca.2020.01.011, 2020.

Chapter 6

PETROGENESIS OF THE OLIVINE CUMULATE OUTCROP *ISSOLE* – THE MISSING LINK BETWEEN THE SÉÍTAH AND MÁAZ FORMATIONS IN JEZERO CRATER, MARS

Hernández-Montenegro, J. D., et al., Petrogenesis of the olivine cumulate outcrop *Issole* – The missing link between the Séítah and Máaz formations in Jezero crater, Mars, *Icarus*, *437*, 116,620, doi:10.1016/j.icarus.2025.116620,

Author contributions: J.D. Hernández-Montenegro performed petrological modeling and geochemical interpretation of PIXL compositional data, contributed to data analysis and interpretation, and wrote the manuscript. Coauthors contributed rover data acquisition, mineralogical interpretation, extensive discussions, and manuscript revisions., 2025.

Abstract

Two lithologic units have been mapped and studied on the floor of Jezero crater, Mars: Séítah, which consists of layered olivine-rich cumulates, and Máaz, a series of basaltic to trachyandesitic lava flows. While Séítah and Máaz are close in proximity and stratigraphy, their potential geologic and petrological relationship remains unclear. Here, we present observations from the Planetary Instrument for X-ray Lithochemistry (PIXL) of an olivine cumulate outcrop – *Issole* – within the Séítah formation. The rock analyzed at *Issole* is a wehrlite dominated by olivine ($Fo_{46\pm1}$) and interstitial phases, including augite, late olivine, spinel, and feldspathic material. Compared to other outcrops from Séítah, *Issole* is more iron-rich and records substantial alteration processes. We combine mineral chemistry, textural analysis, and thermodynamic modeling to show that Séítah olivines crystallized from a basaltic parent magma, compositionally similar to the most primitive basalts in the Máaz formation. Crystallization of this parent magma produces residual melts that follow the magmatic differentiation trend defined by Máaz basalts. Moreover, the mineral assemblages predicted by our model during crystallization are consistent with observations from Séítah rocks but show some differences in composition. These differences can be reconciled by considering post-cumulus processes that modified the mineral assemblage in Séítah, including Fe-Mg exchange between

olivine and pyroxene. Our results indicate that Séítah and Máaz are likely genetically related, and their formation involved both accumulation of crystals at depth and eruption of lavas. The emplacement of Séítah likely occurred as a near-surface, sill-like igneous intrusion into previously erupted Máaz lava flows. The relationship between Séítah and Máaz demonstrates that magmatic differentiation processes, similar to those responsible for the formation of some Martian meteorites, can produce highly diverse lithologies and mineral textures in the Martian crust.

1. Introduction

The Mars 2020 Perseverance rover landed at the Octavia E. Butler (OEB) site in Jezero crater on February 18, 2021 (Figure 1). On the crater's floor, Perseverance explored two lithological units informally known as the Séítah ('amidst the sand' in Navajo) and Máaz (the Navajo word for "Mars") formations (*Sun et al*., 2023). Detailed observations by the Perseverance rover confirmed previously inferred compositions for these units from orbital data (*Goudge et al*., 2015; *Stack et al*., 2020) while also providing evidence for their igneous origin (*Beyssac et al*., 2023; *Farley et al*., 2022; *Liu et al*., 2022; *Scheller et al*., 2022; *Udry et al*., 2023). Séítah is now interpreted as an olivine-bearing unit with mafic to ultramafic composition, most likely representing a differentiated igneous cumulate with density stratification (*Beyssac et al*., 2023; *Farley et al*., 2022; *Liu et al*., 2022; *Treiman et al*., 2025; *Wiens et al*., 2022). In contrast, Máaz is thought to represent a series of variably evolved lava flows dominated by pyroxene and plagioclase (*Horgan et al*., 2023; *Schmidt et al*., 2025; *Udry et al*., 2023).

While Séítah and Máaz are in direct contact, with Séítah lying stratigraphically below Máaz, the relationship between them remains unclear. The proposed models for their igneous formation broadly fall into two categories. In the first, the Séítah olivine cumulates are interpreted as rocks formed by crystal settling in a magma chamber, which later lost its upper portion through weathering and erosion (*Wiens et al*., 2022). The source of the Séítah olivine is at this time unconstrained but has been related to the olivine-rich unit in the Nili Fossae region outside Jezero, which was constrained to be Fo44-66 using orbital observations (*Brown et al*., 2020). Máaz then formed by subsequent eruption and crystallization of unrelated lava flows on the erosional surface at the top of Séítah (*Beyssac et al*., 2023; *Udry et al*., 2023; *Wiens et al*., 2022). In contrast, the second model proposes that both units formed from the same (or a related) magma source, with Séítah representing the cumulate

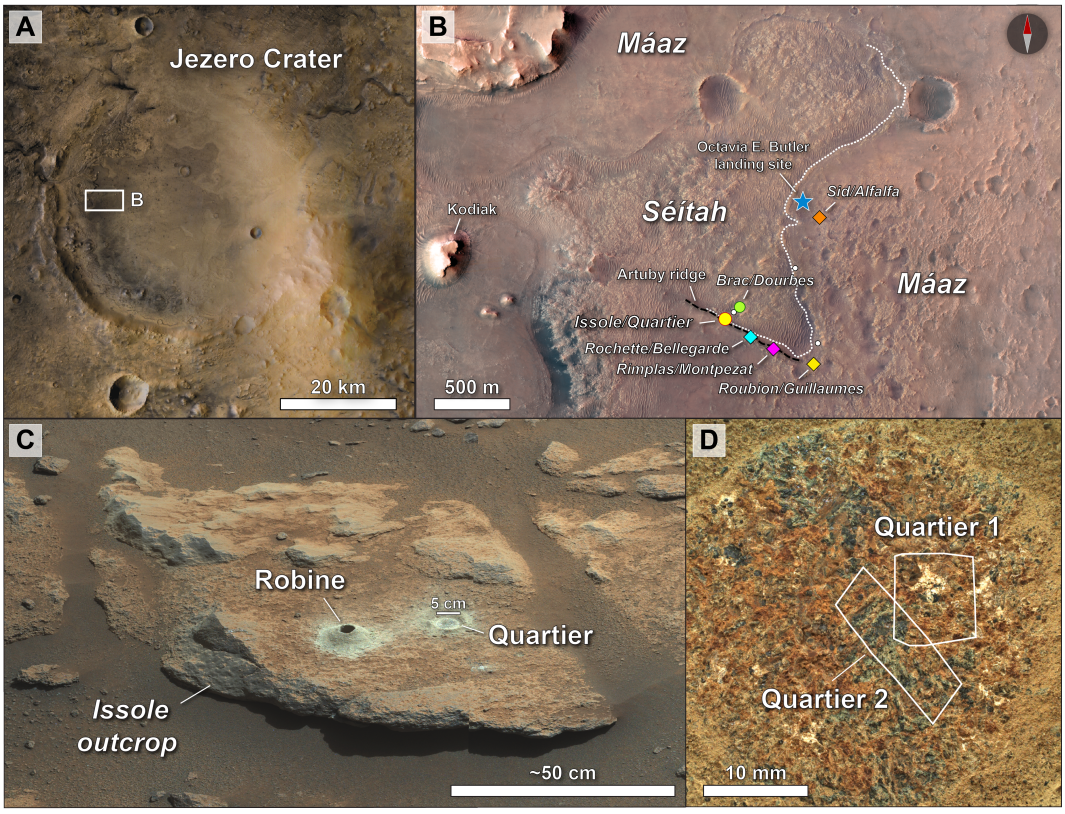


Figure 6.1: **(A)** Overview of Jezero crater on a Context camera (CTX) image showing the general location of the study area. **(B)** High Resolution Imaging Science Experiment (HiRISE; *Fergason et al.*, 2020) map showing the location of outcrops and corresponding abrasion patches analyzed by the PIXL instrument. Outcrops in Séítah and Máaz correspond to colored circles and diamonds, respectively. The white dots are PIXL targets with analyses on natural surfaces (non-abraded targets). The white dotted line marks the approximate limit between Séítah and Máaz, whereas the black dashed line is the Artuby ridge. **(C)** Mastcam-Z (*Bell et al.*, 2021) image of the Issole outcrop (Sol 298) showing the location of the Robine sample core and the Quartier abrasion patch. **(D)** WATSON color image of the Quartier abrasion patch with PIXL scan regions outlined in white.

products of crystal settling in a magma chamber and Máaz rocks crystallizing from the melts complementary to Séítah (*Treiman et al.*, 2025; *Wiens et al.*, 2022).

Unequivocal evidence of a relationship (or lack thereof) between Séítah and Máaz will only be possible upon complete geochemical and geochronological characterization of returned samples from Mars (*Simon et al.*, 2023; *Sun et al.*, 2023). Until then, evaluating existing petrogenetic models is essential for understanding the geological history of Jezero crater and establishing a framework for ongoing and future exploration efforts by Perseverance. Resolving the relationship between these units also contributes to our understanding of Mars' igneous evolution, offering insights into magmatic differentiation and crustal formation processes. A genetic link between Séítah and Máaz would demonstrate that igneous processes from single magmatic systems play a critical role in the mineral and lithological diversity of the Martian crust. In contrast, unrelated origins would suggest that lithological diversity can reflect complex magmatic and volcanic histories, even within relatively small regions. The study of Séítah cumulates can help establish a potential link between Séítah and Máaz and their possible emplacement mechanisms. Showing that the parent magmas that fractionated the olivine cumulates in the Séítah formation can also produce melt and mineral compositions like those observed in Máaz rocks would indicate a potential petrogenic relationship between Séítah and Máaz (*Treiman et al.*, 2025). Conversely, if the differentiation paths of magmas parental to Séítah diverge from the trend defined by Máaz rocks, the two formations are likely unrelated.

This study presents new observations from the Planetary Instrument for X-ray Lithochemistry (PIXL; *Allwood et al.*, 2020) of an evolved, iron-rich igneous cumulate outcrop (*Issole*) within the Séítah formation, near the contact with Máaz. These observations provide a unique opportunity to evaluate the competing models for the relationship between Séítah and Máaz. Our results include mineral chemistry and bulk composition data for the cumulate, including detailed petrographic characterization and textural analysis. We combine these data with thermodynamic modeling to estimate potential parental magma compositions for the cumulate. Using our best match for a parental magma, we then model melt crystallization to evaluate its evolution in bulk composition and crystallizing phase assemblages. Our modeling results suggest that this parent magma is compositionally similar to the most primitive basaltic compositions found in Máaz. Its crystallization sequence broadly agrees with the magmatic differentiation trend defined by Máaz rocks and their con-

stituent minerals. Hence, our findings support a petrogenetic link between Séítah and Máaz. The crystallization of Séítah cumulates requires initial rapid cooling followed by slower cooling in a subsurface environment. This is consistent with a sill-like magmatic body intruding into Máaz lava flows, previously erupted from the same magmatic system, although not necessarily from the same parental melt.

2. Background

2.1 Geological Context

Jezero crater is located within the Nili Planum cratered highlands at the western margin of the ~4.0 Ga Isidis Basin and northeast of the Syrtis Major Hesperian volcanic province (*Werner*, 2008). Jezero has a diameter of ~45 km and was formed at ~3.8-4.0 Ga by an impact on earlier Noachian basement (*Goudge et al*., 2015; *Mandon et al*., 2020; *Werner*, 2008). An open-basin lake subsequently formed, fed by a river network active during the late Noachian to early Hesperian (*Fassett and Head*, 2008; *Mangold et al*., 2020). This sedimentary activity in Jezero resulted in deposition of lacustrine and fluvial sediments, including the well-preserved clay- and carbonate-bearing western delta, which is a key target in the search for evidence of ancient life on Mars (*Ehlmann et al*., 2008a, 2008b; *Fassett and Head*, 2008; *Goudge et al*., 2015). Underlying the sedimentary units in Jezero are the Séítah and Máaz formations, which comprise the basement of Jezero crater (*Farley et al*., 2022; *Stack et al*., 2020; *Sun et al*., 2023).

Séítah and Máaz were investigated by Perseverance using a combination of remote sensing and proximity science instruments. Rock formations in Séítah are layered and olivine-rich (*Liu et al*., 2022; *Wiens et al*, 2022), and one outcrop investigated by PIXL is confirmed to be an olivine-rich wehrlite (*Liu et al*., 2022). The layered olivine-rich rocks in Séítah are likely formed by settling of olivine crystals from an iron-rich magma crystallizing near the Martian surface (*Liu et al*. 2022). By contrast, Máaz is a suite of ferroan basaltic-to-trachyandesitic lava flows, likely resulting from intracrustal magma differentiation (*Udry et al*., 2023; *Schmidt et al*., 2025; *Wiens et al*., 2022). The primary igneous minerals in both units experienced variable aqueous alteration, resulting in the formation of secondary minerals such as carbonates, sulfates, and hydrated silicates (*Scheller et al*., 2022; *Siljeström et al*., 2024; *Tice et al*., 2022).

Along Perseverance's traverse, the contact between Séítah and Máaz was defined at the base of Artuby Ridge, a scarp exposing the lower Máaz formation (*Crumpler et*

al. 2023; *Farley et al*. 2022, *Sun et al*. 2023). Although this contact was obscured by regolith, observations from the Radar Imager for Mars Subsurface Experiment (RIMFAX) revealed that Máaz uncomformably overlies Séítah (*Farley et al*., 2022; *Hamran et al*., 2022; *Shoemaker et al*., 2024). RIMFAX data also showed that Séítah layers dip subparallel to Máaz near their contact but become more horizontal with depth, suggesting that Séítah may intrude into Máaz (*Hamran et al*., 2022; *Wiens et al*., 2022). However, later RIMFAX observations pointed to the potential erosion of Séítah before Máaz emplacement, with possible depositional hiatuses and(or) periods of volcanic quiescence (*Shoemaker et al*. 2024), which contradicts a possible intrusive relationship between the two units.

2.2 Perseverance's Investigation of the Séítah Formation

Remote sensing activities in Séítah included the Mastcam-Z (*Bell et al*., 2021) and SuperCam (*Wiens et al*., 2020) instruments, which provided outcrop-scale observations of rock structures and elemental and mineral compositions at distance (e.g., *Bell et al*., 2022; *Beyssac et al*., 2023; *Mandon et al*., 2023; *Rice et al*., 2023; *Wiens et al*., 2022). Proximity science, which refers to high-resolution observations made with the rover's arm positioned just a few centimeters from a rock surface, was conducted using WATSON/SHERLOC (*Bhartia et al*., 2021) and PIXL (*Allwood et al*., 2020). These instruments provided microscopic-scale textural and compositional information on rock targets (e.g., *Corpolongo et al*., 2023; *Liu et al*., 2022; *Tice et al*., 2022). Observations during proximity science were made on natural and abraded rock surfaces created to remove dust and coating. These abraded targets are circular patches ~1 cm deep and ~5 cm in diameter made with Perseverance's abrasion tool. A detailed description of the typical workflow and activities performed by each science instrument onboard the Perseverance rover is provided in *Sun et al*. (2023).

Initial Perseverance observations in Séítah were conducted on sol 202 when the rover first visited the *Issole* outcrop and performed only remote sensing activities (*Crumpler et al*. 2023; *Sun et al*. 2023). Then, the rover drove to the *Bastide* and *Brac* outcrops, where the targets *Garde* (sol 206) and *Dourbes* (sol 253) were abraded. Two samples, *Sallete* (sol 262) and *Coulettes* (sol 271), were collected at *Brac*, representing the first sample pair from Séítah (*Simon et al*., 2023). The rover then returned to *Issole* on Sol 286 to investigate Séítah at the proximity of its contact with Máaz (Figure 1B; *Crumpler et al*., 2023; *Sun et al*., 2023). At *Issole*, Perseverance abraded a target named *Quartier*. on sol 292 (Figure 1C and 1D; *Sun*

et al. 2023) and collected two additional samples, *Robine* (Figure 1C) and *Malay*, on sols 298 and 337, respectively (*Simon et al*. 2023; *Sun et al*. 2023).

2.3 Observations at *Issole*

The *Issole* outcrop is part of the broader *Issole* member of Séítah and is located within ~10-20 meters north of the base of Artuby Ridge (*Beyssac et al*., 2023; *Crumpler et al*., 2023). Remote and proximity science observations of *Issole* and the *Quartier* abrasion patch revealed that *Issole* is a weathered and altered ultramafic igneous rock, potentially representing the upper portion of a cumulate sequence observed in deeper sections of Séítah (*Beyssac et al*., 2023; *Crumpler et al*., 2023; *Rice et al*., 2023). Olivine is the primary constituent, followed by pyroxene (*Beyssac et al*., 2023; *Rice et al*., 2023), with alteration phases that include sulfates, carbonates, hydrated silicates, perchlorates/chlorates, and phosphates (*Corpolongo et al*., 2023; *Mandon* et al., 2023; *Siljeström et al*., 2024). Organic molecules were also detected in *Quartier*. associated with aqueous alteration processes (*Corpolongo et al*., 2023; *Sharma et al*., 2023). The two samples collected at *Issole* were considered strategic for the astrobiological objectives of the mission (*Simon et al*., 2023; *Sun et al*., 2023). Furthermore, the proximity of *Issole* to the contact with Máaz makes it a key location to investigate the formation and relationship of the Séítah and Máaz formations and better understand the geological context of Jezero crater.

3. Methods

3.1 PIXL Analytical Techniques on *Issole*

The PIXL instrument was used to collect two X-ray fluorescence (XRF) scans within the *Quartier* abrasion patch on the *Issole* outcrop. The two maps covered areas of ~7 × 7 mm and ~4 × 12.5 mm, with a step size of 125 μm, corresponding to raster images with 3260 and 3343 pixels, which we will refer to as *Quartier* 1 (sol 294) and *Quartier* 2 (sol 301), respectively (Figure 1D). X-ray energy-dispersive spectra were obtained for each pixel unit (PMC: PIXL Motor Count) in the two scan regions on the *Quartier* abrasion using the two detectors in the PIXL instrument (A and B). The analyses were conducted with dwell times of 10 s at a standoff distance of 25.5 mm from the front face of the instrument to the surface of the rock.

Reflectance optical images of the abraded patch were also acquired using PIXL's micro context camera (MCC) with a field of view of ~46 × 39 mm and a spatial resolution of ~50 μm/pixel (*Allwood et al*., 2020). Four images were obtained using ultraviolet (UV, 385 nm), blue (B, 447 nm), green (G, 523 nm), and near-infrared

(NIR, 723 nm) light-emitting diodes (*Klevang et al*., 2023). These images were used to produce pseudocolor images and ratios between different bands, which, combined with compositional maps, aided the characterization of textural and modal features in *Quartier*. The radiometric correction algorithm allows a more quantitative examination of the reflectance property of the target in these wavelengths (*Henneke et al*., 2023).

The correlation between the compositional and reflectance measurements is both based on the geometrical calibration of PIXL's Sensor Assembly (SA) and continuous *in-situ* tracking of terrain standoff distance and lateral movement throughout PIXL's scanning operation. The pre-flight geometric calibration enables highly accurate mapping of the XRF beam, as a function of distance, to the frame of the MCC, which is a static instrument relation. Throughout the scanning process, multiple standoff measurements are acquired by the Structured Light Illuminators and the MCC and combined by the bundle of 3D cloud points that characterize the terrain of the scan. During the 8-10 hours scan duration, the thermal environment changes drastically, affecting the position of the arm-mounted instrument as a function of temperature. This thermal drift is also measured in situ using Terrain Relative Navigation (TRN) and compensates for the ~1 mm positional drift (*Klevang et al*., 2024). Combined with the instrument calibration and in situ measurements, the co-registration between XRF and reflectance measurements is within subpixel level at ~16 microns along the boresight and ~20 microns in the lateral direction. These effects are all included and compensated for in PIXL's data processing software PIXLISE (*Barber and Davidoff*, 2022).

3.2 Data processing

The bulk composition of both scan areas was calculated from a single bulk sum spectrum obtained from individual PMCs for each PIXL detector separately. These bulk sum spectra were then converted to input files for PIQUANT (*Heirwegh et al*., 2022), which outputs the best-fit concentrations and errors of each element considered (Supplementary Table S1). The final concentration of each oxide was determined from the lowest value of each detector to reduce potential overestimation due to x-ray diffraction (Table 1). The reported uncertainties associated with each oxide result from variability around the relevant x-ray peaks used for elemental quantification, which may reflect compositional heterogeneities, surface roughness, diffraction peak artifacts, instrument positioning, or background subtraction, for example (*Heirwegh et al*., 2022). Two raw bulk compositions were determined for

the combined scan regions: one "as analyzed", considering all PMCs (n = 6603), and a "low alteration" composition (n = 2647), which removes PMCs with spectra suggesting significant salt concentrations (Table 1). Lastly, a third bulk composition was estimated from the "low alteration" composition by subtracting the remaining Cl as NaCl and SO_3 as $CaSO_4$ and $MgSO_4$ in proportions that maintain the initial molar MgO/CaO ratio and renormalized to 100% (Table 1).

XRF spectra were also used to derive major element compositions of individual PMC in the two scan areas. These individual PMC compositions were corrected for geometric and diffraction effects using a routine procedure implemented in PIXLISE (*Heirwegh et al.*, 2022). *Schmidt et al.* (2025) give a detailed description of this procedure. Following data processing and corrections, we also used PIXLISE to build compositional expressions to create elemental distribution maps and visualize mineral compositions in projection space. These expressions included molar proportions of major oxides, sums of oxides, and elemental ratios. Additionally, to aid textural analysis, diffraction maps for the two PIXL scans were created from PIXLISE expressions following *Tice et al.* (2022) (see Supplementary Material and Supplementary Figure S1).

3.3 Phase equilibrium modeling

Phase equilibria calculations for partial melting of *Quartier* and crystallization of parental liquids were conducted using `Perple_X` (*Connolly and Petrini*, 2002; version 6.9.0) with the thermodynamic database of *Holland and Powell* (2011; hpver633). We considered activity–composition ($a - x$) relationships for silicate melt, olivine, clinopyroxene, orthopyroxene, and spinel from *Holland et al.* (2018), ilmenite from *White et al.* (2002), and ternary feldspar from *Holland and Powell* (2003). All calculations were conducted in the system K_2O–Na_2O–CaO–FeO–MgO–Al_2O_3–SiO_2–H_2O–TiO_2–Fe_2O_3–Cr_2O_3 (KNCFMASHTOCr), although the H_2O content is assumed to be zero. Although primary minerals in the *Quartier* abrasion may contain some MnO and phosphate occurrences may be primary, MnO and P_2O_5 were excluded because the $a - x$ relationships for the melt phase do not include these oxides.

We estimated the equilibrium compositions of intercumulus liquid and olivine at different melt fractions by simulating partial melting of the bulk *Quartier* composition after removing alteration components, including Cl^-- and SO_3-bearing phases (Table 1). The calculations were performed from the solidus to the liquidus,

with temperatures ranging ~1030–1490 °C. These partial melting simulations do not assume a constant Fe^{2+}–Mg distribution coefficient between olivine and melt ($K_D^{Ol/Liq}$), as commonly assumed to describe equilibrium conditions for Martian rocks (*Filiberto and Dasgupta*, 2011). Instead, different $K_D^{Ol/Liq}$ values result from minimization of the Gibbs free energy at specific pressure and temperature conditions. Furthermore, equilibrium and fractional crystallization calculations for calculated intercumulus liquids that could potentially represent parent magmas were conducted from 1500 °C to 900 °C in 1 °C steps. All calculations were conducted at 0.1 GPa, under oxidation conditions defined by $Fe^{3+}/\Sigma Fe$ ratios of 0.05, 0.10, and 0.15, which correspond to an oxygen fugacity of approximately −2 to +1 log units relative to the fayalite–magnetite–quartz (FMQ) buffer (*Kress and Carmichael*, 1991).

4. *ISSOLE/QUARTIER* COMPOSITION

4.1 Bulk rock composition

Table 1 presents major element compositions for the combined scanned areas in *Quartier* as measured by PIXL in the first column, after removal of spots with significant alteration in the second column, and the normalized composition without chlorine- and sulfate-bearing species in the third column. Compared to the average bulk composition for *Issole* from SuperCam measurements (*Beyssac et al*., 2023), the composition of *Quartier* is slightly more ferroan (Mg# 48 vs. 52), has lower Al/Si (0.06 vs. 0.14), and a similar (Fe + Mg)/Si ratio of ~1. Additionally, the PIXL composition has lower SiO_2 and Al_2O_3, and higher CaO contents, whereas Na_2O, K_2O, and TiO_2 are similar. The bulk composition of the *Quartier* abrasion is consistent with the interpretation of *Issole* as a mafic to ultramafic rock with significant alteration, suggested by relatively low analytical totals and high Cl and SO_3 contents. Removal of alteration components such as NaCl, $MgSO_4$, and $CaSO_4$ results in a considerable decrease in Na_2O, a moderate increase in CaO, and only a slight increase in the bulk Mg#.

4.2 Mineralogy

We categorized the minerals in the *Quartier* abrasion patch into two groups: primary minerals, defined as those resulting from igneous crystallization, and secondary minerals, formed by later alteration of primary minerals or introduction of external fluids. Primary and secondary minerals present in the scan regions of *Quartier* were identified from clusters and mixing trends defined by compositional data of

PMCs plotted in ternary diagrams, where ideal mineral endmembers are located in defined regions (Figure 2). Their morphology and spatial distribution within the *Quartier* scan areas were determined using compositional maps (Figure 3). We also qualitatively inferred the presence of primary minerals beyond PIXL scan areas on the abrasion patch based on spatial correspondence between minerals in compositional maps (Figure 3) and color intensities in MCC and SHERLOC context images (Figure 4).

4.2.1 Primary mineralogy

Four categories of PMC clusters likely corresponding with primary igneous phases were identified: olivine, clinopyroxene, spinel, and feldspar or feldspathic mesostasis (Figures 2A–B). The classification scheme for each mineral considered characteristic elemental ratios and heuristic thresholds for compositional variables on a case-by-case basis. The grouping criteria used in each case are summarized in the Supplementary Material. The olivine and augite groups contain only PMCs representing relatively unaltered compositions, allowing us to estimate their composition from the average of each group. However, other olivine and clinopyroxene PMCs, not included in these groups due to variable alteration and/or mixing with neighboring spots, can be identified by their similar compositional characteristics and spatial association with the unaltered PMCs (Figures 2A–B and Figure 3). By contrast, all spinel and feldspathic PMCs display strong mixing components with other primary and secondary phases, resulting from grains smaller than the beam size (Figures 2A–B). Thus, a stoichiometric composition for these minerals could not be determined from the average of the PMCs containing them, and the compositions reported reflect variable degrees of mixing.

Primary olivine (Ol-1) is compositionally homogeneous with $Fo_{46\pm1}$ (n = 126) and a mean molar FeO/MnO ratio of ~ 60.2 (Figure 5A; Table 2; Supplementary Table S2). Clinopyroxene also shows minor chemical variability and falls within the field of augite (Aug) with a composition of $Wo_{39\pm2}En_{37\pm2}Fs_{24\pm1}$ (n = 97) (Figure 5B; Table 2; Supplementary Table S3). The mean molar FeO/MnO ratio of augite is ~ 69.5. For spinel, the average composition of the selected PMCs is reported in Table 3 (n = 70; see also Supplementary Table S4), but their composition is strongly influenced by mixing with olivine and augite (Figure 2A). On the Si–Cr–Ti ternary (Figure 5C), spinel PMCs project to intermediate compositions and suggest the presence of distinct grains varying between Cr-Ti-Fe-bearing spinel and chromite.

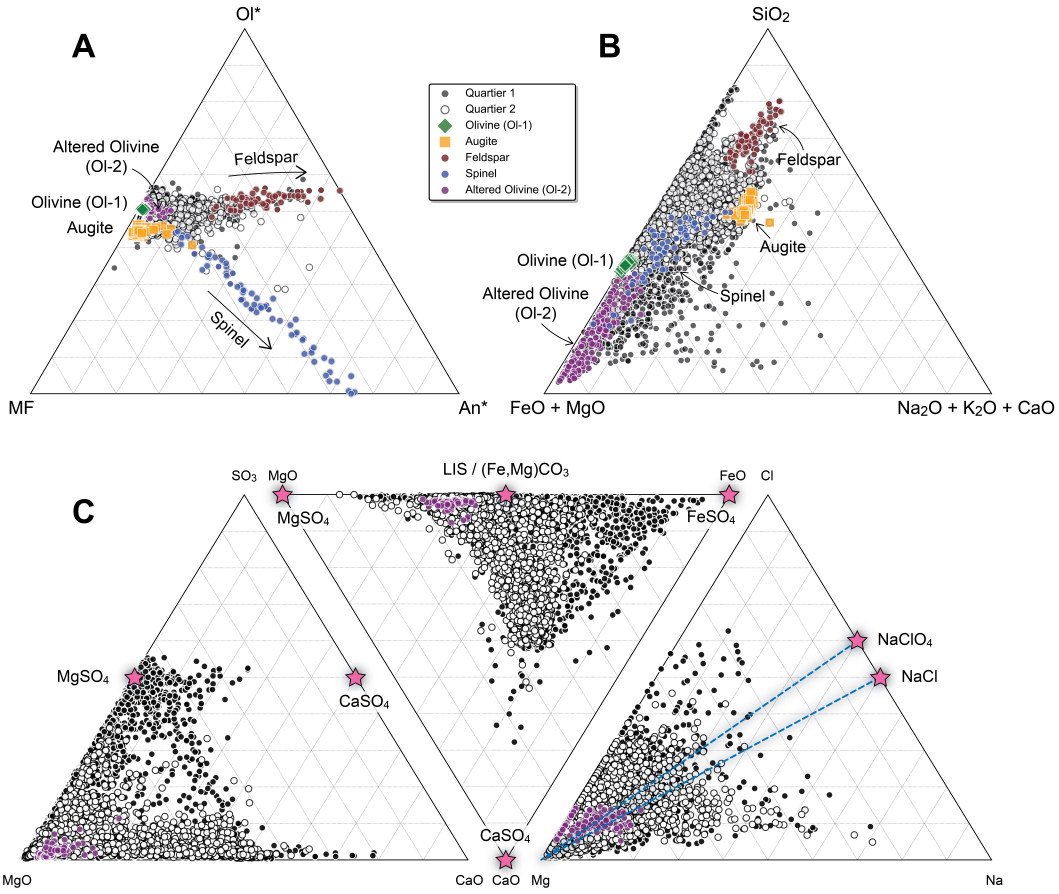


Figure 6.2: Ternary diagrams showing compositions and mixing trends for spots in the scan regions of Quartier. The ternaries Ol*–MF–An* **(A)** and SiO_2–(FeO + MgO)–($Na_2O + K_2O + CaO$) **(B)** display primary phases and mixing trends between them. Relatively fresh olivine (Ol-1) and augite (Aug) analyses are shown as green diamonds and yellow squares, respectively. Feldspar (brown circles) and spinel (blue circles) spots exhibit variable mixing with olivine and augite. Purple circles are interpreted as altered, more ferroan olivine (Ol-2). The remaining data, not assigned to a mineral, are shown as grey circles for Quartier 1 and white circles for Quartier 2. The variables Ol* and An* in **(A)** are calculated as described by *Herzberg and O'Hara* (1998), whereas MF is an empirical expression defined as FeO + MgO − 3×K_2O − 3×Na_2O, used to separate mafic from felsic silicates. The ternaries in **(C)** are used to identify trends defined by secondary phases. SO_3–MgO–CaO shows mixing trends between endmember compositions of sulfate species (left). The projected location of carbonates, LIS, and sulfates is plotted in the ternary CaO–FeO–MgO (center). Mixing relationships between chlorine species are shown in the ternary Cl–Mg–Na (right). All the oxide components used in ternary diagrams for primary and secondary phases are expressed in molar proportions.

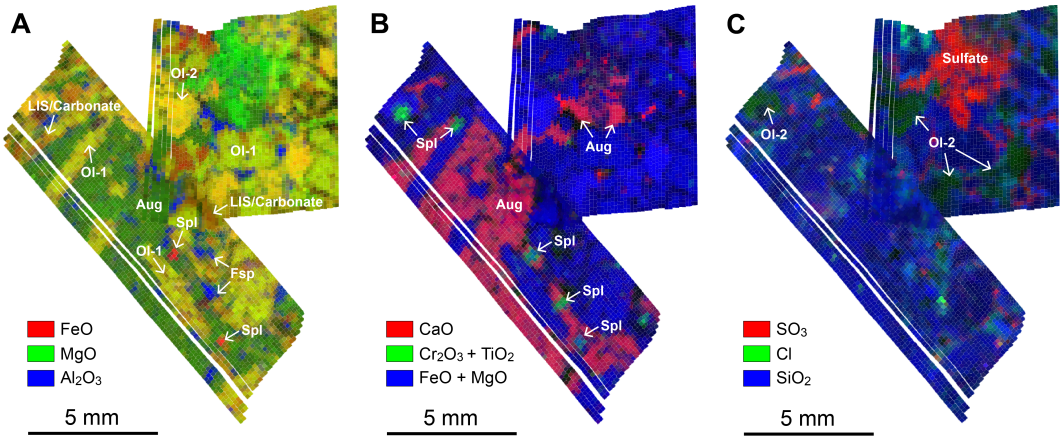


Figure 6.3: Compositional maps from PIXL data in the Quartier 1 and Quartier 2 scan areas. The maps highlight primary and secondary phases in the abrasion patch through different RGB combinations (R: Red, G: Green, B: Blue). Major oxides and elements are in weight percent. *(A)* R: FeO, G: MgO, B: Al_2O_3. *(B)* R: CaO, G: Cr_2O_3 + TiO_2, B: FeO + MgO. *(C)* R: SO_3, G: Cl, B: SiO_2. Mineral abbreviations are based on *Warr* (2021).

Lastly, we inferred a stoichiometric composition of $Ab_{66}An_{14}Or_{19}$ from the average coordinates of the PMCs with a strong feldspathic component on the Ab-An-Or plane (n = 65) (Figure 5D; Table 3; Supplementary Table S5).

4.2.2 Secondary mineralogy

Figures 3C and 4A reveal distinct interstitial domains surrounding olivine crystals, characterized by green and yellow tones, respectively. These domains, comprising a significant portion of the abrasion patch mineral assemblage, are characterized by high Cl, low SO_3 (Figure 3C), low analytical totals, and variable SiO_2 contents that are nonetheless lower than those of olivine and augite (Table 3; Supplementary Table S6). Their Mg# is relatively homogeneous, averaging 38 ± 2, more ferroan than primary olivine and augite. Moreover, the CaO content is significantly lower than augite, while the mean molar FeO/MnO ratio is similar to that of Ol-1 (61.5). These altered domains also plot close to olivine on Figure 2A, and project away from it toward higher molar FeO + MgO on Figure 2B. We interpret these regions to likely represent a distinct occurrence of more ferroan primary olivine that was subsequently altered to carbonate or hydrous silicates (Ol-2). However, these domains may also be affected by variable degrees of mixing with other primary and secondary phases.

We did not attempt to quantify the composition of other secondary minerals beyond the estimations required for their removal. The presence of such secondary

minerals was inferred from ternary diagrams for SO_3-, Cl-, and carbonate-bearing species (Figure 2C). The detected phases include sulfates, carbonates, and chlorines/oxychlorines, consistent with previous work from other instruments (*Corpolongo et al*., 2023; *Mandon et al*., 2023; *Siljeström et al*., 2024). We also inferred the presence of a low-Fe–Mg–silicate (LIS) phase, previously identified by *Tice et al*. (2022) as a mixture component present only in areas smaller than the PIXL analytical spot size, which may or may not represent a true mineral. Further details on the timing and products of aqueous alteration in *Issole* are presented in the Supplementary Material.

5. Petrography and textural features

Analysis of RGB composite maps reveals that the primary assemblage of the PIXL scan regions in *Quartier* is dominated by olivine (~61%) and augite (35%), whereas spinel (~2%) and feldspar (~2%) are present only in subordinate proportions (Figure 3A and 3B; Supplementary Figure S2). Relatively pristine olivine regions in Figure 3A appear in light green, whereas more altered olivine is expressed in pale orange to yellow colors. Augite can be distinguished from olivine in Figure 3A by its darker green tone resulting from lower MgO contents. Similarly, its high CaO content produces a distinctive reddish color in Figure 3B. The spatial overlap between Figure 4A and the compositional maps in Figure 3 indicates that olivine and augite are also the main minerals beyond the PIXL scan regions, with proportions of ~79% and ~16%, respectively, whereas spinel and feldspar together represent less than ~5% of the abrasion (see Supplementary Figure S2). *Issole/Quartier* can thus be classified as a wehrlite, similar to the other ultramafic cumulates in *Bastide* and *Brac* (*Liu et al*., 2022).

The green areas (intermediate G/NIR values) in Figure 4A correspond to Ol-1 and contain common inclusions of finer material in light blue and yellow that may represent altered spots or possible melt inclusions. Overall, these olivine crystals exhibit a predominant polyhedral (prismatic) habit with grain sizes of ~2–7 mm in length and ~1–2 mm in width, with some crystals more elongated than others. Several Ol-1 crystals display lobate embayments and internal voids resembling mantled dendritic or skeletal olivine textures observed in some Martian meteorites (Figure 6A; *Eckley et al*., 2024). Other crystals appear to consist of linked skeletal units forming elongated structures similar to chain textures produced experimentally during rapid magma cooling (Figure 6B and 6C; Donaldson, 1976).

The yellow regions (low G/NIR values), interpreted to represent an altered form of a later, more ferroan occurrence of primary olivine (Ol-2), exhibit variable sizes and irregular shapes with diffuse grain boundaries (Figure 4A). These regions tend to occupy interstitial spaces between Ol-1 crystals, enclosing them in a poikilitic-like structure (Figure 6D). However, spots with similar reflectance to Ol-2 also partially coat preexisting Ol-1 grains, suggesting alteration of early-formed olivine crystals (Figure 3A). No clear distinction between Ol-1 and Ol-2 can be made from SHERLOC/WATSON mosaics, where both appear in reddish colors (Figure 3B).

Augite (Aug) regions exhibit a relatively homogeneous dark blue color in Figure 4A (high G/NIR values), contrasting with olivine-bearing areas in green and yellow. Augite crystals in the *Quartier* abrasion range from ~1–10 mm and commonly surround olivine crystals. A poikilitic relationship, with augite enclosing earlier-formed olivine, is recognizable across the abrasion patch (Figure 4A), characteristic of poikilitic shergottites (Figure 6D; *Udry et al.*, 2020; *Wang et al.*, 2017). The augite oikocrysts have irregular interstitial shapes and exhibit straight contacts with olivine (Figures 3A, 3B, and 4A).

Spinel and feldspathic material cannot be distinguished in MCC or WATSON/SHERLOC images but are instead identified from compositional maps (Figure 3). PMCs strongly influenced by Fe-rich spinel appear bright red in Figure 3A and green to cyan in Figure 3B as Fe increases. At least five spinel clusters can be recognized in the PIXL scan regions of *Quartier*; they form rounded groups of five to ten PMCs with widths of 0.2–0.5 mm. In contrast, PMCs with a strong feldspar component appear blue in Figure 3A due to high Al_2O_3. These clusters form irregular interstitial patches of ~0.2 to ~1 mm, likely representing feldspar or felspathic mesostasis corresponding to residual interstitial melt.

Finally, secondary alteration phases in Figure 4A can only be inferred from the uneven color distribution in some regions. However, some compositional variations and spatial relationships with primary minerals can be observed in the compositional maps (Figure 3). The color variability described for olivine in Figure 3A likely reflects the significant presence of carbonate and LIS. These alteration components appear more common at grain boundaries but are also variably abundant on the surfaces of both olivine and augite grains. Moreover, chlorine-bearing phases, expressed by green to cyan tones with variable intensities, are heterogeneously distributed across the abrasion patch and appear associated with Ol-2 regions (Figure 3C). Sulfates are readily distinguishable in visible context images as light-toned

material occurring along grain boundaries or as localized patches across the abrasion (Figure 4B). A striking large sulfate patch of ~4 mm is present in *Quartier* 1, likely filling preexisting void space in the rock (Figure 4B). This and other minor interstitial sulfate occurrences in the PIXL scans appear as red regions in Figure 3C and are surrounded by primary silicates and chlorine-rich areas. Previous studies have shown that sulfates in Séítah rocks, including *Quartier*, also occur in association with carbonates and phosphates (*Corpolongo et al.*, 2023; *Siljeström et al.*, 2024). The high degree of alteration in the *Quartier* abrasion is consistent with the relatively poor crystallinity observed in the diffraction maps of the PIXL scan regions (Supplementary Figure S1).

6. Evidence of *Issole* as an igneous cumulate

Similar to other outcrops investigated by the Perseverance rover in the Séítah formation, petrographic features, bulk chemistry, and mineral compositions observed in the *Quartier* abrasion indicate that the *Issole* outcrop is an olivine-rich cumulate of igneous origin. Specifically, the presence of euhedral olivine crystals surrounded by a substantial proportion of interstitial phases points to a mesocumulate texture, in which a significant fraction of the rock consists of material crystallized between cumulus olivine grains (Fig. 4A). These interstitial phases are dominated by augite and late-stage olivine oikocrysts (Ol-2) that enclose earlier olivine chadacrysts (Ol-1), defining a poikilitic texture similar to that identified in the *Dourbes* abrasion patch within the *Brac* outcrop (*Liu et al.*, 2022).

Notably, the olivine compositions in *Quartier* (Ol-1: Fo_{46} and Ol-2: Fo_{38}; Fig. 5A) are not in equilibrium with the bulk composition (Mg# = 48), indicating that the bulk chemistry does not represent that of a fully crystallized parental magma. Olivine compositions are also more ferroan than those measured in *Dourbes* (Fo_{55}; Fig. 5A; *liu*, 2022), implying that *Issole* crystallized from a more evolved melt. This compositional variability is consistent with density-driven stratification within the Séítah formation (*Wiens et al.*, 2022), in which *Issole* represents the upper, more iron-rich portion of the unit.

7. Comparison with Martian Meteorites

Issole exhibits textural and mineralogical similarities to other Martian cumulate rocks, particularly the poikilitic shergottite, chassignite, and nakhlite meteorites (*Corrigan et al.*, 2015; *Eckley et al.*, 2024; *Hewins et al.*, 2020; *Jambon et al.*, 2016; *Ostwald et al.*, 2024; *Udry et al.*, 2020). This resemblance suggests that *Issole*

formed through similar magmatic processes as these meteorites, which are believed to have formed through accumulation of minerals fractionated from variably differentiated basaltic magmas (*Udry et al*., 2020), a process that may have been common on the Martian surface (*Ody et al*., 2013; *Udry and Day*, 2018). Comparing and contrasting *Issole* with these meteorites is key to understanding potential mechanisms for its formation and its implications for the evolution of the Martian crust.

Poikilitic shergottites are characterized by distinct poikilitic domains (*Udry et al*., 2020). In these domains, early-formed olivine and chromite chadacrysts are enclosed by large, zoned pyroxene oikocrysts. These domains are surrounded by feldspar-rich non-poikilitic areas also containing later-stage olivine, calcium-rich pyroxene, titanium-rich spinel, phosphates, and sulfides (*Combs et al*., 2019; *Kizovski et al*., 2019; *Rahib et al*., 2019; *Udry et al*., 2020; *Wang et al*., 2017). Notably, the compositions of the olivine, spinel, and pyroxene differ between the poikilitic domains and the surrounding feldspar-rich areas (*Kizovski et al*., 2019; *Wang et al*., 2017). The *Quartier* abrasion patch displays similar petrographic relationships to poikilitic shergottites, including the characteristic poikilitic texture and the presence of mantled dendritic (or even 'hopper') olivine (Figure 4A and 6A). However, the olivine and pyroxenes in *Quartier* are more iron-rich than those in poikilitic shergottites (Figure 5A and 5B).

Chassignites and nakhlites likely originated from the same magmatic system, representing a coherent suite of igneous cumulates (*McCubbin et al*., 2013; *Udry and Day*, 2018). Chassignites are dominated by compositionally homogenous Mg-rich olivine, often poikilitically enclosed by anhedral high- and low-Ca pyroxenes (*Beck et al*., 2006; *He et al*., 2013; *Hewins et al*., 2020; *Ostwald et al*., 2024; *Udry and Day*, 2018; *Wu et al*., 2021). Minor amounts of mesostasis comprised of plagioclase, alkali feldspar, Fe-Ti-Cr oxides, and apatite are also present (*Hewins et al*., 2020). While similar textures and mineral assemblages are present in *Quartier*, there are also some mineralogical differences from the chassignites. For example, the forsterite content of olivine in chassignites varies between ~54–80 (*He et al*., 2013; *Hewins et al*., 2020; *Ostwald et al*., 2024; *Udry and Day*, 2018), higher than measured in *Quartier*, which likely reflects crystallization from a more primitive liquid. Moreover, PIXL only detected high-calcium pyroxene (augite) in the *Quartier* scan regions (Figures 3A and 3B), contrasting with chassignites, which contain both low- and high-calcium pyroxenes (*Beck et al*., 2006; *He et al*., 2013; *Hewins et al*., 2020). However, SuperCam LIBS measurements indicate that low-calcium pyrox-

ene with a more ferroan composition than that of chassignites is present elsewhere in the *Issole* outcrop (*Beyssac et al*., 2023).

Nakhlites, on the other hand, are characterized by cumulus clinopyroxene with varying amounts of olivine and intercumulus mesostasis, which includes plagioclase, phosphates, titanomagnetite, iron-rich olivine, and iron-sulfide minerals (*Corrigan et al*., 2015; *Goodrich et al*., 2013). Although the grain sizes of cumulus minerals in nakhlites are comparable to those of olivine in the *Quartier* abrasion, nakhlites lack poikilitic textures (*Udry et al*., 2020). Moreover, while the olivine and pyroxene compositions in *Quartier* fall within the range of those observed in nakhlites (Figure 5A and 5B; *Balta et al*., 2017; *Jambon et al*., 2016; *McCubbin et al*., 2013; *Ostwald et al*., 2024; *Sautter et al*., 2012), *Quartier* is dominated by olivine whereas nakhlites are dominated by clinopyroxene (*Udry et al*., 2020).

In sum, the mineral chemistry in the *Quartier* abrasion closely resembles that of nakhlites, with both containing olivine and clinopyroxene more ferroan than those in poikilitic shergottites. By contrast, even the most ferroan chassignite (NWA 8694; *Hewins et al*., 2020) contains more forsteritic olivine (Fo_{54}) than measured in *Quartier*. This suggests that primary minerals in *Issole* likely crystallized from a melt with a composition intermediate between those that produced chassignites and nakhlites. On the other hand, the poikilitic texture and presence of mantled dendritic olivine make the *Quartier* abrasion petrographically more similar to the poikilitic shergottites and the chassignites. These textures are consistent with magmatic undercooling during crystallization and cumulate formation, supporting the possibility of common olivine crystallization from undercooled magmas on Mars (*Ostwald et al*., 2024; *Eckley et al*., 2024). The *Issole* outcrop in Séítah likely provides evidence of magmatic differentiation in the Martian crust (*Schmidt et al*., 2025), a process through which Séítah and Máaz could potentially be linked.

8. Petrogenesis of Issole

8.1 Formation of an olivine cumulate

The formation of *Issole* olivine cumulate is similar to that of *Brac* discussed in *Liu et al*. (2022), but the olivine morphology suggests a slightly different initial state of formation. Let us imagine a system that begins with a parental magma, initially saturated with olivine, as indicated by the occurrence of only olivine chadacrysts within the *Dourbes* and *Quartier* abrasions. Most of the olivine crystals in *Quartier* (Ol-1) are polyhedral like in *Dourbes*, but some resemble mantled dendritic and

chain textures as discovered in shergottites (*Eckley et al.*, 2024), which suggests initial disequilibrium growth due to magma undercooling (*Donaldson*, 1976; *Eckley et al.*, 2024; *Faure et al.*, 2007, 2003; *Ostwald et al.*, 2024). As the melt crystallizes and olivine crystals ripen, the temperature and compositional disequilibrium decreases, allowing olivine to form with a polyhedral habit (*Welsch et al.*, 2013). Some mantled dendritic or skeletal crystals can be preserved as the infilling of hollow faces during olivine growth may be only partial (*Welsch et al.*, 2013). Eventually, the initial magma undercooling is overcome, and olivine continues to crystallize in equilibrium with the melt (*Welsch et al.*, 2013).

Gravitational settling of olivine crystals can occur concurrently with crystal growth during 'sedimentation' events each time a critical concentration of crystals is achieved (*Sparks et al.*, 1993). This process results in the formation of fine-scale stratified layers at the base of the magmatic system (*Latypov et al.*, 2020; *Namur et al.*, 2015). The layers contain olivine crystals, foreign to the melt at the base, and interstitial, or intercumulus, magma trapped within the porous spaces between the crystals. Because the critical crystal concentration is believed to be very low for igneous layering formed by olivine precipitation (*Naslund and McBirney*, 1996; *Sparks et al.*, 1993), the initial olivine of a discrete layer would represent the instantaneous olivine composition at each sedimentation event. In contrast, the compositional stratification of the entire cumulate pile likely reflects fractional crystallization if all layers share the same parental magma (*Latypov et al.*, 2020; *Namur et al.*, 2015).

We interpret the *Dourbes* and *Quartier* abrasion patches to individually represent localized centimeter-scale layers within the cumulate pile. Accordingly, after removal of alteration phases, their bulk composition is approximately equivalent to that of an initial state with olivine crystals (Ol-1) plus intercumulus melt. The interstitial assemblage was then formed by intercumulus melt crystallization, including crystallization of late olivine (Ol-2) around the preexisting Ol-1 crystals. Both olivine and interstitial phases may have crystallized with a composition different from that preserved in the *Quartier* abrasion patch today. However, diffusion re-equilibration at magmatic temperatures, particularly in Mg and Fe, likely caused changes in the initial mineral chemistry. In the following text, the parental magma refers to the intercumulus melt.

8.2 Parental magmas for *Issole*

8.2.1 Intercumulus magmas

We estimated the composition of possible intercumulus liquids by simulating partial melting of the *Quartier* bulk composition using Perple_X (see Methods section). The composition used for modeling corresponds to the low alteration bulk composition of *Quartier* after complete removal of Cl and SO_3 as sodium chloride and calcium sulfate, respectively (Third column in Table 1). To facilitate the discussion, we refer here to liquids estimated with a $Fe^{3+}/\Sigma Fe$ ratio of 0.05 for the *Quartier* bulk composition, with calculations at a constant pressure of 0.1 GPa (~9 km depth assuming a crustal density of 3000 kg m^{-3}). However, liquid compositions were also obtained assuming $Fe^{3+}/\Sigma Fe$ ratios of 0.10 and 0.15 (Supplementary Figures S3 and S4; Supplementary Tables S7 and S8). The resulting liquids are compositionally similar to those estimated with a $Fe^{3+}/\Sigma Fe$ ratio of 0.05 in the system, but their liquidus temperatures can be significantly lower. Some models for evolved compositions predict minute amounts of spinel in the liquidus to accommodate excess Cr_2O_3 in the system. This has been recognized as a common problem of thermodynamic relationships for spinel and liquid equilibria (Balta and McSween, 2013; Holland et al., 2018; Jennings and Holland, 2015). Thus, we will refer here to the olivine liquidus as the 'effective' liquidus, corresponding to the temperature of the onset of olivine crystallization.

From these phase equilibria calculations, we obtained unique melt compositions at specific melt fractions from the solidus to the liquidus, where the melt fraction is equivalent to the proportion of interstitial melt. 'Pseudo liquidus' diagrams were then used to assess whether these melts represent potential parent magmas for *Quartier* (Figure 7A). The plane olivine–diopside–plagioclase projected from quartz/enstatite is particularly convenient for identifying liquids saturated in olivine or multiply saturated with olivine and augite. Permitted parent magmas fall in the olivine field along the tie line connecting the bulk composition of *Quartier* with predicted intercumulus melt compositions (Figure 7A). Any point on this line represents a specific proportion of interstitial liquid. By contrast, liquid compositions plotting along the olivine–augite cotectic are too evolved to form a cumulate with only olivine chadacrysts (Figure 7A).

A parent magma saturated with only olivine requires that the PIXL scan regions on the *Quartier* abrasion initially consisted of at least ~60 % interstitial melt (Figure 7A). The most evolved parent magma candidates, representing proportions of

intercumulus melt ~60–70 wt.%, plot close to the region of basaltic shergottites, whereas more primitive melts, approaching the bulk composition of *Quartier*, are compositionally closer to olivine-phyric shergottites (Figure 7A). All possible parent magmas lie in the field of basalts in the total alkalis versus silica diagram (TAS; Figure 7B). These potential parent magma compositions tend to have lower normative plagioclase and total alkalis contents than other igneous Martian rocks, particularly basalts from the Máaz formation, and Gusev and Gale craters (Figure 7; Schmidt et al., 2025; Udry et al., 2023). However, their total alkalis and silica contents are still comparable to those of basaltic and olivine-phyric shergottites and some basalts from Gusev crater (Figure 7B).

Table 4 presents the composition of some calculated intercumulus magma compositions that could be parental to *Quartier*. The liquid Mg# and olivine compositions at the liquidus vary from ~32 and Fo_{59}, for 60 % intercumulus melt, to ~43 and Fo_{73}, for 90 % intercumulus melt, resulting in lower K_D values for more primitive liquids. Accordingly, liquidus temperatures for these melts vary between 1223 °C and 1437 °C for the most to the least evolved melt compositions, respectively. An increase in the ferric iron proportion of the system from 0.05 to 0.15 would cause a slight increase in the Mg# of the liquid and hence a decrease in the Fo content of olivine at the liquidus. However, these minor changes due to increasing oxidation would be sufficient to significantly decrease liquidus temperatures. For example, the predicted liquidus for IC-70-5 composition is 1305 °C, whereas that of IC-70-15 is 1214 °C.

It is worth noting that the bulk composition of *Quartier* measured from the PIXL scan regions may not be representative of the whole cumulate layer in the Issole outcrop. These areas are particularly rich in augite compared to what is observed for the entire abrasion patch from MCC images (Figure 4A), suggesting they likely represent a region within the abrasion patch that had a large proportion of interstitial melt, in line with our estimates of at least 60 % of initial melt in the cumulate. However, the initial proportions of cumulus olivine and interstitial liquid do not affect their equilibrium composition but instead the bulk composition of the cumulate. This means that for different initial proportions of olivine and liquid in the cumulate, their compositions at equilibrium would remain the same while the bulk cumulate composition is adjusted. In short, although our approach is specific to localized areas within the abrasion patch, it still yields a parental magma composition common to the whole cumulate rock.

8.3 Crystallization of the parent magmas

For the intermulus melts obtained from partial melting calculations with the bulk *Quartier* composition to be valid parental magmas, their crystallization must be able to account for the interstitial mineral assemblages seen in the cumulate. We modeled equilibrium and fractional crystallization of the liquid compositions representing intercumulus melt proportions between 60 wt.% and 90 wt.%. Figures 8 and 9 show phase proportions, along with liquid Mg# and olivine Fo content, produced during equilibrium and fractional crystallization of these melts. Also, estimated liquid and mineral compositions at specific temperatures are summarized in Tables 5 and 6. Throughout this section, we will continue to focus on melt compositions produced in systems with $Fe^{3+}/\Sigma Fe$ of 0.05. Results for higher oxidation conditions are presented in the Supplementary Material (Supplementary Tables S7 and S8).

Both equilibrium and fractional crystallization of these liquid compositions produce the primary phase assemblages observed within the *Quartier* abrasion (Figures 8 and 9). As mentioned above, the modeled liquid compositions have olivine as the liquidus phase, with temperatures varying from 1223 °C for IC-60-5 to 1437 °C for IC-90-5. All models predict the onset of augite crystallization at temperatures ~1200 °C, regardless of the $Fe^{3+}/\Sigma Fe$ and crystallization mode, where the most evolved liquids are closer to the olivine–augite cotectic (Figure 7A). Moreover, minor (non-negligible) amounts of spinel start to crystallize, along with olivine, at temperatures ranging from ~1200–1300 °C, where increasing $Fe^{3+}/\Sigma Fe$ ratios result in higher modal proportions of spinel without significant changes in its crystallization temperature. Feldspar crystallization is predicted starting at temperatures of ~1020–1050 °C and ~1000–1010 °C for equilibrium and fractional crystallization, respectively.

The olivine compositions predicted from these parent magmas via equilibrium crystallization evolve from Fo_{58-73} at the liquidus to Fo_{24-38} at the lowest temperature of olivine stability, where the most forsteritic compositions correspond to the most primitive liquids (Figure 8). The liquidus olivine for fractional crystallization is the same as that of equilibrium crystallization, but the instantaneous olivine composition evolves to nearly pure fayalite at temperatures close to the solidus (Figure 9). However, the average olivine composition, i.e., the composition integrated over the entire crystallization range, varies from Fo_{24} for the most evolved melt (IC-60-5) to Fo_{50} for the most primitive (IC-90-5) (Figure 9).

The augite composition produced by equilibrium crystallization evolves similarly

for all the considered starting compositions. Predicted compositions are in the range Wo_{35-36} $En_{39-42}Fs_{22-24}$ at the start of crystallization and $Wo_{30-33}En_{25-33}Fs_{32-43}$ at solidus temperatures, showing a decrease in enstatite and a corresponding increase in ferrosilite components with more extensive crystallization (Table 5). By contrast, the instantaneous compositions predicted for fractional crystallization have progressively higher ferrosilite contents, starting at $Wo_{35-36}En_{35-42}Fs_{21-27}$ and ending at $Wo_{40-41}En_{0-1}Fs_{57-58}$, with the most evolved initial melt compositions corresponding to higher enstatite contents (Table 6). However, at the solidus, the average augite composition produced by all the considered intercumulus melts is similar, in the range $Wo_{39}En_{16-18}Fs_{2-43}$.

In both crystallization modes, the initial spinel compositions predicted are chromite, magnetite, and spinel-bearing (Tables 5 and 6). However, the chromite component is rapidly depleted, and the average spinel transitions into a composition dominated by ulvöspinel and magnetite. On the other hand, the evolution of feldspar is slightly different for each crystallization mode. In equilibrium crystallization, the predicted feldspar is dominated by intermediate plagioclase with compositions varying from $Ab_{41-53}An_{45-58}Or_{1-2}$ at the start of crystallization to $Ab_{47-52}An_{42-48}Or_{5-6}$ at the solidus (Table 5). In contrast, the instantaneous felspar predicted for fractional crystallization has higher anorthite, with compositions starting at $Ab_{30-35}An_{64-70}Or_1$, which become progressively more albitic during crystallization. The last feldspar predicted to crystallize has a significant orthoclase component, with a composition of $Ab_{13}An_{36}Or-51$ (Table 6). However, such compositions would only be observed if complete fractional crystallization is achieved.

A key difference between equilibrium and fractional crystallization is the stable phase assemblage near the solidus (Tables 5 and 6). During equilibrium crystallization, the olivine composition becomes progressively less forsteritic, reaching values as low as Fo_{25-40} at the last stages of olivine crystallization (Figure 8). When the proportion of residual liquid is ~20 wt.%, ferrosilite-bearing orthopyroxene begins to crystallize via reaction between olivine and melt (Figure 8; Supplementary Table S8). Fractional crystallization, by contrast, leads to a more pronounced FeO enrichment in the liquid, which results in crystallization of nearly pure fayalite at temperatures close to the solidus (Figure 9). This also results in progressive enrichment of SiO_2 in the liquid due to removal of olivine and augite, producing quartz in equilibrium with fayalitic olivine (Figure 9).

Although the models are in good agreement with the mineral assemblage observed

in *Quartier*, some notable discrepancies exist between observed and predicted phase compositions. In particular, the olivine measured in *Quartier* is more ferroan than that produced by any model at the liquidus. This implies that if the cumulate layer formed by settling of olivine crystals with compositions close to that at the liquidus, that composition must have become modified to the preserved composition by diffusive re-equilibration, with extensive Fe–Mg exchange between olivine and interstitial phases. Internal homogenization of zoned olivine crystals formed during cumulate formation can also lower their overall Fo content. However, the contribution of this process is not sufficient to explain the olivine compositions measured in *Quartier*. For example, a cumulate formed by fractional crystallization of IC-60-5, with 40 wt.% olivine Fo_{59}, could only produce an average olivine composition ~Fo_{53} (Figure 9). Other more primitive parent magma compositions, starting with lower proportions of olivine, would form even more forsteritic average olivine compositions upon complete crystallization and intracrystal homogenization, requiring more extensive diffusive re-equilibration (Figure 9).

On the other hand, the augite composition measured in *Quartier* has a similar Wo content as the average augite estimated from the fractional crystallization models at temperatures below ~1100 °C (Table 6). Equilibrium crystallization models, however, predict slightly lower Wo values at similar temperatures. With both crystallization modes, the average enstatite component of augite decreases from ~40 to ~20, whereas the average ferrosilite content increases from ~20 to ~40 (Tables 5 and 6). This indicates that the augite composition expected in *Quartier* after crystallization of the intercumulus melt should be more ferroan than that preserved in the cumulate. However, this discrepancy is consistent with our hypothesis of Fe–Mg exchange between olivine and augite at subsolidus conditions. Under the proposed model for cumulate formation, the olivine and augite compositions may have been initially richer in Fo and Fs, respectively. However, later diffusive Fe and Mg atom exchange between olivine and augite caused their initial compositions to move away from magmatic equilibrium conditions. This is also in line with the similarity in the Wo content analyzed by PIXL in augite in *Quartier* and that of the compositions predicted by the models, which are also relatively constant across the crystallization range (Tables 5 and 6). Limited Ca exchange between olivine and augite left Wo virtually unaffected by diffusion, with the augite composition of *Quartier* reflecting mainly variations in the Fs and En components.

The predicted spinel species from the models are consistent with the detection of

spinel grains with compositions varying between chromite and magnetite–ulvöspinel (Tables 5 and 6). By contrast, modeled plagioclase compositions are in marked contrast with the plagioclase in *Quartier* (i.e., ~$Ab_{72}An_7Or_{22}$). Both equilibrium and fractional crystallization models yield relatively variable, but overall intermediate plagioclase compositions (Tables 5 and 6). Orthoclase-bearing feldspar is predicted to crystallize from the most residual melts formed under fractional crystallization. However, none of the modeled melt compositions can produce albitic feldspar, as inferred for *Quartier*. At least partially, some differences between modeled and measured feldspar compositions can be attributed to the significant removal of Na_2O to obtain the chloride-free composition used for modeling. Also, the observed plagioclase in *Quartier* can be largely influenced by post-magmatic alteration, becoming more albite-rich due to secondary alteration (e.g., *Hövelmann et al.*, 2010).

Our preferred parental melt compositions correspond to intercumulus melt proportions of 60%. First, these melts are consistent with the textural implications of our simplified model of cumulate formation. Expected porosities for cumulate rocks formed by mechanical accumulation of crystals (i.e., orthocumulates) are in the order of 50–60% (*Schmidt et al.*, 2012; *Tegner et al.*, 2009), in agreement with ~40 wt.% cumulus olivine. This suggests that *Quartier* may have started as an orthocumulate that progressively evolved to a mesocumulate upon densification and crystallization of the intercumulus melt. Second, the estimated K_D for these melt compositions at the liquidus (~0.33) is closer to values expected for olivine and melt in equilibrium in Martian basalts (i.e., ~0.35 ± 0.01; *Filiberto and Dasgupta*, 2011). More primitive melt compositions representing higher proportions of intercumulus melt yield lower K_D values, comparable with primitive terrestrial basalts saturated with olivine (Tables 5 and 6).

In summary, crystallization models of intercumulus melts with olivine on their liquidus indicate these liquids could be parental to *Issole*. These melts may generate the observed primary phase assemblages in *Quartier*, although some discrepancies exist between their predicted and observed composition. These discrepancies can be reconciled by considering post-cumulus modification of the mineral assemblage. In particular, Fe–Mg exchange between olivine and pyroxene after cumulate formation can explain the more ferroan olivine and enstatite-rich augite compositions measured in *Quartier* compared to model predictions. The differences in the plagioclase composition measured in *Quartier* and those predicted by the models likely reflect post-magmatic re-equilibration but may also be an artifact of the removal of alter-

ation phases. Our results support the hypothesis that the *Quartier* cumulate formed from an intercumulus melt with olivine on its liquidus, followed by post-cumulus re-equilibration of the mineral assemblage. Also, based on textural and equilibrium assumptions for the formation of Martian olivine cumulates under our model framework, the most suitable parent magmas for *Quartier* are those representing ~60% intercumulus melt.

8.4 A link between Séítah and the Máaz formation

We use our modeling results to investigate the possibility of a petrogenetic link between the Séítah formation and the lava flows from Máaz. If such a link exists, then the magmatic evolution of a parental magma for *Issole/Quartier* should resemble the differentiation trend of the basaltic suite from Máaz. This relationship can be tested by comparing the predicted crystallization path of our preferred parent melt composition against the differentiation pattern defined by Máaz. Figure 10 shows liquid lines of descent (LLD) for different major oxides for equilibrium and fractional crystallization of this liquid composition. Most oxides show relatively good agreement between the predicted crystallization path and the differentiation trend observed in the Máaz suite (*Schmidt et al*., 2025; *Udry et al*., 2023). SiO_2 and K_2O contents increase with decreasing MgO as the melt crystallizes (Figure 10A and 10D), whereas FeO, CaO, and TiO_2 decrease (Figure 10B and 10C; Supplementary Figure S9). Al_2O_3 and Na_2O in the melt increase with olivine and augite crystallization and then decrease when the melt reaches plagioclase saturation (Supplementary Figure S9). For most oxides, the IC-60-5 composition is similar to that of the most primitive basalts of the Máaz formation, *Montpezat* and lower Máaz, except for significantly lower Al_2O_3 and Na_2O contents in our calculated parent magma (Supplementary Figure S9). More intermediate rocks in Máaz have MgO ranging ~2–3 wt.%, including *Bellegarde*, *Guillaumes*, Upper Máaz, and the Content member. These MgO contents are predicted after ~30–40 % fractional or ~40–60 % equilibrium crystallization. By contrast, the models reproduce the MgO content of *Alfalfa*, the most evolved rock in Máaz, after ~50 % fractional crystallization or complete equilibrium crystallization.

The compositions of *Alfalfa*, *Bellegarde*, *Guillaumes*, and *Montpezat* measured by PIXL in Máaz (*Schmidt et al*., 2025), as well as those of Upper Máaz and the Content member, measured by SuperCam (*Udry et al*., 2023), show reasonable agreement with both modes of crystallization for the parent liquid of *Quartier*, at least for some major oxides. Both fractional and equilibrium crystallization models show a

relatively good fit with the SiO_2 contents of SuperCam compositions (Figure 10A). While the SiO_2 in *Alfalfa* is only predicted through fractional crystallization, the compositions of Guillaumes and Bellegarde exhibit SiO_2 contents ~5 wt.% lower than liquids predicted by the models at similar MgO (Figure 10A). The slightly higher FeO contents of Guillaumes and Bellegarde, relative to the parent magma, are also best reproduced by fractional crystallization, whereas the FeO in *Alfalfa* and the compositions determined with SuperCam are closer to the LLD defined by equilibrium crystallization (Figure 10B). By contrast, the equilibrium crystallization model shows a remarkable overlap with the CaO contents measured by PIXL, while the SuperCam compositions have consistently lower CaO than the predicted liquids at equivalent MgO contents (Figure 10C). Similarly, liquids expected with equilibrium crystallization are closer in their K_2O content to both PIXL and SuperCam compositions. However, except for Alfalfa, the models tend to yield lower K_2O than those measured in the rocks (Figure 10D).

The predicted crystallization products of our proposed parental melt are also consistent with the overall mineralogy of Máaz (Figures 8 and 9). PIXL targets from this unit are dominated by augite and(or) plagioclase, with relatively minor olivine (<10 vol.%; Schmidt et al., 2025). *Alfalfa* and Bellegarde also have significant mesostasis (59 and 34 vol.%, respectively), while Guillaumes and Bellegarde contain significant iron-bearing oxides (~10 and 31 vol.%, respectively). Olivine and clinopyroxene compositions from Máaz rocks are progressively more iron-rich with increasing degree of differentiation, spanning values from Fo_{20} to Fo_3 and $Wo_{35}En_{26}Fs_{39}$ to $Wo_{30}En_6Fs_{65}$, respectively (Schmidt et al., 2025), while feldspar has compositions between andesine and oligoclase ($An_{38-19}Or_{5-15}Ab_{52-71}$; *Schmidt et al*., 2025). The fractional crystallization model yields instantaneous olivine compositions similar to those observed in Máaz at temperatures below ~1080 °C. These temperatures are consistent with modeled augite compositions with En < 26 at ~1100 °C, although these predicted compositions also yield Wo_{38-40} and Fs_{35-57} (Tables 5 and 6). Also, predicted plagioclase compositions tend to be less albite- and orthoclase-rich than the ranges measured in Máaz. Lastly, the prediction of the fayalite–quartz association at the later stages of fractional crystallization, or ferrosilite-bearing orthopyroxene for equilibrium crystallization (Supplementary Table S9), may be consistent with the occurrence of "forbidden-zone" pyroxene or the possible detection of pyroxferroite in Máaz rocks (*Schmidt et al*., 2025; *Udry et al*., 2023).

While our modeled crystallization paths are, by construction, subject to the uncertainties introduced by our assumptions and the thermodynamic models themselves, the trend defined by rocks from Máaz does not necessarily have to define a perfect crystallization path either. Instead, it may reflect the inherent complexities specific to each sample or that analyzed Máaz rocks likely do not represent unmodified liquid compositions. Additionally, the lower Al_2O_3 and Na_2O contents of the predicted melts, compared to the Máaz differentiation trend, reflect the low Al_2O_3 measured by PIXL on the *Quartier* abrasion patch and an overestimated decrease in Na_2O due to the removal of chlorine from the bulk composition. We therefore expect no perfect fit between calculated LLDs and the compositional data measured in Máaz rocks. However, their overall similarity allows us to conclude that an approximate solution to a parent magma for *Quartier* would follow a crystallization path that resembles the magmatic differentiation trend seen in Máaz. This similarity may also indicate a common magmatic history between Máaz and Séítah.

8.5 Implications for emplacement of the Séítah formation

The Máaz formation represents a basaltic suite that overlies the olivine-bearing cumulate rocks from the Séítah formation (*Beyssac et al.*, 2023; *Schmidt et al.*, 2025; *Udry et al.*, 2023). Our findings support a petrogenetic link between Séítah and Máaz, where the predicted magmatic evolution of melts parental to *Quartier* (Figure 10), along with their crystallization products (Figures 8 and 9), is consistent with the composition and mineral assemblages observed in Máaz rocks. This relative agreement suggests a complementary nature between the Máaz and Séítah formations. However, this does not necessarily imply differentiation from a single parental liquid but may simply reflect a common magmatic system for the two units.

Olivine textures in *Quartier* preserve some clues about the crystallization and emplacement history of Séítah. While most olivine grains in *Quartier* exhibit a polyhedral habit, some crystals preserve mantled dendritic and chain textures (Figures 4 and 6), similar to those in shergottite meteorites (*Eckley et al.*, 2024). These textures also form in natural and experimental lavas with terrestrial compositions with degrees of undercooling varying from >60 °C, required to form chained and dendritic textures, to <20 °C, where polyhedral habits develop (*Donaldson*, 1976; *Faure et al.*, 2003; *Welsch et al.*, 2013). Therefore, we interpret the olivine textures in *Quartier* as evidence of rapid crystallization from initial magma undercooling, followed by near-equilibrium crystallization with minimal or no undercooling.

Our preferred parent magma for *Quartier* (60 % intercumulus melt) is consistent with olivine-to-melt proportions expected during the formation of igneous cumulates and olivine–melt equilibrium conditions inferred for Martian basalts (*Schmidt et al*., 2012; *Tegner et al*., 2009). This composition has an olivine liquidus temperature of ~1220 °C, which could be lower depending on the water content of the magma during crystallization. However, the initial magma undercooling may have resulted from rapid magma ascent and degassing, although crustal assimilation or intrusion into a previous batch of more evolved magma could also be possible. Increased magma viscosity and crystallinity may have resulted in magma stalling at depth as shallow subsurface igneous intrusion. Slow cooling and sustained Fe–Mg diffusion then permitted the formation of olivine crystals with polyhedral habit and partial homogenization of olivine and augite compositions.

The intrusion of Séítah into the Máaz lava flows as a sill-like structure or laccolith is consistent with the model described above (Figure 11). In this model, the Máaz basaltic suite initially formed from erupted lavas that differentiated through fractional crystallization within the crust (Figure 11A; *Schmidt et al*., 2025). Subsequent emplacement of the Séítah olivine cumulates as a magmatic intrusion into the Máaz flows resulted in localized upward tilting of the Máaz layers near the contact zone (Figure 11B; *Farley et al*., 2022; *Hamran et al*., 2022). Following complete magma crystallization and subsequent aqueous alteration, erosion removed the overlying Máaz layers, exposing the Séítah cumulates at the surface of Jezero crater (Figure 11C). This emplacement mechanism shares similarities with those inferred for nakhlite and chassignite meteorites (*Udry and Day*, 2018), which are texturally and compositionally close to Quartier. However, alternative models, such as crystallization within a thick lava flow or pond, could also explain some of the textural and compositional features observed in the Séítah formation (*Farley et al.*, 2022; *Liu et al.*, 2022).

9. Summary and Conclusions

The layered rocks exposed in the *Issole* outcrop of the Séítah formation on the Jezero's crater floor, investigated by the Perseverance rover, are igneous cumulates. Based on the observations reported here for the *Quartier* abrasion patch, we interpret these rocks as formed via settling of olivine crystals in equilibrium with a liquid of basaltic composition, which can be approximated to that of the parental magma. The textural features preserved in early olivine crystals (Ol-1) in *Quartier* reflect initial crystallization under disequilibrium conditions due to significant magma

undercooling, later transitioning to conditions closer to equilibrium. The interstitial mineral assemblage in *Quartier* was produced by crystallization of the intercumulus liquid, producing a wehrlite with augite and later olivine (Ol-2), as well as minor spinel and feldspar (or mesostasis). The initial proportion of intercumulus melt was likely ~60 %, with olivine liquidus temperatures of at least ~1220 °C. However, the olivine and augite compositions predicted by our models differ from those measured by the PIXL instrument, requiring Fe–Mg diffusion to achieve more ferroan olivine and magnesian pyroxene compositions. The evolution of the liquid compositions resulting from crystallization of the melt interpreted as the parent of *Quartier/Issole* are similar to the magmatic trend defined by Máaz rocks.

Moreover, the mineral assemblages and compositions produced by the crystallization of the parent magma are consistent with those observed in Máaz basalts. These similarities indicate that Séítah and Máaz were likely formed by differentiation of the same magmatic system, where the formation of Séítah cumulates was dominated by crystal accumulation, while Máaz rocks mainly reflect differentiation and crystallization of magmatic liquids. Séítah was likely emplaced into Máaz lava flows as a near-surface, sill-like body, such as a laccolith, following magma ascent from a deeper magma source. The relationship between the two units demonstrates that magmatic differentiation processes in the Martian crust can create highly diverse lithologies and mineral assemblages. These processes resemble those responsible for the petrogenesis of some Martian meteorites and their mineral textures.

10. References

Allwood, A.C., et al., 2020. PIXL: Planetary Instrument for X-ray Lithochemistry. *Space Sci. Rev.* 216, 134.

Balta, J.B., McSween Jr., H.Y., 2013. Application of the Melts Algorithm to Martian Compositions and Implications for Magma Crystallization. *J. Geophys. Res. Planets* 118, 2502–2519.

Balta, J.B., Sanborn, M.E., Mayne, R.G., Wadhwa, M., McSween Jr, H.Y., Crossley, S.D., 2017. Northwest Africa 5790: A Previously Unsampled Portion of the Upper Part of the Nakhlite Pile. *Meteorit. Planet. Sci.* 52, 36–59.

Barber, T., Davidoff, S., 2022. PIXLise/piquant: 3.2.11 Open Source.

Beck, P., Barrat, J.A., Gillet, Ph., Wadhwa, M., Franchi, I.A., Greenwood, R.C., Bohn, M., Cotten, J., van de Moortèle, B., Reynard, B., 2006. Petrography and

Geochemistry of the Chassignite Northwest Africa 2737 (NWA 2737). *Geochim. Cosmochim. Acta* 70, 2127–2139.

Bell, J.F., et al., 2022. Geological, Multispectral, and Meteorological Imaging Results from the Mars 2020 Perseverance Rover in Jezero Crater. *Sci. Adv.* 8.

Bell, J.F., et al., 2021. The Mars 2020 Perseverance Rover Mast Camera Zoom (Mastcam-Z) Multispectral, Stereoscopic Imaging Investigation. *Space Sci. Rev.* 217, 24.

Beyssac, O., et al., 2023. Petrological Traverse of the Olivine Cumulate Séítah Formation at Jezero Crater, Mars: A Perspective from SuperCam Onboard Perseverance. *J. Geophys. Res. Planets* 128.

Bhartia, R., et al., 2021. Perseverance's Scanning Habitable Environments with Raman and Luminescence for Organics and Chemicals (SHERLOC) Investigation. *Space Sci. Rev.* 217, 58.

Brown, A.J., Viviano, C.E., Goudge, T.A., 2020. Olivine-carbonate Mineralogy of the Jezero Crater Region. *J. Geophys. Res. Planets* 125.

Combs, L.M., et al., 2019. Petrology of the Enriched Poikilitic Shergottite Northwest Africa 10169: Insight Into the Martian Interior. *Geochim. Cosmochim. Acta* 266, 435–462.

Connolly, J.A.D., Petrini, K., 2002. An Automated Strategy for Calculation of Phase Diagram Sections and Retrieval of Rock Properties As a Function of Physical Conditions. *J. Metamorph. Geol.* 20, 697–708.

Corpolongo, A., et al., 2023. SHERLOC Raman Mineral Class Detections of the Mars 2020 Crater Floor Campaign. *J. Geophys. Res. Planets* 128.

Corrigan, C.M., Velbel, M.A., Vicenzi, E.P., 2015. Modal Abundances of Pyroxene, Olivine, and Mesostasis in Nakhlites. *Meteorit. Planet. Sci.* 50, 1497–1511.

Donaldson, C.H., 1976. An Experimental Investigation of Olivine Morphology. *Contrib. Mineral. Petrol.* 57, 187–213.

Eckley, S.A., et al., 2024. New Olivine Morphologies in Shergottites Reveal Complex Thermal Histories of Martian Magmas. *Geochim. Cosmochim. Acta* 373, 197–210.

Ehlmann, B.L., et al., 2008a. Clay minerals in delta deposits and organic preservation potential on Mars. *Nat. Geosci.* 1, 355–358.

Ehlmann, B.L., et al., 2008b. Orbital Identification of Carbonate-Bearing Rocks on Mars. *Science* 322, 1828–1832.

Farley, K.A., et al., 2022. Aqueously Altered Igneous Rocks Sampled on the Floor of Jezero Crater, Mars. *Science* 377.

Fassett, C.I., Head, J.W., 2008. Valley Network-fed, Open-basin Lakes on Mars. *Icarus* 198, 37–56.

Faure, F., et al., 2007. Textural Evolution of Polyhedral Olivine Experiencing Rapid Cooling Rates. *Contrib. Mineral. Petrol.* 153, 405–416.

Faure, F., et al., 2003. A Developmental Model of Olivine Morphology. *Contrib. Mineral. Petrol.* 145, 251–263.

Filiberto, J., Dasgupta, R., 2011. Fe^{2+}–Mg Partitioning between Olivine and Basaltic Melts. *Earth Planet. Sci. Lett.* 304, 527–537.

Goodrich, C.A., Treiman, A.H., Filiberto, J., Gross, J., Jercinovic, M., 2013. K2o-rich Trapped Melt in Olivine in the Nakhla Meteorite: Implications for Petrogenesis of Nakhlites and Evolution of the Martian Mantle. *Meteorit. Planet. Sci.* 48, 2371–2405.

Goudge, T.A., Mustard, J.F., Head, J.W., Fassett, C.I., Wiseman, S.M., 2015. Assessing the Mineralogy of the Watershed and Fan Deposits of the Jezero Crater Paleolake System, Mars. *J. Geophys. Res. Planets* 120, 775–808.

Hamran, S.E., et al., 2022. Ground Penetrating Radar Observations of Subsurface Structures in the Floor of Jezero Crater, Mars. *Sci. Adv.* 8.

He, Q., Xiao, L., Hsu, W., Balta, J.B., McSween, H.Y., Liu, Y., 2013. The Water Content and Parental Magma of the Second Chassignite NWA 2737: Clues from Trapped Melt Inclusions in Olivine. *Meteorit. Planet. Sci.* 48, 474–492.

Henneke, J., Klevang, D., Liu, Y., Jørgensen, J., Denver, T., Rice, M., VanBommel, S., Toldbo, C., Hurowitz, J., Tice, M., Tosca, N., Johnson, J., Winhold, A., Allwood, A., Bell, J., 2023. A Radiometric Correction Method and Performance Characteristics for PIXL's Multispectral Analysis Using LEDs. *Space Sci. Rev.* 219, 68.

Heirwegh, C.M., Elam, W.T., O'Neil, L.P., Sinclair, K.P., Das, A., 2022. The Focused Beam X-ray Fluorescence Elemental Quantification Software Package Piquant. *Spectrochim. Acta Part B At. Spectrosc.* 196, 106520.

Hernández-Montenegro, J. D., 2025. Supporting Information: Petrogenesis of the olivine cumulate outcrop Issole – the missing link between the Séítah and Máaz formations in Jezero crater, Mars. *Zenodo*.

Herzberg, C., O'Hara, M.J., 2002. Plume-associated Ultramafic Magmas of Phanerozoic Age. *J. Petrol.* 43, 1857–1883.

Hewins, R.H., Humayun, M., Barrat, J.-A., Zanda, B., Lorand, J.-P., Pont, S., Assayag, N., Cartigny, P., Yang, S., Sautter, V., 2020. Northwest Africa 8694, a Ferroan Chassignite: Bridging the Gap between Nakhlites and Chassignites. *Geochim. Cosmochim. Acta* 282, 201–226.

Holland, T., Powell, R., 2003. Activity–composition Relations for Phases in Petrological Calculations. *Contrib. Mineral. Petrol.* 145, 492–501.

Holland, T.J.B., Green, E.C.R., Powell, R., 2018. Melting of Peridotites through to Granites. *J. Petrol.* 59, 881–900.

Holland, T.J.B., Powell, R., 2011. An Improved and Extended Internally Consistent Thermodynamic Dataset. *J. Metamorph. Geol.* 29, 333–383.

Horgan, B., et al., 2023. Mineralogy, Morphology, and Emplacement History of the Maaz Formation. *J. Geophys. Res. Planets* 128.

Hövelmann, J., Putnis, A., Geisler, T., Schmidt, B.C., Golla-Schindler, U., 2010. The Replacement of Plagioclase Feldspars by Albite. *Contrib. Mineral. Petrol.* 159, 43–59.

Jambon, A., et al., 2016. Northwest Africa 5790: Revisiting Nakhlite Petrogenesis. *Geochim. Cosmochim. Acta* 190, 191–212.

Jennings, E.S., Holland, T.J., 2015. A Simple Thermodynamic Model for Melting of Peridotite. *J. Petrol.* 56, 869–892.

Kizovski, T.V., et al., 2019. Detailed Mineralogy and Petrology of Highly Shocked Poikilitic Shergottite NWA 6342. *Meteorit. Planet. Sci.* 54, 768–784.

Klevang, D.A., et al., 2023. Pre-flight Geometric and Optical Calibration of PIXL. *Space Sci. Rev.* 219, 11.

Klevang, D.A., et al., 2024. Pre- and In-flight Performance of Terrain Relative Navigation on PIXL's Micro Context Camera. *IEEE Aerospace Conference Proceedings*.

Kress, V.C., Carmichael, I.S.E., 1991. The Compressibility of Silicate Liquids. *Contrib. Mineral. Petrol.* 108, 82–92.

Latypov, R.M., et al., 2020. Dynamics of Evolving Magma Chambers. *Earth-Sci. Rev.* 210, 103388.

Liu, Y., et al., 2022. An Olivine Cumulate Outcrop on the Floor of Jezero Crater, Mars. *Science*.

Mandon, L., et al., 2023. Reflectance of Jezero Crater Floor: 2. Mineralogical Interpretation. *J. Geophys. Res. Planets* 128.

Mandon, L., et al., 2020. Refining the Age, Emplacement and Alteration Scenarios of the Olivine-rich Unit. *Icarus* 336, 113436.

Mangold, N., et al., 2020. Fluvial Regimes, Morphometry, and Age of Jezero Crater Paleolake Inlet Valleys. *Astrobiology* 20, 994–1013.

McCubbin, F.M., et al., 2013. A Petrogenetic Model for the Comagmatic Origin of Chassignites and Nakhlites. *Meteorit. Planet. Sci.* 48, 819–853.

Namur, O., et al., 2015. Igneous Layering in Basaltic Magma Chambers. *Springer Geology*.

Naslund, H.R., McBirney, A.R., 1996. Mechanisms of Formation of Igneous Layering. *Developments in Petrology*.

Ody, A., et al., 2013. Global Investigation of Olivine on Mars. *J. Geophys. Res. Planets* 118, 234–262.

Ostwald, A., et al., 2024. Complex Zoning in the Nakhlite and Chassignite Martian Meteorites. *Geochim. Cosmochim. Acta* 380, 1–17.

Rahib, R.R., et al., 2019. Mantle Source to Near-surface Emplacement of Poikilitic Shergottites. *Geochim. Cosmochim. Acta* 266, 463–496.

Rice, M.S., et al., 2023. Spectral Variability of Rocks and Soils on the Jezero Crater Floor. *J. Geophys. Res. Planets* 128.

Sautter, V., Toplis, M.J., Lorand, J.-P., Macri, M., 2012. Melt Inclusions in Augite from the Nakhlite Meteorites: A Reassessment of Nakhlite Parental Melt and Implications for Petrogenesis. *Meteorit. Planet. Sci.* 47, 330–344.

Scheller, E.L., et al., 2022. Aqueous Alteration Processes in Jezero Crater, Mars–implications for Organic Geochemistry. *Science* 378, 1105–1110.

Schmidt, M.E., et al., 2025. Diverse and Highly Differentiated Lava Suite in Jezero Crater, Mars: Constraints on Intracrustal Magmatism Revealed by Mars 2020 PIXL. *Science Advances* 11.

Schmidt, M.W., Forien, M., Solferino, G., Bagdassarov, N., 2012. Settling and Compaction of Olivine in Basaltic Magmas: An Experimental Study on the Time Scales of Cumulate Formation. *Contrib. Mineral. Petrol.* 164, 959–976.

Sharma, S., et al., 2023. Diverse Organic-mineral Associations in Jezero Crater, Mars. *Nature* 619, 724–732.

Shoemaker, E.S., et al., 2024. Evidence of Sulfate-rich Fluid Alteration in Jezero Crater Floor, Mars. *J. Geophys. Res. Planets* 129.

Simon, J.I., et al., 2023. Samples Collected from the Floor of Jezero Crater with the Mars 2020 Perseverance Rover. *J. Geophys. Res. Planets* 128.

Sparks, R.S., Huppert, H.E., Koyaguchi, T., Hallworth, M.A., 1993. Origin of Modal and Rhythmic Igneous Layering by Sedimentation in a Convecting Magma Chamber. *Nature* 361, 246–249.

Stack, K.M., et al., 2020. Photogeologic Map of the Perseverance Rover Field Site in Jezero Crater Constructed by the Mars 2020 Science Team. *Space Sci. Rev*. 216, 127.

Sun, V.Z., et al., 2023. Overview and Results from the Mars 2020 Perseverance Rover's First Science Campaign on the Jezero Crater Floor. *J. Geophys. Res. Planets 128*.

Tegner, C., Thy, P., Holness, M.B., Jakobsen, J.K., Lesher, C.E., 2009. Differentiation and Compaction in the Skaergaard Intrusion. *J. Petrol.* 50, 813–840.

Tice, M.M., et al., 2022. Alteration History of Séítah Formation Rocks Inferred by PIXL X-ray Fluorescence, X-ray Diffraction, and Multispectral Imaging on Mars. *Sci. Adv.* 8.

Treiman, A.H., Hernández-Montenegro, J.D., Wiens, R.C., Wade, L.A., 2025. The Brac/Dourbes olivine-cumulate rock, Séítah Formation, Jezero Crater floor, Mars: Its Parent Magma, and Relation to Basalts of the Máaz Formation. *J. Geophys. Res. Planets*

Udry, A., Day, J.M.D., 2018. 1.34 Billion-year-old Magmatism on Mars Evaluated from the Co-genetic Nakhlite and Chassignite Meteorites. *Geochim. Cosmochim.*

Acta 238, 292–315.

Udry, A., Howarth, G.H., Herd, C.D.K., Day, J.M.D., Lapen, T.J., Filiberto, J., 2020. What Martian Meteorites Reveal About the Interior and Surface of Mars. *J. Geophys. Res. Planets* 125.

Udry, A., et al., 2023. A Mars 2020 Perseverance SuperCam Perspective on the Igneous Nature of the Máaz Formation at Jezero Crater and Link with Séítah, Mars. *J. Geophys. Res. Planets* 128.

Wang, S.-Z., et al., 2017. Petrogenesis and Shock Metamorphism of the Enriched Lherzolitic Shergottite Northwest Africa 7755. *Meteorit. Planet. Sci.* 52, 2437–2457.

Warr, L.N., 2021. Ima–cnmnc Approved Mineral Symbols. *Mineralogical Magazine* 85, 291–320.

Welsch, B., et al., 2013. Dendritic Crystallization: A Single Process for All the Textures of Olivine in Basalts? *J. Petrol.* 54, 539–574.

Werner, S.C., 2008. The Early Martian Evolution—constraints from Basin Formation Ages. *Icarus* 195, 45–60.

White, R.W., Powell, R., Clarke, G.L., 2002. The Interpretation of Reaction Textures in Fe-rich Metapelitic Granulites of the Musgrave Block, Central Australia. *J. Metamorph. Geol.* 20, 41–55.

Wiens, R.C., et al., 2020. The SuperCam Instrument Suite on the Nasa Mars 2020 Rover. *Space Sci. Rev.* 217, 4.

Wiens, R.C., et al., 2022. Compositionally and Density Stratified Igneous Terrain in Jezero Crater, Mars. *Sci. Adv.* 8.

Wu, P., Gazel, E., Udry, A., Setera, J.B., Ostwald, A., 2021. Melt Inclusions in Chassignite NWA 2737. *Meteorit. Planet. Sci.* 56, 1328–1349.

Table 6.1: Quartier major element compositions.

Quartier Bulk	As analyzed: n = 6603		Low alteration: n = 2647		Low alteration minus Cl- and SO_3-bearing phases
Oxide	wt.%	1σ	wt.%	1σ	wt.%
Na_2O	2.1	0.6	1.7	0.5	0.9
MgO	13.9	0.7	13.7	0.7	14.7
Al_2O_3	2.0	0.5	2.1	0.5	2.3
SiO_2	37.6	1.9	41.7	2.1	44.7
P_2O_5	0.4	0.3	0.2	0.2	0.2
SO_3	4.9	0.3	1.0	0.3	—
Cl	1.0	0.4	0.5	0.2	—
K_2O	0.2	0.2	0.2	0.2	0.2
CaO	4.5	0.4	6.1	0.3	6.5
TiO_2	0.6	0.2	0.7	0.3	0.8
Cr_2O_3	0.2	0.2	0.3	0.2	0.3
MnO	0.6	0.2	0.6	0.2	0.6
FeO_T	27.7	1.4	26.8	1.3	28.7
Total	95.7		95.6		100.0
Mg/Ca	4.30		3.13		3.13
Al/Si	0.06		0.06		0.06
(Fe+Mg)/Si	1.17		1.03		1.03
Mg#	47		48		48

11. Tables

Table 6.2: Average olivine and augite compositions.

Phases	Olivine (Ol–1; n = 126)		Altered ferroan olivine (Ol–2; n = 189)		Augite (n = 97)	
Oxide	wt.%	1σ	wt.%	1σ	wt.%	1σ
Na_2O	0.36	0.31	1.37	1.30	0.91	0.62
MgO	19.72	0.91	17.67	2.14	12.21	0.88
Al_2O_3	0.30	0.26	0.91	0.74	1.13	0.71
SiO_2	35.18	1.01	13.85	7.25	50.26	2.41
P_2O_5	0.05	0.03	0.05	0.09	0.16	0.84
SO_3	0.58	0.36	0.67	0.51	0.49	0.32
Cl	0.24	0.10	1.85	0.37	0.37	0.22
K_2O	—	—	0.00	0.00	0.01	0.06
CaO	0.20	0.10	1.45	0.55	17.78	1.11
TiO_2	—	—	0.25	1.79	0.15	0.12
Cr_2O_3	—	—	0.08	0.60	0.05	0.04
MnO	0.69	0.18	0.83	0.13	0.19	0.06
FeO_T	42.08	0.86	51.79	6.05	13.71	1.30
Total	99.4		90.8		97.4	
Fo	46	1	38	2		
Wo					39	2
En					37	2
Fs					24	2
Fe/Mn	60.2	15.5	61.5	12.2	69.5	21.2

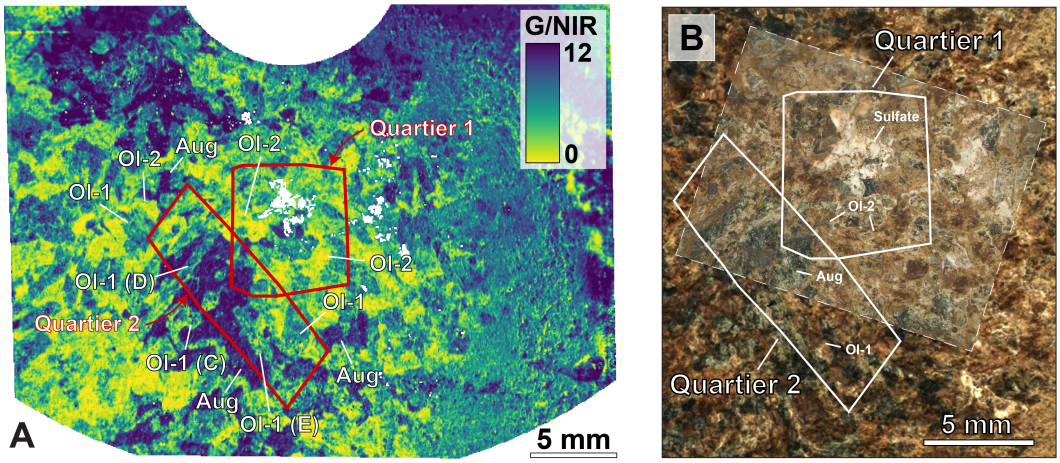


Figure 6.4: Overview images of the Quartier abrasion patch in Issole. **(A)** Green (G; 530 nm) to near-infrared (NIR; 735 nm) ratio of reflected optical images from the PIXL's micro context camera (MCC). Olivine appears in green (Ol-1) and bright yellow (Ol-2), and augite in dark blue (Aug). **(B)** SHERLOC/WATSON zoomed-in context images of the PIXL scan regions in the Quartier abrasion patch. The white dashed line encloses a higher resolution (10.1 μm/pixel) colorized image acquired with SHERLOC's Autofocus Context Imager (ACI) (see *Corpolongo et al.*, (2023) and *Scheller et al.*, (2022) for details on image processing). PIXL XRF scan areas in **(A)** and **(B)** are outlined in red and white, respectively.

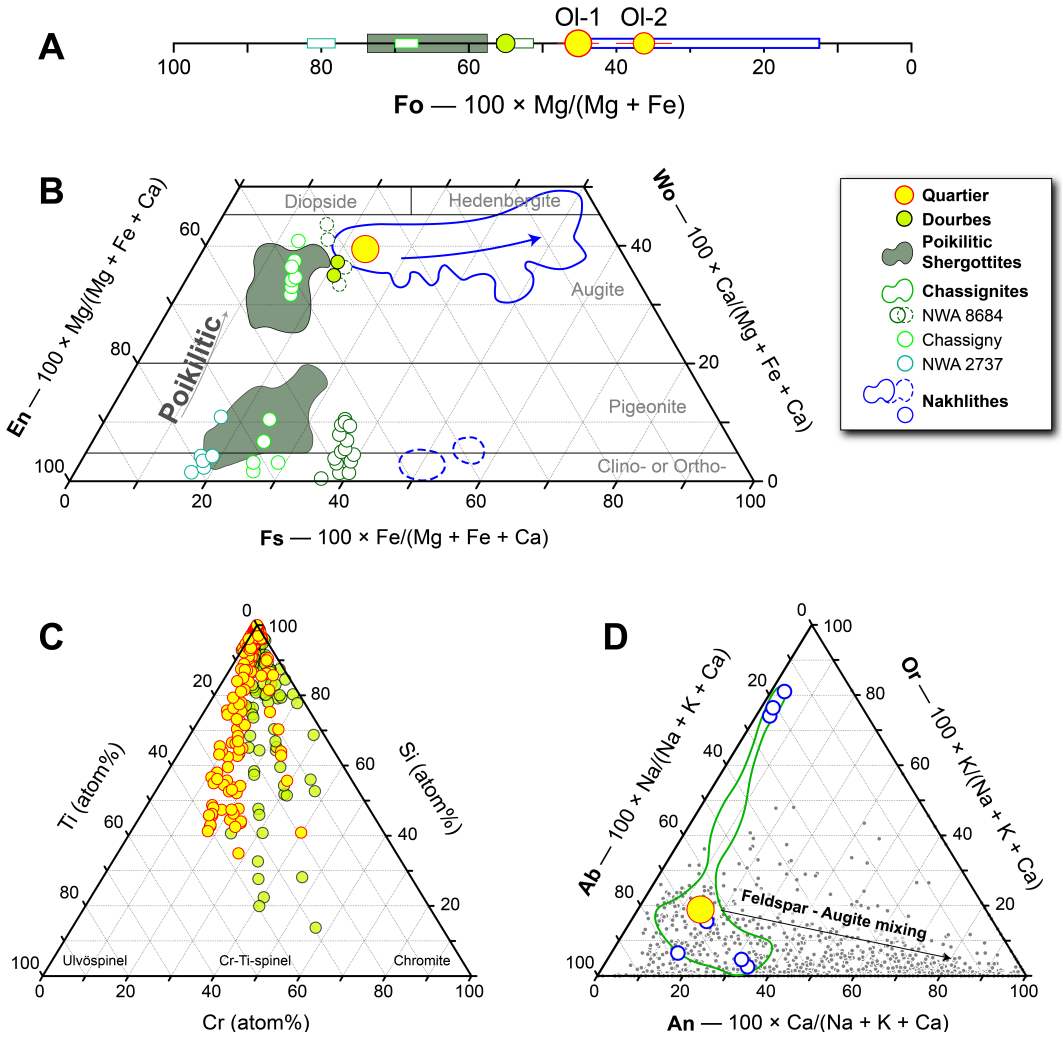


Figure 6.5: Compositional diagrams of primary minerals in Quartier and other Martian cumulate rocks for reference. **(A)** Forsterite content in olivine (Fo). **(B)** Composition of augite expressed as wollastonite (Wo), enstatite (En), and ferrosilite (Fs) components. **(C)** Si-Ti-Cr ternary showing mixing trends between silicate minerals and Fe-Ti-Cr spinel in Quartier and Dourbes. **(D)** Inferred composition of feldspar in Quartier shown as percentages of anorthite (An), albite (Ab), and orthoclase (Or). This composition is the average of the spots identified as feldspar-bearing (n = 50; brown circles in Figure 2A and 4B). Grey dots are all Quartier spots projected on the same plane.

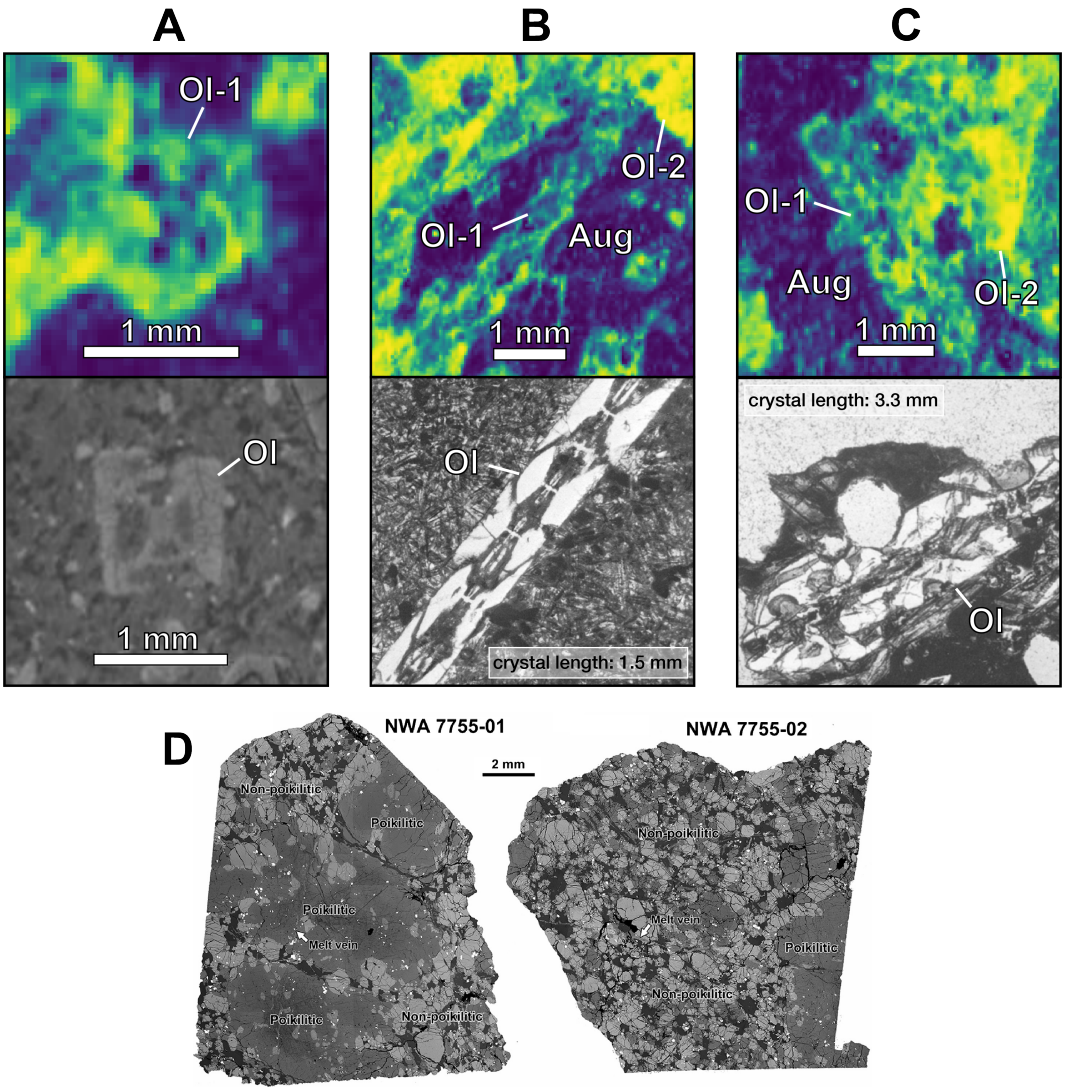


Figure 6.6: Petrographic textures within the Quartier abrasion patch in Issole and comparable textures in Martian meteorites and produced in magma cooling experiments. **(A)** olivine crystals with mantled dendritic texture in Quartier (up) and olivine-phyric shergottite Tissint (bottom) (modified from *Eckley et al.*, 2024). **(B-C)** Chain olivine textures in Quartier (up) and produced during cooling experiments of peridotite melts (bottom) (images taken from *Donaldson*, 1976; scale reported as crystal length). **(D)** Poikilitic and non-poikilitic textures in poikilitic shergottite NWA 7755 (modified from *Wang et al.*, 2017).

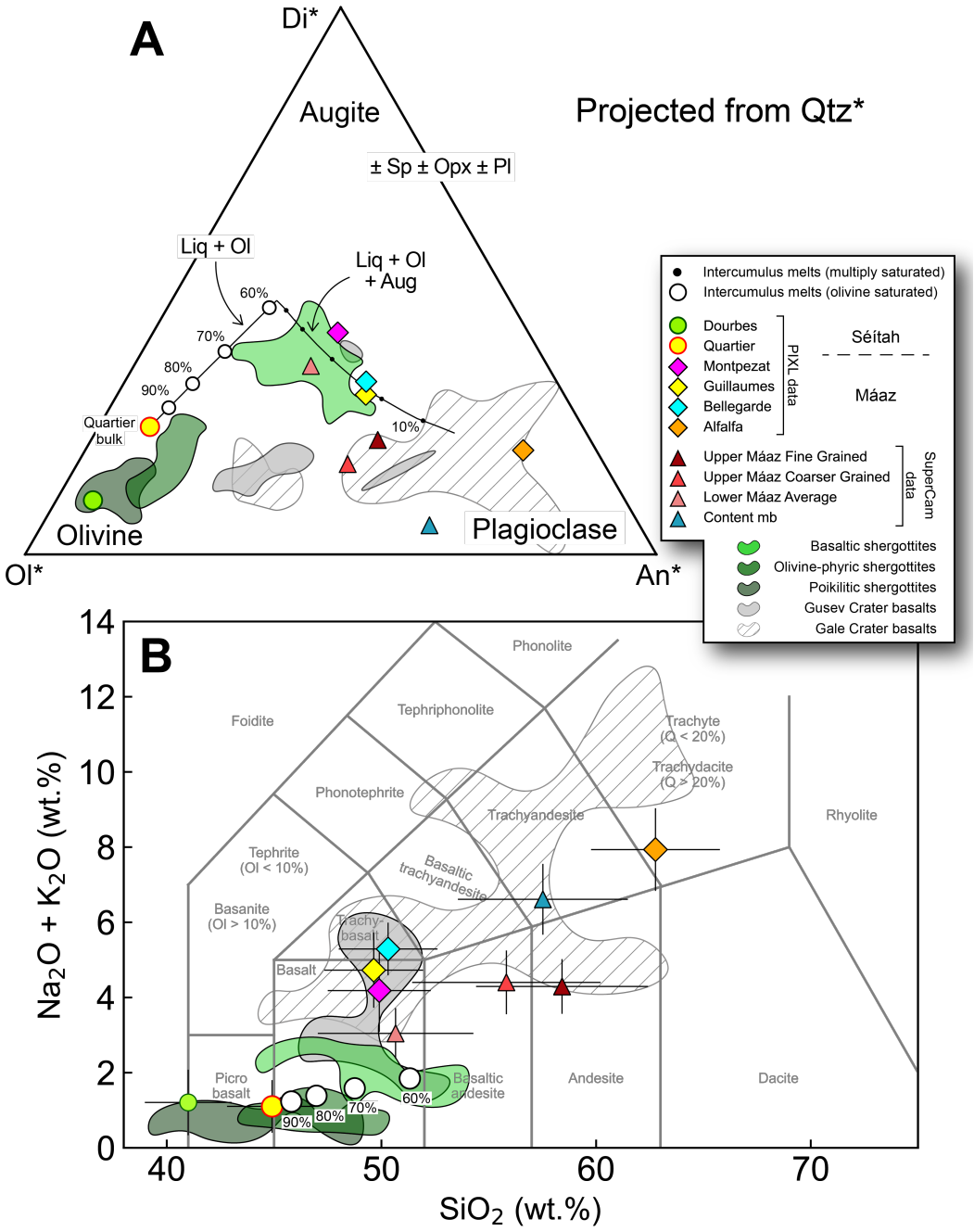


Figure 6.7: **(A)** 'Pseudoliquidus' diagram for intercumulus melts produced by partial melting of Quartier. Coordinates on the Ol*–Di*–Pl* plane are projected from Qtz and calculated from mole percent oxide compositions (mole %) following *Herzberg and O'Hara* (2002): $\mathrm{Ol} = -1.5\times\mathrm{TiO_2}+0.5\times(\mathrm{Al_2O_3}+\mathrm{Cr_2O_3}+\mathrm{FeO^*}+\mathrm{MnO}+\mathrm{MgO}-\mathrm{CaO}-\mathrm{Na_2O}+\mathrm{NiO})+3.0\times\mathrm{K_2O}$; $\mathrm{Di} = 1.0\times\mathrm{CaO}-1.0\times\mathrm{Al_2O_3}+1.0\times\mathrm{Na_2O}+1.0\times\mathrm{K_2O}$; $\mathrm{Pl} = 1.0\times\mathrm{Al_2O_3}+1.0\times\mathrm{Na_2O}+1.0\times\mathrm{K_2O}$. The asterisk denotes coordinates were normalized to 1. The solid black line corresponds with all the projected liquid compositions with proportions varying from 0 to 100 %. The black dots and white circles represent liquid fractions in 10 wt.% increments. The white circles are liquids saturated with olivine only (potential parent melts), whereas the dots are liquids cosaturated with other phases (non-permitted parent melts). **(B)** Total alkalis

Figure 6.7: (continued): versus silica (TAS) diagram showing the composition of the estimated intercumulus melts (white circles). In both *(A)* and *(B)*, the bulk compositions of Dourbes and Quartier measured by PIXL are shown as green and yellow circles. Basaltic rocks from Máaz measured by PIXL are shown as colored diamonds, while the triangles are the compositions measured by SuperCam. All the compositions measured by PIXL and SuperCam were normalized to 100 % in the same compositional system as the intercumulus liquids with Perple_X. The regions corresponding to the compositional ranges of basaltic, olivine-phyric, and poikilitic shergottites, as well as basaltic rocks from Gusev and Gale crater, are plotted for reference. The intercumulus melts projected in this diagram were estimated with a $Fe^{3+}/\Sigma Fe$ of 0.05 for the system. Results obtained with $Fe^{3+}/\Sigma Fe$ ratios of 0.10 and 0.15 are given in Supplementary Figures S3 and S4; however, differences are minimal.

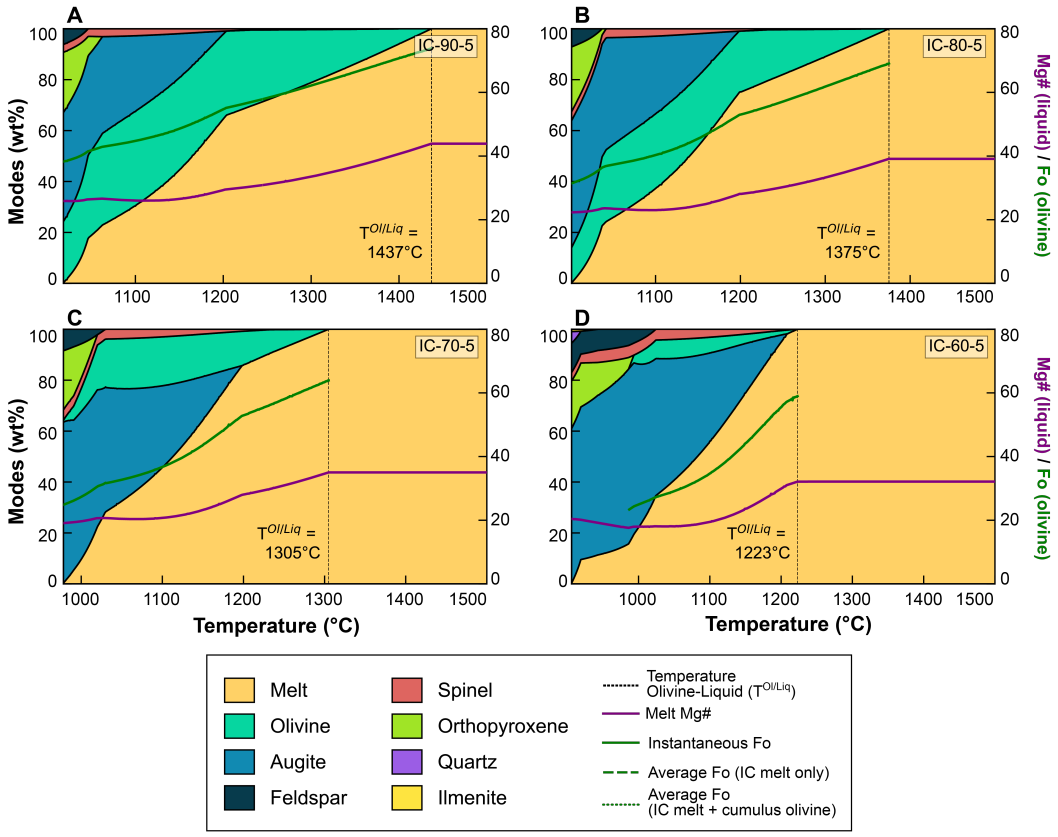


Figure 6.8: Modal boxes of phases produced by equilibrium crystallization of calculated intercumulus melts corresponding to melt proportions of 60 % **(A)**, 70 % **(B)**, 80 % **(C)**, and 90 % **(D)**. The 'effective' olivine liquidus temperature for each model is marked by the dashed vertical line. The solid lines are the Mg# of the melt (purple) and the Fo content of olivine (green), where both Mg# and Fo are defined as $100 \cdot Mg/(Mg + Fe)$. The initial $Fe^{3+}/\Sigma Fe$ ratio for the melt is assumed to be 0.05. Results for equilibrium crystallization with initial $Fe^{3+}/\Sigma Fe$ of 0.10 and 0.15 are given in Supplementary Figures S5 and S6.

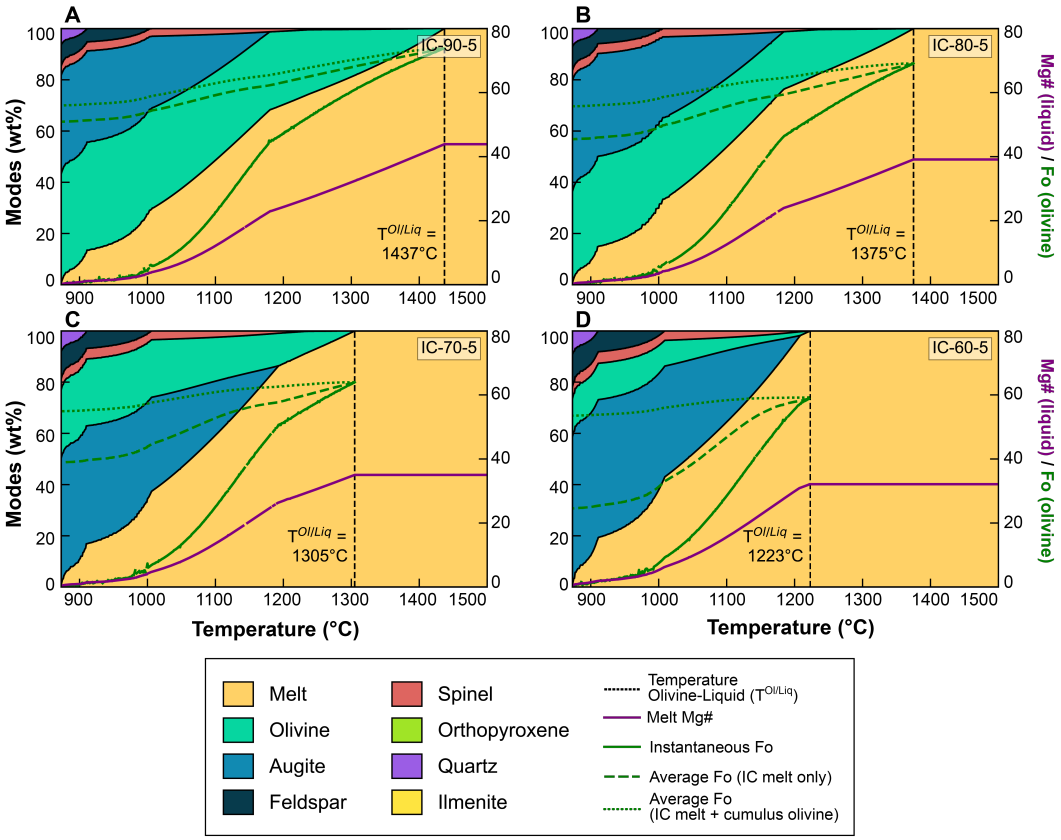


Figure 6.9: Modal boxes of phases produced by fractional crystallization of calculated intercumulus melts corresponding to melt proportions of 60 % **(A)**, 70 % **(B)**, 80 % **(C)**, and 90 % **(D)**. The "effective" olivine liquidus temperature for each model is marked by the dashed vertical line. The solid lines show the Mg# of the melt (purple) and the instantaneous Fo content of olivine (green), where both Mg# and Fo are defined as $100 \times \mathrm{Mg}/(\mathrm{Mg} + \mathrm{Fe})$. The dashed green line represents the average Fo content of olivine crystallizing from the intercumulus melt, whereas the dotted green line represents the average Fo content of the cumulus olivine plus that crystallizing from the intercumulus melt. The initial $\mathrm{Fe}^{3+}/\Sigma\mathrm{Fe}$ ratio of the melt is assumed to be 0.05. Results for equilibrium crystallization with initial $\mathrm{Fe}^{3+}/\Sigma\mathrm{Fe}$ ratios of 0.10 and 0.15 are shown in Supplementary Figures S7 and S8.

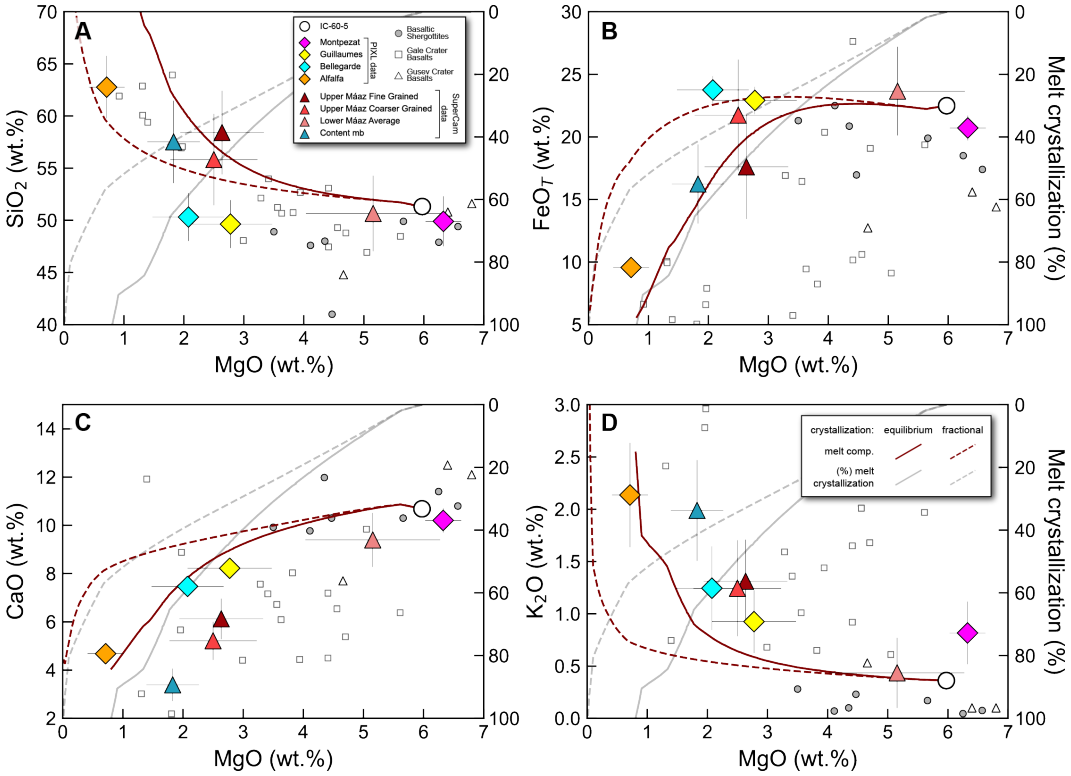


Figure 6.10: Bivariate diagrams showing changes in composition during fractional (dashed red line) and equilibrium (solid red line) crystallization of the preferred parental melt for Quartier (IC–60), represented as liquid lines of descent (LLD). **(A)** MgO versus SiO_2; **(B)** MgO versus FeO_T; **(C)** MgO versus CaO; and **(D)** MgO versus K_2O. Diagrams plotting MgO versus Al_2O_3, MgO versus Na_2O, and MgO versus TiO_2 are shown in Supplementary Figure S9. The weight percent of liquid crystallization (secondary y-axis) is shown by the gray lines for fractional (dashed) and equilibrium (solid) crystallization. Basaltic rocks from Máaz measured by PIXL are shown as colored diamonds, whereas the triangles represent compositions measured by SuperCam. All compositions measured by PIXL and SuperCam were normalized to 100 % in the same compositional system as the intercumulus liquids calculated with Perple_X. Basaltic shergottites (gray circles), Gale crater basalts (white squares), and Gusev crater basalts (white triangles) are shown for reference. The initial $Fe^{3+}/\Sigma Fe$ ratio of the melt is assumed to be 0.05. Results for equilibrium crystallization with an initial $Fe^{3+}/\Sigma Fe$ ratio of 0.10 are shown in Supplementary Figures S10 and S11.

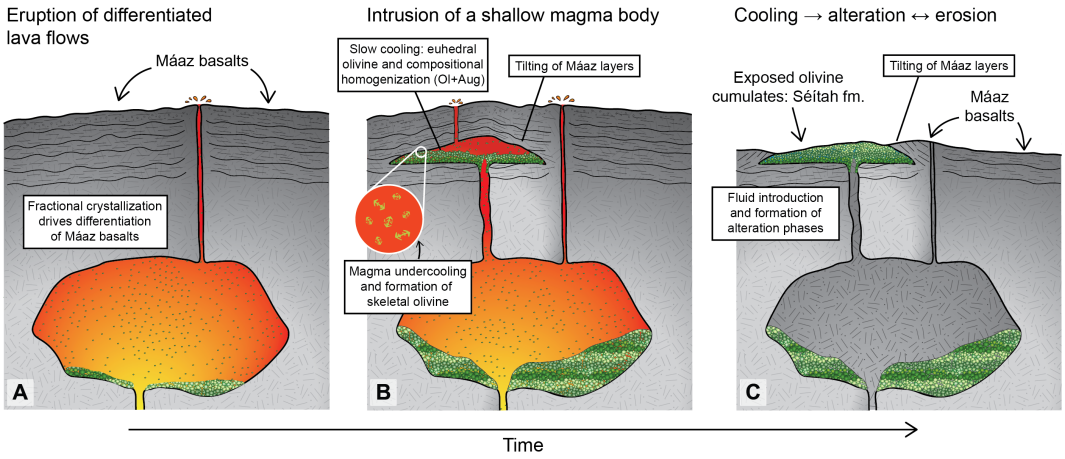


Figure 6.11: Schematic illustration of the emplacement model for Séítah olivine cumulates as an igneous intrusion, as described in this study. **(A)** Differentiated lava flows erupt at the surface, producing layered basalts of the Máaz formation. **(B)** An intrusive, sill-like body derived from the same magmatic source is emplaced within the Máaz basalt layers. Rapid magma ascent leads to undercooling and the development of skeletal textures in crystallizing olivine. Slower cooling within a shallow magma reservoir occurs under near-equilibrium conditions, allowing polyhedral olivine to crystallize and chemically homogenize with later augite crystals through Fe–Mg diffusion. Emplacement of the intrusion results in tilting of the Máaz layers adjacent to the contact. **(C)** Following magmatic cooling, the introduction of aqueous fluids produces alteration phases observed across multiple outcrops in Séítah. Subsequent erosion removes the overlying Máaz formation, exposing the olivine cumulates of the Séítah formation.

Table 6.3: Average feldspar and spinel compositions.

Phases	Spinel (n = 70)		Feldspar (n = 65)	
Oxide	wt.%	1σ	wt.%	1σ
Na_2O	2.73	1.19	4.95	1.34
MgO	7.98	1.98	5.43	1.48
Al_2O_3	2.14	0.74	11.09	2.08
SiO_2	26.72	6.09	50.23	4.40
P_2O_5	0.16	0.37	0.39	0.80
SO_3	1.08	1.17	1.34	2.38
Cl	1.28	0.69	0.83	0.51
K_2O	0.05	0.08	2.13	0.49
CaO	2.37	2.50	1.87	1.53
TiO_2	14.32	7.04	0.12	0.09
Cr_2O_3	7.83	3.52	0.00	0.01
MnO	0.12	0.13	0.06	0.07
FeO_T	28.44	10.07	6.21	2.44
Total	95.22		84.65	
Cr/Ti	0.70	0.54	—	—
Cr/(Cr+Al)	0.68	0.12	—	—
Mg/(Mg+Fe)	0.35	0.09	—	—
Ab			66	10
An			14	12
Or			19	4

Table 6.4: Intercumulus melt compositions obtained from partial melting of the Quartier bulk composition. Oxides are expressed in weight percent.

Intercumulus melt	SiO_2	TiO_2	Al_2O_3	Cr_2O_3	Fe_2O_3	FeO	MgO	CaO	Na_2O	K_2O	$Fe^{3+}/\Sigma Fe$
IC–90–5	45.80	0.84	2.52	0.37	1.79	27.90	12.24	7.30	0.99	0.24	0.05
IC–90–10	45.58	0.84	2.51	0.37	3.59	26.53	12.09	7.27	0.99	0.24	0.10
IC–90–15	46.57	0.93	2.79	0.27	3.93	26.46	9.64	8.05	1.10	0.27	0.15
IC–80–5	46.97	0.94	2.83	0.34	1.99	27.47	9.90	8.17	1.11	0.27	0.05
IC–80–10	46.77	0.94	2.82	0.27	3.98	26.01	9.67	8.15	1.11	0.27	0.10
IC–80–15	48.05	1.04	3.14	0.17	4.29	25.26	7.48	9.02	1.23	0.30	0.15
IC–70–5	48.75	1.08	3.24	0.24	2.24	25.79	7.80	9.28	1.27	0.31	0.05
IC–70–10	48.54	1.07	3.23	0.17	4.40	24.23	7.55	9.24	1.27	0.31	0.10
IC–70–15	50.46	0.98	3.58	0.10	4.42	22.69	5.80	10.22	1.41	0.34	0.15
IC–60–5	51.32	1.23	3.78	0.15	2.52	22.49	5.97	10.68	1.49	0.36	0.05
IC–60–10	51.29	0.99	3.76	0.10	4.51	21.16	5.87	10.50	1.46	0.36	0.10

Note: Intercumulus melts are named using the prefix IC followed by the proportion of melt in the cumulate, and the $Fe^{3+}/\Sigma Fe$ ratio assumed for the bulk Quartier composition.

Table 6.5: Predicted compositions of primary phases during equilibrium crystallization of intercumulus melts ($Fe^{3+}/\Sigma Fe = 0.05$).

Intercumulus	Melt		Olivine	Augite				Spinel						Feldspar			
liquid	T (°C)	Cryst. (%)	Mg#	Fo	T (°C)	Wo (%)	En (%)	Fs (%)	T (°C)	X_{Hc}	X_{Mt}	X_{Sp}	X_{Usp}	X_{Crm}	T (°C)	Ab	An	Or
IC–90–5	1437 (l.)	0	43	73	–	–	–	–	1411	−0.41	0.35	0.41	0.00	0.64	–	–	–	–
	1400	6	40	70	–	–	–	–	1400	−0.39	0.35	0.39	0.00	0.64	–	–	–	–
	1300	21	33	62	1203	36	40	23	1300	−0.29	0.39	0.29	0.01	0.60	–	–	–	–
	1200	35	29	54	1200	36	40	23	1200	−0.43	0.26	0.43	0.49	0.25	–	–	–	–
	1100	70	26	44	1100	34	36	28	1100	−0.33	0.26	0.34	0.67	0.06	1046	53	45	2
	1018 (s.)	100	25	38	1018 (s.)	33	33	32	1018 (s.)	−0.26	0.26	0.27	0.71	0.01	1018 (s.)	58	34	8
IC–80–5	1375 (l.)	0	39	69	–	–	–	–	1375	−0.37	0.36	0.37	0.00	0.63	–	–	–	–
	1300	11	33	61	–	–	–	–	1300	−0.28	0.39	0.29	0.01	0.60	–	–	–	–
	1200	25	28	53	1198	36	39	24	1200	−0.43	0.24	0.43	0.55	0.21	–	–	–	–
	1100	63	23	40	1100	35	33	30	1100	−0.29	0.24	0.30	0.71	0.04	1037	46	52	1
	1001 (s.)	100	22	31	1001 (s.)	32	29	37	1001 (s.)	−0.20	0.27	0.21	0.71	0.01	1001 (s.)	56	36	7
IC–70–5	1305 (l.)	0	35	63	–	–	–	–	1318	−0.31	0.39	0.31	0.01	0.60	–	–	–	–
	1300	1	34	63	–	–	–	–	1300	−0.30	0.40	0.30	0.01	0.59	–	–	–	–
	1200	14	28	52	1198	36	39	24	1200	−0.50	0.17	0.50	0.70	0.13	–	–	–	–
	1100	54	20	36	1100	36	31	31	1100	−0.27	0.21	0.28	0.77	0.01	1030	43	56	1
	1000	90	19	27	1000	31	27	41	1000	−0.16	0.28	0.18	0.70	0.01	1000	50	47	3
	978 (s.)	100	19	24	978 (s.)	30	26	43	978 (s.)	−0.14	0.27	0.16	0.71	0.00	978 (s.)	52	42	6
IC–60–5	1223 (l.)	0	32	58	1208	35	42	22	1225	−0.26	0.44	0.26	0.01	0.54	–	–	–	–
	1200	5	29	55	1200	36	41	22	1200	−0.63	0.09	0.63	0.90	0.01	–	–	–	–
	1100	44	19	34	1100	36	30	32	1100	−0.27	0.19	0.27	0.80	0.00	1024	41	58	1

Continued on next page

Table 6.5. Continued.

Intercumulus		Melt		Olivine	Augite				Spinel						Feldspar			
liquid	T (°C)	Cryst. (%)	Mg#	Fo	T (°C)	Wo (%)	En (%)	Fs (%)	T (°C)	X_{Hc}	X_{Mt}	X_{Sp}	X_{Usp}	X_{Crm}	T (°C)	Ab	An	Or
	1000	78	17	24	1000	36	30	32	1000	−0.14	0.28	0.16	0.70	0.00	1000	43	55	1
	906 (s.)	100	20	–	906 (s.)	32	25	42	906 (s.)	−0.10	0.37	0.12	0.62	0.00	906 (s.)	47	48	5

Note: s. and *l.* are *solidus* and *liquidus*, respectively

Table 6.6: Predicted compositions of primary phases during fractional crystallization of intercumulus melts ($Fe^{3+}/\Sigma Fe = 0.05$).

Intercumulus liquid	Melt			Olivine		Augite							Spinel (instantaneous composition)						Feldspar (instantaneous composition)			
	T (°C)	Cryst. (%)	Mg#	Fo	Fo*	T (°C)	$Wo_{in.}$	$En_{in.}$	$Fs_{in.}$	Wo*	En*	Fs*	T (°C)	X_{Hc}	X_{Mt}	X_{Sp}	X_{Usp}	X_{Crm}	T (°C)	Ab	An	Or
IC-90-5	1437 (l.)	0	43	73	73	–	–	–	–	–	–	–	1409	−0.40	0.35	0.41	0.00	0.64	–	–	–	–
	1400	6	40	70	72	–	–	–	–	–	–	–	1400	−0.39	0.36	0.39	0.00	0.64	–	–	–	–
	1300	19	31	60	67	–	–	–	–	–	–	–	1300	−0.27	0.39	0.27	0.01	0.60	–	–	–	–
	1200	30	24	47	63	1181	36	35	27	36	35	27	1200	−0.46	0.11	0.46	0.86	0.04	–	–	–	–
	1100	51	12	22	59	1100	39	21	38	38	28	32	1100	−0.16	0.19	0.16	0.81	0.00	1006	32	67	1
	1000	72	3	4	53	1000	41	5	53	39	20	39	1000	0.01	0.46	0.01	0.51	0.00	1000	26	74	0
	900	92	0	0	51	900	40	0	58	39	16	43	900	0.02	0.75	0.00	0.22	0.00	900	35	62	3
	873 (s.)	99	0	0	50	873 (s.)	41	0	58	39	16	43	873 (s.)	0.02	0.49	0.00	0.49	0.00	873 (s.)	13	36	51
IC-80-5	1375 (l.)	0	39	69	69	–	–	–	–	–	–	–	1376	−0.37	0.36	0.37	0.00	0.63	–	–	–	–
	1300	10	32	61	65	–	–	–	–	–	–	–	1300	−0.28	0.39	0.28	0.01	0.60	–	–	–	–
	1200	22	25	48	60	1185	36	36	26	36	36	26	1200	−0.48	0.11	0.49	0.86	0.04	–	–	–	–
	1100	46	12	23	55	1100	39	22	37	38	29	31	1100	−0.17	0.18	0.17	0.81	0.00	1005	30	70	1
	1000	70	3	5	49	1000	41	6	52	39	20	39	1000	0.01	0.56	0.02	0.42	0.00	1000	31	69	1
	900	91	0	0	45	900	40	1	58	39	17	43	900	0.03	0.82	0.00	0.15	0.00	900	37	60	3
	873 (s.)	99	0	0	45	873 (s.)	41	0	58	39	16	43	873 (s.)	0.02	0.52	0.00	0.46	0.00	873 (s.)	13	36	51

Note: s., *l.*, and *in.* denote *solidus*, *liquidus*, and *instantaneous*, respectively. * indicates average value

12. Supplemental Materials

12.1 Primary mineral identification

The following are general rules we used for identifying PMCs corresponding to primary phases.

- **Olivine:** $Ol^* > 0.75$, $Di^* < 0.25$, and $0.4 < SiO_2/(FeO + MgO) < 0.6$.
- **Clinopyroxene:** $Di^* > 0.7$ and $An^* < 0.25$.
- **Feldspar:** $Ol^* > 0.45$, $Na_2O+CaO+K_2O > 1$ wt%, and $SiO_2/(FeO+MgO) > 2.3$.
- **Spinel:** $Al_2O_3/(TiO_2 + Cr_2O_3) < 0.25$, with analytical totals exceeding 80 wt%.

The variables Ol^*, Di^*, and An^* are mineral coordinates in compositional space projected from Qtz^* that were useful for grouping distinct phases (*Herzberg and O'hara* 1998), along with the parameter MF, which we defined as FeO + MgO - $3\times K_2O$ - $3\times Na_2O$. In all cases, oxides are expressed in molar percent.

12.2 Average compositions of olivine and augite

To obtain relatively pristine compositions of olivine and augite, the mineral identification clusters were further screened to exclude PMCs affected by significant alteration or mixing with other primary or secondary phases. Only PMCs with analytical totals above 97 wt.%, $Na_2O < 1$ wt.%, and SO_3 + Cl < 2 wt.% were considered for olivine (n = 126), whereas analytical totals above 95 wt.% and SO_3 + Cl < 2.0 wt.% were considered for augite (n = 97). The resulting PMCs compositions were then corrected for mixing with sulfates and chlorines/oxychlorines following the method of *Tice et al.* (2022). We assumed all the SO_3 was present as $CaSO_4$ and $MgSO_4$. The necessary amounts of CaO and MgO were subtracted to remove all the SO_3 present in a proportion that maintained the initial molar ratio of CaO/(CaO+MgO). Similarly, to correct for chlorines/oxychlorines, Na_2O or Cl were subtracted from the analyses in a one-to-one molar ratio. For olivine, any remaining Cl or Na_2O was considered part of inclusions or minor mixing with neighboring mineral phases. The olivine and clinopyroxene compositions reported in Table 2 were obtained as the average of all their corresponding PMCs after corrections were applied.

12.3 Detection of crystalline domains from x-ray diffraction maps

Diffraction peaks detected from differences in the spectra from the two X-ray detectors were used to produce diffraction maps of the two scan areas (Supplementary Figure S1). These maps were used, when possible, to aid mineral identification and petrographic characterization. The maps were generated by normalizing energy levels of diffraction peaks to a color scale, with color intensities proportional to peak intensities. Diffraction maps displaying continuous areas defined by contiguous pixels with similar colors likely correspond to the similar crystalline domains – i.e., the same crystal. In contrast, pixels with similar colors and intense tonalities but spatially separated likely correspond to different crystals of the same phase in a similar orientation. Pixels showing dark tones reflect low intensity diffraction peaks likely corresponding with poor crystallinity phases.

The diffraction map in Quartier shows a combination of crystalline and non-diffracting phases (Supplementary Figure S1), consistent with the presence of relatively fresh primary minerals, but also extensive alteration of these phases in some regions. Augite is the most distinctive phase showing predominantly light green colors that persist over neighboring pixels defining single-crystal domains with sizes between ~2–4 mm along their longest side. Part of a single augite crystal is also shown in red at the bottom edge of the scan area. Unaltered olivine crystals ~2–4 mm long (Ol-1), and located in separate regions of the scan area, show dark green colors that indicate a similar crystallographic orientation. Other olivine crystals with more rounded shape and enclosed by augite appear in bright yellow with diffraction peaks at higher energy. However, most of the olivine in the scan area, including Ol-1 and Ol-2 domains, is shown in dark tones, suggesting poor crystallinity due to alteration. Spinel-bearing pixels have uniform red, yellow, and green colors, pointing to crystals with different preferential orientation. Feldspar areas, by contrast, are poorly crystalline as also indicated by their dark tones in the diffraction map (Supplementary Figure S1).

12.4 Aqueous alteration in *Issole*

The main alteration phases identified in the Quartier abrasion correspond to LIS, carbonate, sulfates, and chlorine/oxychlorines. The occurrence and spatial distribution of these phases is consistent with multiple events of aqueous alteration in the Séítah formation, as has been suggested in previous studies (e.g., *Corpolongo et al*. 2023; *Mandon et al*. 2023; *Scheller et al*. 2022; *Siljeström et al*. 2024; *Tice et al*. 2022). The LIS and Fe–Mg carbonate phases appear to replace and surround

olivine crystals in the two scan areas, indicating a first stage of partial dissolution and replacement of olivine. This alteration likely occurred at low temperatures via interaction with water-rich fluids, possibly from meteoric or shallow groundwater sources (*Tice et al*., 2022). The absence of secondary iron oxides and formation of carbonates indicates that the fluids were not highly oxidizing and may have been CO_2-bearing. The second stage of alteration resulted from infiltration of concentrated brines carrying SO_4, Mg, and Ca ions in solution, which led to precipitation of Mg–Ca-bearing sulfates without significant olivine dissolution. This form of alteration has also been recognized in Máaz and may account for a regional event affecting the crater floor units in Jezero. Lastly, the presence of Na-rich chlorines in Quartier, which tend to pervasively overprint all the pre-existing phases, most likely resulted from a later alteration event in which saline brines precipitated chlorine/oxychlorine species (*Tice et al*. 2022).

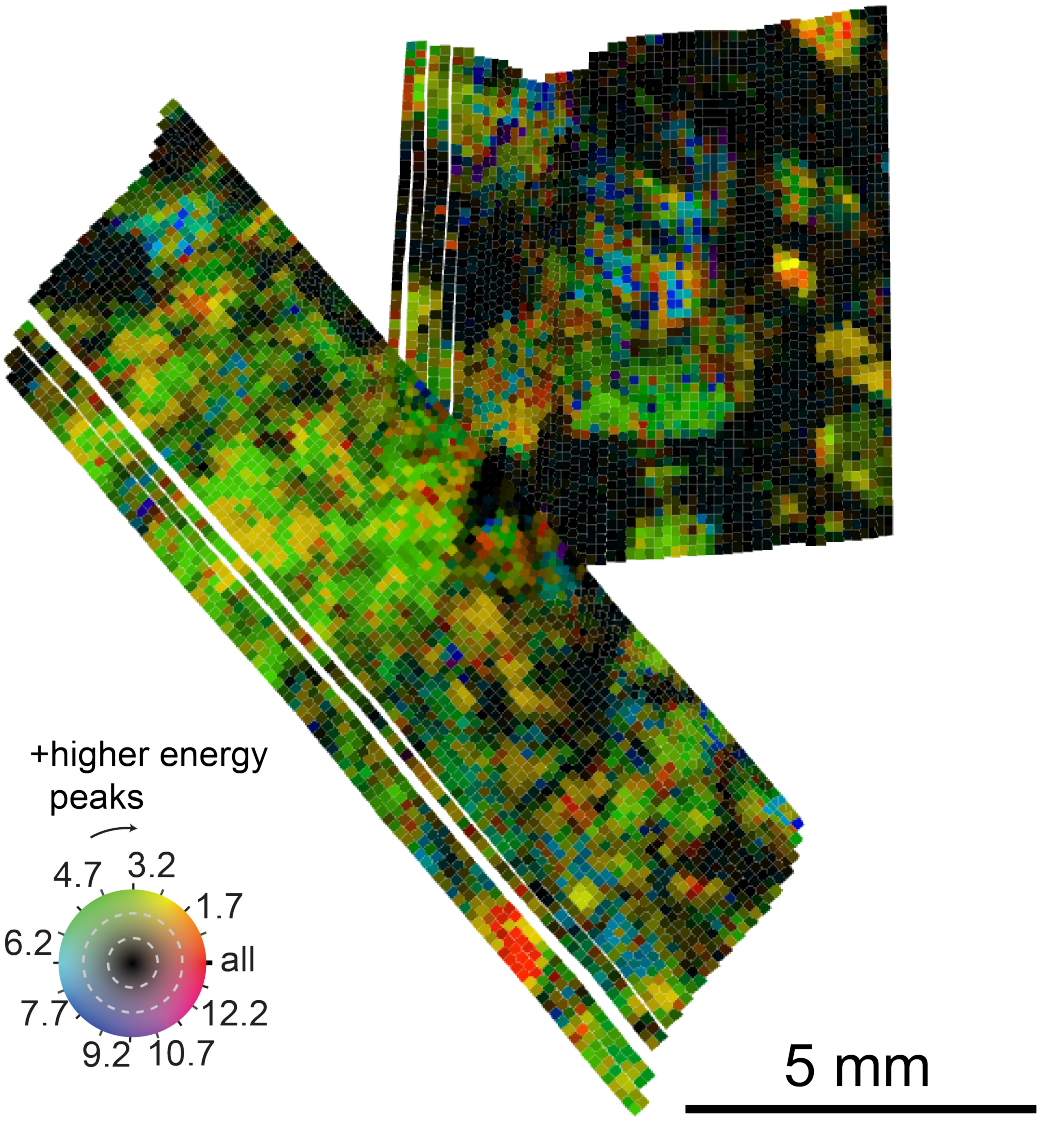


Figure S6.1: Diffraction map of the two PIXL scan regions. Energy levels of diffraction peaks are normalized to color scale and color intensities are proportional to peak intensities. Continuous areas defined by contiguous pixels with similar colors likely correspond to single crystals. Spatially separate pixels displaying similar colors and tones may correspond to different crystals of the same phase in a similar orientation. Pixels showing dark tones reflect low intensity diffraction peaks associated with poor crystallinity phases.

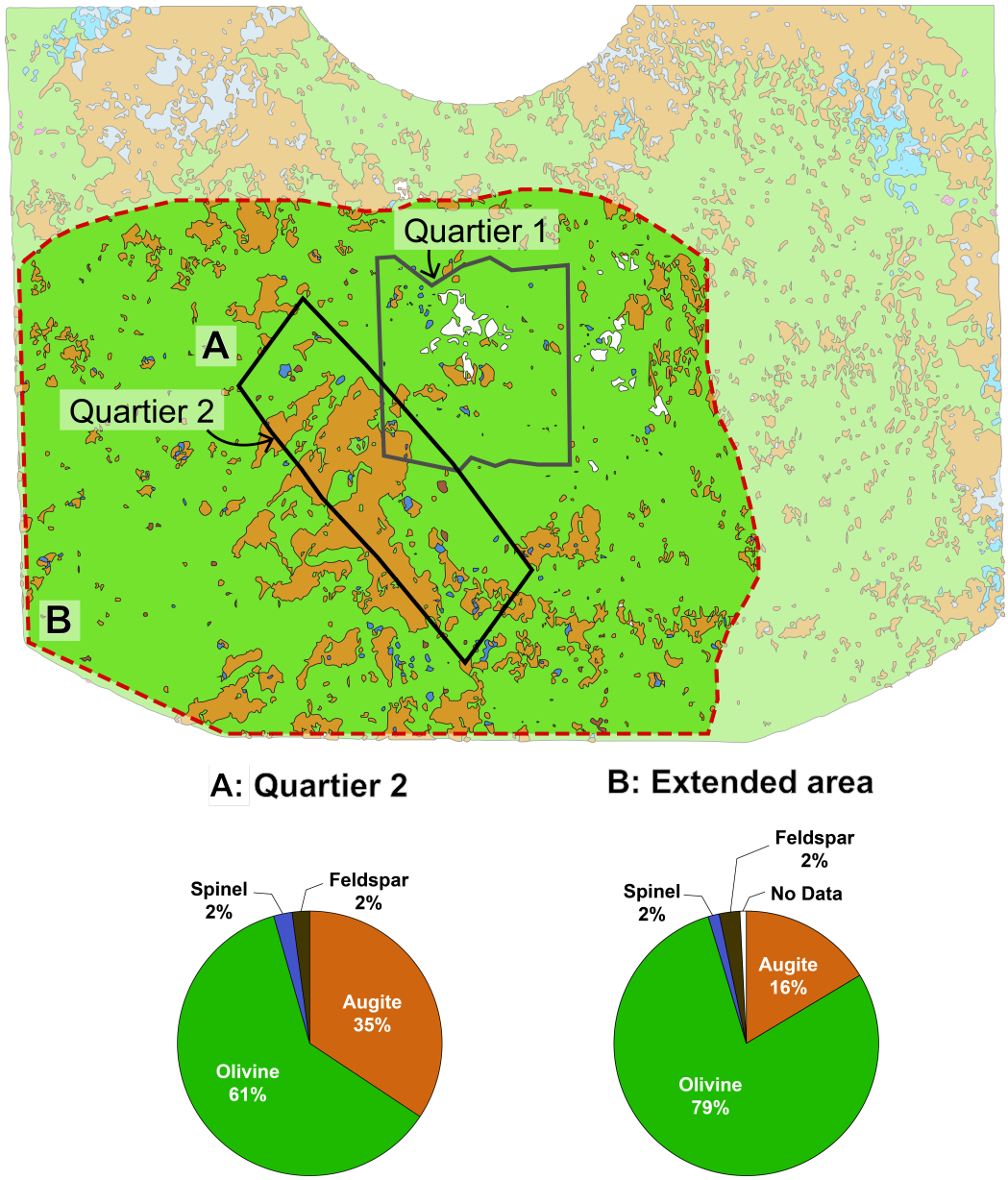


Figure S6.2: Reclassified image from MCC and XRF data. Image classification implemented a Random Forest algorithm and used the primary phases identified in Quartier 2 as training datasets (*Lanari et al.* 2019). Region B is an extended area that shows predicted mineral abundances from the classification algorithm. Mineral proportions indicate Quartier can be classified as a wehrlite.

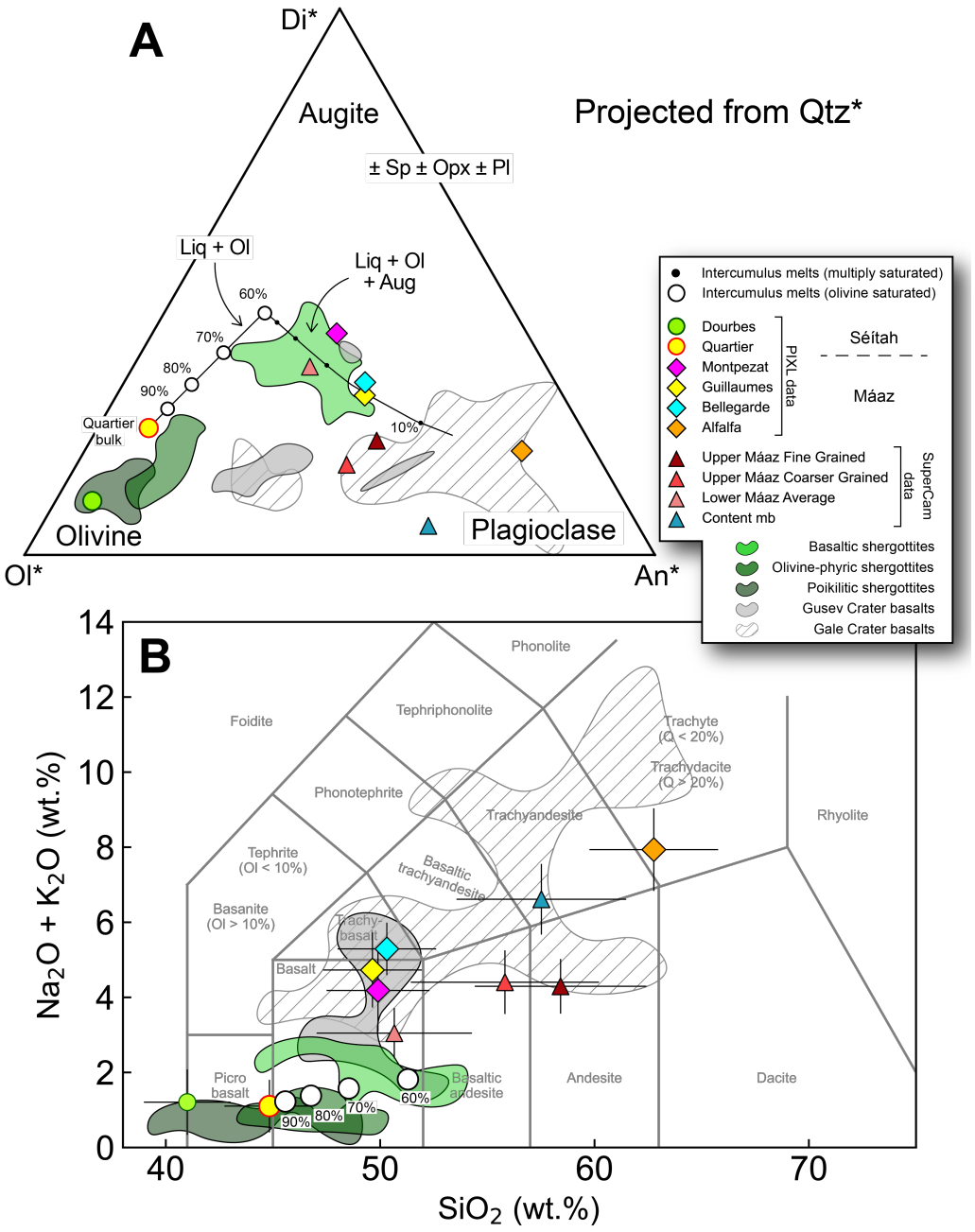


Figure S6.3: **(A)** 'Pseudoliquidus' diagram of intercumulus melts produced by Quartier partial melting. Solid black line: projected liquid compositions (0 to 100 % melting). Black dots and white circles represent liquid fractions in 10 wt.% increments. White circles: liquids only saturated with olivine (potential parent melts). Dots: liquids cosaturated with other phases (non-permitted parent melts). **(B)** Total alkalis versus silica (TAS) diagram showing compositions of estimated intercumulus melts (white circles). In both **(A)** and **(B)**, bulk compositions of Dourbes and Quartier measured by PIXL are shown as green and yellow circles. Basaltic rocks from Máaz measured by PIXL are shown as colored diamonds, while triangles are the compositions measured by SuperCam. All compositions measured by PIXL and SuperCam were normalized to 100 % in the same compositional system as the intercumulus liquids with Perple_X. Regions corresponding to the compositional ranges of basaltic, olivine-phyric, and poikilitic shergottites, and basaltic rocks from Gusev and Gale crater, are plotted for reference. Projected intercumulus melts were estimated with a $Fe^{3+}/\Sigma Fe$ of 0.10 for the system.

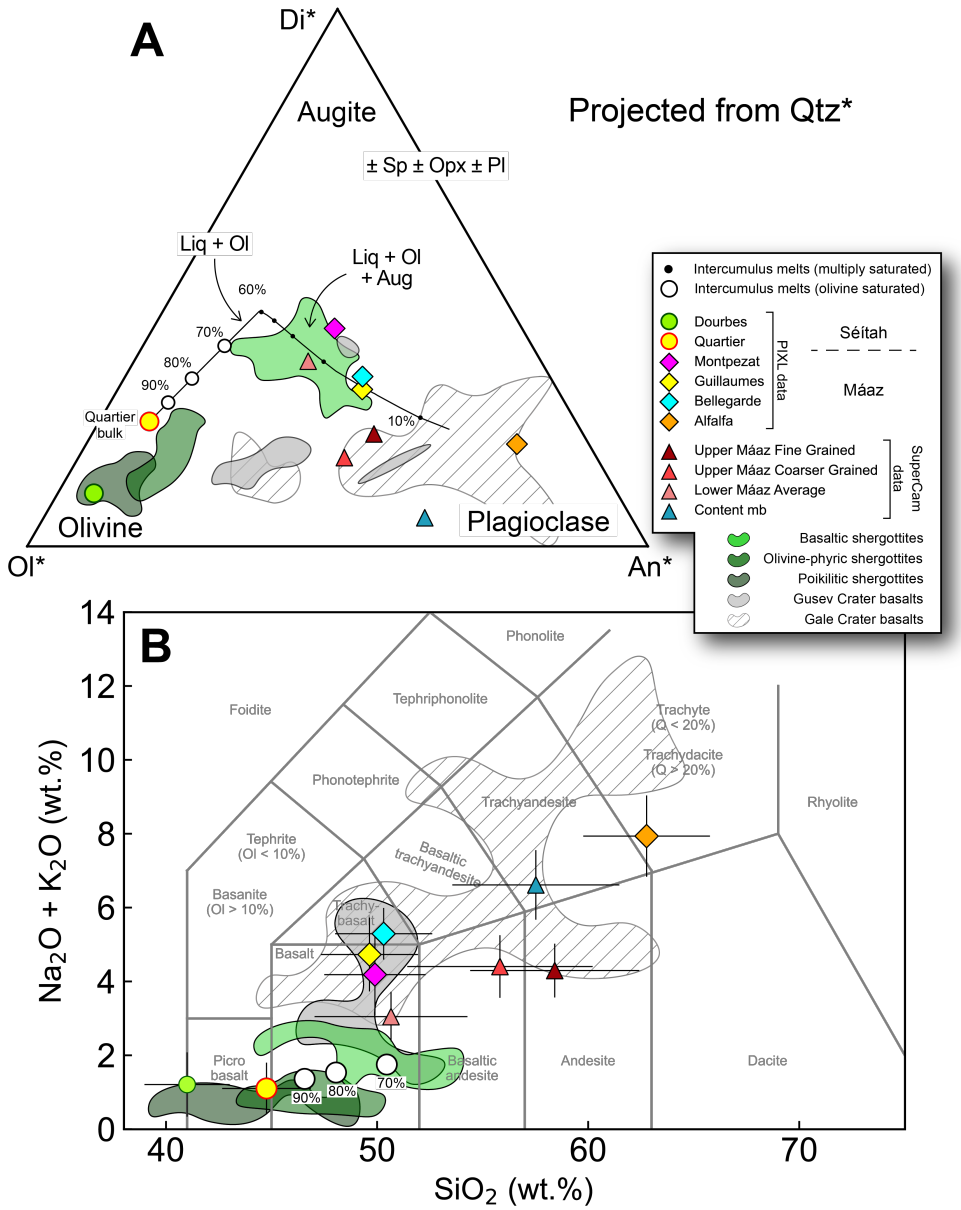


Figure S6.4: **(A)** 'Pseudoliquidus' diagram for intercumulus melts produced by Quartier partial melting. Solid black line: projected liquid compositions (0 to 100 % melting). Black dots & white circles are liquid fractions in 10 wt.% increments. White circles: liquids saturated with olivine only (potential parent melts). Dots: liquids cosaturated with other phases (non-permitted parent melts). **(B)** TAS diagram showing the composition of the estimated intercumulus melts (white circles). In both **(A)** & **(B)**, bulk compositions of Dourbes & Quartier measured by PIXL shown as green & yellow circles. Basaltic rocks from Máaz measured by PIXL shown as colored diamonds, and triangles are the compositions measured by SuperCam. All compositions measured by PIXL & SuperCam were normalized to 100 % in the same compositional system as the intercumulus liquids with Perple_X. Regions corresponding to the compositional ranges of basaltic, olivine-phyric, and poikilitic shergottites, and basaltic rocks from Gusev and Gale crater, are plotted for reference. Projected intercumulus melts were estimated with a system $Fe^{3+}/\Sigma Fe$ of 0.15.

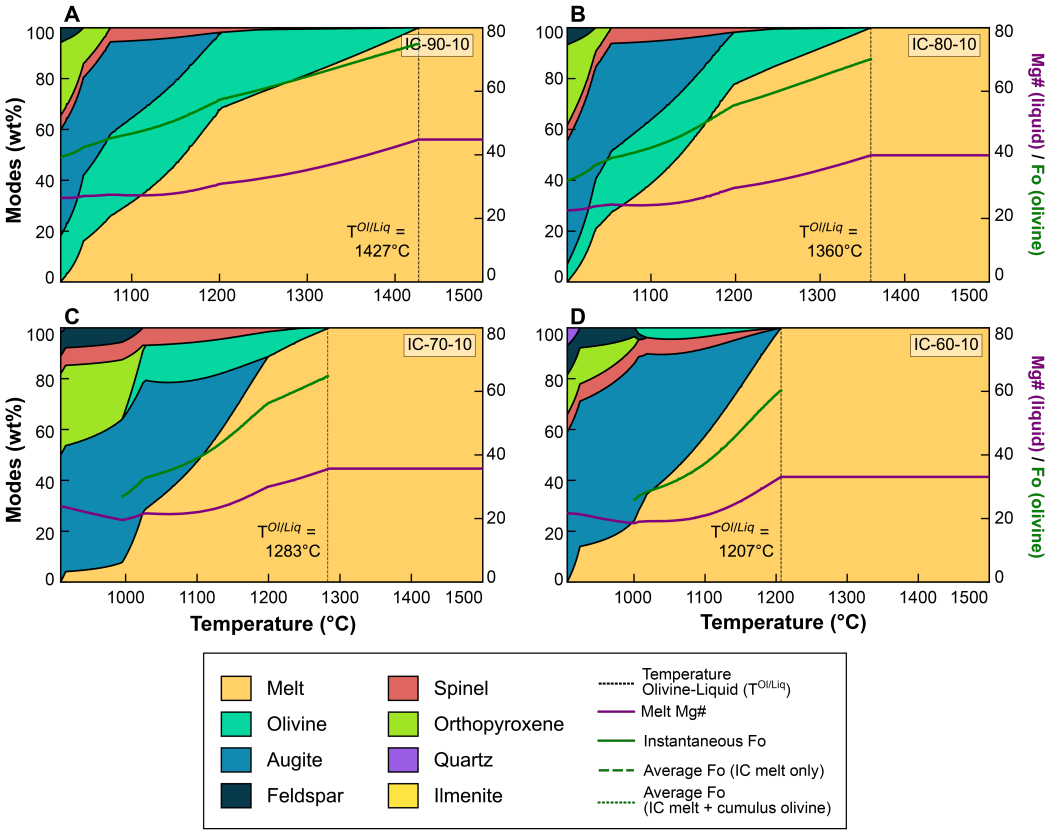


Figure S6.5: Modal boxes of phases produced by equilibrium crystallization of calculated intercumulus melts corresponding to melt proportions of 60% (A), 70% (B), 80% (C), and 90% (D). The 'effective' olivine liquidus temperature for each model is marked by the dashed vertical line. The solid lines are the Mg# of the melt (purple) and the Fo content of olivine (green), where both Mg# and Fo are defined as $100 \times \mathrm{Mg}/(\mathrm{Mg} + \mathrm{Fe})$. The initial $\mathrm{Fe}^{3+}/\Sigma\mathrm{Fe}$ ratio for the melt is assumed to be 0.10.

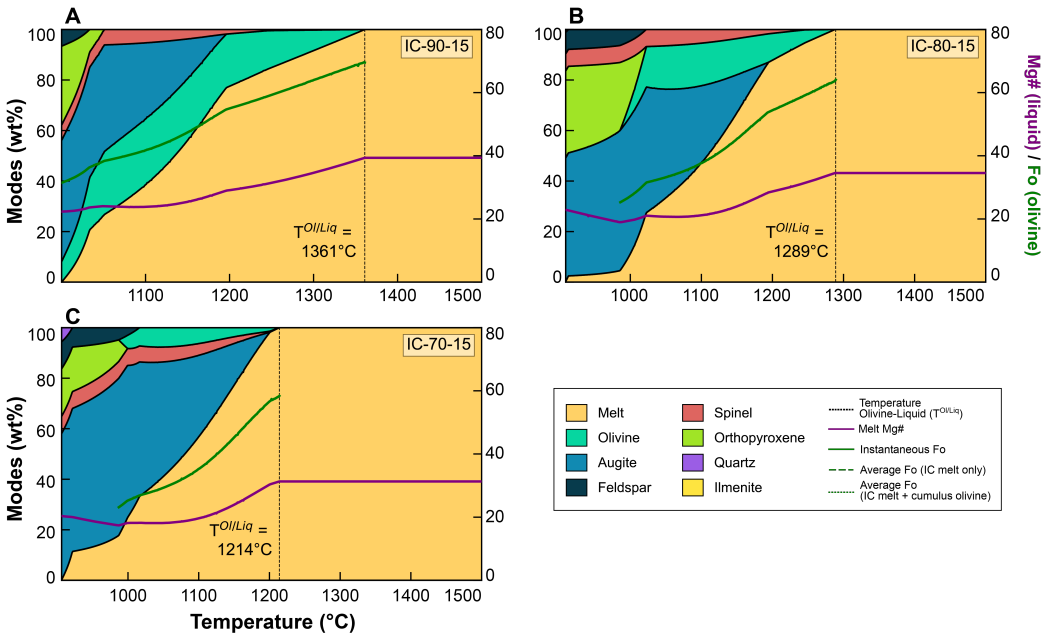


Figure S6.6: Modal boxes of phases produced by equilibrium crystallization of calculated intercumulus melts corresponding to melt proportions of 90% (A), 80% (B), and 70% (C). The 'effective' olivine liquidus temperature for each model is marked by the dashed vertical line. The solid lines are the Mg# of the melt (purple) and the Fo content of olivine (green), where both Mg# and Fo are defined as $100 \times \mathrm{Mg}/(\mathrm{Mg}+\mathrm{Fe})$. The initial $\mathrm{Fe}^{3+}/\Sigma\mathrm{Fe}$ ratio for the melt is assumed to be 0.15.

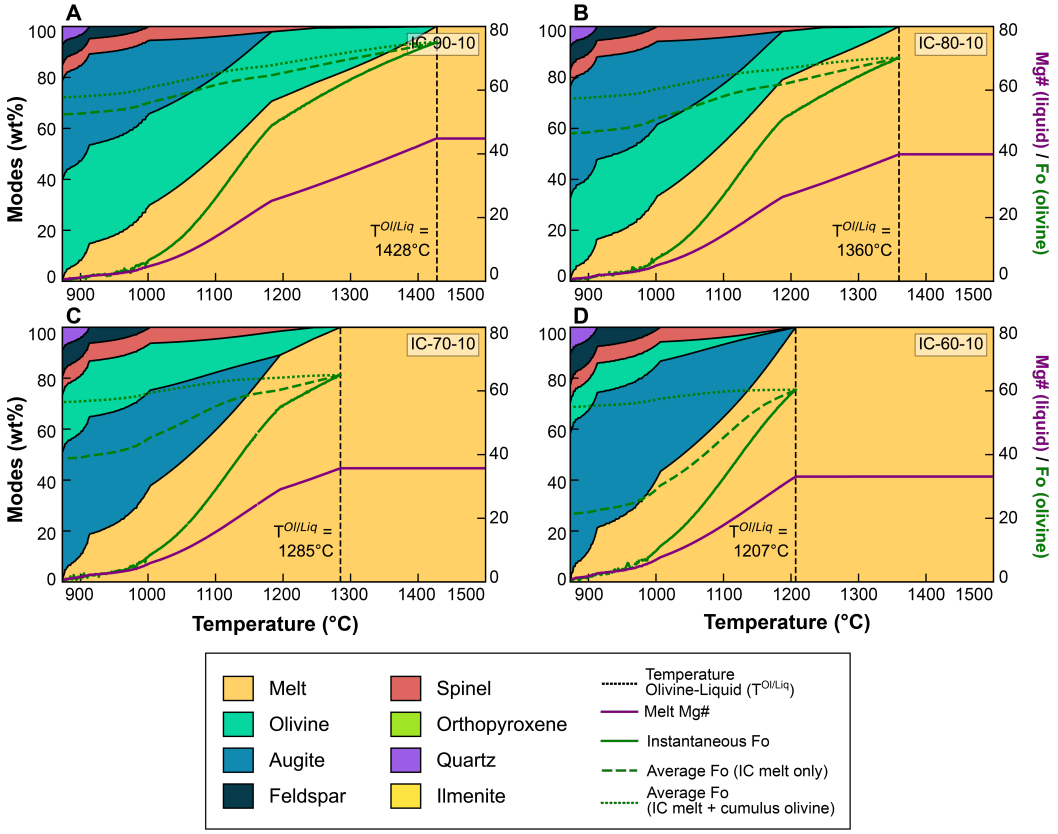


Figure S6.7: Modal boxes of phases produced by fractional crystallization of calculated intercumulus melts corresponding to melt proportions of 90% (A), 80% (B), 70% (C), and 60% (D). The 'effective' olivine liquidus temperature for each model is marked by the dashed vertical line. The solid lines are the Mg# of the melt (purple) and the instantaneous Fo content of olivine (green), where both Mg# and Fo are defined as $100 \times \mathrm{Mg}/(\mathrm{Mg} + \mathrm{Fe})$. The dashed green line is the average Fo content of the olivine that crystallizes from the intercumulus melt. The dotted green line is the average Fo content of the cumulus olivine plus that crystallizying from the intercumulus melt. The initial $\mathrm{Fe}^{3+}/\Sigma\mathrm{Fe}$ ratio for the melt is assumed to be 0.10.

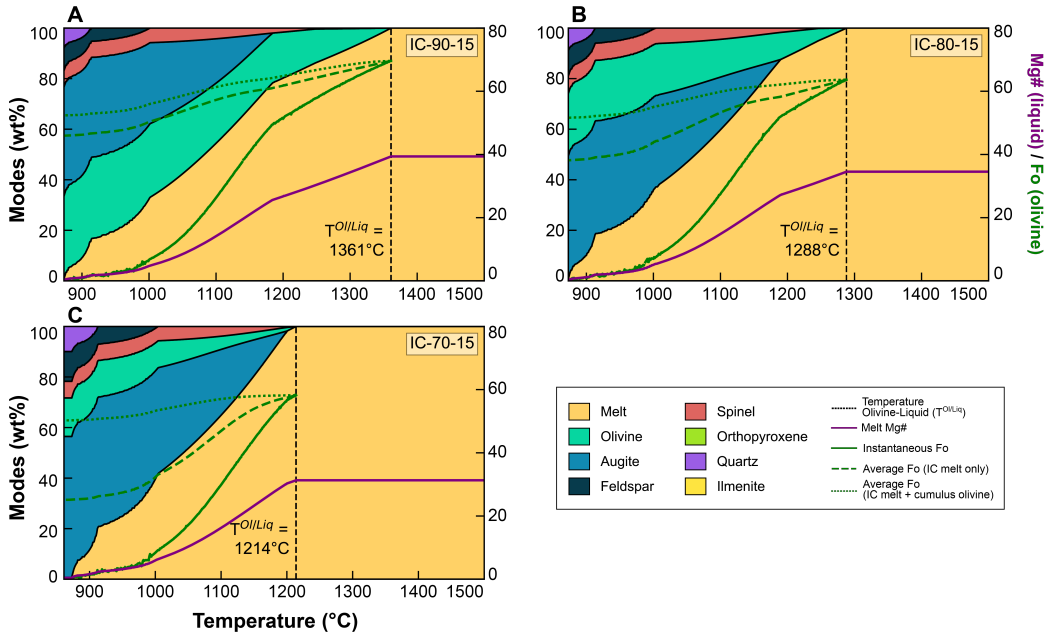


Figure S6.8: Modal boxes of phases produced by fractional crystallization of calculated intercumulus melts corresponding to melt proportions of 90% (A), 80% (B), and 70% (C). The 'effective' olivine liquidus temperature for each model is marked by the dashed vertical line. The solid lines are the Mg# of the melt (purple) and the instantaneous Fo content of olivine (green), where both Mg# and Fo are defined as $100 \times \mathrm{Mg}/(\mathrm{Mg}+\mathrm{Fe})$. The dashed green line is the average Fo content of the olivine that crystallizes from the intercumulus melt. The dotted green line is the average Fo content of the cumulus olivine plus that crystallizying from the intercumulus melt. The initial $\mathrm{Fe}^{3+}/\Sigma\mathrm{Fe}$ ratio for the melt is assumed to be 0.15.

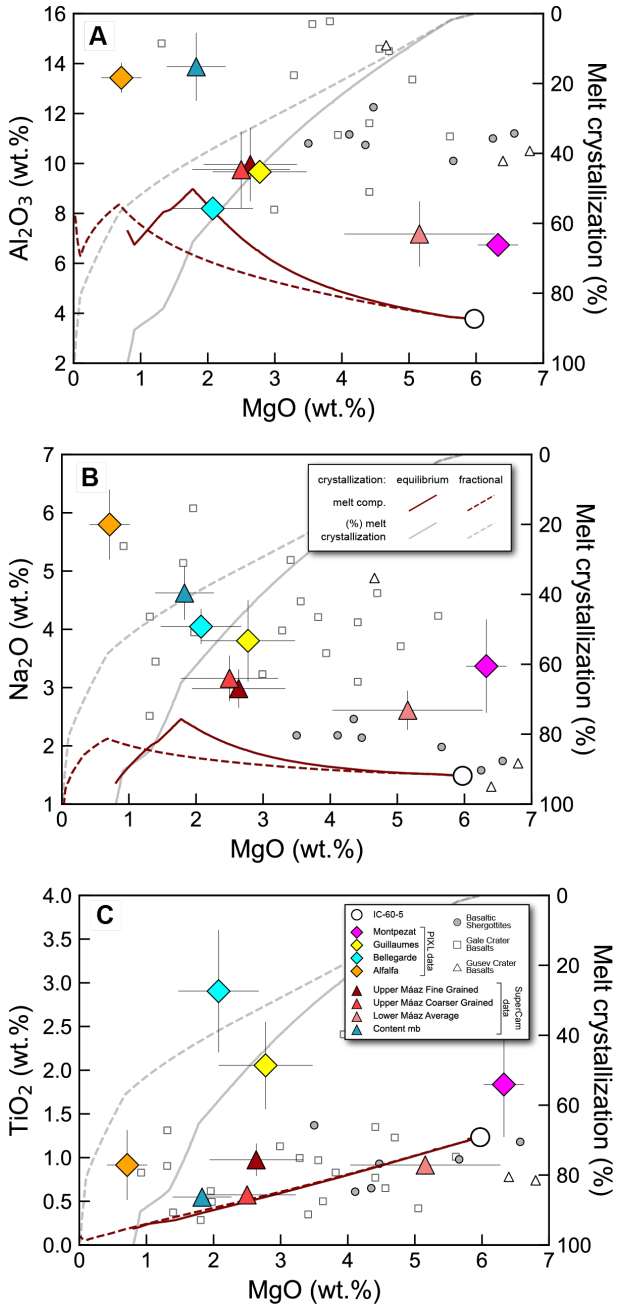


Figure S6.9: Bivariate diagrams showing changes in composition during fractional (dashed red line) and equilibrium (solid red line) crystallization of the preferred parental melt for Quartier, represented as liquid lines of descent (LLD). (A) MgO vs. Al_2O_3; (B) MgO vs. Na_2O; and (C) MgO vs. TiO_2. The weight percent of liquid crystallization (secondary y-axis) is shown by the gray lines for fractional (dashed) and equilibrium (solid) crystallization. Basaltic rocks from Máaz measured by PIXL are shown as colored diamonds, while the triangles are the compositions measured by SuperCam. All the compositions measured by PIXL and SuperCam were normalized to 100 % in the same compositional system as the intercumulus liquids with Perple_X. Basaltic shergottites (grey circles), Gale crater basalts (white squares), and Gusev crater basalts (white triangles) are shown for reference. The initial $Fe^{3+}/\Sigma Fe$ ratio for the melt is assumed to be 0.05. The data points and LLD show only minimal changes with respect to Figure S11.

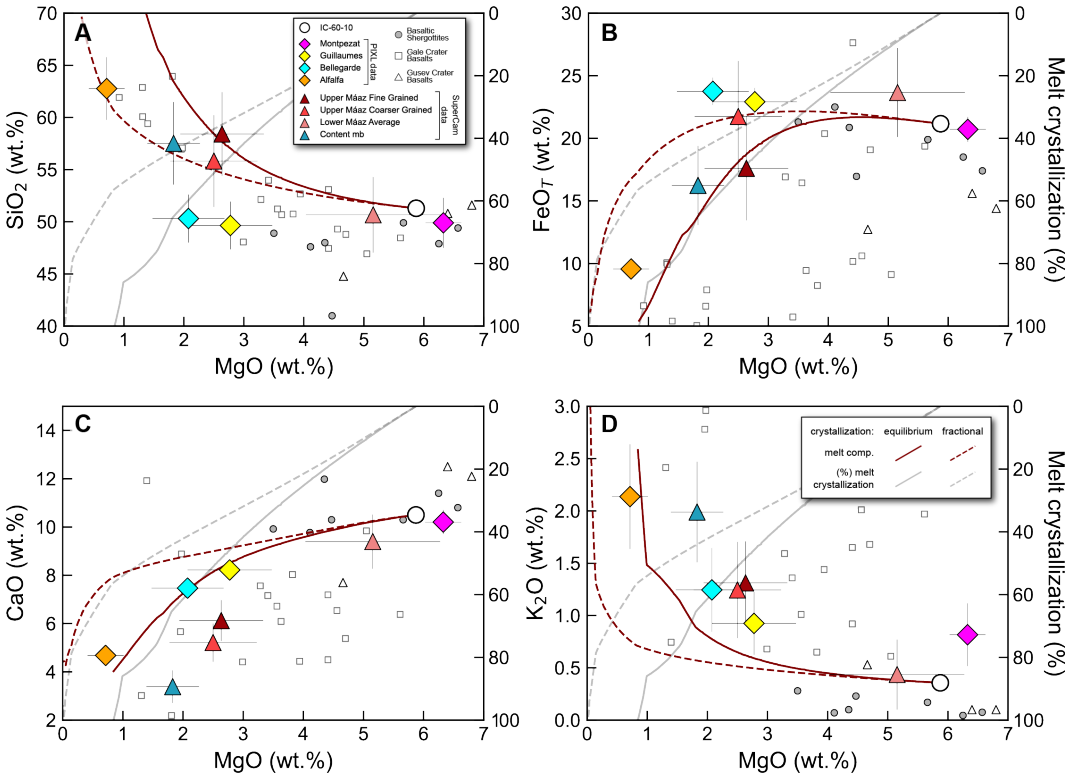


Figure S6.10: Bivariate diagrams showing changes in composition during fractional (dashed red line) and equilibrium (solid red line) crystallization of the preferred parental melt for Quartier (IC-40), represented as liquid lines of descent (LLD). (A) MgO vs. SiO_2; (B) MgO vs. FeO_T; (C) MgO vs. CaO; and (D) MgO vs. K_2O. The weight percent of liquid crystallization is shown by the gray lines for fractional (dashed) and equilibrium (solid) crystallization. Basaltic rocks from Máaz measured by PIXL are shown as colored diamonds, while the triangles are the compositions measured by SuperCam. All the compositions measured by PIXL and SuperCam were normalized to 100 % in the same compositional system as the intercumulus liquids with Perple_X. Basaltic shergottites (grey circles), Gale crater basalts (white squares), and Gusev crater basalts (white triangles) are shown for reference. The initial $Fe^{3+}/\Sigma Fe$ ratio for the melt is assumed to be 0.10.

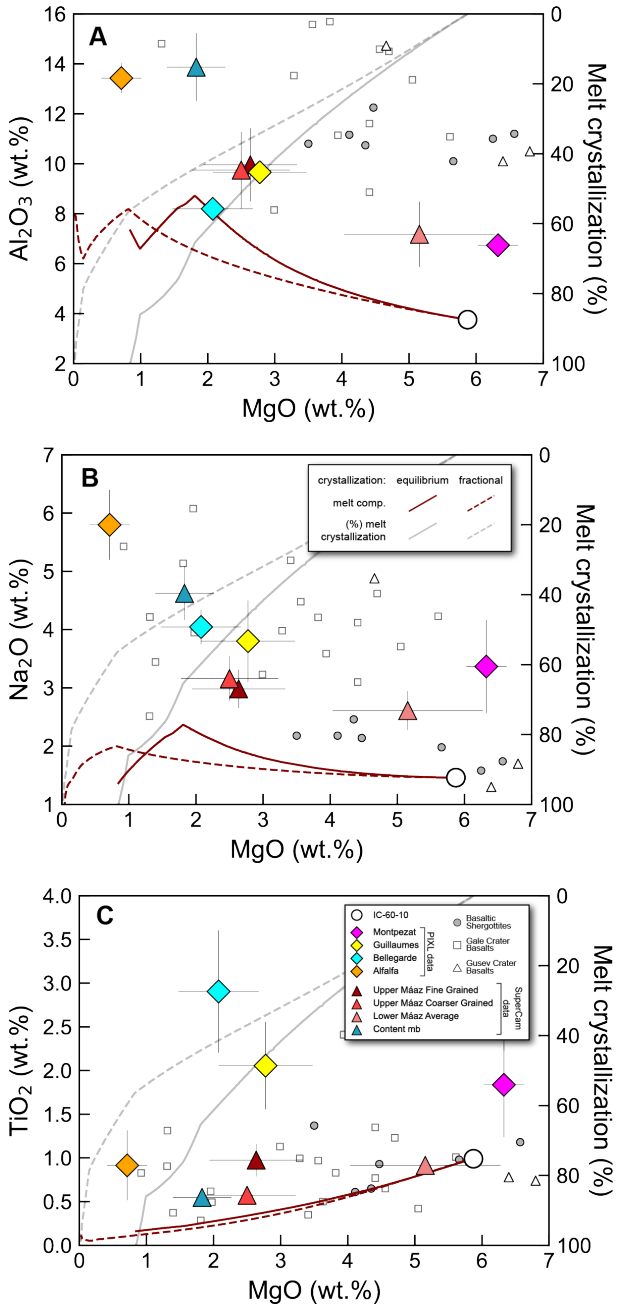


Figure S6.11: Bivariate diagrams showing changes in composition during fractional (dashed red line) and equilibrium (solid red line) crystallization of the preferred parental melt for Quartier, represented as liquid lines of descent (LLD). (A) MgO vs. Al_2O_3; (B) MgO vs. Na_2O; and (C) MgO vs. TiO_2. The weight percent of liquid crystallization is shown by the gray lines for fractional (dashed) and equilibrium (solid) crystallization. Basaltic rocks from Máaz measured by PIXL are shown as colored diamonds, while the triangles are the compositions measured by SuperCam. All the compositions measured by PIXL and SuperCam were normalized to 100 % in the same compositional system as the intercumulus liquids with Perple_X. Basaltic shergottites (grey circles), Gale crater basalts (white squares), and Gusev crater basalts (white triangles) are shown for reference. The initial $Fe^{3+}/\Sigma Fe$ ratio for the melt is assumed to be 0.15. The data points and LLD show only minimal changes with respect to Figure S9

12.5 Additional References

Corpolongo A. et al. 2023. SHERLOC Raman Mineral Class Detections of the Mars 2020 Crater Floor Campaign. *Journal of Geophysical Research: Planets*.

Herzberg C., and O'hara M. J. 1998. *Phase equilibrium constraints on the origin of basalts, picrites, and komatiites. Earth-Science Reviews* 44:39–79.

Lanari P., Vho A., Bovay T., Airaghi L., and Centrella S. 2019. Quantitative compositional mapping of mineral phases by electron probe micro-analyser. *Geological Society, London, Special Publications* 478:39–63.

Mandon L. et al. 2023. Reflectance of Jezero Crater Floor: 2. Mineralogical Interpretation. *Journal of Geophysical Research: Planets*.

Scheller E. L. et al. 2022. Aqueous alteration processes in Jezero crater, Mars—implications for organic geochemistry. *Science* 378:1105–1110.

Siljeström S. et al. 2024. Evidence of Sulfate-Rich Fluid Alteration in Jezero Crater Floor, Mars. *Journal of Geophysical Research: Planets*.

Tice M. M. et al. 2022. Alteration history of Séítah formation rocks inferred by PIXL x-ray fluorescence, x-ray diffraction, and multispectral imaging on Mars. *Science Advances*.